



Deliverable 2.12

## New airfoils for high rotational speed wind turbines

Edited by: Helge Aagaard Madsen

September 2015

Agreement n.:	308974
Duration	November 2012 – October 2017
	DTU Wind



The research leading to these results has received funding from the European Community's Seventh Framework Programme under grant agreement

---

### PROPRIETARY RIGHTS STATEMENT

This document contains information, which is proprietary to the "INN WIND.EU" Consortium. Neither this document nor the information contained herein shall be used, duplicated or communicated by any means to any third party, in whole or in parts, except with prior written consent of the "INN WIND.EU" consortium.

---



## Document information

Document Name:	New airfoils for high rotational speed wind turbines
Document Number:	Deliverable 2.12
Authors:	K Boorsma (ECN), A Muñoz (CENER), B Méndez (CENER), S Gómez (CENER), A Irisarri (CENER), X Munduate (CENER), MG Sieros (CRES), P Chaviaropoulos (CRES/NTUA), S Voutsinas (NTUA), J Prospathopoulos (NTUA), M Manolesos (NTUA), WZ Shen (DTU), WJ Zhu (DTU), HAa Madsen
Document Type	Report
Dissemination level	PU
Review:	Flemming Rasmussen
Date:	September 2015
WP:	WP2: Lightweight Rotor
Task:	Task 2.1: Aerodynamic concepts for high speed, low solidity offshore rotors
Approval:	Approved by Author

## TABLE OF CONTENTS

LIST OF FIGURES & TABLES .....	6
EXECUTIVE SUMMARY .....	13
CHAPTER 1 INTRODUCTION .....	14
1.1 Scope and Objectives .....	14
1.2 Overview of the report.....	14
CHAPTER 2 DESIGN OF HIGH EFFICIENCY THICK AIRFOILS FOR THE OUTER PART OF THE BLADE FOR OFFSHORE APPLICATIONS .....	16
2.1 Scope and objectives.....	16
2.2 Design of a new airfoil family .....	16
2.2.1 Methodology .....	16
2.2.2 Requirements .....	17
2.2.1 Results .....	19
2.2.2 Discussion.....	25
2.3 Application of thick airfoils .....	27
2.3.1 Sectional characteristics.....	27
2.3.2 Blade planform design .....	29
2.3.3 Load case performance .....	35
2.4 Conclusions .....	40
CHAPTER 3 BLADE ROOT AIRFOIL DESIGNS AND ANALYSIS OF AERODYNAMICS - CENER.....	41
3.1 Introduction .....	41
3.2 Study of INN WIND blade root aerodynamics using CFD.....	41
3.2.1 Definition of the tools used during the study .....	43
3.2.2 Calculation of the local operating parameters.....	43
3.2.3 Cases description .....	44
3.2.4 Case 1 .....	45
3.2.5 Case 2 .....	52
3.2.6 Case 3 .....	58
3.2.7 Conclusions.....	63
3.3 State of the art of flat-back and high thickness airfoils.....	64
3.4 XFOIL correction for flat-back and high thickness airfoils .....	68
3.5 Design of root region airfoils .....	75
3.5.1 Dakota and the Genetic Algorithms.....	76
3.5.2 Setting XFOIL parameters .....	78
3.5.3 Design of the 50%-thick airfoil.....	83
3.6 CFD study of the designed airfoils .....	87
3.6.1 40%-thick airfoil .....	87
3.6.2 50%-thick airfoil .....	91
3.7 CFD study of special configurations.....	94
3.7.1 Tripping.....	95
3.7.2 Gurney flap.....	95
3.7.3 Splitter plate.....	97
3.8 Synthesis and conclusions .....	99
CHAPTER 4 DESIGN OF AIRFOILS FOR LOW INDUCTION ROTORS - CRES .....	101
4.1 Scope and objectives.....	101
4.2 Design specifications.....	101

4.3	Design methodology .....	102
4.3.1	Parameterization .....	102
4.3.2	Objective function .....	102
4.3.3	Constrains .....	102
4.3.4	Optimization algorithm .....	103
4.4	Designed airfoils .....	103
4.4.1	18% thick airfoils .....	103
4.4.2	21% thick airfoils .....	106
4.4.3	24% thick airfoils .....	108
4.4.4	30% thick airfoils .....	109
4.4.5	40% thick airfoil .....	111
4.4.6	Inter-family comparisons .....	113
4.5	Synthesis and conclusions .....	115
CHAPTER 5 NUMERICAL SIMULATION OF LOW LIFT AND ELLIPTICALLY SHAPED AIRFOILS DESIGNED BY CRES AND WINDTUNNEL MEASUREMENTS ON AIRFOILS WITH DRAG REDUCTION DEVICES - NTUA		
116		
5.1	Scope and objectives .....	116
5.2	Computational tools and simulations details .....	116
5.2.1	Navier Stokes solver MaPFlow .....	116
5.2.2	Viscous-inviscid interaction solver Foil2w .....	117
5.3	Performance of elliptically shaped airfoils .....	117
5.3.1	Results and discussion .....	118
5.4	Performance of CRES' LL 10-90 profiles .....	122
5.4.1	18% thick airfoil .....	122
5.4.2	21% thick airfoil .....	122
5.4.3	24% thick airfoil .....	122
5.4.4	30% thick airfoil .....	122
5.5	Wind tunnel measurements for the 30% profile .....	125
5.5.1	Description of the experimental set-up .....	125
5.5.2	Pressure measurement results .....	131
5.5.3	Stereo PIV results .....	140
5.5.4	Hot wire results .....	147
5.6	Synthesis and conclusions .....	149
CHAPTER 6 DESIGN AND ANALYSIS OF TIP SECTION AIRFOILS TAKING INTO ACCOUNT COMPRESSIBLE EFFECTS .....		
151		
6.1	Scope and objectives .....	151
6.2	Description of the design method .....	151
6.3	Design code validation .....	152
6.4	Results .....	153
CHAPTER 7 SUMMARY AND CONCLUSIONS .....		
160		
7.1	Detailed conclusions and assessment .....	160
7.2	Final comments to airfoil design .....	162
REFERENCES .....		
163		

## LIST OF FIGURES & TABLES

Figure 2.2-1 Example of geometric parameterization .....	16
Figure 2.2-2 Illustration of profile thickness definition .....	19
Figure 2.2-3 Illustration of TE panel curvature requirement.....	19
Figure 2.2-4 Shape of the 36% thick airfoils .....	20
Figure 2.2-5 Comparison of lift (left) and drag curves (right) for the 36% thick airfoil.....	21
Figure 2.2-6 Comparison of lift over drag ratio (left) and moment (right) for the 36% thick airfoil ...	21
Figure 2.2-7 Shape of the 30% thick airfoils .....	22
Figure 2.2-8 Comparison of lift (left) and drag curves (right) for the 30% thick airfoil.....	23
Figure 2.2-9 Comparison of lift over drag ratio (left) and moment (right) for the 30% thick airfoil ...	23
Figure 2.2-10 Shape of the 24% thick airfoils .....	24
Figure 2.2-11 Comparison of lift (left) and drag curves (right) for the 24% thick airfoil .....	25
Figure 2.2-12 Comparison of lift over drag ratio (left) and moment (right) for the 24% thick airfoil	25
Figure 2.2-13 Calculated statistics of angle of attack variation for DLC1.2 normal turbulence (left) and DLC1.3 extreme turbulence (right) of the INN WIND reference turbine. The minimum and maximum angle of attack are indicated by the triangles, the mean value by the blue circle and three times the standard deviation range by the red lines. ....	26
Figure 2.3-1 Comparison of lift (left) and lift over drag ration (right) between the FFA 24% and 30% thick airfoil, as calculated by RFOIL .....	28
Figure 2.3-2 Comparison of lift (left) and lift over drag ration (right) between the FFA 24% and 30% thick airfoil, using the specified polars within INN WIND .....	28
Figure 2.3-3 Comparison of lift (left) and lift over drag ration (right) between the FFA 24% and ECN 30% thick airfoil, as calculated by RFOIL .....	29
Figure 2.3-4 Comparison of blade planform (chord, twist, thickness) between the INN WIND reference and the redesign using RFOIL.....	30
Figure 2.3-5 Comparison of blade planform (chord, twist, thickness) between the RFOIL reference and the two options of the FFA 30% redesign. The planforms with varying chord or thickness are denoted with <code>_c</code> and <code>_t</code> respectively. ....	32
Figure 2.3-6 Comparison of blade planform (chord, twist, thickness) between the RFOIL reference and the two options of the ECN 30% redesign. The planforms with varying chord or thickness are denoted with <code>_c</code> and <code>_t</code> respectively. ....	34
Figure 2.3-7 Calculated rotor characteristics using Phatas for constant wind velocity (left), together with a zoomed view (right) .....	37
Figure 2.3-8 Comparison of load case performance as a function of time. From top to bottom: wind speed, rotor speed, tip speed ratio and aerodynamic power .....	38
Figure 2.3-9 Comparison of angle of attack variation as a function of time for the load case depicted in Figure 2.3-8. From top to bottom: Rotor azimuth and angle of attack at 84%R for blade 1, 2 and 3.....	39
Figure 3.2-1 Studied airfoils from the INN WIND blade .....	42
Figure 3.2-2 Relationship between several operating parameters of the wind turbine. Lines represent characteristic points (blue if pitch=0). Points represent the studied cases .....	44
Figure 3.2-3 Suction side. Streamlines and studied profiles.....	45
Figure 3.2-4 Suction side. Streamlines and Cfx contours (yellow, Cfx>0 and grey, Cfx<0). ....	45
Figure 3.2-5 Pressure side. Streamlines and studied profiles. ....	45
Figure 3.2-6 Pressure side. Streamlines and Cfx contours (yellow, Cfx>0 and grey, Cfx<0). ....	45
Figure 3.2-7 Pressure contour and streamlines. 3D simulation of the t/c=30% airfoil for “case 1”	46
Figure 3.2-8 Pressure contour and streamlines. 2D simulation of the t/c=30% airfoil for “case 1”	46
Figure 3.2-9 Pressure coefficient. Simulations of the t/c=30% airfoil for “case 1” .....	47
Figure 3.2-10 Friction coefficient “X” direction. Simulations of the t/c=30% airfoil for “case 1” .....	47
Figure 3.2-11 Friction coefficient “Y” direction. Simulations of the t/c=30% airfoil for “case 1” .....	47
Figure 3.2-12 Friction coefficient “Z” direction. Simulations of the t/c=30% airfoil for “case 1” .....	47
Figure 3.2-13 Pressure coefficient. Simulations of the t/c=30% airfoil for “case 1” .....	48
Figure 3.2-14 Pressure contour and streamlines. 3D simulation of the t/c=40% airfoil for “case 1” .....	49

Figure 3.2-15 Pressure contour and streamlines. 2D simulation of the $t/c=40\%$ airfoil for “case 1”	49
Figure 3.2-16 Pressure coefficient. Simulations of the $t/c=40\%$ airfoil for “case 1”	49
Figure 3.2-17 Friction coefficient “X” direction. Simulations of the $t/c=40\%$ airfoil for “case 1”	49
Figure 3.2-18 Friction coefficient “Y” direction. Simulations of the $t/c=40\%$ airfoil for “case 1”	50
Figure 3.2-19 Friction coefficient “Z” direction. Simulations of the $t/c=40\%$ airfoil for “case 1”	50
Figure 3.2-20 Pressure contour and streamlines. 3D simulation of the $t/c=50\%$ airfoil for “case 1”	51
Figure 3.2-21 Pressure contour and streamlines. 2D simulation of the $t/c=50\%$ airfoil for “case 1”	51
Figure 3.2-22 Pressure coefficient. Simulations of the $t/c=50\%$ airfoil for “case 1”	51
Figure 3.2-23 Friction coefficient “X” direction. Simulations of the $t/c=50\%$ airfoil for “case 1”	51
Figure 3.2-24 Friction coefficient “Y” direction. Simulations of the $t/c=50\%$ airfoil for “case 1”	52
Figure 3.2-25 Friction coefficient “Z” direction. Simulations of the $t/c=50\%$ airfoil for “case 1”	52
Figure 3.2-26 Suction side. Streamlines and studied profiles.	52
Figure 3.2-27 Suction side. Streamlines and $C_{fx}$ contours (yellow, $C_{fx}>0$ and grey, $C_{fx}<0$ ).	52
Figure 3.2-28 Pressure side. Streamlines and studied profiles.	53
Figure 3.2-29 Pressure side. Streamlines and $C_{fx}$ contours (yellow, $C_{fx}>0$ and grey, $C_{fx}<0$ ).	53
Figure 3.2-30 Pressure contour and streamlines. 3D simulation of the $t/c=30\%$ airfoil for “case 2”	54
Figure 3.2-31 Pressure contour and streamlines. 2D simulation of the $t/c=30\%$ airfoil for “case 2”	54
Figure 3.2-32 Pressure coefficient. Simulations of the $t/c=30\%$ airfoil for “case 2”	54
Figure 3.2-33 Friction coefficient “X” direction. Simulations of the $t/c=30\%$ airfoil for “case 2”	54
Figure 3.2-34 Friction coefficient “Y” direction. Simulations of the $t/c=30\%$ airfoil for “case 2”	55
Figure 3.2-35 Friction coefficient “Z” direction. Simulations of the $t/c=30\%$ airfoil for “case 2”	55
Figure 3.2-36 Pressure contour and streamlines. 3D simulation of the $t/c=40\%$ airfoil for “case 2”	55
Figure 3.2-37 Pressure contour and streamlines. 2D simulation of the $t/c=40\%$ airfoil for “case 2”	55
Figure 3.2-38 Pressure coefficient. Simulations of the $t/c=40\%$ airfoil for “case 2”	56
Figure 3.2-39 Friction coefficient “X” direction. Simulations of the $t/c=40\%$ airfoil for “case 2”	56
Figure 3.2-40 Friction coefficient “Y” direction. Simulations of the $t/c=40\%$ airfoil for “case 2”	56
Figure 3.2-41 Friction coefficient “Z” direction. Simulations of the $t/c=40\%$ airfoil for “case 2”	56
Figure 3.2-42 Pressure contour and streamlines. 3D simulation of the $t/c=50\%$ airfoil for “case 2”	57
Figure 3.2-43 Pressure contour and streamlines. 2D simulation of the $t/c=50\%$ airfoil for “case 2”	57
Figure 3.2-44 Pressure coefficient. Simulations of the $t/c=50\%$ airfoil for “case 2”	57
Figure 3.2-45 Friction coefficient “X” direction. Simulations of the $t/c=50\%$ airfoil for “case 2”	57
Figure 3.2-46 Friction coefficient “Y” direction. Simulations of the $t/c=50\%$ airfoil for “case 2”	58
Figure 3.2-47 Friction coefficient “Z” direction. Simulations of the $t/c=50\%$ airfoil for “case 2”	58
Figure 3.2-48 Suction side. Streamlines and studied profiles.	58
Figure 3.2-49 Suction side. Streamlines and $C_{fx}$ contours (yellow, $C_{fx}>0$ and grey, $C_{fx}<0$ ).	58
Figure 3.2-50 Pressure side. Streamlines and studied profiles.	58
Figure 3.2-51 Pressure side. Streamlines and $C_{fx}$ contours (yellow, $C_{fx}>0$ and grey, $C_{fx}<0$ ).	59
Figure 3.2-52 Pressure contour and streamlines. 3D simulation of the $t/c=30\%$ airfoil for “case 3”	59
Figure 3.2-53 Pressure contour and streamlines. 2D simulation of the $t/c=30\%$ airfoil for “case 3”	59
Figure 3.2-54 Pressure coefficient. Simulations of the $t/c=30\%$ airfoil for “case 3”	60
Figure 3.2-55 Friction coefficient “X” direction. Simulations of the $t/c=30\%$ airfoil for “case 3”	60
Figure 3.2-56 Friction coefficient “Y” direction. Simulations of the $t/c=30\%$ airfoil for “case 3”	60
Figure 3.2-57 Friction coefficient “Z” direction. Simulations of the $t/c=30\%$ airfoil for “case 3”	60
Figure 3.2-58 Pressure contour and streamlines. 3D simulation of the $t/c=40\%$ airfoil for “case 3”	61

Figure 3.2-59 Pressure contour and streamlines. 2D simulation of the $t/c=40\%$ airfoil for “case 3”	61
Figure 3.2-60 Pressure coefficient. Simulations of the $t/c=40\%$ airfoil for “case 3”	61
Figure 3.2-61 Friction coefficient “X” direction. Simulations of the $t/c=40\%$ airfoil for “case 3”	61
Figure 3.2-62 Friction coefficient “Y” direction. 2D simulation of the $t/c=40\%$ airfoil for “case 3”	62
Figure 3.2-63 Friction coefficient “Z” direction. 2D simulation of the $t/c=40\%$ airfoil for “case 3”	62
Figure 3.2-64 Pressure contour and streamlines. 3D simulation of the $t/c=50\%$ airfoil for “case 3”	62
Figure 3.2-65 Pressure contour and streamlines. 2D simulation of the $t/c=50\%$ airfoil for “case 3”	62
Figure 3.2-66 Pressure coefficient. Simulations of the $t/c=50\%$ airfoil for “case 3”	63
Figure 3.2-67 Friction coefficient “X” direction. Simulations of the $t/c=50\%$ airfoil for “case 3”	63
Figure 3.2-68 Friction coefficient “Y” direction. Simulations of the $t/c=50\%$ airfoil for “case 3”	63
Figure 3.2-69 Friction coefficient “Z” direction. Simulations of the $t/c=50\%$ airfoil for “case 3”	63
Figure 3.3-1 DU airfoils shape (1)	64
Figure 3.3-2 DU airfoils shape (2)	64
Figure 3.3-3 DU airfoils lift (1). Delft experiments	65
Figure 3.3-4 DU airfoils lift (2). Delft experiments	65
Figure 3.3-5 DU airfoils polar (1). Delft experiments	65
Figure 3.3-6 DU airfoils polar (2). Delft experiments	65
Figure 3.3-7 FX airfoils shape (1)	66
Figure 3.3-8 FX airfoils shape (2)	66
Figure 3.3-9 FX airfoils lift (1). Stuttgart experiments	66
Figure 3.3-10 FX airfoils lift (2). Stuttgart experiments	66
Figure 3.3-11 FX airfoils polar (1). Stuttgart experiments	67
Figure 3.3-12 FX airfoils polar (2). Stuttgart experiments	67
Figure 3.4-1 Explanation of the lift curve modification	69
Figure 3.4-2 Explanation of the drag curve modification	70
Figure 3.4-3 DU95W180: Delft experiments, XFOIL calculation and modified curve	70
Figure 3.4-4 DU95W180: Delft experiments, XFOIL calculation and modified curve	70
Figure 3.4-5 DU97W300: Delft experiments, XFOIL calculation and modified curve	71
Figure 3.4-6 DU97W300: Delft experiments, XFOIL calculation and modified curve	71
Figure 3.4-7 FX84W175: Stuttgart experiments, XFOIL calculation and modified curve	71
Figure 3.4-8 FX84W175: Stuttgart experiments, XFOIL calculation and modified curve	71
Figure 3.4-9 FX77-343: Stuttgart experiments, XFOIL calculation and modified curve	72
Figure 3.4-10 FX77-343: Stuttgart experiments, XFOIL calculation and modified curve	72
Figure 3.4-11 FX77-500: Stuttgart experiments, XFOIL calculation and modified curve	72
Figure 3.4-12 FX77-500: Stuttgart experiments, XFOIL calculation and modified curve	72
Figure 3.4-13 Relation between the trailing edge gap and the thickness	74
Figure 3.4-14 Relation between the TE gap and the lift slope error for all the airfoils	74
Figure 3.4-15 Relation between the TE gap and the drag coefficient error for airfoils separated in groups	75
Figure 3.5-1 Evolution of the geometry through generations	77
Figure 3.5-2 Evolution of the objective function through generations	78
Figure 3.5-3 Reference and new airfoil of the 40% thickness	79
Figure 3.5-4 Lift coefficient calculation with XFOIL for the reference and new airfoil of the 40% thickness. Continuous line $n=9$ ; dashed line $n=0.1$	80
Figure 3.5-5 Transition calculation with XFOIL for the reference and new airfoil of the 40% thickness. Continuous line $n=9$ ; dashed line $n=0.1$	80
Figure 3.5-6 Efficiency calculation with XFOIL for the reference and new airfoil of the 40% thickness. Continuous line $n=9$ ; dashed line $n=0.1$	80
Figure 3.5-7 Polar calculation with XFOIL for the reference and new airfoil of the 40% thickness. Continuous line $n=9$ ; dashed line $n=0.1$	80
Figure 3.5-8 Reference and new airfoil of the 40% thickness	81
Figure 3.5-9 Lift coefficient calculation with XFOIL for the reference and new airfoil of the 40% thickness. Continuous line $n=9$ ; dashed line $n=0.1$	82

Figure 3.5-10 Transition calculation with XFOIL for the reference and new airfoil of the 40% thickness. Continuous line $n=9$ ; dashed line $n=0.1$ .....	82
Figure 3.5-11 Efficiency calculation with XFOIL for the reference and new airfoil of the 40% thickness. Continuous line $n=9$ ; dashed line $n=0.1$ .....	82
Figure 3.5-12 Polar calculation with XFOIL for the reference and new airfoil of the 40% thickness. Continuous line $n=9$ ; dashed line $n=0.1$ .....	82
Figure 3.5-13 Reference and new airfoil of the 50% thickness .....	83
Figure 3.5-14 Lift coefficient calculation with XFOIL for the reference and new airfoil of the 50% thickness. Solid line $n=9$ ; dashed line $n=0.1$ .....	84
Figure 3.5-15 Transition calculation with XFOIL for the reference and new airfoil of the 50% thickness. Solid line $n=9$ ; dashed line $n=0.1$ .....	84
Figure 3.5-16 Efficiency calculation with XFOIL for the reference and new airfoil of the 50% thickness. Continuous line $n=9$ ; dashed line $n=0.1$ .....	84
Figure 3.5-17 Polar calculation with XFOIL for the reference and new airfoil of the 50% thickness. Continuous line $n=9$ ; dashed line $n=0.1$ .....	84
Figure 3.5-18 Reference and new airfoil of the 50% thickness .....	85
Figure 3.5-19 Lift coefficient calculation with XFOIL for the reference and new airfoil of the 50% thickness. Continuous line $n=9$ ; dashed line $n=0.1$ .....	86
Figure 3.5-20 Transition calculation with XFOIL for the reference and new airfoil of the 50% thickness. Continuous line $n=9$ ; dashed line $n=0.1$ .....	86
Figure 3.5-21 Efficiency calculation with XFOIL for the reference and new airfoil of the 50% thickness. Continuous line $n=9$ ; dashed line $n=0.1$ .....	86
Figure 3.5-22 Polar calculation with XFOIL for the reference and new airfoil of the 50% thickness. Continuous line $n=9$ ; dashed line $n=0.1$ .....	86
Figure 3.6-1 Lift coefficient calculation with WMB for the reference and new airfoil (L12T7) of the 40% thickness. Solid line, transitional $n=9$ ; dashed line, fully turbulent.....	88
Figure 3.6-2 Polar calculation with WMB for the reference and new airfoil (L12T7) of the 40% thickness. Solid line, transitional $n=9$ ; dashed line, fully turbulent .....	88
Figure 3.6-3 Lift coefficient calculation with WMB for the reference and new airfoil (L12T17) of the 40% thickness. Solid line, transitional $n=9$ ; dashed line, fully turbulent.....	88
Figure 3.6-4 Polar calculation with WMB for the reference and new airfoil (L12T17) of the 40% thickness. Solid line, transitional $n=9$ ; dashed line, fully turbulent .....	88
Figure 3.6-5 Lift coefficient calculation with WMB for the two new airfoils of the 40% thickness. Solid line transitional $n=9$ ; dashed line, fully turbulent .....	89
Figure 3.6-6 Polar calculation with WMB for the two new airfoils of the 40% thickness. Solid line transitional $n=9$ ; dashed line, fully turbulent.....	89
Figure 3.6-7 U velocity contour and streamtraces. 40%-thick reference airfoil. Transitional.....	90
Figure 3.6-8 U velocity contour and streamtraces. 40%-thick reference airfoil. Fully turbulent. ....	90
Figure 3.6-9 U velocity contour and streamtraces. L12T7 reference airfoil. Transitional. ....	90
Figure 3.6-10 U velocity contour and streamtraces. L12T7 reference airfoil. Fully turbulent.....	90
Figure 3.6-11 U velocity contour and streamtraces. L12T17 reference airfoil. Transitional.....	91
Figure 3.6-12 U velocity contour and streamtraces. L12T17 reference airfoil. Fully turbulent.....	91
Figure 3.6-13 Lift coefficient calculation with WMB for the reference and new airfoil (L11T6) of the 50% thickness. Solid line transitional $n=9$ ; dashed line, fully turbulent.....	91
Figure 3.6-14 Polar calculation with WMB for the reference and new airfoil (L11T6) of the 50% thickness. Solid line transitional $n=9$ ; dashed line, fully turbulent .....	91
Figure 3.6-15 Lift coefficient calculation with WMB for the reference and new airfoil (L11T17) of the 50% thickness. Solid line transitional $n=9$ ; dashed line, fully turbulent.....	92
Figure 3.6-16 Polar calculation with WMB for the reference and new airfoil (L11T17) of the 50% thickness. Solid line transitional $n=9$ ; dashed line, fully turbulent .....	92
Figure 3.6-17 Lift coefficient calculation with WMB for the two new airfoils of the 50% thickness. Solid line transitional $n=9$ ; dashed line, fully turbulent .....	92
Figure 3.6-18 Polar calculation with WMB for the two new airfoils of the 50% thickness. Solid line transitional $n=9$ ; dashed line, fully turbulent.....	92
Figure 3.6-19 U velocity contour and streamtraces. 50%-thick reference airfoil. Transitional. ....	93
Figure 3.6-20 U velocity contour and streamtraces. 50%-thick reference airfoil. Fully turbulent. ....	93

Figure 3.6-21 U velocity contour and streamtraces. L11T6 reference airfoil. Transitional. ....	93
Figure 3.6-22 U velocity contour and streamtraces. L11T6 reference airfoil. Fully turbulent. ....	93
Figure 3.6-23 U velocity contour and streamtraces. L11T17 reference airfoil. Transitional. ....	94
Figure 3.6-24 U velocity contour and streamtraces. L11T17 reference airfoil. Fully turbulent. ....	94
Figure 3.7-1 Lift coefficient for the L11T6 for transitional and tripped calculations. ....	95
Figure 3.7-2 Polar curve for the L11T6 for transitional and tripped calculations. ....	95
Figure 3.7-3 Gurney flap geometries. ....	96
Figure 3.7-4 Lift coefficient for the L11T6 and the gurney flap configurations. Fully turbulent calculations. ....	96
Figure 3.7-5 Polar curve for the L11T6 and the gurney flaps configurations. Fully turbulent calculations. ....	96
Figure 3.7-6 U velocity contour and streamtraces. L11T6 airfoil. Fully turbulent. TE detail. ....	97
Figure 3.7-7 U velocity contour and streamtraces. L11T6 airfoil with gurney_flap_1. Fully turbulent. TE detail. ....	97
Figure 3.7-8 Splitter plate geometries ....	97
Figure 3.7-9 Lift coefficient for the L11T6 and the splitter plate geometries Fully turbulent calculations. ....	98
Figure 3.7-10 Polar curve for the L11T6 and the splitter plate geometries. Fully turbulent calculations. ....	98
Figure 3.7-11 U velocity contour and streamtraces. L11T6 airfoil. Fully turbulent. TE detail. ....	98
Figure 3.7-12 U velocity contour and streamtraces. L11T6 airfoil with splitter_plate_2. Fully turbulent. TE detail. ....	98
Figure 4.4-1: Three airfoil designs of 18% thickness. LL stands for Low Lift while HL for High Lift. The weighting percentages (laminar – turbulent) are also shown in the legend. ....	104
Figure 4.4-2: Lift and drag (left) versus angle of attach ‘alfa’ for the 18% LL 10-90 airfoil. XFOIL calculations have been performed for three different transition settings, fully turbulent, N=4 and N=9. The transition location along the airfoil suction and pressure side for different ‘alfa’ is shown in the right figure ....	105
Figure 4.4-3: Performance (L/D) of the three 18% airfoils for the three different transition settings considered ....	105
Figure 4.4-4: Three airfoil designs of 21% thickness. LL stands for Low Lift while HL for High Lift. The weighting percentages (laminar – turbulent) are also shown in the legend ....	106
Figure 4.4-5: Lift and drag (left) versus angle of attach ‘alfa’ for the 21% LL 10-90 airfoil. XFOIL calculations have been performed for three different transition settings, fully turbulent, N=4 and N=9. The transition location along the airfoil suction and pressure side for different ‘alfa’ is shown in the right figure ....	107
Figure 4.4-6: Performance (L/D) of the three 21% airfoils for the three different transition settings considered ....	107
Figure 4.4-7: Three airfoil designs of 24% thickness. LL stands for Low Lift while HL for High Lift. The weighting percentages (laminar – turbulent) are also shown in the legend ....	108
Figure 4.4-8: Lift and drag (left) versus angle of attach ‘alfa’ for the 24% LL 10-90 airfoil. XFOIL calculations have been performed for three different transition settings, fully turbulent, N=4 and N=9. The transition location along the airfoil suction and pressure side for different ‘alfa’ is shown in the right figure ....	108
Figure 4.4-9: Performance (L/D) of the three 24% airfoils for the three different transition settings considered ....	109
Figure 4.4-10: Three airfoil designs of 30% thickness. LL stands for Low Lift while HL for High Lift. The weighting percentages (laminar – turbulent) are also shown in the legend ....	110
Figure 4.4-11: Lift and drag (left) versus angle of attach ‘alfa’ for the 30% LL 20-80 airfoil. XFOIL calculations have been performed for three different transition settings, fully turbulent, N=4 and N=9. The transition location along the airfoil suction and pressure side for different ‘alfa’ is shown in the right figure ....	110
Figure 4.4-12: Performance (L/D) of the three 30% airfoils for the three different transition settings considered ....	111
Figure 4.4-13: LL 20-80 airfoil designs of 40% thickness. ....	112

Figure 4.4-14: Lift and drag (left) versus angle of attach 'alfa' for the 40% LL 20-80airfoil. XFOIL calculations have been performed for three different transition settings, fully turbulent, N=4 and N=9. The transition location along the airfoil suction and pressure side for different 'alfa' is shown in the right figure ..... 112

Figure 4.4-15: Performance (L/D) of the three 40% airfoils for the three different transition settings considered ..... 113

Figure 4.4-16: The family of Low Lift profiles. Left the 30-70 and right the 10-90/20-80 designs 113

Figure 4.4-17: Performance (L/D) of the Low Lift family profiles at fully turbulent flow conditions. Left the 30-70 and right the 1<sub>(2)</sub>0-9<sub>(8)</sub>0 designs ..... 114

Figure 4.4-18: Performance (L/D) of the Low Lift family profiles for N=4. Left the 30-70 and right the 1<sub>(2)</sub>0-9<sub>(8)</sub>0 designs ..... 114

Figure 5.3-1: NTUA-25% elliptic airfoil..... 117

Figure 5.3-2 Lift and drag curves for the NACA64418..... 119

Figure 5.3-3: Comparison of efficiency plots from all the cases considered ..... 120

Figure 5.3-4: Snapshots indicating the wake development at two angles of attack Compared to a sharp edged flat back airfoil, instead of well-formed vortex structures, elongated regions of shear are formed that are attenuated quickly. .... 121

Figure 5.4-1: Performance (L/D) of the 18% LL 10-90 airfoil for transitional and fully turbulent flow conditions. Comparison among MaPFlow (CFD solver), Foil2w (viscous-inviscid interaction solver) and XFOIL calculations. Fixed transition locations were taken from XFOIL using the e<sup>N</sup> model with N=4..... 123

Figure 5.4-2: Performance (L/D) of the 21% LL 10-90 airfoil for transitional and fully turbulent flow conditions. Comparison among MaPFlow (CFD solver), Foil2w (viscous-inviscid interaction solver) and XFOIL calculations. Fixed transition locations were taken from XFOIL using the e<sup>N</sup> model with N=4..... 123

Figure 5.4-3: Performance (L/D) of the 24% LL 10-90 airfoil for transitional and fully turbulent flow conditions. Comparison among MaPFlow (CFD solver), Foil2w (viscous-inviscid interaction solver) and XFOIL calculations. Fixed transition locations were taken from XFOIL using the e<sup>N</sup> model with N=4..... 124

Figure 5.4-4: Performance (L/D) of the 30% LL 20-80 airfoil for transitional and fully turbulent flow conditions. Comparison among MaPFlow (CFD solver), Foil2w (viscous-inviscid interaction solver) and XFOIL calculations. Fixed transition locations were taken from XFOIL using the e<sup>N</sup> model with N=4..... 124

Figure 5.5-1: The LI30 and the LI30-FB10 airfoil profiles..... 125

Figure 5.5-2: Detail of the FB airfoil TE. 1<sup>st</sup> group of Drag Reduction Devices ..... 127

Figure 5.5-3: Detail of the FB airfoil TE. 2<sup>nd</sup>group of Drag Reduction Devices ..... 128

Figure 5.5-4: Drawing of the wing model with Flap + Splitter device ..... 128

Figure 5.5-5: Schematic planform view of the test set up showing the wing, the fences, the pressure and the Stereo PIV cameras along with the measurement plane and the camera contained angle ( $\varphi$ ) is also indicated. .... 129

Figure 5.5-6: Sample size effect on the measured streamwise velocity component (U) at a point right after the plane wing TE. .... 131

Figure 5.5-7: Hot wire probe location ..... 131

Figure 5.5-8: Lift coefficient variation with angle of attack for the LI30 airfoil under tripped and untripped conditions ..... 132

Figure 5.5-9: Drag coefficient variation with angle of attack for the LI30 airfoil under tripped and untripped conditions ..... 133

Figure 5.5-10: L/D variation with lift coefficient for the LI30 airfoil under tripped and untripped conditions..... 133

Figure 5.5-11: Lift coefficient variation with angle of attack for the LI30 airfoil under tripped and untripped conditions ..... 134

Figure 5.5-12: Drag coefficient variation with angle of attack for the LI30 airfoil under tripped and untripped conditions ..... 134

Figure 5.5-13: L/D variation with lift coefficient for the LI30 airfoil under tripped and untripped conditions..... 135

Figure 5.5-14: Lift coefficient variation with angle of attack. Comparison between the plane airfoil and the airfoil with Splitter, Cavity, Extended Cavity, Offset Cavity and Flap .....	136
Figure 5.5-15: Drag coefficient variation with angle of attack. Comparison between the plane airfoil and the airfoil with Splitter, Cavity, Extended Cavity, Offset Cavity and Flap .....	136
Figure 5.5-16: L/D variation with lift coefficient. Comparison between the plane airfoil and the airfoil with Splitter, Cavity, Extended Cavity, Offset Cavity and Flap .....	137
Figure 5.5-17: Lift coefficient variation with angle of attack. Comparison between the airfoil with Offset Cavity, Flap, Flap + Splitter, Flap + Cavity, Flap + Extended Cavity and Flap + Offset Cavity	138
Figure 5.5-18: Drag coefficient variation with angle of attack. Comparison between the airfoil with Offset Cavity, Flap, Flap + Splitter, Flap + Cavity, Flap + Extended Cavity and Flap + Offset Cavity	138
Figure 5.5-19:L/D variation with lift coefficient. Comparison between the airfoil with Offset Cavity, Flap, Flap + Splitter, Flap + Cavity, Flap + Extended Cavity and Flap + Offset Cavity .....	139
Figure 5.5-20: Pressure coefficient distribution along the wing chord at $\alpha = 6.4^\circ$ for the plane airfoil and the airfoil with Flap, Offset Cavity and Flap with Offset Cavity .....	140
Figure 5.5-21: Stereo PIV measurement window for each case .....	141
Figure 5.5-22: Mean velocity magnitude contours and streamlines. The location of the saddle point in the wake is also indicated. ....	142
Figure 5.5-23: Spanwise vorticity contours.....	143
Figure 5.5-24: $u'v'$ shear Reynolds stress contours.....	144
Figure 5.5-25: $u'u'$ normal Reynolds stress contours .....	145
Figure 5.5-26: $v'v'$ normal Reynolds stress contours.....	146
Figure 5.5-27: Definition of $h^*$ for each TE device.....	148
Figure 5.5-28: St and St* data for the plane airfoil and the four best performing drag reduction devices .....	149
Table 2.2-1 – Aerodynamic performance requirement specification.....	18
Table 2.2-2 – TE thickness requirement specification.....	18
Table 2.2-3 – Overview of operational conditions as input to RFOIL .....	20
Table 2.3-1 – Performance of INN WIND reference versus the RFOIL redesign .....	30
Table 2.3-2 – Performance of RFOIL reference versus the FFA 30% redesigns. ....	32
Table 2.3-3 – Performance of RFOIL reference versus the ECN 30% redesigns. ....	34
Table 2.3-4 – Summary of load case performance averaged over relevant load cases for 9 m/s average wind speed .....	37
Table 3.2-1 – Airfoil thickness and position along the blade .....	42
Table 3.2-2 – Operating condition of the studied cases.....	45
Table 3.2-3 – Local operating conditions for the selected blade sections in “case 1” .....	46
Table 3.2-4 – Pressure lift coefficient for the different simulations. "Case2" airfoil t/c=30% .....	48
Table 3.2-5 – Local operating conditions for the selected blade sections in “case 2” .....	53
Table 3.2-6 – Local operating conditions for the selected blade sections in “case 3” .....	59
Table 3.3-1 – Summary of the state-of-the-art for high-thickness blunt-trailing-edge airfoils characteristics .....	68
Table 3.4-1 – Numerical values used for the correction of XFOIL data .....	73
Table 3.5-1 – Design parameters for the L12T7 .....	79
Table 3.5-2 – Design parameters for the L12T17 .....	81
Table 3.5-3 – Design parameters for the L11T6.....	83
Table 3.5-4 – Design parameters for the L11T6.....	85
Table 3.5-5 – Corrected XFOIL data for the reference and the design airfoils .....	87
Table 3.6-1 – WMB data for the reference and the design airfoils .....	94
Table 3.7-1 – WMB data for the L11T6 airfoil and the special configurations .....	99
Table 4.2-1–Intended thickness and operating conditions .....	101

## EXECUTIVE SUMMARY

The rotor concept studies carried out at an early stage in the INN WIND.EU project [1] showed the need for dedicated airfoil designs to realize the full potential of the new rotor designs. One of the overall tendencies in the new rotor designs is the use of more slender and longer blades. Slender blades can be achieved by using thicker airfoils which means that the chord can be decreased for the same load on the blade. The use of a 30% thick airfoil out to the tip of the blade has been investigated (ECN, Chapter 2). Decreasing the chord means a lower solidity for the rotor which gives room for increasing the blade length, at least considering quasi steady loads. However, the aerodynamic loading on the blade can also be lowered by operating the turbine at a lower lift which is the basic idea behind the Low Induction Rotor (LIR). This requires dedicated airfoils for the outer part of the blade which are designed for operation at a low lift of e.g. 0.8 (CRES, Chapter 4).

The inboard rotor aerodynamics are complex due to the combination of thick airfoils needed for carrying the high bending moments and the big variations in angle of attack AoA caused by the low tangential velocity component which means that the variation in axial inflow causes bigger variations in AoA than at the tip of the blade. Some separation of the flow at the trailing edge is thus often seen even below rated power leading to 3D flow due to a spanwise flow component. These complex flow mechanisms have been investigated in Chapter 3 by CENER in order to have an improved basis for design of thick blade root airfoils. The improved design basis comprised an adaptation of the XFOIL code to simulate such thick airfoils and afterwards design of different versions of a 40 and 50% airfoil was demonstrated.

Aerodynamic characteristics of thick airfoils have further been investigated by wind tunnel measurements on a 30% root airfoil, designed by CRES, and conducted by NTUA (Chapter 5). The measurements comprised surface pressure measurements as well as PIV flow field measurements. Several trailing edge add-on devices were also tested.

Increasing the tip speed is also a way to achieve a more slender blade design. However, increasing the speed above e.g. 90m/s indicates that compressible effects should be taken into account in the airfoil and blade design [1]. Such airfoil designs including compressible effects have been demonstrated (DTU Chapter 6) by design of an airfoil for the tip part of the two-bladed version of the 10MW reference rotor.

## CHAPTER 1 INTRODUCTION

### 1.1 Scope and Objectives

The work reported here covers the activities in Subtask 2.1.2 “New aerofoil design” in the Innwind.EU project. Subtask 2.1.2 is one of three subtasks in TASK 2.1 “Aerodynamic concepts for high speed, low solidity offshore rotors”. Within this task, aerodynamic concepts for high speed, low solidity offshore rotors are explored, designed and analysed. In the first part of the project within Subtask 2.1.1 “New aerodynamic blade designs” a number of rotor concepts were studied comprising e.g. the Low Induction Rotor (LIR) concept and a two-bladed version of the 10MW INN WIND Reference Wind Turbine [1]. It was realized during these rotor concept studies that in order to obtain the full potential as concerns power production and load limits, new airfoil designs were required with performance characteristics matching the requirements originating from the rotor optimizations. As an example it was shown that the LIR rotor should have airfoils with optimal performance at a design lift around 0.8 where the common operating lift range for present wind turbine airfoils is 1.2-1.3.

The specific targets of the reported work are:

- Airfoils with a low maximum lift for low induction rotors will be designed. The impact of using high performance, thick airfoils on the outer part of the blade will be investigated.
- For the inner part of the blade a specific root airfoil will be designed.
- The influence of compressible effects on airfoil characteristics and performance at high/ inflow speed will be explored.
- New airfoil designs taking into account compressible effects in the design process will be carried out.

### 1.2 Overview of the report

The work within the subtask was divided by the five partners ECN, CENER, CRES, NTUA and DTU into the following contributions:

ECN:

- Design of a new family of advanced airfoils for offshore application
- Investigate the impact of high efficiency thick airfoils at the outer part of the blade
- Investigate the impact of non conventional thick airfoils on the rotor performance

CENER:

- Study of the INN WIND rotor root airfoil aerodynamics
- Design of root airfoil using CENER´s airfoil design tool
- CFD calculations to characterize the new airfoil performance using CENER´s CFD code WMB

CRES:

- Design of airfoils for low induction rotors. Low lift airfoils for thicknesses of 24%, 30% and 36%, as replacement for the FFA airfoils in an alternative design

NTUA:

- Numerical simulation of the 24%, 30% and 36% thick airfoils designed by CRES
- Wind tunnel measurements and numerical simulation of the 36% airfoil in various configurations
- Numerical simulation of elliptically shaped airfoils

DTU:

- Carry out simplified investigations with the XFOIL, Q3UIC and FLUENT codes to see the main effects on airfoil performance of compressibility
- Design an aerofoil for the tip section of the two-bladed rotor for a tip speed of 110 m/s

The above partner contributions are presented in five separate chapters which follow below. Finally there is a chapter with summary and conclusions.

## CHAPTER 2 DESIGN OF HIGH EFFICIENCY THICK AIRFOILS FOR THE OUTER PART OF THE BLADE FOR OFFSHORE APPLICATIONS

K Boorsma

### 2.1 Scope and objectives

The contribution of ECN is focused on development of technology for application in offshore wind energy. As such a new airfoil family for offshore applications is developed, as described in Section 2.2. In addition to that the application of thick airfoils towards the outboard section is researched both in terms of sectional performance as well as the effect on blade design and corresponding performance. Here, also the application of the developed airfoils as described in Section 2.2 is under consideration. This part of the work is described in Section 2.3, followed by the conclusions in Section 2.4.

### 2.2 Design of a new airfoil family

A new airfoil family is designed for application to offshore wind turbines. The airfoils are designed for a conventional rotor and blade design in the sense that the axial induction factor for design conditions in partial load approximates  $1/3$  in accordance with the Betz limit for a maximum power coefficient. For this particular study the airfoils were designed with this concept in mind, and focus was given to the application in an offshore environment. The resulting profiles will be evaluated by comparison to the FFA profiles that were used for the INN WIND reference turbine. As such the most important Sections are the 36%, 30% and 24% thick airfoils as they cover the largest and most important part of the blade (from 30%R to the tip). Hence the research focuses on these three profiles. The following sections give more detail about the methodology, requirements and finally the results.

#### 2.2.1 Methodology

In the present work, a numerical optimization based approach has been used in order to have an efficient design method able to deal with multiple requirements coming from different disciplines. In particular, a gradient based algorithm (GBA) [2] has been used. The shape of the airfoils is described by 4 Bezier curves of third order, in accordance with the formulation proposed by Grasso [3]. An example of the parameterization is sketched in Figure 2.2-1. The design variables are the vertical and horizontal positions of the control points.

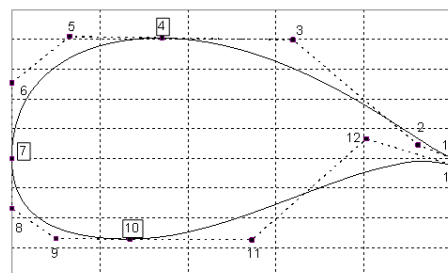


Figure 2.2-1 Example of geometric parameterization

During the design, the ECN panel code RFOIL [4] has been implemented to calculate the performance of the candidate shapes. RFOIL is a modified version of XFOIL [5] featuring an improved prediction around the maximum lift coefficient and capabilities of predicting the effect of rotation on airfoil characteristics. Regarding the maximum lift in particular, numerical stability improvements were obtained by using the Schlichting velocity profiles for the turbulent boundary layer, instead of the Swafford velocity profiles. Furthermore, the shear lag coefficient in Green's lag entrainment equation of the turbulent boundary-layer model was adjusted, and deviation from the equilibrium flow has been coupled to the shape factor of the boundary layer.

### 2.2.2 Requirements

The novelty of the present work is that the goal of the design process is not to obtain a single airfoil, but a complete set of geometries with good aerodynamic and structural characteristics. In addition to this, those characteristics and the geometrical properties should vary in a consistent and gradual way so that they are compatible with each other and the blending of the sections is not affected by strange bumps or irregularities.

Using numerical optimization approach during the design implies that all the above mentioned properties and characteristics must be "translated" in terms of requirements. In order to have a family of airfoils, these requirements should be general to be applicable to the complete set of airfoils but, at the same time, able to describe a certain need at a specific area of the blade.

In the present work, a weighted combination of the aerodynamic efficiency and sectional moment of resistance has been adopted as objective function, where the aerodynamic efficiency takes into account the aerodynamics while the moment of resistance counts the structural requirements. Depending on the value of the weighting factor, the design can be driven by aerodynamics or structure.

#### Qualitative requirements

A qualitative description of some key design issues is given below:

- Airfoil must meet stall margin and L/D requirements in rough conditions
- Airfoil should try to maximise clean L/D performance, but not at the expense of rough falling below specified values
- Airfoil must have adequate stall margins
- Airfoil should have gentle stall behaviour
- Airfoil must have high structural efficiency
- Airfoil must have a shape that is easy to manufacture

#### Design conditions

The airfoils were designed to match with specific conditions. For the 30% thick airfoil these were:

- Reynolds number of 6 million (6e6)
- Mach number of 0.2
- Critical amplification factor (N-value) of 9
- Tripped conditions

- 5% chord from LE on upper surface (suction)
- 10% chord from LE on lower surface (pressure)

### Aerodynamic requirements

A more quantitative description of the aerodynamic requirements for this profile is given in Table 4.2-1.

Metric – 30% airfoil	Requirement
RE design ( $\times 10^6$ )	6
CL <sub>op</sub>	1.1
Clean L/D @ CL <sub>op</sub>	>144
Rough L/D @ AoA <sub>op</sub>	>73
Rough CL @ AoA <sub>op</sub>	>1.05
CL <sub>max</sub> (clean)	<2.0
Stall margin to CL <sub>design</sub> (clean)	>3.5deg
Stall margin to CL <sub>design</sub> (rough)	>3.5deg
Stall margin to CL <sub>op</sub> (clean)	>5.0deg
Stall margin to CL <sub>op</sub> (rough)	>5.0deg
CL <sub>max</sub> – CL@AoA <sub>max</sub> +1° (clean)	<0.2
-ve CL <sub>max</sub> (clean)	>-1.0
CM @ CL <sub>op</sub> (clean)	>-0.17

Table 2.2-1 – Aerodynamic performance requirement specification

### Structural requirements

Structural metrics are given either as guides or as specific limits.

#### Flapwise stiffness metric

The flapwise stiffness metric should be calculated as follows:

- Find chordwise location of max. thickness
- Average the thickness values across a 30% chord span, centred at maximum thickness as follows:
  - Take 10 equally spaced points
  - Calculate sum-of-squares average

The value of the metric should be no less than 0.27.

#### Area metric

The area metric is the internal area of the airfoil shape calculated from the unit coordinates. The value of the metric should be no less than 0.16.

#### TE thickness

Location (X)	t/c as % chord (Y)
70% chord	>9
90% chord	>3
100% chord (TE)	>1

Table 2.2-2 – TE thickness requirement specification

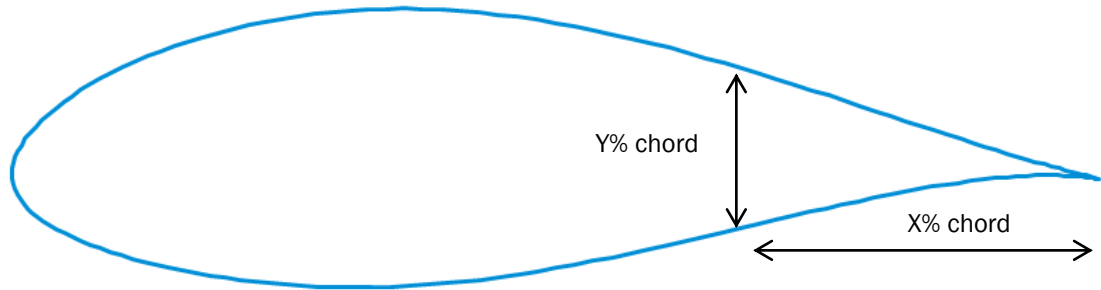


Figure 2.2-2 Illustration of profile thickness definition

*TE panel curvature*

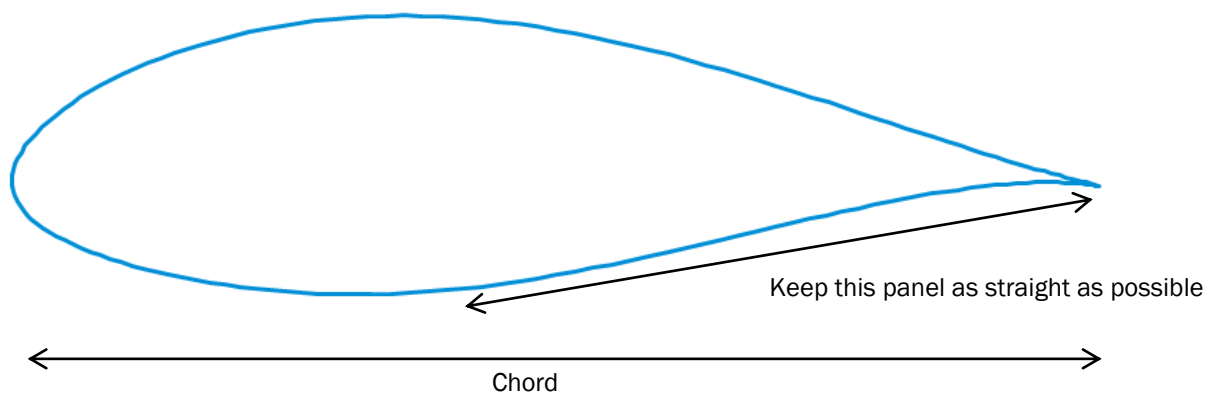


Figure 2.2-3 Illustration of TE panel curvature requirement

### 2.2.1 Results

The resulting profiles are compared to the original FFA profiles from the INN WIND reference rotor. For each profile first the geometry is compared after which the airfoil polars are determined using RFOIL. It is known from comparison to wind tunnel data that the RFOIL drag prediction is yielding relatively low values. Therefore a modified version of RFOIL is used here that adds an empirical drag correction using the momentum thickness [6]. The external conditions (Reynolds number, Mach number, chord to radius ratio) are based on the same reference rotor. For the first two parameters, a minimum and maximum corresponding to the operating range is determined based on blade geometry and specified operational conditions. In addition to that, airfoil performance is computed for both clean (free transition,  $N=9$ ) and rough conditions (transition fixed at 5% chord for both upper and lower surface). This yields a total of 4 polars for each profile. The corresponding conditions used can be found in Table 2.2-3.

To exclude comparison differences due to different aerodynamic solvers (the supplied FFA polars within INN WIND are determined using EllipSys), the polars for the FFA profiles are also calculated using RFOIL.

t/c [%]	Re1 [M]	Re2 [M]	M1 [-]	M2 [-]	c/r1 [-]	c/r2 [-]	transition	
36	6.9	14.3	0.05	0.10	0.24	0.24	free	fixed
30	8.3	17.3	0.06	0.14	0.15	0.15	free	fixed
24	7.9	13.2	0.14	0.24	0.03	0.03	free	fixed

Table 2.2-3 – Overview of operational conditions as input to RFOIL

### 36% thick airfoil

A shape comparison of the 36% thick airfoils is included in Figure 2.2-4. Large differences are notable in the pressure side from 30% chord onwards due to the addition of aft loading. The resulting shape curve towards the pressure side trailing edge might be fragile from a structural point of view.

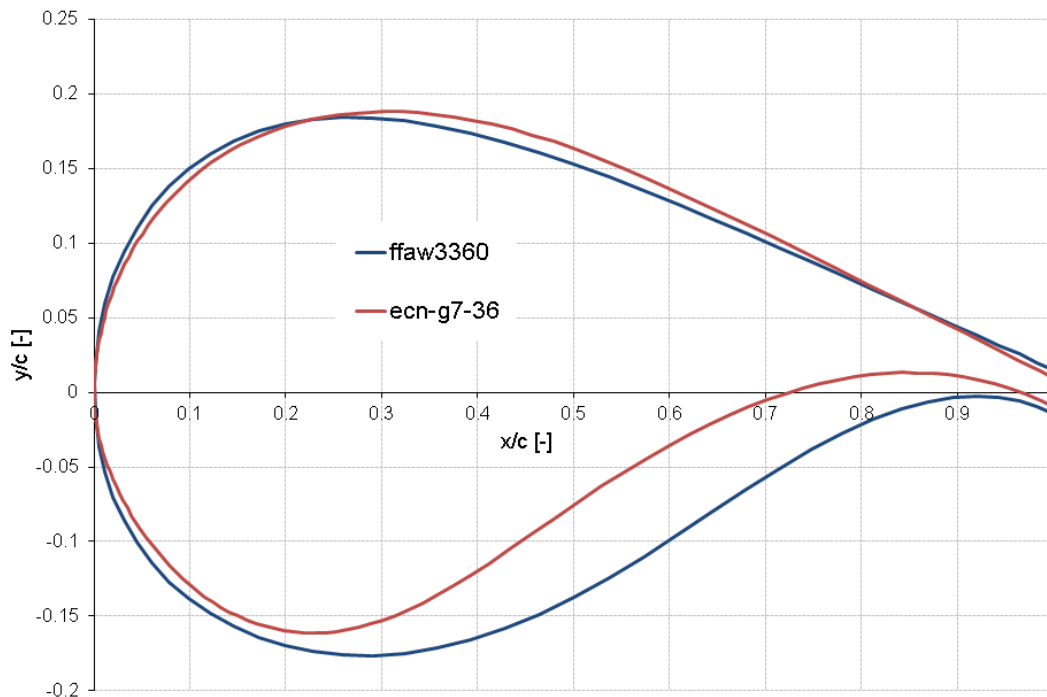


Figure 2.2-4 Shape of the 36% thick airfoils

The resulting predictions are included in Figure 2.2-5 and Figure 2.2-6. For each airfoil, polars are shown for the high Reynolds number (clean and rough) and the low Reynolds number (clean only) from Table 2.2-3, to also illustrate a possible Reynolds effect for the clean configuration. It is clear from the lift curves that the addition of aft loading leads to a lower zero lift angle of attack compared to the FFA airfoil. The high absolute values of the lift coefficient can be explained by the incorporation of rotational effects. Also, for higher angles of attack, the calculations for the newly developed airfoil are not converged and hence a statement about the stall performance is difficult to make. The addition of roughness influences the slope of the  $C_l$ - $\alpha$  curve in the attached flow region. The level of the drag values are comparable between the profiles, slightly lower for the newly developed airfoil. A statement on the resulting lift over drag ratio is again difficult to make, although it can be expected that the maximum is reached at lower angles of attack

compared to the FFA airfoil. The increase in camber comes together with a significantly lower moment coefficient.

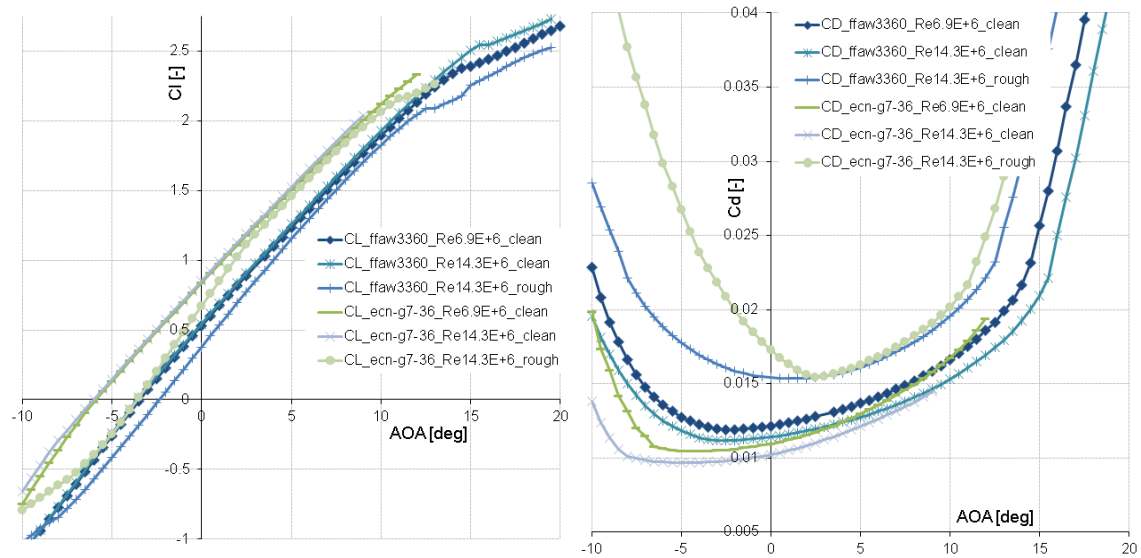


Figure 2.2-5 Comparison of lift (left) and drag curves (right) for the 36% thick airfoil

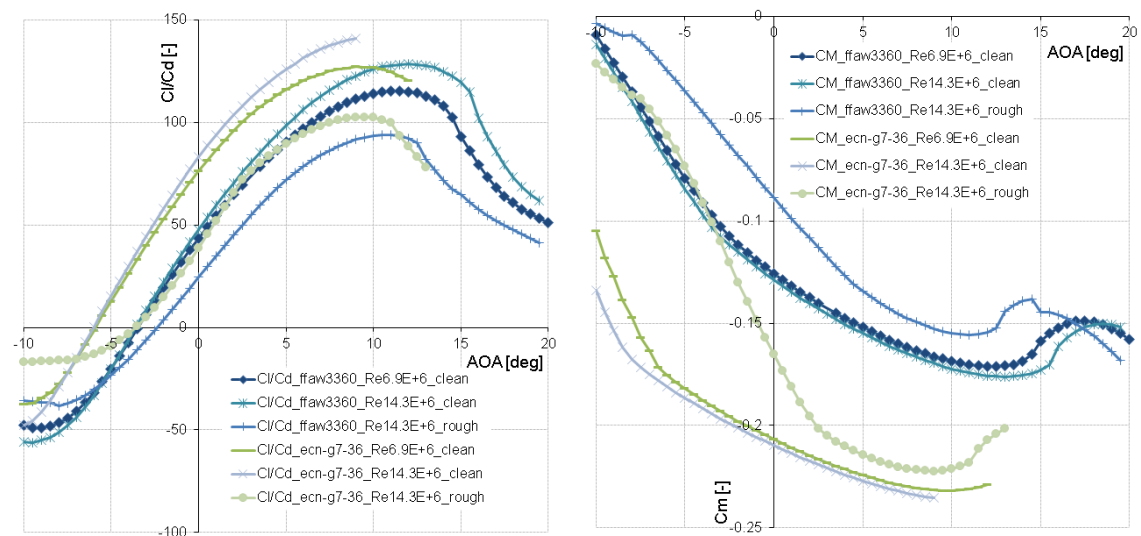


Figure 2.2-6 Comparison of lift over drag ratio (left) and moment (right) for the 36% thick airfoil

### 30% thick airfoil

A shape comparison of the 30% thick airfoils is included in Figure 2.2-7. Although again more aft loading is added, this is counterbalanced by a reduction of camber on the first 30% of the chord on the suction side. The trailing edge is slightly thinner.

The resulting polars are included in Figure 2.2-8 and Figure 2.2-9. As a result of the counterbalancing in the shape, the attached flow part of the lift curve is similar between the two profiles, although there is some divergence for low angles of attack (below 0 degree). The lift coefficient falls off earlier for the developed airfoil, resulting in a lower maximum lift coefficient. As a result the lift over drag ratio is slightly higher, but the maximum is also narrower in the sense that it is only maintained for a small angle of attack range. The performance in terms of lift over drag ratio is similar in rough conditions. The lift decrease on the nose combined with the aft loading results in a significant decrease of the moment coefficient.

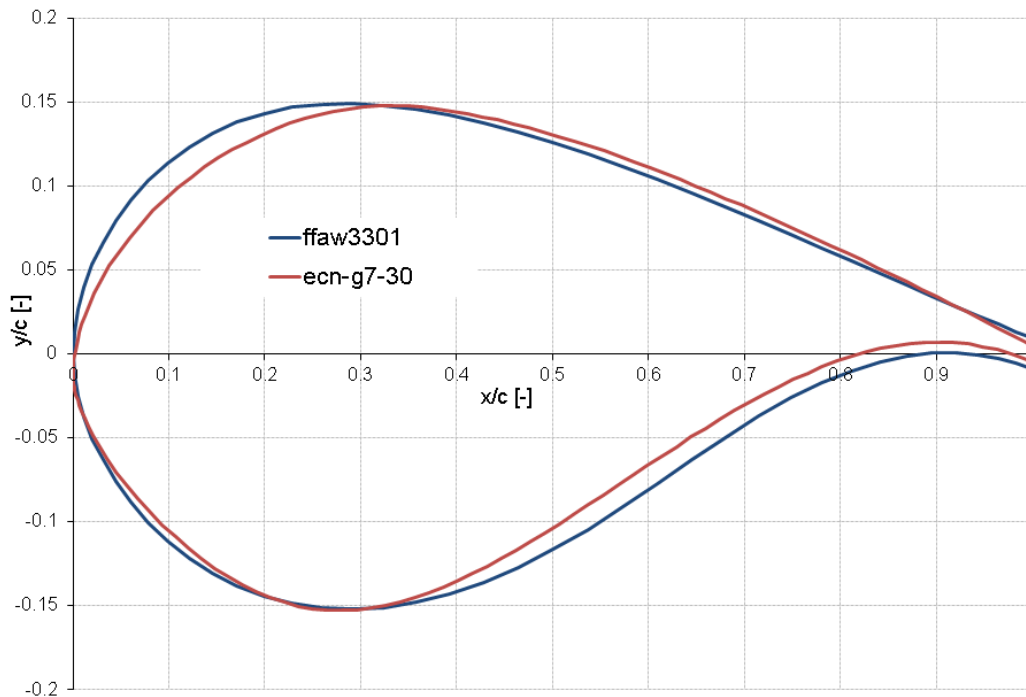


Figure 2.2-7 Shape of the 30% thick airfoils

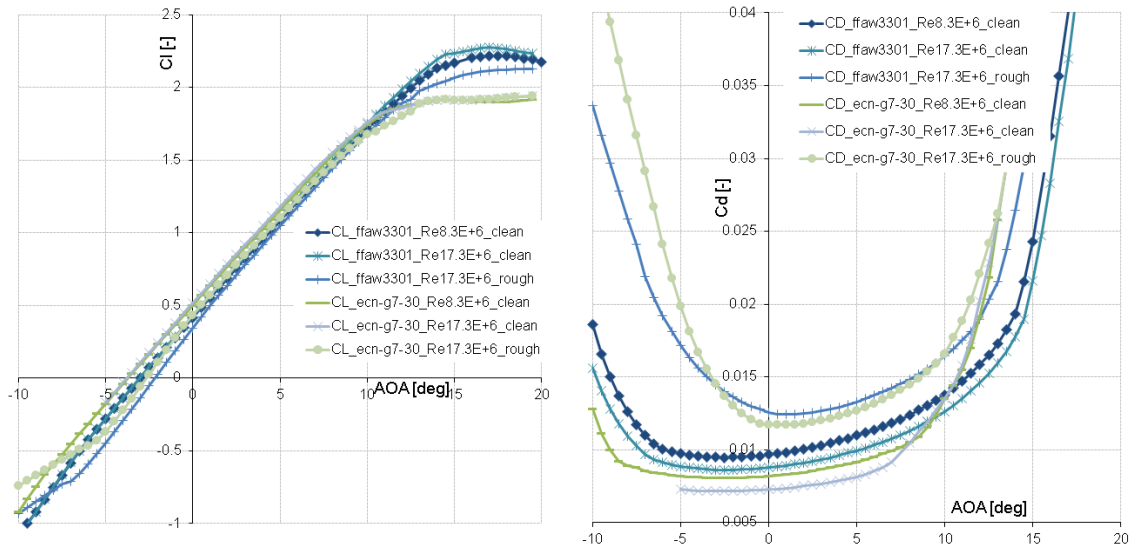


Figure 2.2-8 Comparison of lift (left) and drag curves (right) for the 30% thick airfoil

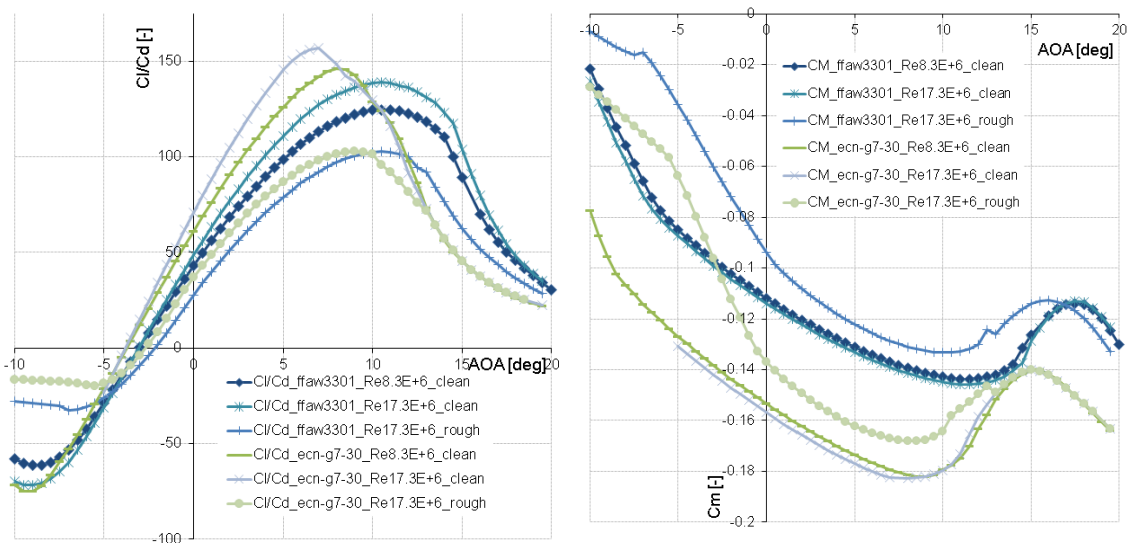


Figure 2.2-9 Comparison of lift over drag ratio (left) and moment (right) for the 30% thick airfoil

### 24% thick airfoil

A shape comparison of the 24% thick airfoils is included in Figure 2.2-10. There is a significant increase in camber over the whole chord compared to the FFA airfoil. The trailing edge thickness as well as shape is relatively thin and questions can be asked towards the achievable structural integrity of this part of the airfoil.

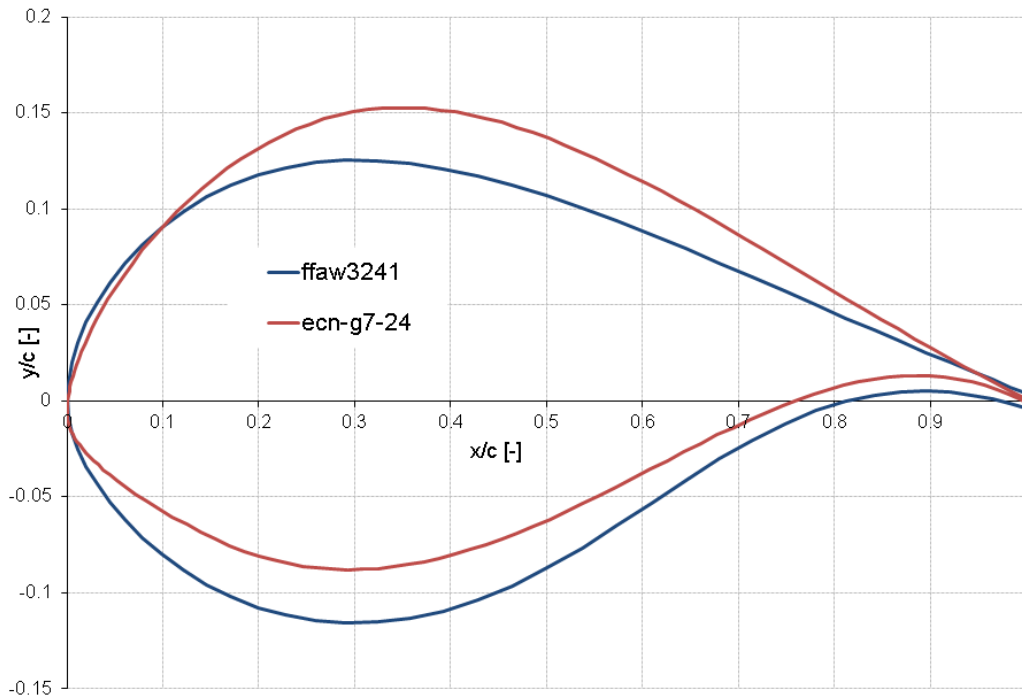


Figure 2.2-10 Shape of the 24% thick airfoils

The resulting predictions are included in Figure 2.2-11 and Figure 2.2-12. Due to the camber increase a clear offset in the lift curve can be observed (about 2.5deg in zero lift angle of attack), and the maximum lift is comparable to the FFA airfoil. However, contrary to the FFA airfoil, there is a significant decrease in maximum lift in the case of roughness. The drag values of the newly developed airfoil are lower in the attached flow region, partly due to the thin trailing edge thickness. The stall is quite abrupt causing a sudden drag increase above roughly 8deg angle of attack. As a result of the above, the lift to drag ratio is rather large (around 210), but the maximum is very narrow and stall degrades the performance drastically and sudden. In case of roughness the performance reduced by a factor of two. Although the relative performance decrease in case of roughness is less for the FFA airfoil, the absolute values of L/D are not that different for rough conditions. However, the FFA profile features a much more gradual stall and a wider performance plateau in terms of angle of attack.

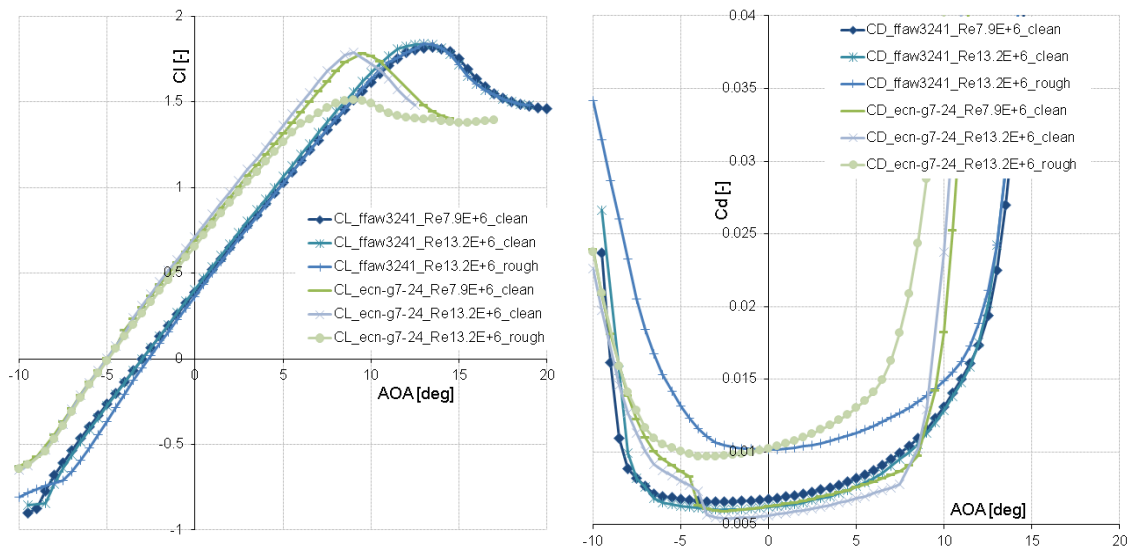


Figure 2.2-11 Comparison of lift (left) and drag curves (right) for the 24% thick airfoil

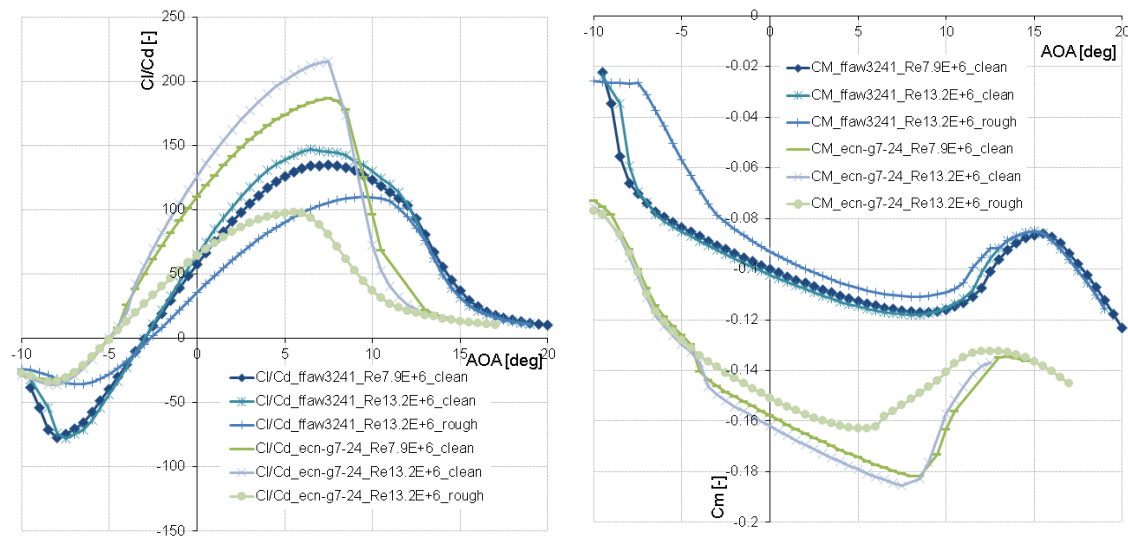


Figure 2.2-12 Comparison of lift over drag ratio (left) and moment (right) for the 24% thick airfoil

## 2.2.2 Discussion

The above presented results show some interesting features for airfoils designed using the described optimization routine. Although the aerodynamic code used both for optimization and evaluation was the same (RFOIL), a large and important portion of the angle of attack range for the 36% airfoil could not be evaluated. Here it is noted that the Reynolds number used during the design differs from the Reynolds number used during the evaluation. The 24% airfoil greatly outperforms the FFA airfoil in terms of maximum lift over drag ratio. However, it looks like the 24% thick airfoil does not deliver the requirements regarding stall margins for the considered Reynolds number. Although the absolute performance in case of roughness is acceptable, the difference with respect to clean conditions is enormous. Structural integrity towards the trailing edge is also questionable for this profile.

The example illustrates one should be careful with using optimization routines and it is difficult to adequately implement all necessary boundary conditions. Uncertainty in aerodynamic modelling will add to that, especially at these high Reynolds numbers. In the end, it is believed engineering judgement will always remain important. The 30% profile however is less extreme in this sense and it would be interesting to verify the added value of this profile in a blade design.

A noticeable difference of the newly designed airfoils in comparison to the FFA airfoils is the narrower angle of attack range for maximum performance (L over D). This is mainly a consequence of the less gradual stall behaviour of these airfoils. However the benefit lies in a higher value of the lift over drag ratio. As a next step it would be worthwhile to evaluate to what extent the drag losses associated with operating off the maximum L over D will affect the power performance. As a first step towards this investigation, angle of attack variations for several design load cases in partial load are calculated using the INNWIND reference turbine modelled using the aero-elastic code Phatas [7][8]. The results are displayed in Figure 2.2-13 for a section located around 80% span. The three times standard deviation range roughly gives a +/- 5 degree variation for normal turbulence while this amounts to +/- 10 degree for the extreme turbulence load cases. Although the angle of attack variation for this turbine and operational conditions seems to be dominated by turbulence and the structural response to it, the contribution of wind shear can also be an important contributor. An example of measured angle of attack variations in the field can be obtained from [9]. To what extent this will influence the overall performance will be further addressed in Section 2.3.3.

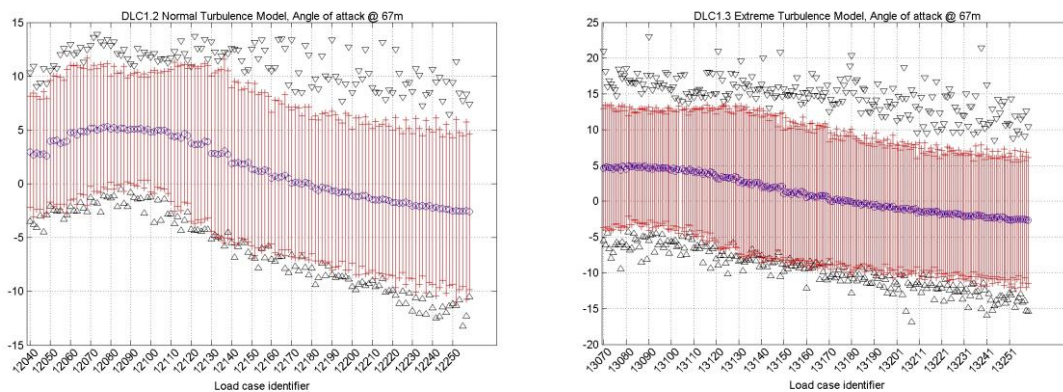


**Figure 2.2-13** Calculated statistics of angle of attack variation for DLC1.2 normal turbulence (left) and DLC1.3 extreme turbulence (right) of the INNWIND reference turbine. The minimum and maximum angle of attack are indicated by the triangles, the mean value by the blue circle and three times the standard deviation range by the red lines.

## 2.3 Application of thick airfoils

The application of a 30% thick airfoil towards the outboard sections has been researched both for the FFA as well as the ECN airfoil. Thereto first the sectional characteristics are compared after which the blade planform has been redesigned to take into account the different airfoil distribution. Finally, in order to check the real life performance, several load case calculations have been performed in partial load using an aero-elastic solver.

### 2.3.1 Sectional characteristics

As a first step towards application of a 30% thick airfoil, the performance of the FFA and ECN 30% thick airfoils are compared to the FFA 24% thick airfoil. This is done using RFOIL (same version as described in Section 2.2.1), without the inclusion of rotational effects. The results for the FFA profile are illustrated in Figure 2.3-1. Although the Reynolds numbers are not identical, the shown trend of these profiles with Reynolds number in Section 2.2.1 indicates this is not a major player in the regime considered. It appears that although the maximum lift increases for the 30% airfoil, the maximum lift over drag ratio slightly decreases, occurring at a higher angle of attack. The effect of roughness in terms of maximum lift coefficient is large in comparison to the 24% profile. Since the polars of these airfoils have also been provided within the framework of the INN WIND project, calculated by EllipSys3D including free transition, a similar comparison has been made in Figure 2.3-2. Although the difference is small, the lift over drag ratio for the 24% thick profile slightly exceeds the value of the 30% thick airfoil. Surprisingly, the maximum lift of the 24% thick profile now exceeds the value for the 30% thick airfoil. Uncertainty in airfoil data should be kept in mind whilst interpreting the results of the corresponding redesign. The sectional characteristics of the FFA 24% and ECN 30% thick airfoils are compared in Figure 2.3-3. There is a small offset in zero lift angle of attack for the clean conditions. The maximum lift over drag ratio and its corresponding angle of attack are similar, although the variation is slightly more pointy than the 24% FFA profile. Since results of the ECN airfoil are only available through RFOIL, it was chosen to use the polars from RFOIL in the remainder of the work.

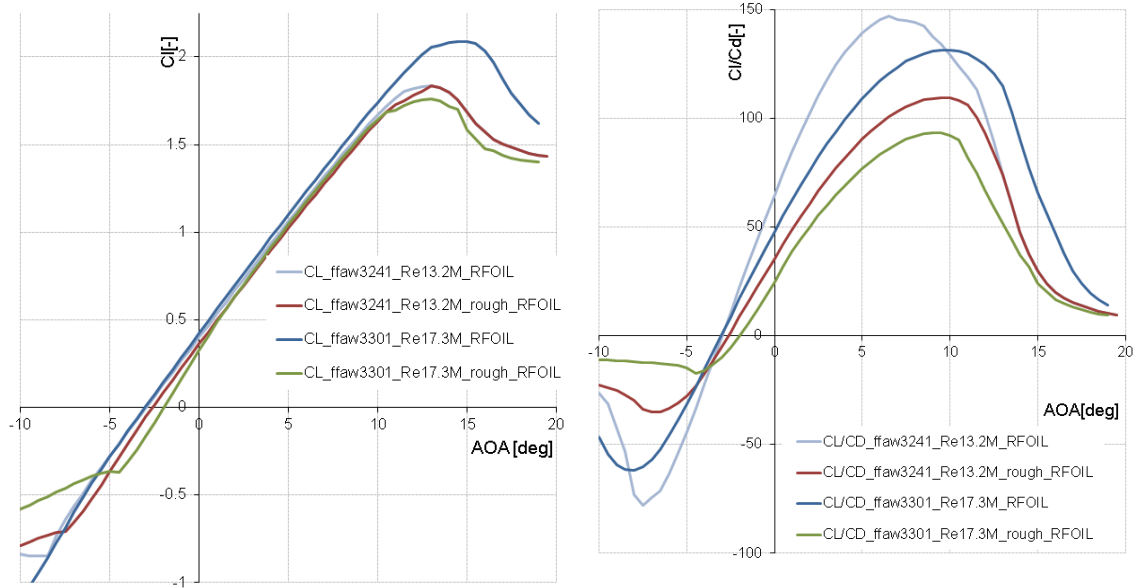


Figure 2.3-1 Comparison of lift (left) and lift over drag ratio (right) between the FFA 24% and 30% thick airfoil, as calculated by RFOIL

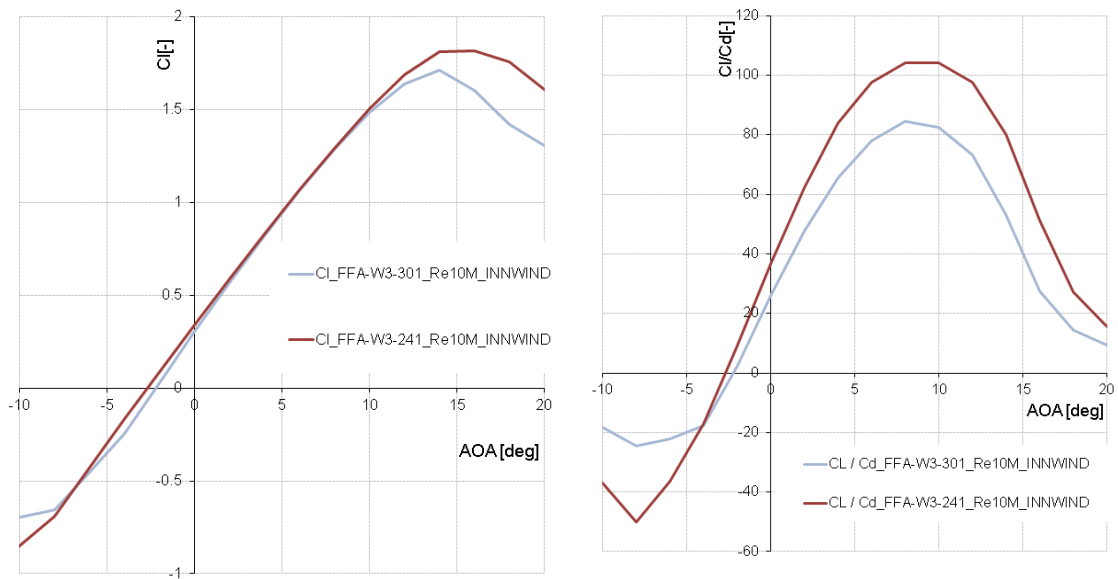


Figure 2.3-2 Comparison of lift (left) and lift over drag ratio (right) between the FFA 24% and 30% thick airfoil, using the specified polars within INNWIND

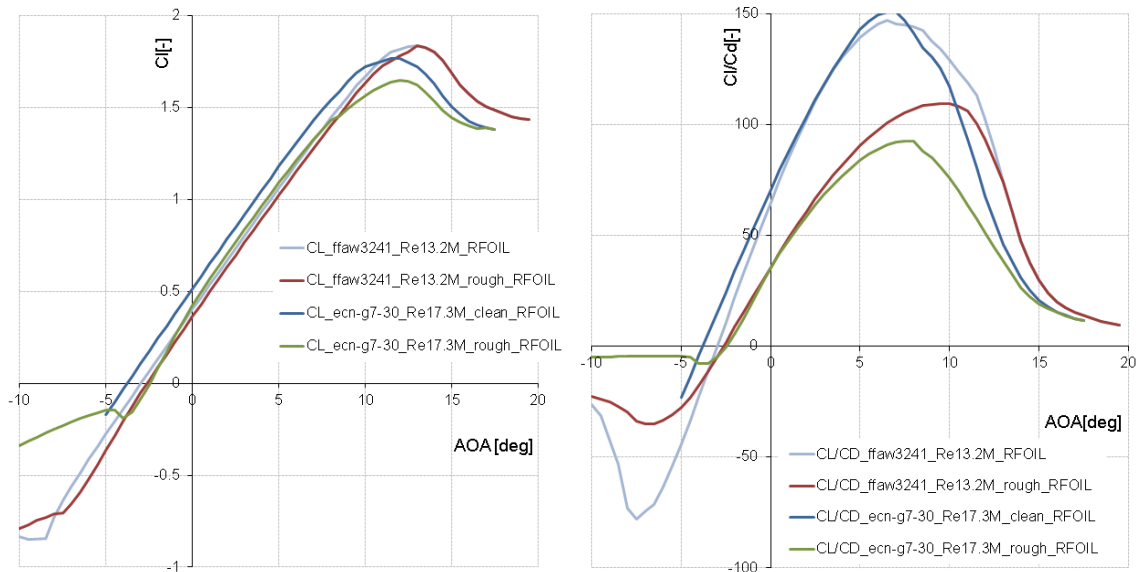


Figure 2.3-3 Comparison of lift (left) and lift over drag ratio (right) between the FFA 24% and ECN 30% thick airfoil, as calculated by RFOIL

### 2.3.2 Blade planform design

To determine the effect of application of thick airfoils on the turbine performance, the blade planform has to be redesigned. The tool BOT [10] is used which allows to design a (rigid) blade geometry for optimizing annual yield by using quasi steady aerodynamics in the form of BEM theory. In the current work the optimization is only performed in partial load (constant pitch angle), which reduces the optimization to obtaining a maximum power coefficient  $C_p$ . Firstly the reference turbine has to be redesigned to incorporate the generated RFOIL polars instead of the supplied INN WIND polars. In that way a valid reference is obtained to evaluate the application of thick airfoils. Secondly the blade planform is redesigned, replacing the 24% thick profile with a 30% thick profile. Here, both the FFA and ECN airfoil are subject to a redesign. Polars featuring free transition have been selected for this purpose. Implementing the thicker airfoil can be achieved in numerous ways. Two different possibilities are highlighted here, namely reducing the chord length (maintaining the same absolute thickness) and increasing the absolute thickness (maintaining the chord length). The first option aims at reducing the flatwise fatigue loads (which in turn allows to reduce blade mass used for flatwise bending stiffness) while the second open aims at mass reduction in the girders due to increased height to achieve the same bending stiffness.

#### Reference turbine redesign using RFOIL polars

The polars of the 36%, 30% and 24% thick FFA profiles have been replaced by the corresponding free transition polars calculated by RFOIL. Chord and twist are optimized for maximum  $C_p$  and small changes in absolute thickness are allowed. The tip speed ratio is kept the same, resulting in the design visualized in Figure 2.3-4. Due to the higher lift of the RFOIL polars (especially for the 30% profile), the chord is reduced and the twist is increased. The resulting performance is highlighted in Table 2.3-1. Here it is noted that the

performance in terms of  $C_p$  significantly increases. This is due to the fact that the INN WIND reference does not feature an optimized axial induction factor of  $1/3$  (at least for the polars used) and the increased lift over drag ratio of the RFOIL calculated polars. As a results of the first effect, the thrust coefficient  $C_t$  is higher than for the INN WIND reference model. This might not be desirable with respect to the associated loads, but the purpose here is to create a reference for evaluating the application of thick airfoils.

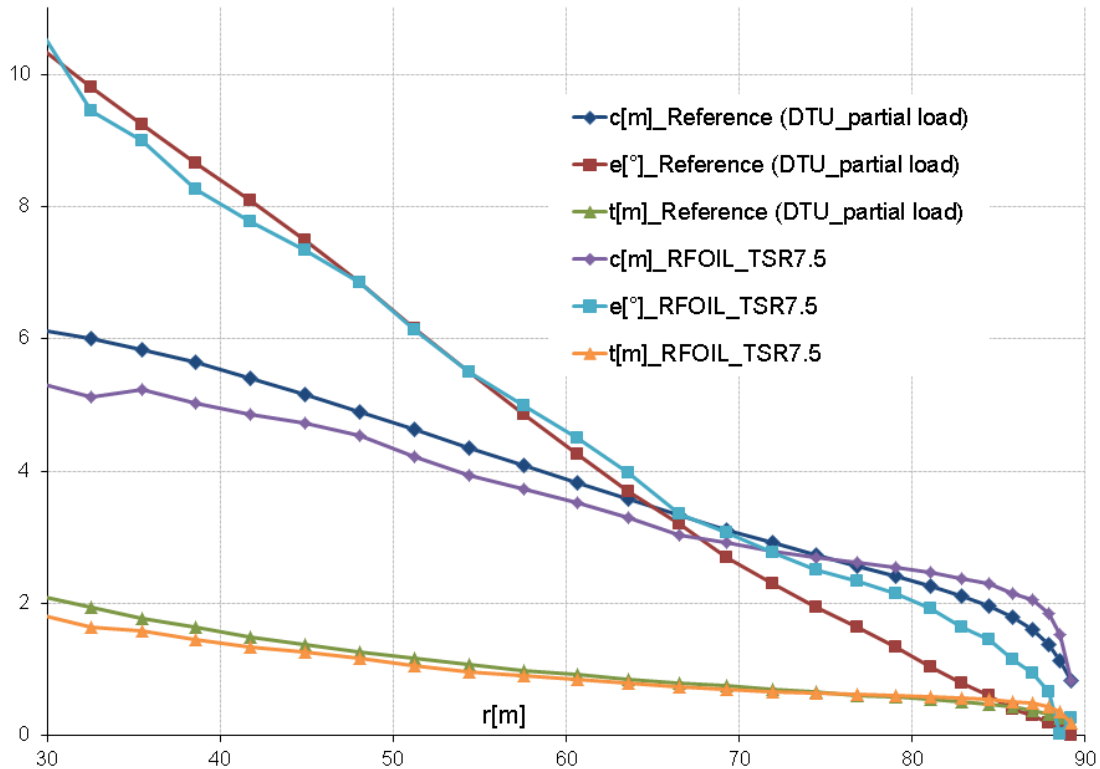


Figure 2.3-4 Comparison of blade planform (chord, twist, thickness) between the INN WIND reference and the redesign using RFOIL

Design	$C_p$ [-]	$\Delta C_p$ [%INN W]	$C_t$ [-]	AOA@80%R [deg]	TSR [-]	Pitch [deg]
<b>INN WIND</b>	0.4861		0.7773	7.0	7.5	-2.5
<b>RFOIL ref redesign</b>	0.5060	4.09	0.8374	6.5	7.5	-3.1

Table 2.3-1 – Performance of INN WIND reference versus the RFOIL redesign

### FFA 30% redesign

As mentioned above, two redesigns are performed:

- Increasing the absolute thickness with a factor 30/24 while maintaining the chord length. Twist is adjusted accordingly.
- Reducing chord length with a factor 24/30 while maintaining absolute thickness. Twist is adjusted accordingly.

The resulting blade planforms are shown in Figure 2.3-5. The corresponding performance is highlighted in Table 2.3-2. Fixing the chord or thickness for a fixed tip speed ratio (TSR) will result in a given twist and hence angle of attack to maintain the Betz limit at an axial induction of  $1/3$ . This is however not necessarily the angle of attack for which the L over D ratio has its maximum to minimize drag losses. Therefore the sensitivity to tip speed ratio is also investigated. There are however several mechanisms at play here, since apart from changing airfoil characteristics, increasing the tip speed ratio will generally increase drag losses, reduce tip losses and also reduced rotation losses for the same power value. It is noted that for the reported values in Table 2.3-2 at tip speed ratios other than 7.5, a twist optimization was not performed.

From Figure 2.3-2Figure 2.3-1 it became clear that the angle of attack for maximum L over D is higher for the 30% thick airfoil compared to the 24% airfoil. Reducing the TSR to 7.0 for the varying thickness concept results in a power increase, most probably because the operating angle of attack is too low for a TSR of 7.5. For the varying chord concept, the resulting angle of attack is already higher compared to the reference design. This is a consequence of the lower chord length, necessitating a higher lift coefficient to achieve the desired rotor induced velocities. As a result, the  $C_p$  values are slightly higher than for the varying thickness concept.

More importantly it can be observed that the decrease of  $C_p$  due to the exchange between the 30% and 24% thick profile remains limited to 0.6% for the varying chord and 1.2% for the varying thickness concept. To verify the given power losses and balance them against loads and mass decrease in terms of cost, load case performance will have to be assessed in Section 2.3.3.

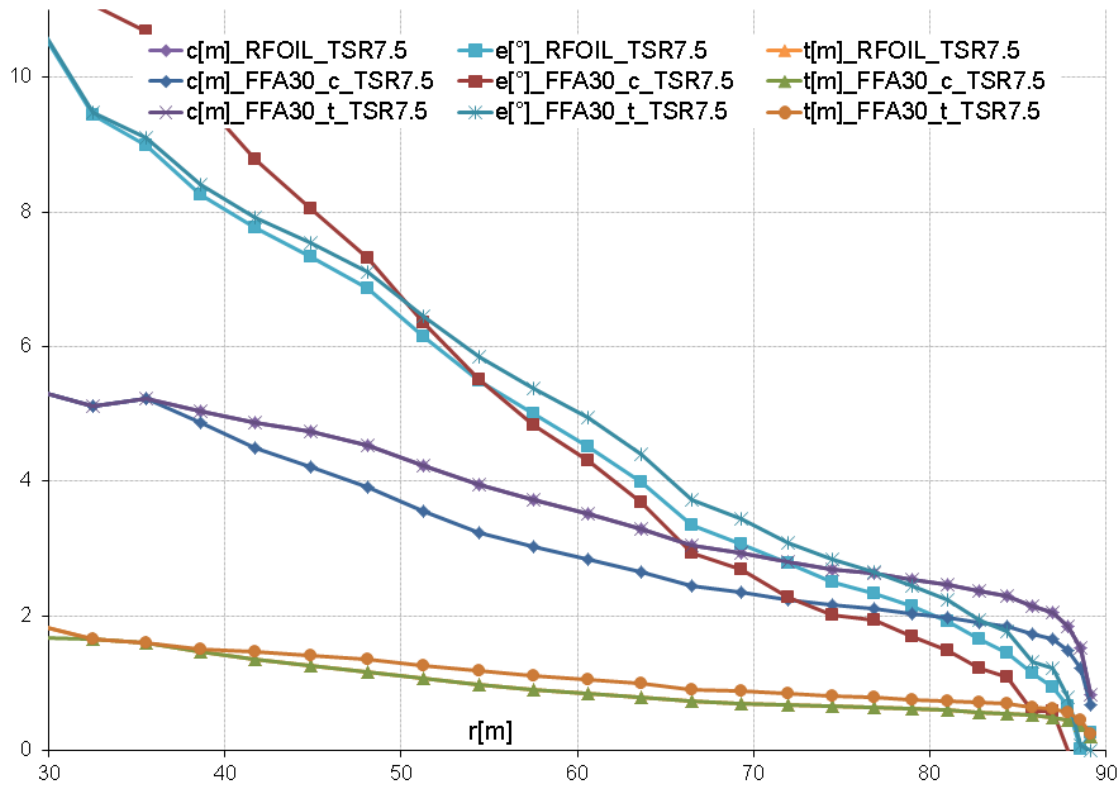


Figure 2.3-5 Comparison of blade planform (chord, twist, thickness) between the RFOIL reference and the two options of the FFA 30% redesign. The planforms with varying chord or thickness are denoted with *\_c* and *\_t* respectively.

Design	Cp [-]	$\Delta C_p$ [%ref]	Ct [-]	AOA@80%R [deg]	TSR [-]	Pitch [deg]
<b>RFOIL ref redesign</b>	0.5060		0.8374	6.5	7.5	-3.1
<b>chord variation</b>	0.5032	-0.55	0.8410	8.7	7.5	-5.1
<b>chord variation</b>	0.5017	-0.85	0.8151	10.0	7.0	-5.4
<b>chord variation</b>	0.5009	-1.01	0.8433	7.4	8.0	-3.9
<b>thickness variation</b>	0.5000	-1.19	0.8418	6.3	7.5	-3.2
<b>thickness variation</b>	0.5017	-0.85	0.8412	7.6	7.0	-4.1
<b>thickness variation</b>	0.4961	-1.96	0.8472	5.3	8.0	-2.6

Table 2.3-2 – Performance of RFOIL reference versus the FFA 30% redesigns.

### ECN 30% redesign

The same exercise as for the FFA 30% thick profile was also performed for the ECN 30% thick airfoil. Hence two redesigns are performed:

- Increasing the absolute thickness with a factor  $30/24$  while maintaining the chord length. Twist is adjusted accordingly.
- Reducing chord length with a factor  $24/30$  while maintaining absolute thickness. Twist is adjusted accordingly.

The resulting blade planforms are shown in Figure 2.3-6. The corresponding performance is highlighted in Table 2.3-3.

From Figure 2.3-2 Figure 2.3-3 it became clear that the angle of attack for maximum  $L$  over  $D$  is of the 30% thick airfoil is very similar to the 24% airfoil. Also the width of the peak is very similar. The lift coefficient is slightly higher for the same angle of attack in the attached flow region. As such similar  $C_p$  performance can be expected which is confirmed in the values given in Table 2.3-3.

For the reduced chord concept the operating angle of attack is quite large due to the high necessary lift coefficient. However, contrary to the FFA redesign for a reduced chord, the angle of attack for maximum lift over drag ration is not shifted upward for the ECN profile. As such we are operating dangerously nearby to stall.

Also for the ECN airfoil redesign it can be observed that the decrease of  $C_p$  due to the exchange between the 30% and 24% thick profile remains limited. To verify the given power performance and balance it against loads and mass decrease in terms of cost, load case performance will have to be assessed in Section 2.3.3.

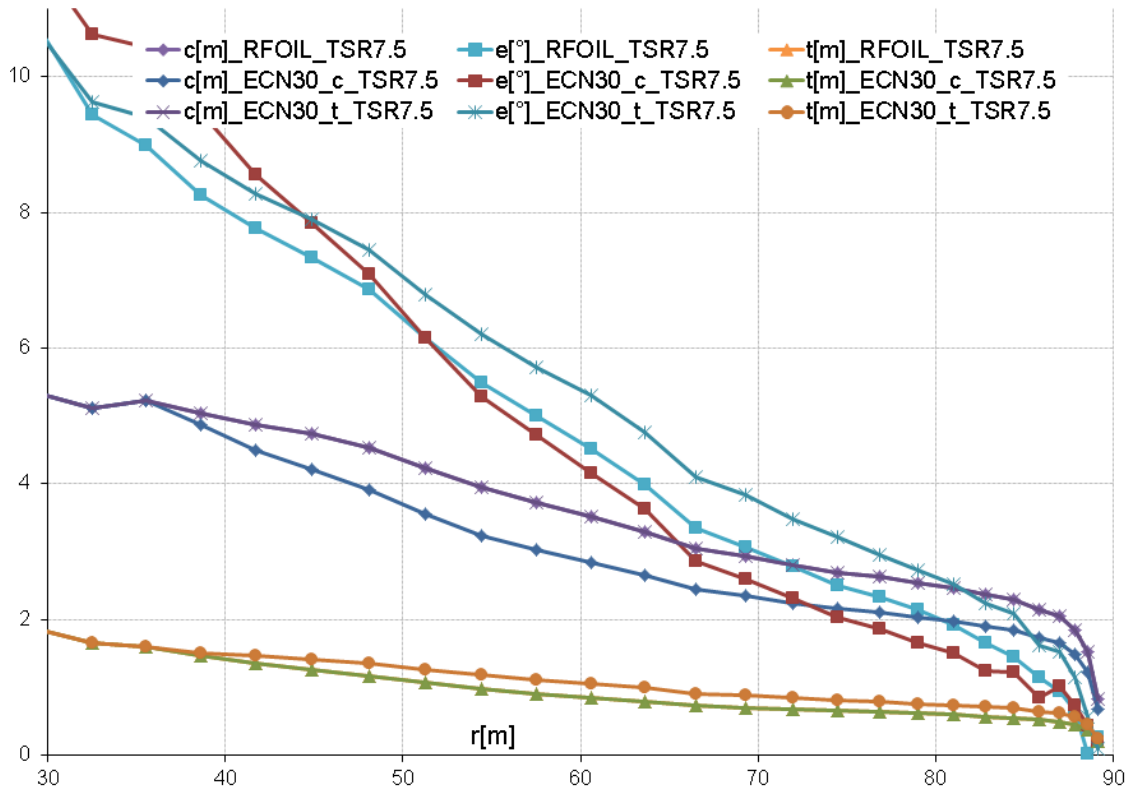


Figure 2.3-6 Comparison of blade planform (chord, twist, thickness) between the RFOIL reference and the two options of the ECN 30% redesign. The planforms with varying chord or thickness are denoted with **\_c** and **\_t** respectively.

Design	Cp [-]	$\Delta C_p$ [%ref]	Ct [-]	AOA@80%R [deg]	TSR [-]	Pitch [deg]
<b>RFOIL ref redesign</b>	0.5060		0.8374	6.5	7.5	-3.1
<b>chord variation</b>	0.5066	0.12	0.8273	8.0	7.5	-4.0
<b>chord variation</b>	0.5011	-0.97	0.8096	9.7	7.0	-5.0
<b>chord variation</b>	0.5074	0.28	0.8466	6.9	8.0	-3.4
<b>thickness variation</b>	0.5067	0.14	0.8424	5.7	7.5	-3.0
<b>thickness variation</b>	0.5043	-0.34	0.7998	6.5	7.0	-3.0
<b>thickness variation</b>	0.5041	-0.38	0.8434	4.6	8.0	-2.3

Table 2.3-3 – Performance of RFOIL reference versus the ECN 30% redesigns.

### 2.3.3 Load case performance

The program PHATAS [7] has been used to assess load case performance. Hereto a full aero-elastic model of the INN WIND turbine was used. The blade planform redesigns with airfoil data updates from Section 2.3.2 are implemented, including the new reference using RFOIL generated polars. For the reference redesign the mass and stiffness distributions were kept the same.

For the varying chord concepts the absolute thickness is the same as the reference, which implies flatwise stiffness is roughly the same for a constant spar cap thickness and associated mass. Although edgewise stiffness slightly decreases for a smaller chord, this effect is assumed to be small here and thus neglected. Contrary to the spar caps for flatwise stiffness, a large contribution to the edgewise stiffness is made up from layers distributed around the skin contour (eventual trailing edge girders excepted). As such chord reduction is estimated to have a less steep effect on mass than absolute thickness variation. Torsional stiffness is also assumed to be the same.

For the varying thickness concept the absolute thickness increases. The design is adjusted to keep the same flatwise strain for the same wind loading. Hence it is assumed that the structural design of the outboard part of the blade is stress (or strain) dominated. As such the gain is converted into mass reduction and a stiffness increase. Spar cap thickness would roughly decrease linearly with an increase in airfoil thickness for the same strain levels. If the portion of the spar caps compared to the total section mass is known an estimate can be made for the mass decrease. The variation of this portion is taken from known structural designs of large blades and applied to complete the mass reduction estimate. The mass moment of inertia is kept the same as for the reference. For a constant strain level, flatwise stiffness is adjusted to increase linearly with thickness, whilst maintain the crosswise and edgewise stiffness constant. As a consequence, blade mass is estimated to decrease by approximately 2%.

The simulations are carried out in accordance with IEC defined production cases for partial load at 9 m/s average wind, featuring two wind seeds and yaw misalignment angles of  $0^\circ$ ,  $-8^\circ$  and  $8^\circ$ . The normal turbulence model is used. The controllers are adjusted for each blade to compare performance at same tip speed ratio and wind speed. Hereto the rotor characteristics in terms of  $C_p$  versus tip speed ratio (for constant wind speed) are calculated (Figure 2.3-7) and fed into the Q-n curve used for each concept. Although the resulting absolute  $C_p$  values showed different values from BOT due to the inclusion of flexibility, wind shear etc, the relative differences between the different concepts are largely the same.

#### Results

The results for each blade concept are averaged over the relevant load cases (the trends were roughly the same between them), resulting in statistics both for power production and fatigue equivalent loads. A summary is given in Table 2.3-4. Regarding power performance it is observed that the trend between the concepts varies significantly from the variation observed for the constant wind calculation. The explanation can be found in Figure 2.3-7, which clearly shows the different performance in off-design conditions. Although the value of maximum  $C_p$  might be high, it is the overall performance that counts, which is dictated by the airfoil performance in the relevant angle of attack range. In Section 2.3.2 it was already noted that the reduced chord concept for the ECN airfoil

operates dangerously nearby to stall. As such the power performance degrades in turbulent wind. As an example, a snapshot of relevant time series for one of the load case is included in Figure 2.3-8 and Figure 2.3-9. This observation opens up the discussion whether using maximum lift over drag ratio together with a safe stall margin as a criterion for airfoil performance should be further detailed using a 'weighted' average over a specified angle of attack range instead. Here it is noted that the performance gradient towards stall is usually steeper than for a decrease in angle of attack. Apart from that, the performance for higher angles of attack than the optimum should probably have a heavier weighting than the lower angles because power scales with the cube of wind speed. In addition to that it would be interesting to explore the possibility to apply pitch control in partial load to reduce angle of attack variations. This could open up a new design space for airfoils, not having to sacrifice maximum lift over drag so much for a safe stall margin. The trend of the fatigue equivalent loads between the concepts is as expected. The reduced thickness concepts feature the same mass reduction and this feeds directly through to the in plane fatigue equivalent blade root bending moment. The reduced chord concepts feature less absolute lift variation and hence a reduced out of plane fatigue equivalent blade root bending moment. The reduction in this equivalent moment for the ECN reduced chord concept is more than twice the value of the FFA reduced chord concept. Probable cause is the reduced lift slope in separated flow conditions in which this blade is operating due to the high design angle of attack. In addition to that the lower average torque for this concept slightly reduces the rotor speed which in turn also lowers turbine loading.

Regarding the overall performance of the thick airfoil concepts it can be stated that, based on the shown calculations, the power performance penalty is limited to non-existent, while the fatigue loads or blade mass show a promising decrease depending on the implementation of the thick airfoils. Whether reducing chord or increasing thickness is favourable remains subject of further study. Most probably the best performance is achieved mixing the two concepts to a certain degree.

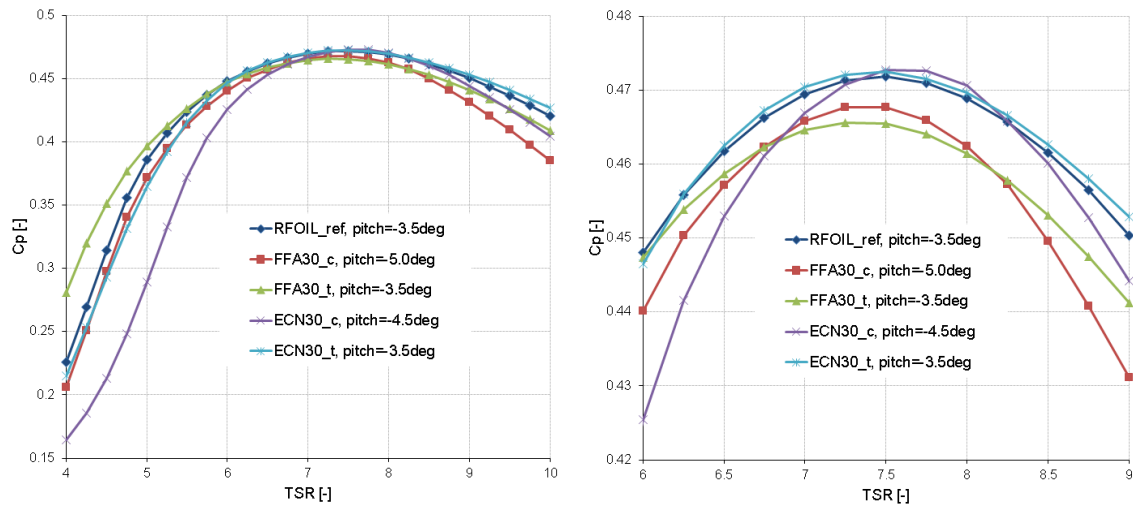
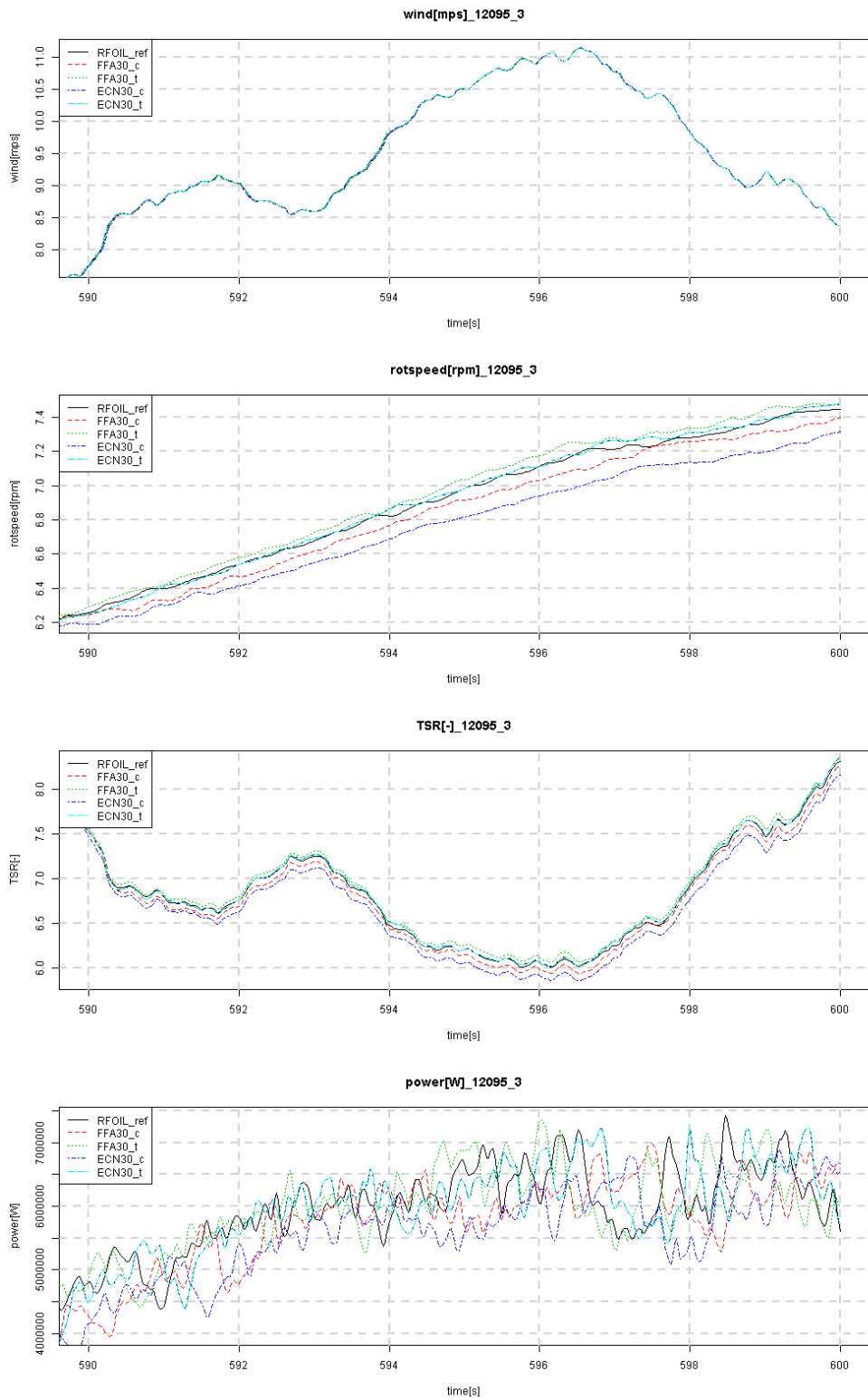


Figure 2.3-7 Calculated rotor characteristics using Phatas for constant wind velocity (left), together with a zoomed view (right)

Design	Power [MW]	Mflat_eq [MNm]	Mlead_eq [MNm]	$\Delta$ Power [%ref]	$\Delta$ Mflat_eq [%ref]	$\Delta$ Mlead_eq [%ref]
<b>RFOIL ref redesign</b>	5.90	17.78	19.10			
<b>FFA30_c</b>	5.81	17.42	19.22	-1.42	-2.03	0.58
<b>FFA30_t</b>	5.84	17.97	18.44	-1.02	1.07	-3.49
<b>ECN30_c</b>	5.81	16.92	19.12	-1.52	-4.81	0.09
<b>ECN30_t</b>	5.91	17.70	18.44	0.15	-0.44	-3.48

Table 2.3-4 - Summary of load case performance averaged over relevant load cases for 9 m/s average wind speed



**Figure 2.3-8 Comparison of load case performance as a function of time. From top to bottom: wind speed, rotor speed, tip speed ratio and aerodynamic power**

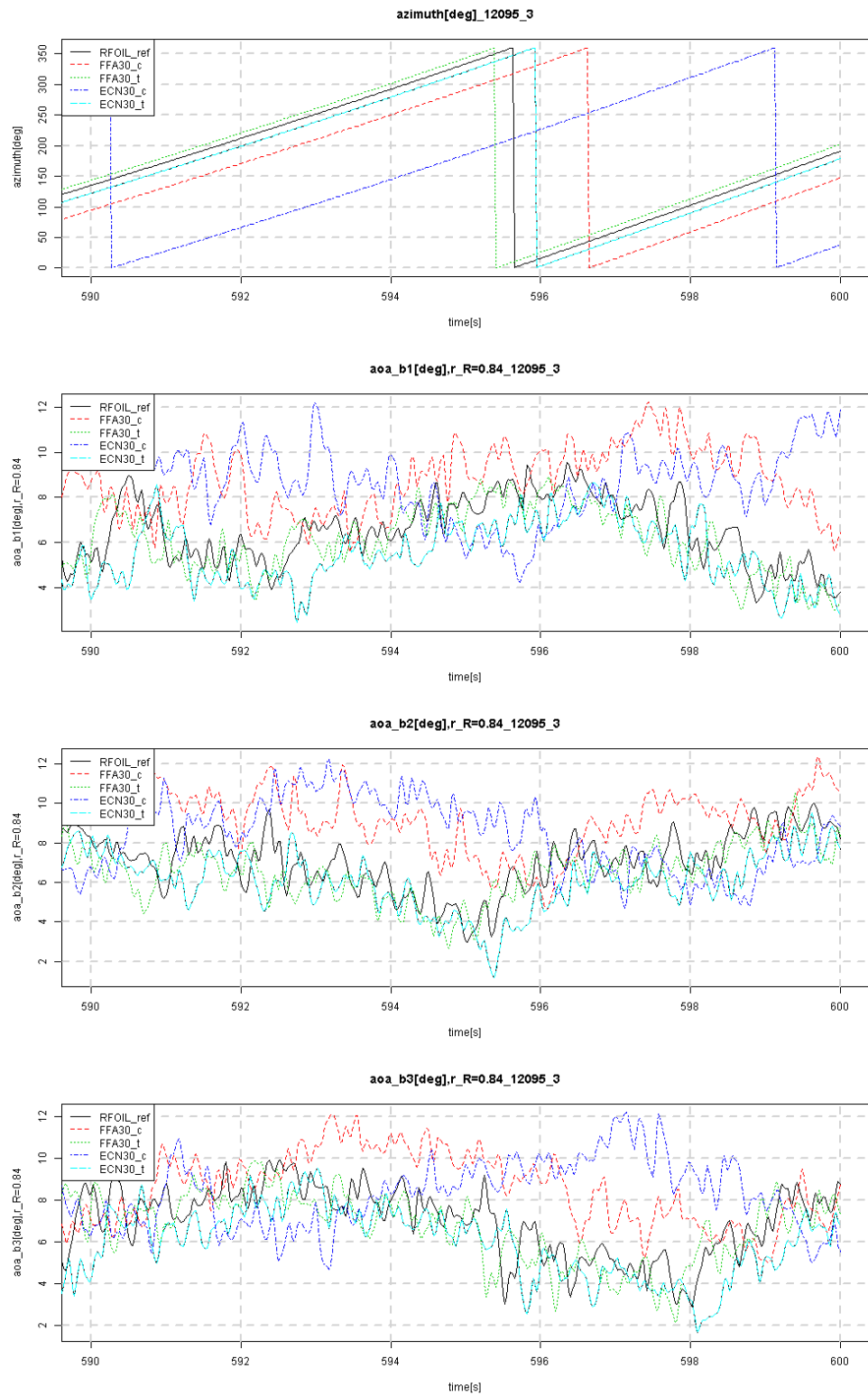


**Figure 2.3-9 Comparison of angle of attack variation as a function of time for the load case depicted in Figure 2.3-8. From top to bottom: Rotor azimuth and angle of attack at 84%R for blade 1, 2 and 3**

## 2.4 Conclusions

The application of new airfoils to large offshore rotors is studied. Firstly, a new set of airfoils was developed and assessed. The performance in terms of maximum lift over drag ratio is greatly improved, but the sudden onset of stall and performance decrease in rough conditions is not as desired. Although the aerodynamic code used both for optimization and evaluation was the same, some criteria (e.g. stall margin, structural integrity and manufacturability of the trailing edge) were not met. This is predominantly the case for the thinnest airfoil developed. A possible cause for the discrepancy in aerodynamic performance lies into the different Reynolds numbers used between the design and evaluation and the validity of the prediction results for high Reynolds numbers.

Secondly the application of thick airfoils towards the outboard sections is studied using both the current as well as the newly developed airfoils. Hereto 4 blade planform redesigns are performed incorporating two different 30% thick airfoils instead of the 24% thick profile as used for the reference case. A concept with reduced chord length as well as increased absolute thickness is design options for the final blade design. Both quasi steady performance as well as dynamic load case performance in partial load is assessed in terms of power and loads. It becomes apparent that the trends in power performance between the concepts significantly differ between the quasi steady and dynamic simulations. The cause lies in the different performance in off-design conditions. As such it is recommended to use a 'weighted' average over a specified angle of attack range as a criterion for airfoil performance optimization instead of maximum lift over drag ratio together with a stall margin. In addition to that it would be interesting to explore the possibility to apply pitch control in partial load to reduce angle of attack variations. This could open up a new design space for airfoils, not having to sacrifice maximum lift over drag so much for a safe stall margin.

Based on the current calculations, the overall performance of the thick airfoil concepts is judged to be promising. The power performance penalty is limited to non-existent, while the fatigue loads or blade mass show a promising decrease depending on the implementation of the thick airfoils. Whether reducing chord or increasing thickness is favorable remains subject of further study. Most probably the best performance is achieved mixing the two concepts to a certain degree. It is noted that upscaling is probably more efficient to reduce the total cost of energy, than trying to reduce the mass of a fixed radius concept.

It is noted that the current study is an initial study including a large amount of assumptions. Future studies should comprise assessment of the accuracy of 2D airfoil performance predictions and an evaluation of the assumptions regarding structural design and full load set performance (including changes in aero-elastic vibrations due to shifting eigen-frequencies). Also airfoil performance for rough conditions should be taken into account.

## CHAPTER 3 BLADE ROOT AIRFOIL DESIGNS AND ANALYSIS OF AERODYNAMICS - CENER

*A Muñoz, B Méndez, S Gómez, A Irisarri, X Munduate*

### 3.1 Introduction

CENER contribution to the development of new airfoils focuses on the blade root region. The objective of this work is to accelerate the production of energy at low wind speeds without forgetting about the tough structural requirements of this zone (especially critical for big wind turbines like the ones considered in this project, between 10 and 20 MW). It is known that concepts such as flat-back airfoils, gurney flaps or vortex generators may help fulfilling those characteristics.

CENER has developed two airfoils for the root blade region (with thickness to chord ratio equal to 40% and 50%). To do so, some previous steps have been needed as explained in the following paragraphs.

The flow in this region is expected to be complex and very different between the 2D and the 3D simulations, consequently, the two first sections of CENER's contribution are related to the study of the flow near the root (3.2 *Study of INN WIND blade root aerodynamics using CFD*) and the current airfoils available for these purposes (3.3 *State of the art of flat-back and high thickness airfoils*).

Panel methods are not conceptually suitable for their use on flat-back airfoils. However, the code used to evaluate aerodynamically the airfoils during the design process is XFOIL. That is the reason why in Section 3.4 (*XFOIL correction for flat-back and high thickness airfoils*) a correction for XFOIL prediction has been developed. This correction is based on wind tunnel data and it is purely empirical.

The last three sections are dedicated to the design process itself (3.5 *Design of root region airfoils*), the CFD study of the new airfoils (3.6 *CFD study of the designed airfoils*) and the study of special configurations of one of the new airfoils (3.7 *CFD study of special configurations*).

### 3.2 Study of INN WIND blade root aerodynamics using CFD

In this section some attention will be paid to the flow in the root region in order to improve the knowledge about the aerodynamics near the root as a tool for future analysis and improved basis for airfoil design. This flow is known to be characterized by an important radial component.

The aforementioned radial flow makes the differences between the 2D and the 3D simulations important. However, it is usual to perform 2D simulations instead of 3D ones because they require less time and resources. For example, the airfoil optimization that will be developed in Section 3.5 will be done with 2D calculations. With the objective of improving the evaluation of the results coming out from the optimization process, it is interesting to understand the differences that will be found between the 2D and the 3D calculations. To quantify those differences, some airfoils of the original blade, will be

selected to be studied in 2D conditions and working within the blade (that is, working under 3D flow).

The three airfoils chosen to represent the flow in that region are characterized by their thickness with respect to their chord (50%, 40% and 30%). Figure 3.2-1 shows the shape of the three airfoils from the original INN WIND blade, and further details are defined in Table 3.2-1.

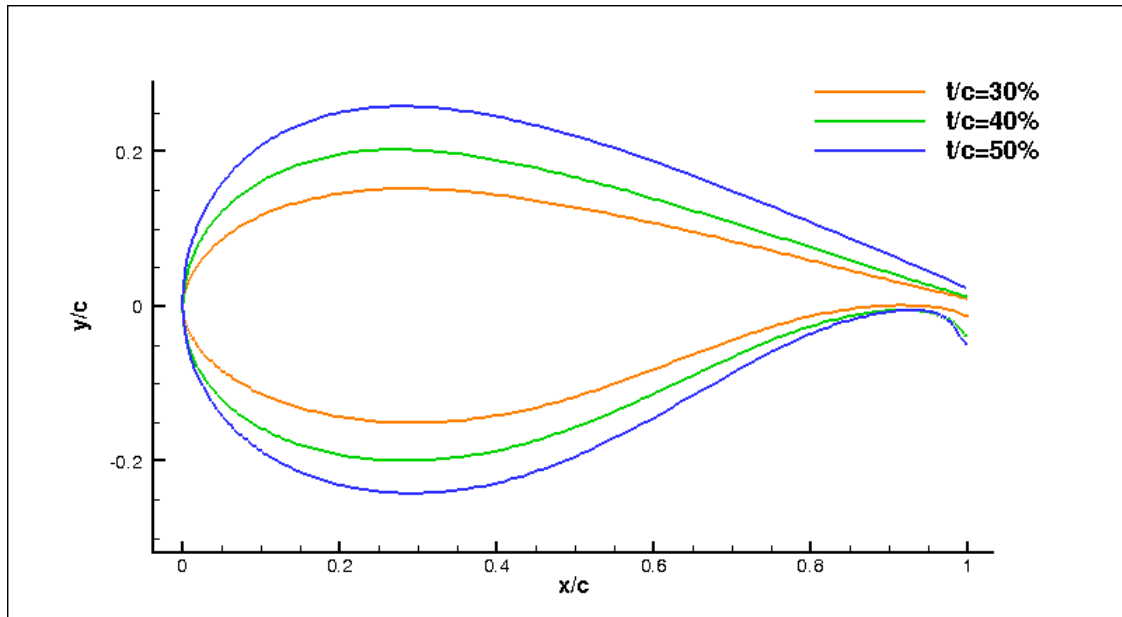


Figure 3.2-1 Studied airfoils from the INN WIND blade

Airfoil name	Thickness/chord (%)	r/R (%)
Innwind30_original_airfoil	30	41
Innwind40_original_airfoil	40	28
Innwind50_original_airfoil	50	22

Table 3.2-1 – Airfoil thickness and position along the blade

To visualize the 3D flow, two approaches have been followed. The first one is the representation of streamlines on the blade surface. The second one is the representation of the flow in a slice of the blade containing the specific airfoil. The cases in which slices are shown, the streamlines have been drawn neglecting the perpendicular speed to the slice to facilitate the visualization. To represent the slices, pressure contours and pressure and friction coefficients have been used.

### 3.2.1 Definition of the tools used during the study

FAST is an aeroelastic computer-aided engineering (CAE) tool for horizontal axis wind turbines, it has been used to calculate the local parameters in each section of the blade by means of the BEM theory. According to [11], FAST is described as follows:

*“FAST is NREL's primary CAE tool for simulating the coupled dynamic response of wind turbines. FAST joins aerodynamics models, hydrodynamics models for offshore structures, control and electrical system (servo) dynamics models, and structural (elastic) dynamics models to enable coupled nonlinear aero-hydro-servo-elastic simulation in the time domain. The FAST tool enables the analysis of a range of wind turbine configurations, including two- or three-blade horizontal-axis rotor, pitch or stall regulation, rigid or teetering hub, upwind or downwind rotor, and lattice or tubular tower. The wind turbine can be modelled on land or offshore on fixed-bottom or floating substructures. FAST is based on advanced engineering models—derived from fundamental laws, but with appropriate simplifications and assumptions, and supplemented where applicable with computational solutions and test data.”*

WMB (Wind Multi Block) is a CFD method developed and validated by CENER and the University of Liverpool for wind turbine aerodynamics analysis (2D and 3D). It is capable of solving the compressible Unsteady Reynolds Averaged Navier-Stokes (URANS) equations on multi-block structured grids using a cell-centred finite-volume method for the spatial discretization. Moving and deforming grids can be calculated using WMB and aeroelastic analysis of structures such as wind turbine blades are analysed based on modal representation. Several turbulence models are implemented in the code. WMB has the capacity to study both fully turbulent and transitional flows around airfoils. In addition, airfoils with distributed roughness on the surface can be calculated using WMB.

For the 3D CFD calculations presented in this work periodicity on time and space has been used and no tower and nacelle have been considered for the simulations. 8 millions of nodes divided in 600 blocks have been used to cover a domain up to 3R to the inflow, 6R to the output and 4R to the far field.

### 3.2.2 Calculation of the local operating parameters

In order to simulate the 2D profiles at the same operating point at which they work in the blade, several parameters are needed. These parameters are the Reynolds number, the Mach number and the angle of attack. As described in [12] the local angle of attack at which a certain section of a blade is working is not easily defined nor calculated. Several approximations have been used to obtain those parameters:

- BEM code: All the three parameters can be obtained from the BEM code output: the Reynolds and the Mach number and the local angle of attack.
- CFD code: From the simulation of the 3D wind turbine, the local angle of attack can be calculated as described in [12].

For each case the Reynolds and the Mach numbers provided by the BEM code have been used. Moreover, 2D CFD calculations have been made at a certain range of angles of attack and specifically at the ones obtained with the BEM and the CFD code. As it is not the focus of this study, the AOA calculated with BEM and with the CFD are only shown for

“Case 1”. For the rest of the cases only the CFD-calculated AOA will appear. The differences remain similar for all the three cases.

### 3.2.3 Cases description

Several operating points of the wind turbine have been chosen to study how the flow behaves in the root region for different conditions. Figure 3.2-2 represents the relation between the wind speed and the rotational speed of the wind turbine. The lines represent the defined operating points of the wind turbine, and the points define where the studied cases have been calculated.

- “Case 1” represents a real operational point of the wind turbine. Both the wind and the rotational speed are in the intermediate region of the operational range.
- “Case 2” is also characterized by a pair wind speed-rotational speed which is defined in the operational curve of the wind turbine. However, this case was simulated with pitch equal to zero to try to change the operational point of the blade. The pitch variation is small and does not change a lot the angles of attack present on the blade.
- “Case 3” was chosen to completely change the normal operation point of the blade. Notice that it does not represent a point in the characteristic operational curve of the turbine.

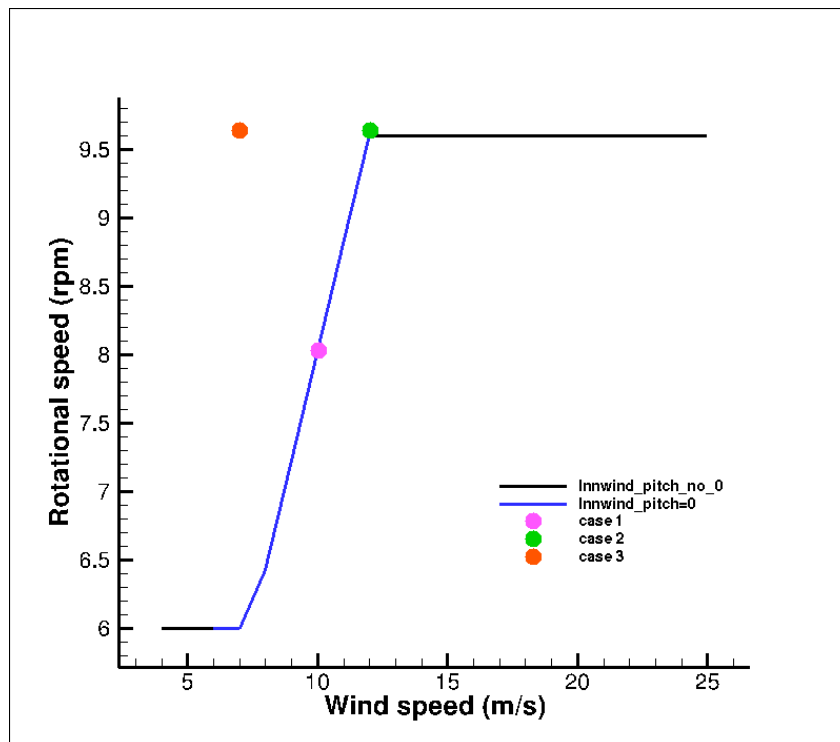


Figure 3.2-2 Relationship between several operating parameters of the wind turbine. Lines represent characteristic points (blue if pitch=0). Points represent the studied cases

	Wind speed (m/s)	Rotation speed (rpm)	Tip speed (m/s)	Pitch (°)
Case 1	10	8.0	75	0
Case 2	12	9.6	90	0
Case 3	7	9.6	90	0

Table 3.2-2 – Operating condition of the studied cases

### 3.2.4 Case 1

In order to visualize the flow over the wind turbine blade, some streamlines have been drawn on the blade surface. Moreover, the blades have been coloured in two styles. One of them shows the position of the three studied sections that correspond with the three airfoils defined in Section 3.2. The other style divides the blade in regions with friction coefficient (along the “X” direction) bigger and smaller than zero with the objective of getting a better comprehension of the separation phenomena.

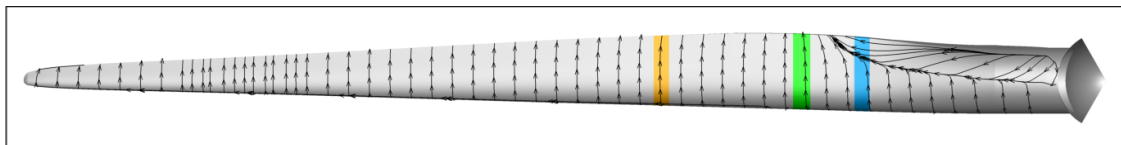


Figure 3.2-3 Suction side. Streamlines and studied profiles.

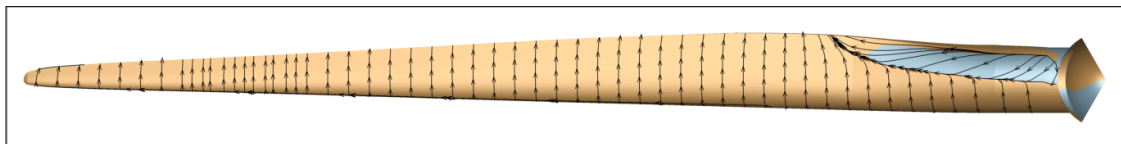


Figure 3.2-4 Suction side. Streamlines and Cfx contours (yellow, Cfx>0 and grey, Cfx<0).

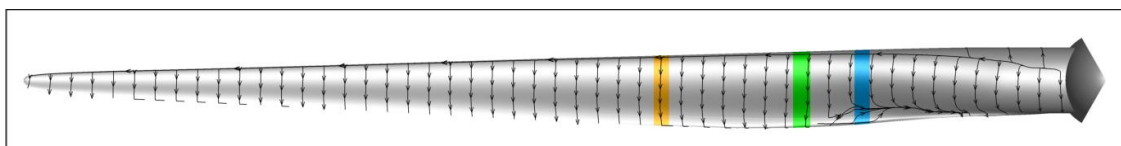


Figure 3.2-5 Pressure side. Streamlines and studied profiles.

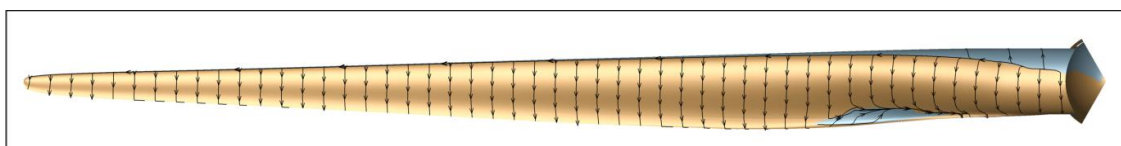


Figure 3.2-6 Pressure side. Streamlines and Cfx contours (yellow, Cfx>0 and grey, Cfx<0).

As seen in Figure 3.2-3 and Figure 3.2-4, the suction side of the blade near the root is affected by a strong separation characterized by an important amount of radial flow. This separation takes place at the last 50% of the chord (more or less) and strongly modifies the flow of the 50%-thick airfoil. It also influences the 40%-thick airfoil. Moreover, the alteration of the flow over the 30%-thick airfoil is small.

In the pressure side of the blade, the separation area is smaller and it affects specially the flow of the 50%-thick profile (see Figure 3.2-5 and Figure 3.2-6).

Table 3.2-3 shows the local operating conditions for the selected airfoils in “case 1”:

Airfoil thickness	Re	M	AOA geometrical (°)	AOA BEM (°)	AOA CFD (°)
30%	12.6e6	0.10	12.5	5.9	6.8
40%	9.7e6	0.07	17.4	7.5	9.0
50%	8e6	0.06	20.2	9.6	11.9

Table 3.2-3 – Local operating conditions for the selected blade sections in “case 1”

#### Airfoil $t/c=30\%$

Figure 3.2-7 and Figure 3.2-8 are useful to get an idea of the air flow but it is very difficult to find similarities or differences between both flows. That is why the pressure and the friction coefficients are shown in Figure 3.2-9 and Figure 3.2-10. These figures show the pressure coefficient obtained in the 3D and the 2D simulations. For the 2D simulations two angles of attack have been represented, the one coming from the BEM code and the one obtained with the 3D CFD simulation (see Table 3.2-1).

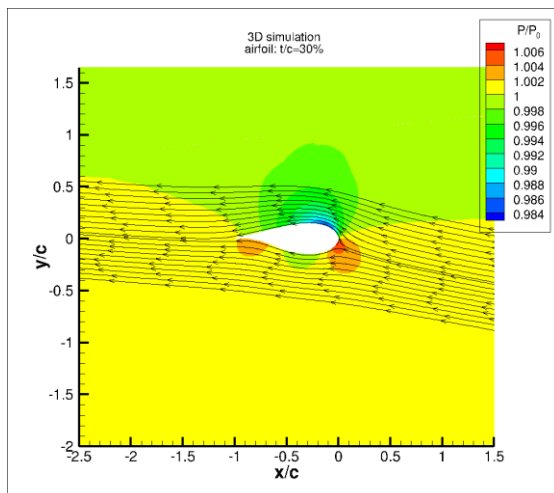


Figure 3.2-7 Pressure contour and streamlines. 3D simulation of the  $t/c=30\%$  airfoil for “case 1”

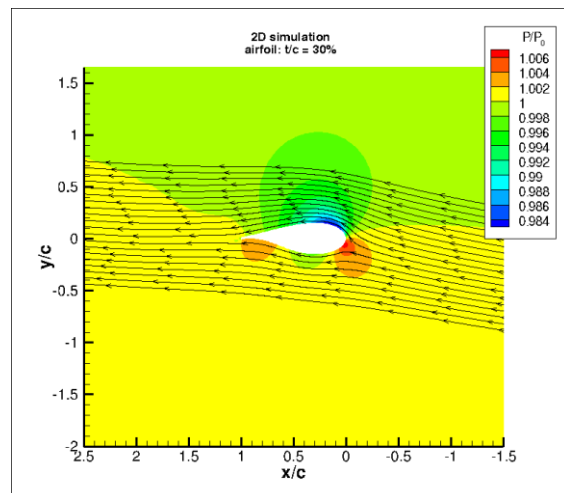


Figure 3.2-8 Pressure contour and streamlines. 2D simulation of the  $t/c=30\%$  airfoil for “case 1”

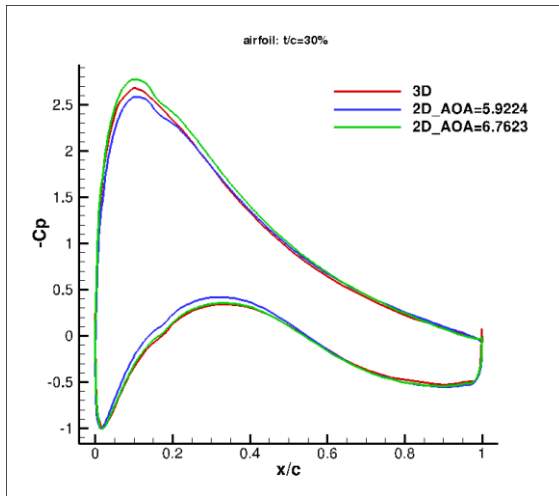


Figure 3.2-9 Pressure coefficient. Simulations of the  $t/c=30\%$  airfoil for “case 1”

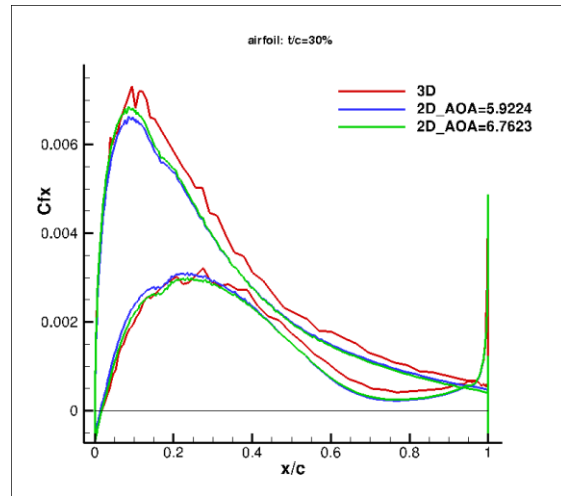


Figure 3.2-10 Friction coefficient “X” direction. Simulations of the  $t/c=30\%$  airfoil for “case 1”

According to the  $C_p$  curve (Figure 3.2-9) the AOA estimated with the CFD 3D calculation matches the pressure side and slightly over predicts the suction side. On the other hand, the simulation that uses the BEM angle of attack as input, underestimates both sides. The friction coefficient in the “X” direction shows good agreement at the leading edge but fails after the maximum peak. Anyway the irregularities present in the curve show some kind of very local curvature fluctuations in the geometry definition.

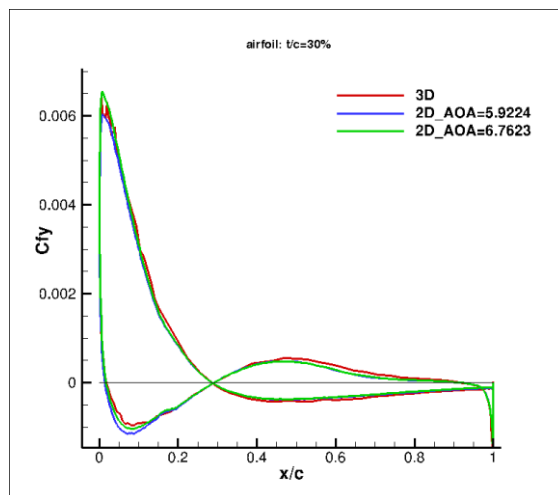


Figure 3.2-11 Friction coefficient “Y” direction. Simulations of the  $t/c=30\%$  airfoil for “case 1”

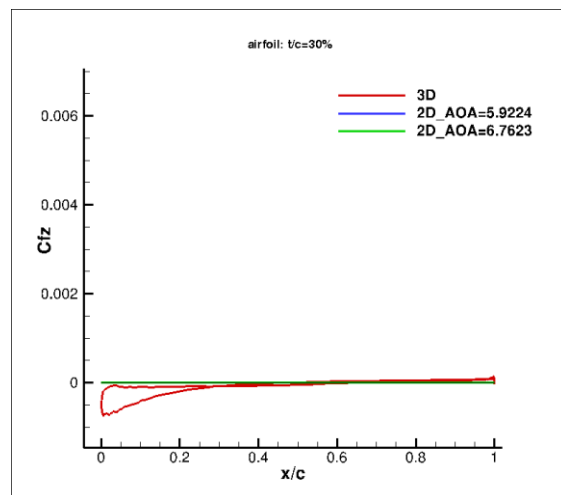


Figure 3.2-12 Friction coefficient “Z” direction. Simulations of the  $t/c=30\%$  airfoil for “case 1”

The friction coefficient along the “Y” direction shows good agreement in all the cases. As expected, the “Z” friction coefficient for the 2D calculations is zero and small for the 3D simulations.

Sometimes the differences appreciated in the  $C_p$  or the  $C_f$  curves may guide to the conclusion that the AOA calculated is slightly different from the one seen by the profile when operating in the blade. To check that assessment, the pressure lift coefficient of the

3D simulation has been calculated, afterwards, that lift has been obtained from a 2D calculation. Those two  $C_p$  curves have been plotted together in Figure 3.2-13. The lift generated by the pressure distribution for each of the simulations shown below, have been collected in Table 3.2-4:

Type of simulation	Source of the AOA	AOA (°)	$C_{Lp}$
2D	BEM code	5.92	1.26
2D	3D CFD simulation	6.76	1.36
2D	Interpolation to match $C_{Lp}$	5.99	1.31
3D	-	-	1.31

Table 3.2-4 – Pressure lift coefficient for the different simulations. "Case2" airfoil  $t/c=30\%$

Figure 3.2-13 shows the pressure coefficient distribution for the AOA that matches the pressure lift coefficient between the 2D and the 3D simulation. The data has been interpolated between the data for  $AOA=5.92^\circ$  and  $AOA=6^\circ$ . Even giving the same integrated lift coefficient, both pressure distributions do not match.

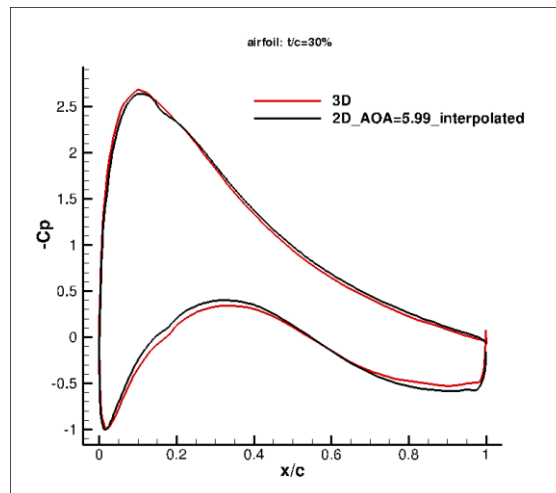


Figure 3.2-13 Pressure coefficient. Simulations of the  $t/c=30\%$  airfoil for "case 1"

Even for sections with small 3D effects, matching the  $C_p$  curve between 2D and 3D simulations is difficult. As it is not the objective of this project, it has been shown as an example of the minimum differences that the  $C_p$  curves will show, but this analysis is progressively going to disappear for the following cases to let the reader focus on the important facts of the study towards the design of blade root airfoils.

### Airfoil $t/c=40\%$

In Figure 3.2-14 and Figure 3.2-15 the differences in the pressure generated around the airfoil begin to be observable.

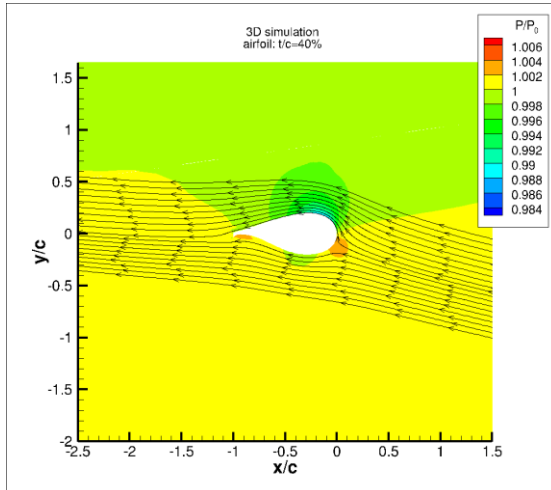


Figure 3.2-14 Pressure contour and streamlines. 3D simulation of the  $t/c=40\%$  airfoil for “case 1”

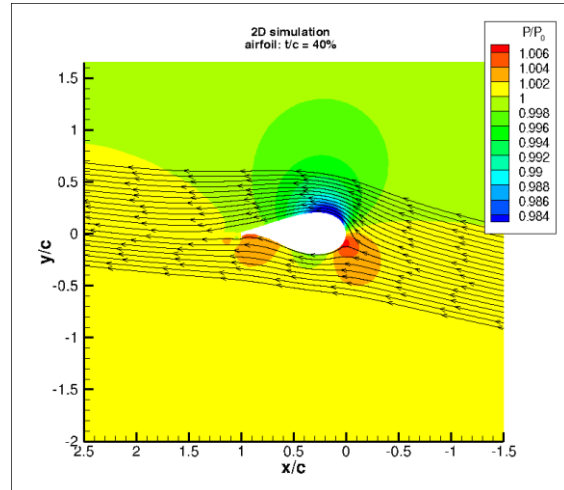


Figure 3.2-15 Pressure contour and streamlines. 2D simulation of the  $t/c=40\%$  airfoil for “case 1”

The pressure and the friction coefficients are shown in Figure 3.2-16 and Figure 3.2-17. These figures show the coefficients obtained in the 3D and the 2D simulations. For the 2D simulations two angles of attack have been represented, the one coming from the BEM code (blue line) and the one obtained with the 3D CFD simulation (green line).

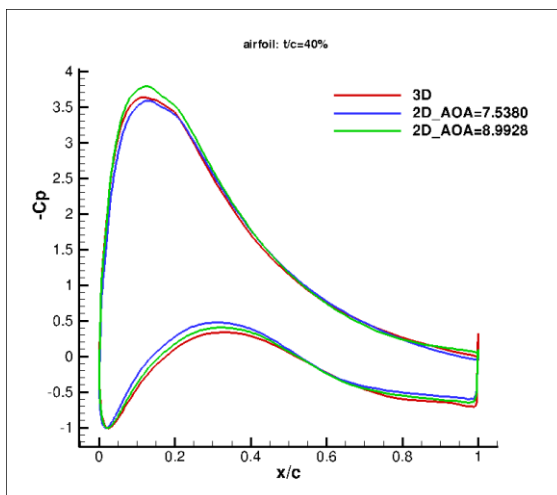


Figure 3.2-16 Pressure coefficient. Simulations of the  $t/c=40\%$  airfoil for “case 1”

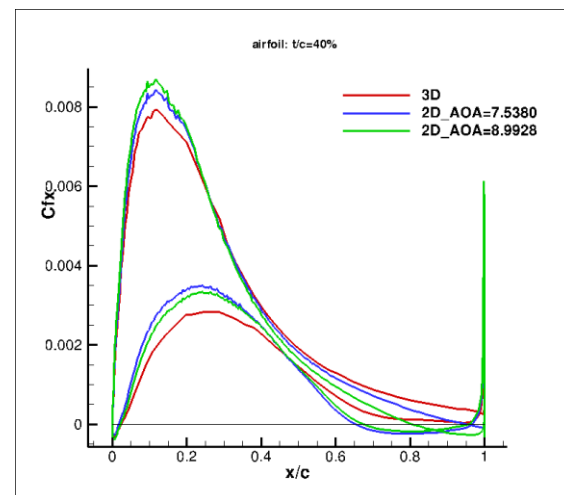


Figure 3.2-17 Friction coefficient “X” direction. Simulations of the  $t/c=40\%$  airfoil for “case 1”

The calculations at the BEM-calculated angle of attack are in good agreement with the suction part of the curve; however, the prediction of the pressure side is not as good as the suction-side one. The angle of attack calculated with the CFD code gives a better approximation to the pressure side than the BEM code does, but it still underpredicts the pressure coefficient. The suction peak is overpredicted by the 2D calculation if the AOA

calculated with the CFD code is used. Differences appear around the maximum peaks and the trailing edge area.

Both angles of attack give rise to bigger friction coefficient along the “X” direction in the frontal part of the airfoil. Instead, in the rear part, they predict a smaller friction coefficient than the 3D does.

According to the  $C_{fx}$ , the flow does not separate in the 3D calculation, but it does in the 2D simulations. At the suction side the flow separates between  $x/c=0.8$  and  $x/c=0.9$  (depending on the AOA) and the separation occurs around  $x/c=0.7$  in the pressure side.

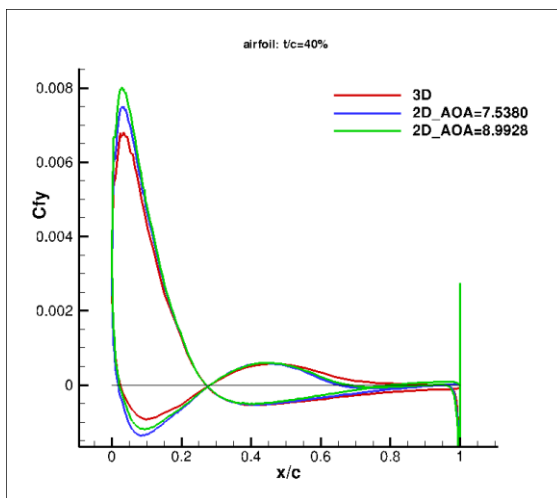


Figure 3.2-18 Friction coefficient “Y” direction. Simulations of the  $t/c=40\%$  airfoil for “case 1”

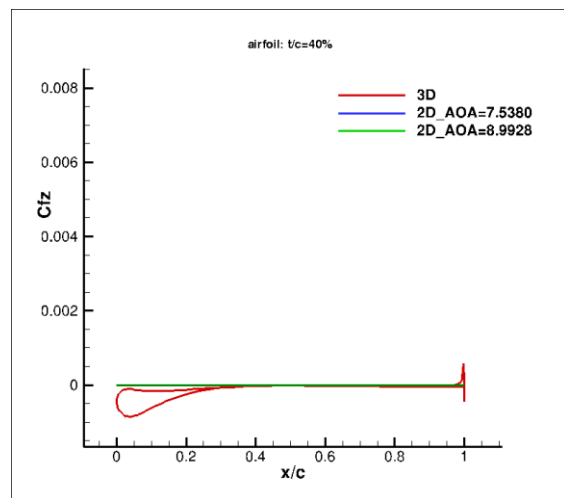


Figure 3.2-19 Friction coefficient “Z” direction. Simulations of the  $t/c=40\%$  airfoil for “case 1”

The friction coefficient in the “Y” direction is slightly overestimated. As expected, the “Z” friction coefficient for the 2D calculations is zero and small for the 3D simulations. Notice that the  $C_{fz}$  is bigger in the leading edge region, showing that the velocities in the “Z” direction are bigger in that area.

### Airfoil $t/c=50\%$

Figure 3.2-20 and Figure 3.2-21 show the big difference in the separation region between the 2D and the 3D simulation. The flow in the 2D case is much more separated.

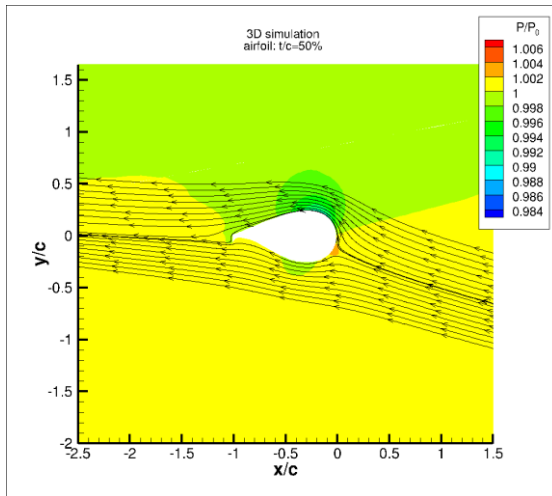


Figure 3.2-20 Pressure contour and streamlines. 3D simulation of the  $t/c=50\%$  airfoil for “case 1”

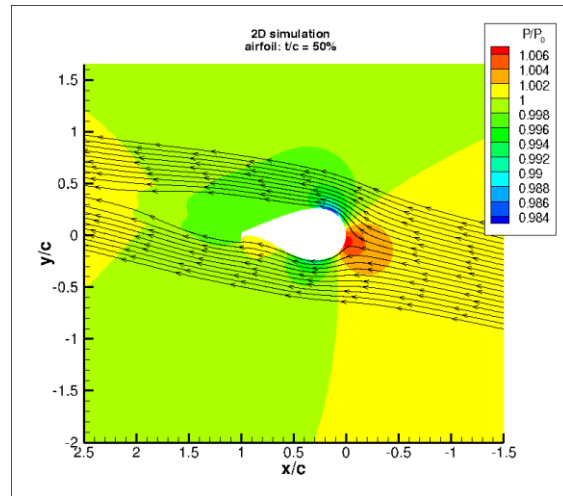


Figure 3.2-21 Pressure contour and streamlines. 2D simulation of the  $t/c=50\%$  airfoil for “case 1”

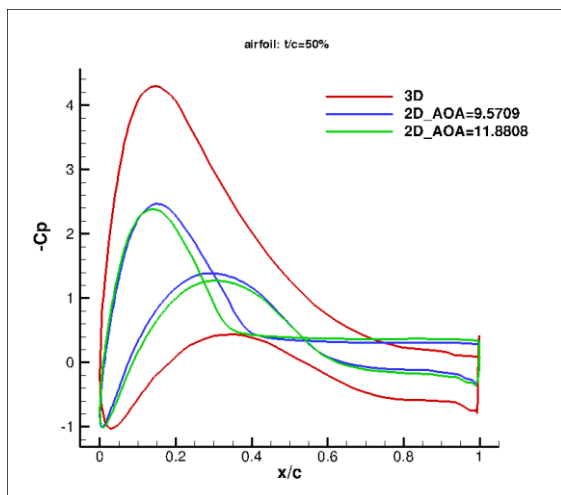


Figure 3.2-22 Pressure coefficient. Simulations of the  $t/c=50\%$  airfoil for “case 1”

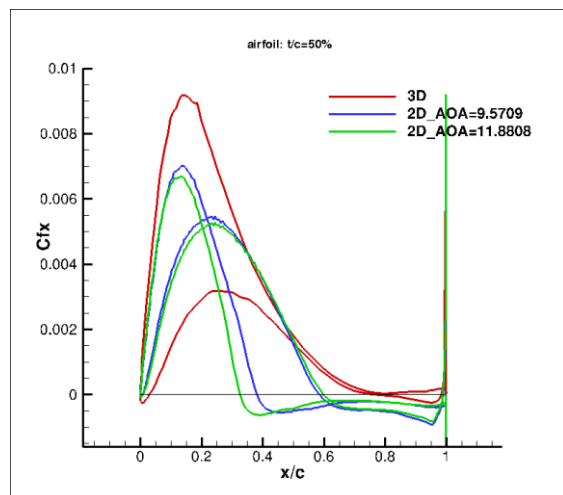


Figure 3.2-23 Friction coefficient “X” direction. Simulations of the  $t/c=50\%$  airfoil for “case 1”

The  $C_p$  curve shows that the angles of attack predicted by the CFD and the BEM codes are smaller than the one “seen” by the airfoil in the 3D calculation. Calculations up to AOA  $10^\circ$  have been made, but the  $C_p$  curve was not reproduced. It was seen in the study of the 30%-thick airfoil that the 3D effects avoid the perfect match of the  $C_p$  curve. Moreover, in this section those effects are expected to be even bigger.

The separation in the 2D case is much more detrimental than in the 3D case because it happens earlier (at earlier AOA and earlier  $x/c$  position). The 2D case separates around  $x/c=0.4$  at the suction side and around  $x/c=0.6$  at the pressure side. However, the 3D flow keeps attached up to  $x/c=0.8$  at both sides.

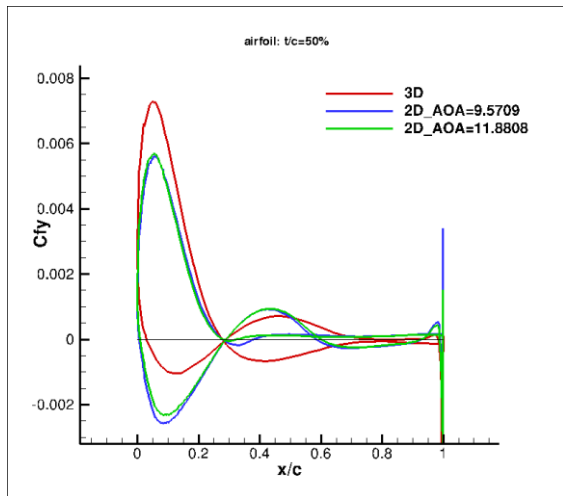


Figure 3.2-24 Friction coefficient “Y” direction. Simulations of the  $t/c=50\%$  airfoil for “case 1”

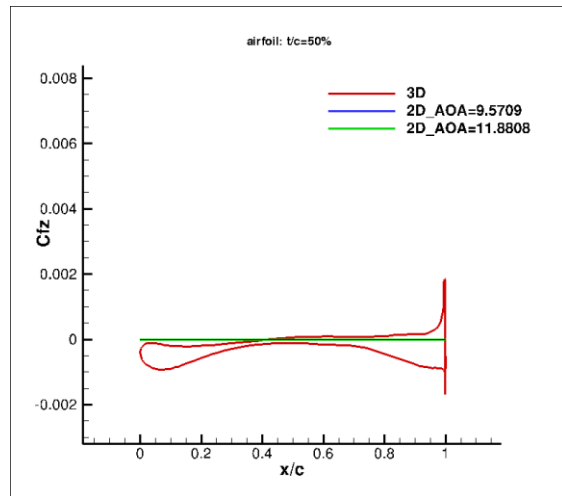


Figure 3.2-25 Friction coefficient “Z” direction. Simulations of the  $t/c=50\%$  airfoil for “case 1”

The friction coefficient in the “Y” direction differs from the 2D to the 3D calculation. As expected, the “Z” friction coefficient for the 2D calculations is zero and small for the 3D simulations. In this case the friction coefficient along the “Z” direction is important not only in the leading edge region but also in the trailing edge area. That means that there is a significant amount of radial flow in those two regions.

In the “case 1”, the 3D rotational effects exist in the whole studied region. The pressure and friction coefficients calculated with the CFD 3D simulation are not the same as the 2D cases, however it has been noticed that the effect is the stronger the closer to the root the analysed regions are.

3D cases show a less detrimental separation than the 2D cases. The separation happens at lower angles of attack in the 2D simulation. That makes the 3D sections generate a higher lift and a lower drag than the expected when analysing the 2D situation.

The radial flow is important in the leading edge region for all the cases but it is also important in the trailing edge for the airfoil that is the closest to the root.

### 3.2.5 Case 2

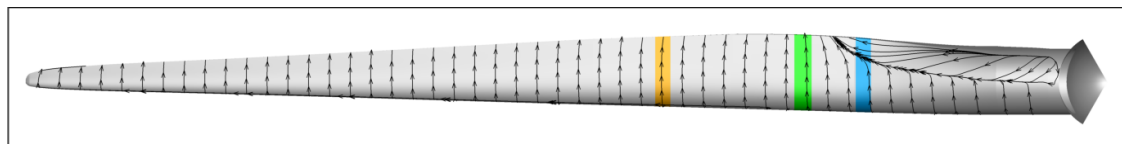


Figure 3.2-26 Suction side. Streamlines and studied profiles.

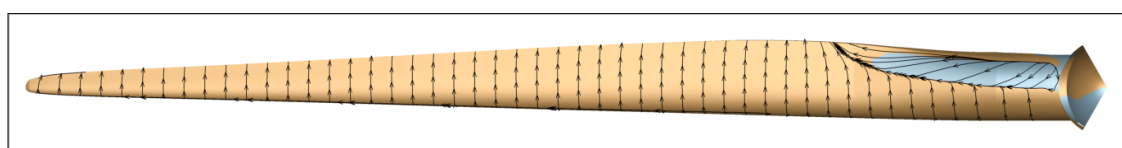


Figure 3.2-27 Suction side. Streamlines and  $C_{fx}$  contours (yellow,  $C_{fx}>0$  and grey,  $C_{fx}<0$ ).

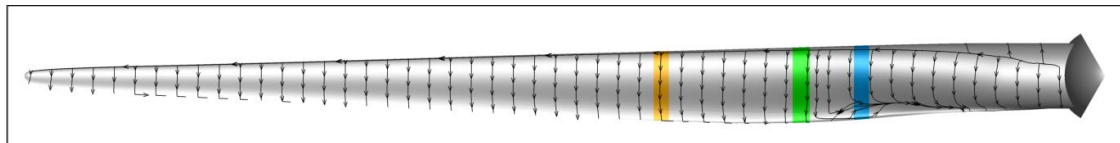


Figure 3.2-28 Pressure side. Streamlines and studied profiles.

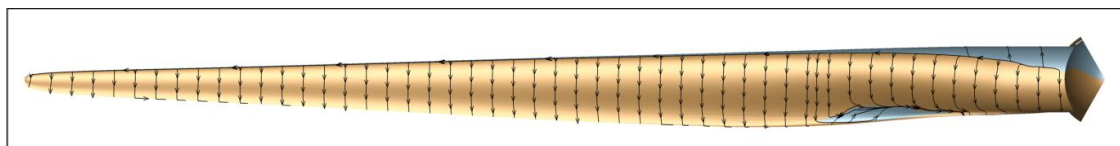


Figure 3.2-29 Pressure side. Streamlines and Cfx contours (yellow, Cfx>0 and grey, Cfx<0).

This case operates at higher wind and rotational speeds with respect to “case 1“, however, as the AOA and the Reynolds number are kept almost constant, the behaviour is very similar.

Table 3.2-5 shows the local operating conditions for the selected airfoils in “case 2“. Notice that only the 2D simulation at the AOA calculated from the 3D-CFD is presented from here on out.

Airfoil thickness	Re	M	AOA geometrical (°)	AOA BEM (°)	AOA CFD (°)
30%	15.2e6	0.11	12.5	5.9	6.7
40%	11.6e6	0.08	17.4	7.5	8.8
50%	9.6e6	0.07	20.2	9.5	11.7

Table 3.2-5 – Local operating conditions for the selected blade sections in “case 2”

#### Airfoil t/c=30%

The airfoil characterized by the 30% thickness is the one showing the smallest three-dimensional effects. That is the reason behind the good match of the curves from the 2D and the 3D simulation. However there are small differences that follow the same tendency as the one studied in “case 1”.

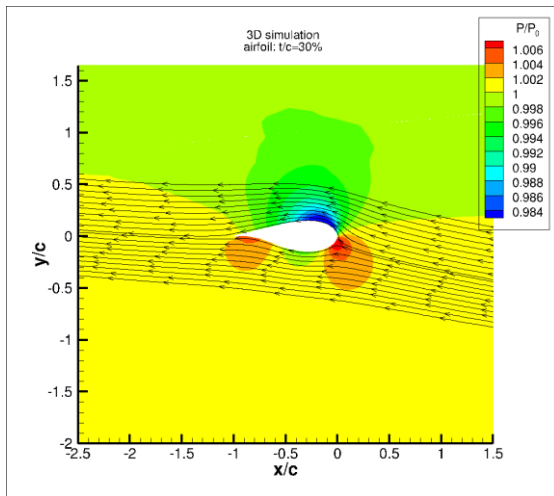


Figure 3.2-30 Pressure contour and streamlines. 3D simulation of the  $t/c=30\%$  airfoil for “case 2”

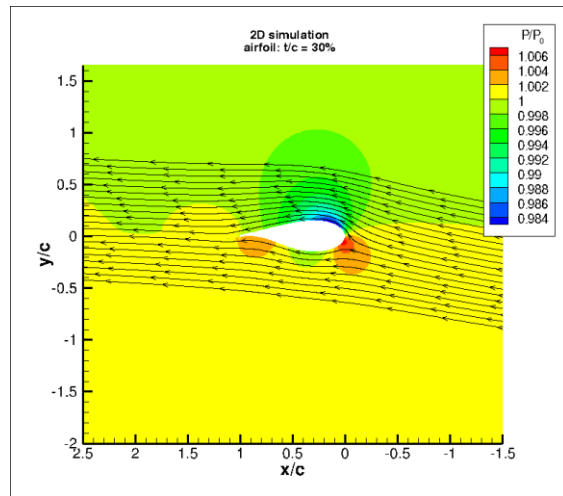


Figure 3.2-31 Pressure contour and streamlines. 2D simulation of the  $t/c=30\%$  airfoil for “case 2”

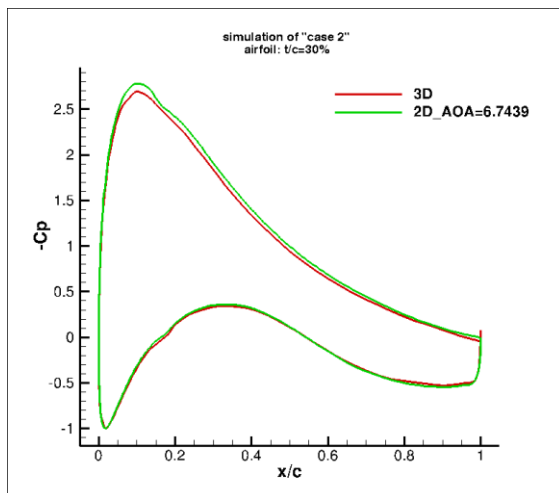


Figure 3.2-32 Pressure coefficient. Simulations of the  $t/c=30\%$  airfoil for “case 2”

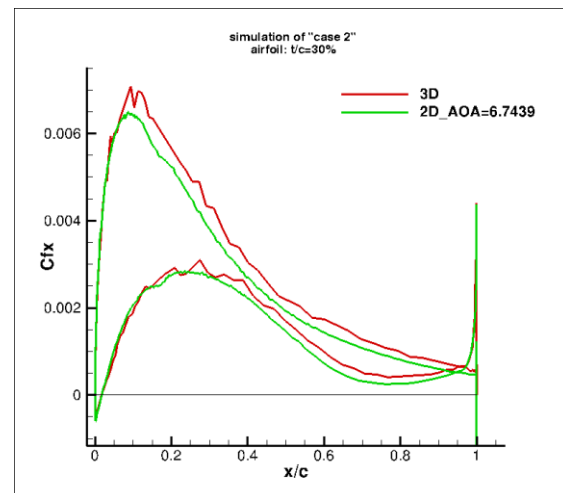


Figure 3.2-33 Friction coefficient “X” direction. Simulations of the  $t/c=30\%$  airfoil for “case 2”

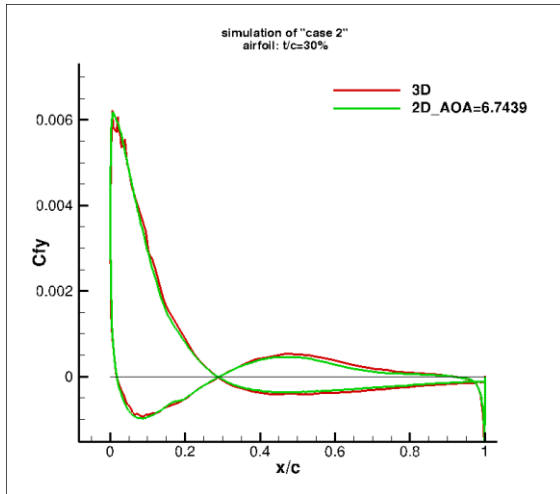


Figure 3.2-34 Friction coefficient "Y" direction. Simulations of the  $t/c=30\%$  airfoil for "case 2"

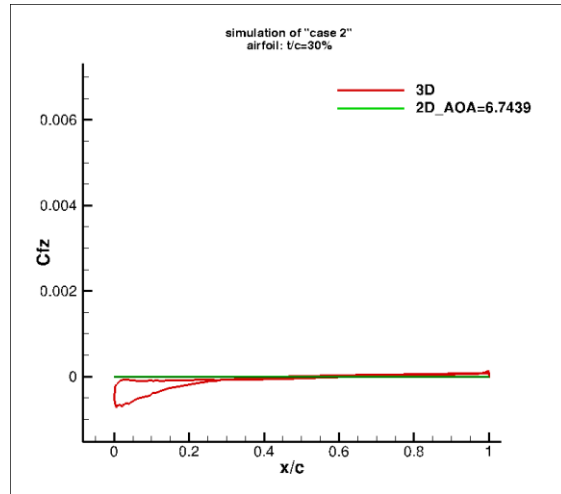


Figure 3.2-35 Friction coefficient "Z" direction. Simulations of the  $t/c=30\%$  airfoil for "case 2"

### Airfoil $t/c=40\%$

As the three-dimensional effects begin to gain importance, the differences between the 2D and the 3D simulation appear. It is very important the fact that the flow separates in the 2D case, while it remains attached for the 3D case.

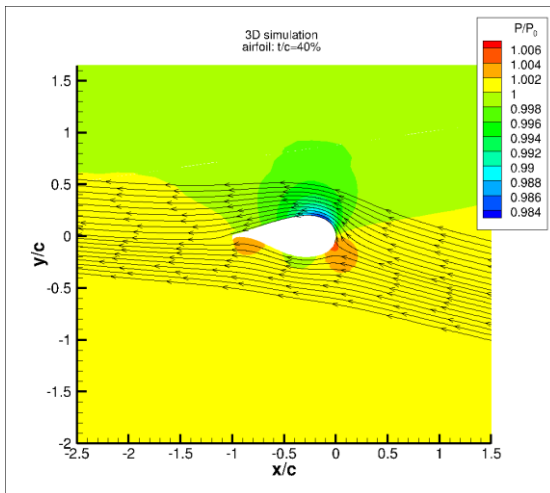


Figure 3.2-36 Pressure contour and streamlines. 3D simulation of the  $t/c=40\%$  airfoil for "case 2"

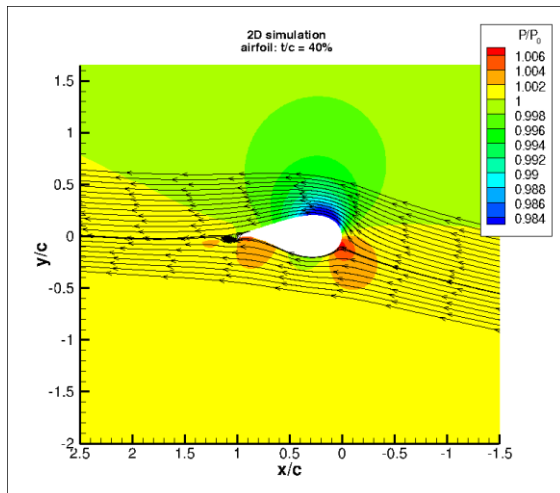


Figure 3.2-37 Pressure contour and streamlines. 2D simulation of the  $t/c=40\%$  airfoil for "case 2"

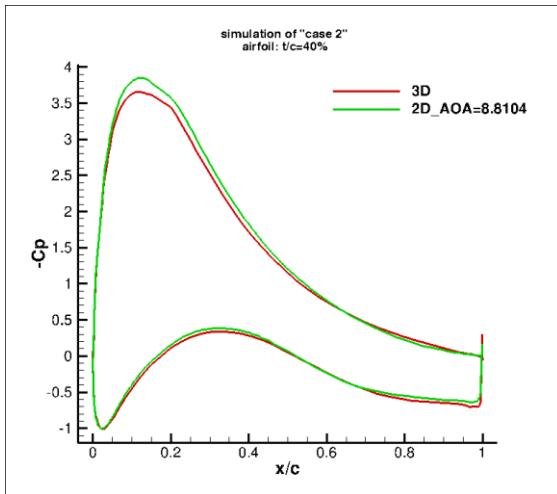


Figure 3.2-38 Pressure coefficient. Simulations of the  $t/c=40\%$  airfoil for "case 2"

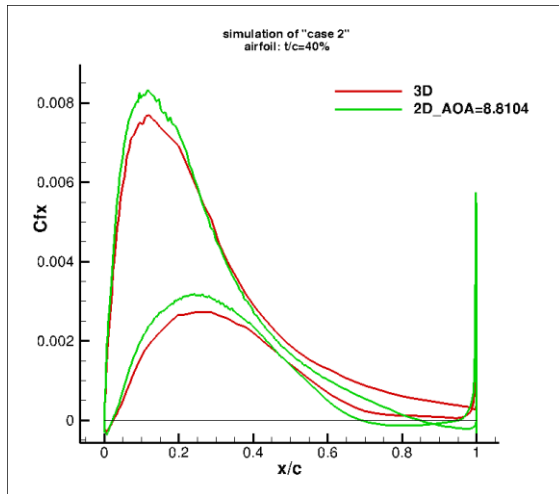


Figure 3.2-39 Friction coefficient "X" direction. Simulations of the  $t/c=40\%$  airfoil for "case 2"

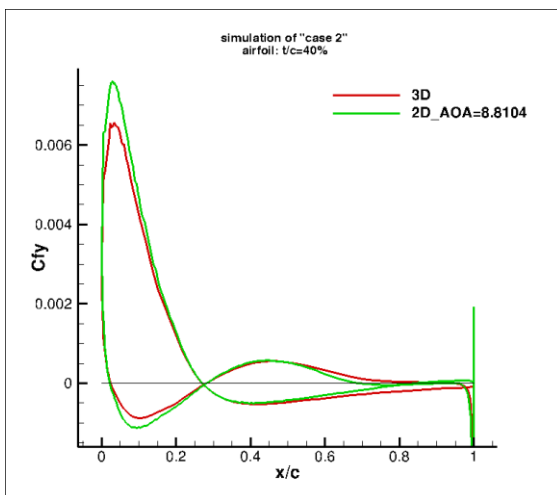


Figure 3.2-40 Friction coefficient "Y" direction. Simulations of the  $t/c=40\%$  airfoil for "case 2"

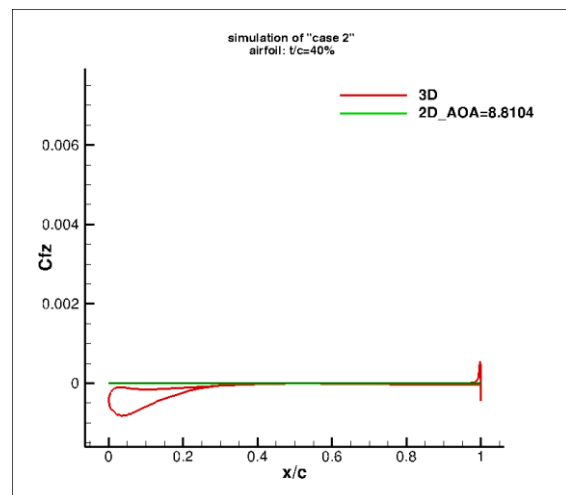


Figure 3.2-41 Friction coefficient "Z" direction. Simulations of the  $t/c=40\%$  airfoil for "case 2"

### Airfoil $t/c=50\%$

The three-dimensional effects are very important. The flow separates at different positions along the blade depending on the type of simulation used (2D or 3D). Of course the flows are very different after the separation point, but they are also very different upstream of those positions.

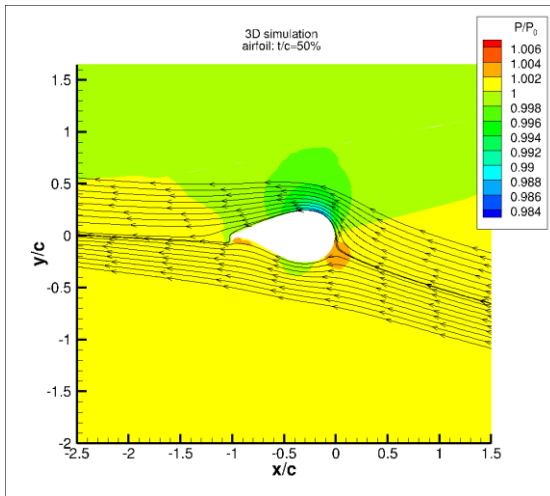


Figure 3.2-42 Pressure contour and streamlines. 3D simulation of the  $t/c=50\%$  airfoil for “case 2”

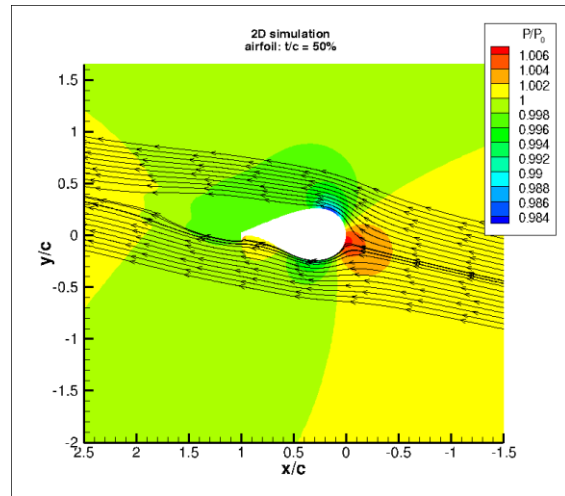


Figure 3.2-43 Pressure contour and streamlines. 2D simulation of the  $t/c=50\%$  airfoil for “case 2”

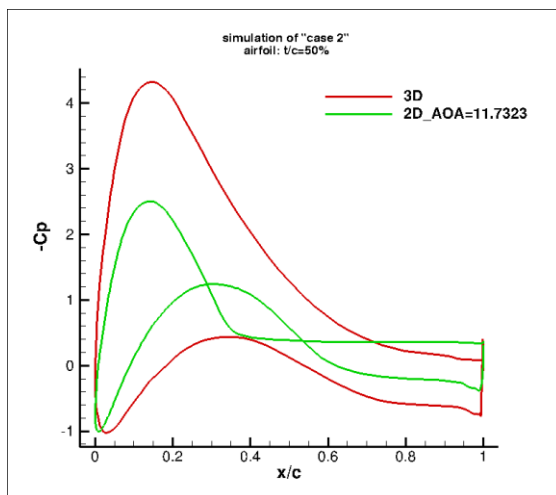


Figure 3.2-44 Pressure coefficient. Simulations of the  $t/c=50\%$  airfoil for “case 2”

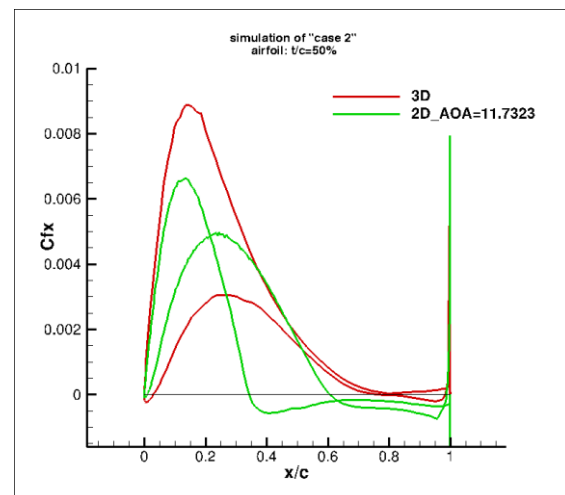


Figure 3.2-45 Friction coefficient “X” direction. Simulations of the  $t/c=50\%$  airfoil for “case 2”

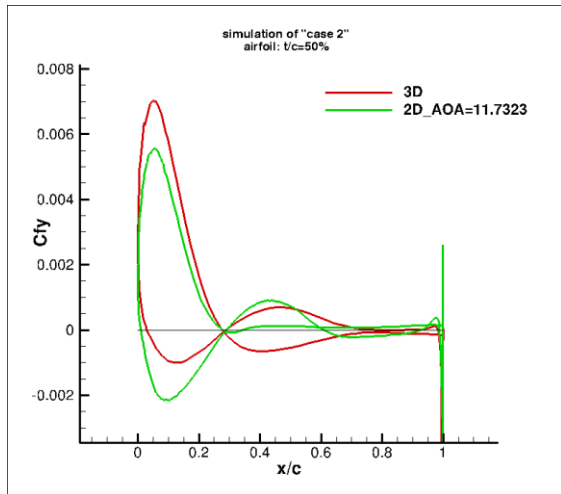


Figure 3.2-46 Friction coefficient “Y” direction. Simulations of the  $t/c=50\%$  airfoil for “case 2”

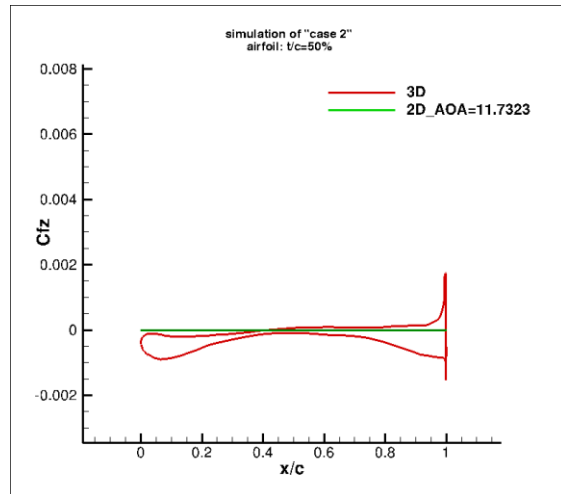


Figure 3.2-47 Friction coefficient “Z” direction. Simulations of the  $t/c=50\%$  airfoil for “case 2”

### 3.2.6 Case 3

In this case, the airfoils are working at lower angles of attack (around  $1^\circ$ ). Remember that this is not a typical operation point of the turbine (the rotational speed is much higher than the one corresponding to this wind speed).

As a consequence, in this case, the separation is more severe in the pressure side than it was before. The separation in the suction side slightly affects the 50%-thick airfoil, but in the pressure side, both the 50%-thick and the 40%-thick airfoils suffer separation in the 3D simulation. The 30%-thick airfoil does not separate neither in the suction side nor in the pressure one.

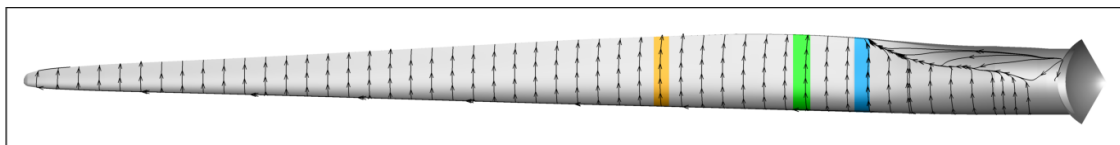


Figure 3.2-48 Suction side. Streamlines and studied profiles.

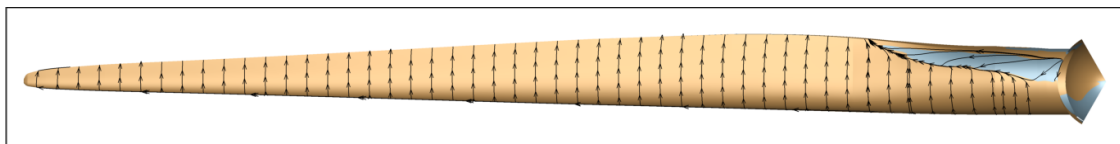


Figure 3.2-49 Suction side. Streamlines and  $C_{fx}$  contours (yellow,  $C_{fx}>0$  and grey,  $C_{fx}<0$ ).

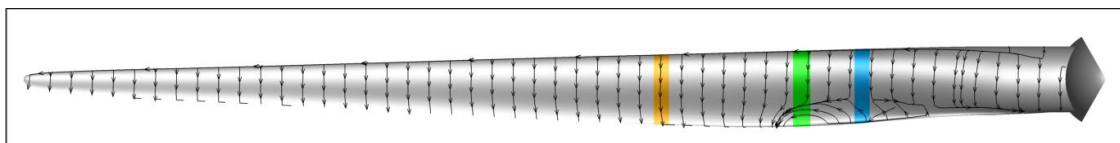


Figure 3.2-50 Pressure side. Streamlines and studied profiles.

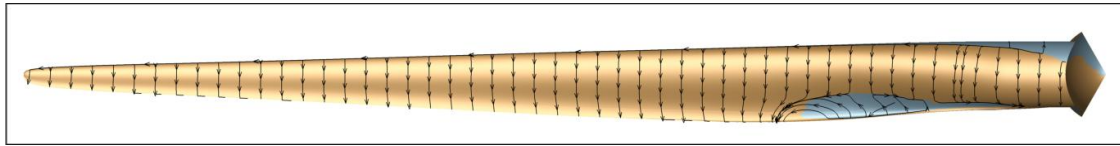


Figure 3.2-51 Pressure side. Streamlines and Cfx contours (yellow,  $C_{fx} > 0$  and grey,  $C_{fx} < 0$ ).

Table 3.2-6 shows the local operating conditions for the selected airfoils in “case 3”:

Airfoil thickness	Re	M	AOA geometrical (°)	AOA BEM (°)	AOA CFD (°)
30%	14.7e6	0.11	5.2	0.3	0.9
40%	11.0e6	0.08	7.4	0.6	1.0
50%	8.8e6	0.06	8.6	1.5	1.7

Table 3.2-6 – Local operating conditions for the selected blade sections in “case 3”

### Airfoil $t/c=30\%$

The flows for the 30%-thick airfoil are very similar one another. The major differences are found in the friction coefficient along the “X” direction in the rear part of the airfoil. Moreover, as shown in other cases, there is an important “Z” velocity in the leading edge area.

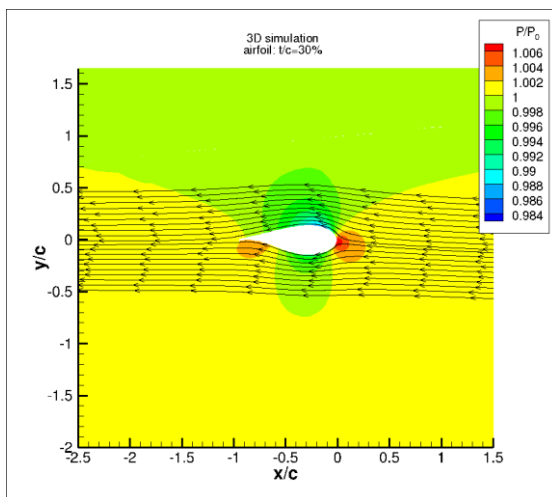


Figure 3.2-52 Pressure contour and streamlines. 3D simulation of the  $t/c=30\%$  airfoil for “case 3”

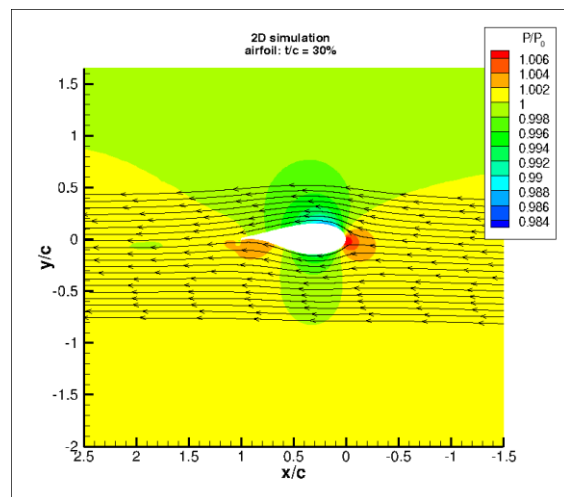


Figure 3.2-53 Pressure contour and streamlines. 2D simulation of the  $t/c=30\%$  airfoil for “case 3”

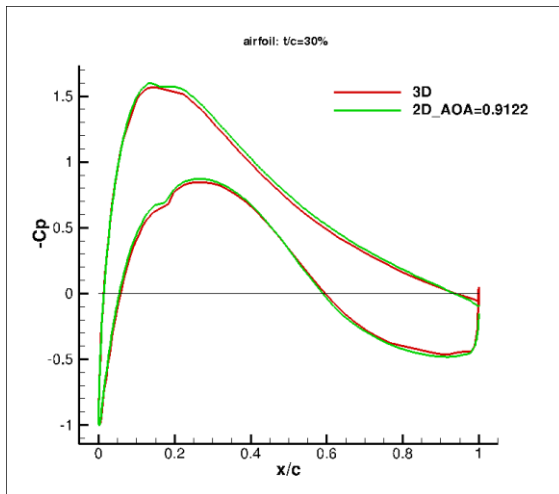


Figure 3.2-54 Pressure coefficient. Simulations of the  $t/c=30\%$  airfoil for “case 3”

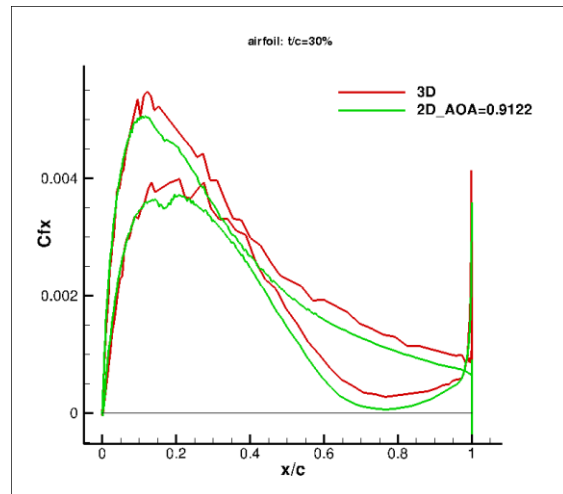


Figure 3.2-55 Friction coefficient “X” direction. Simulations of the  $t/c=30\%$  airfoil for “case 3”

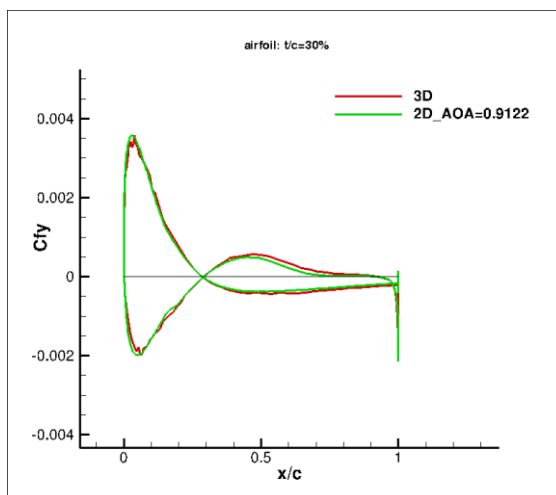


Figure 3.2-56 Friction coefficient “Y” direction. Simulations of the  $t/c=30\%$  airfoil for “case 3”

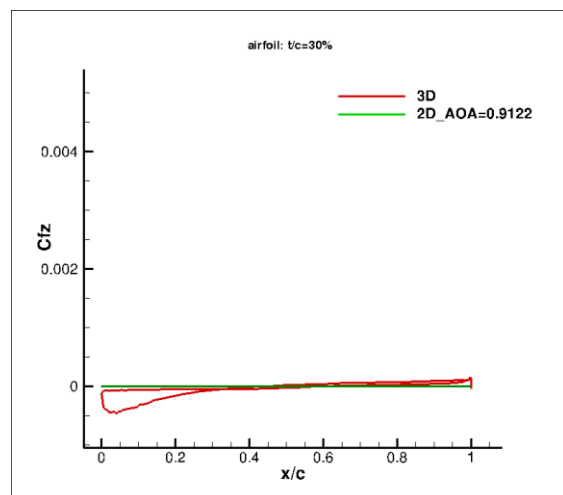


Figure 3.2-57 Friction coefficient “Z” direction. Simulations of the  $t/c=30\%$  airfoil for “case 3”

### Airfoil $t/c=40\%$

The flow in the 2D situation remains attached in the suction side, whereas the pressure side separates around  $x/c=0.6$ . For the 3D simulation, the pressure-side flow separates later than in the 2D case and the suction-side flow do not separates.

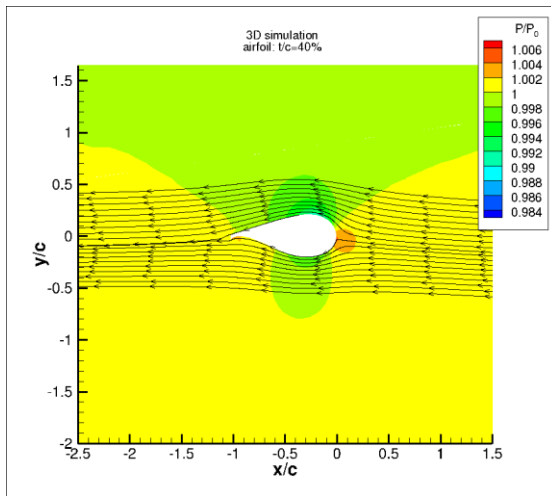


Figure 3.2-58 Pressure contour and streamlines. 3D simulation of the  $t/c=40\%$  airfoil for “case 3”

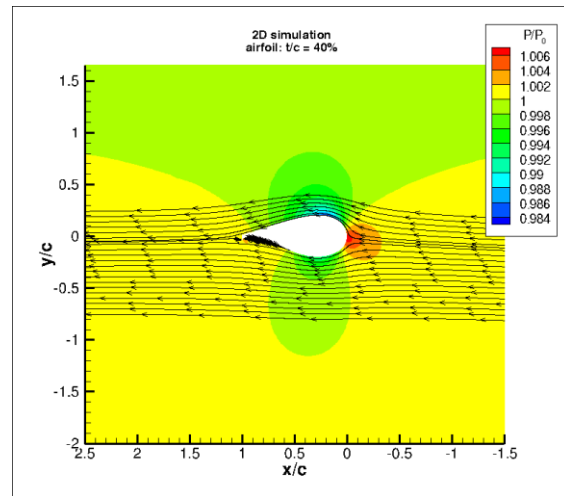


Figure 3.2-59 Pressure contour and streamlines. 2D simulation of the  $t/c=40\%$  airfoil for “case 3”

The  $C_p$  curve shows that the pressure is in better agreement between the 2D and the 3D simulations in the blade side with no separation, in this case, the pressure side.

The 2D simulation reaches higher friction coefficients around the maximum but suffers a stronger slope at the rear part of the airfoil that makes the flow separate earlier.

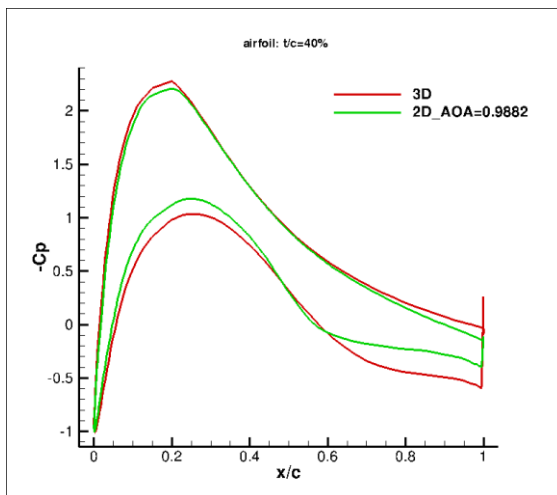


Figure 3.2-60 Pressure coefficient. Simulations of the  $t/c=40\%$  airfoil for “case 3”

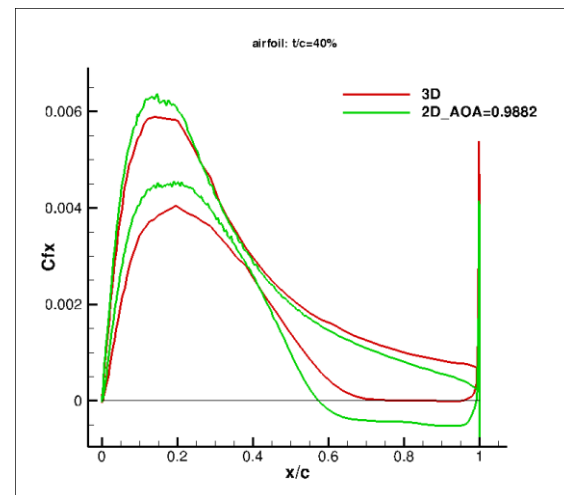


Figure 3.2-61 Friction coefficient “X” direction. Simulations of the  $t/c=40\%$  airfoil for “case 3”

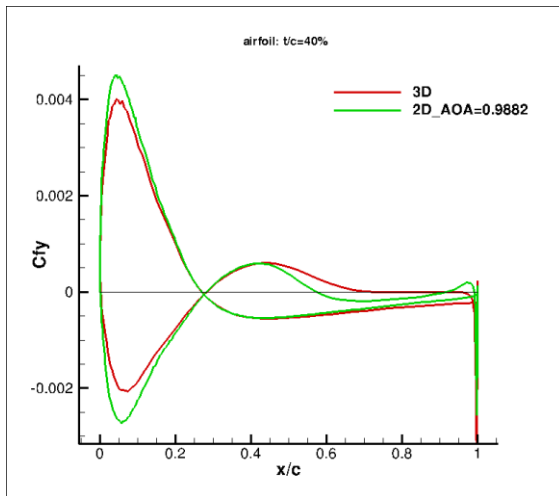


Figure 3.2-62 Friction coefficient “Y” direction. 2D simulation of the  $t/c=40\%$  airfoil for “case 3”

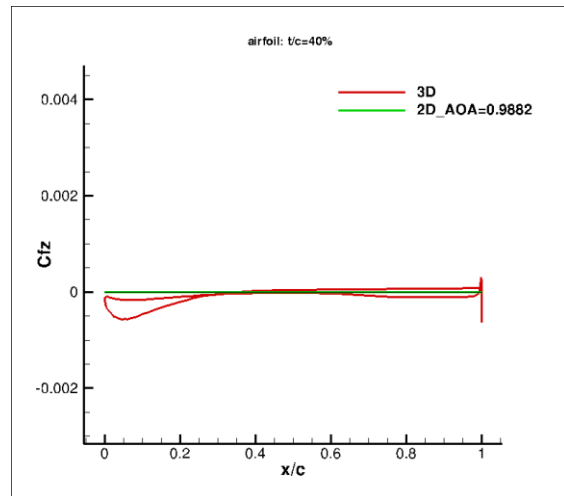


Figure 3.2-63 Friction coefficient “Z” direction. 2D simulation of the  $t/c=40\%$  airfoil for “case 3”

### Airfoil $t/c=50\%$

In this section of the blade, the separation affects at both sides of the blade. The three dimensional effects are so big in this region that the curves of pressure coefficient are very different between the two simulations. The flow in the radial direction is very important all along the airfoil.

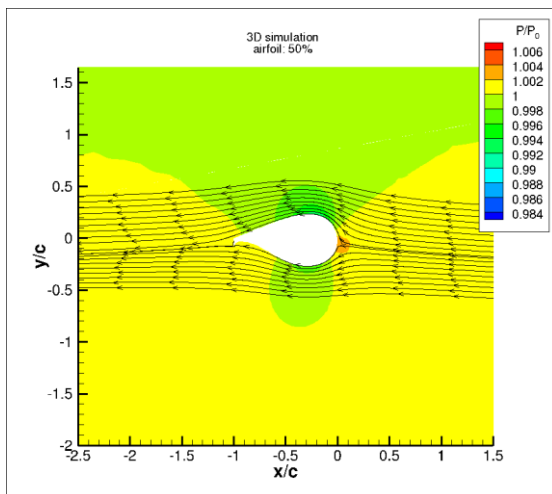


Figure 3.2-64 Pressure contour and streamlines. 3D simulation of the  $t/c=50\%$  airfoil for “case 3”

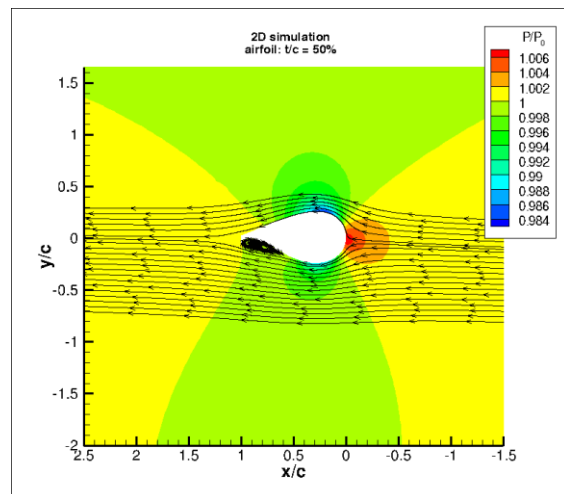


Figure 3.2-65 Pressure contour and streamlines. 2D simulation of the  $t/c=50\%$  airfoil for “case 3”

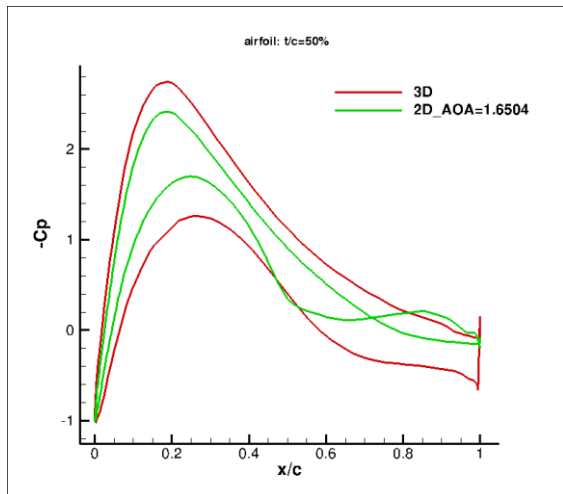


Figure 3.2-66 Pressure coefficient. Simulations of the  $t/c=50\%$  airfoil for “case 3”

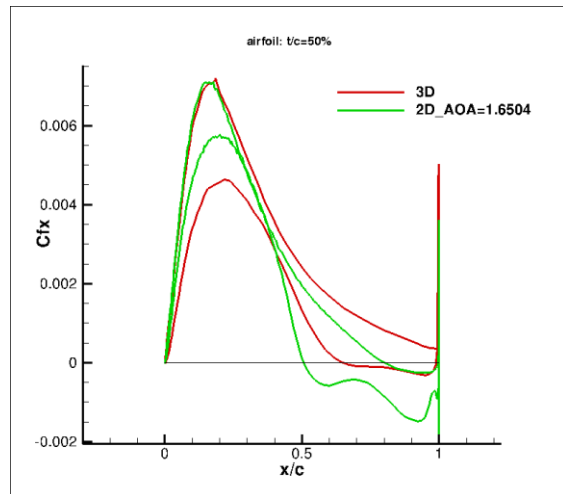


Figure 3.2-67 Friction coefficient “X” direction. Simulations of the  $t/c=50\%$  airfoil for “case 3”

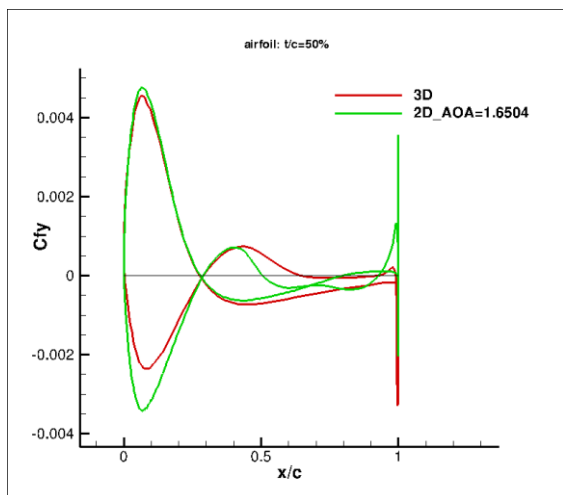


Figure 3.2-68 Friction coefficient “Y” direction. Simulations of the  $t/c=50\%$  airfoil for “case 3”

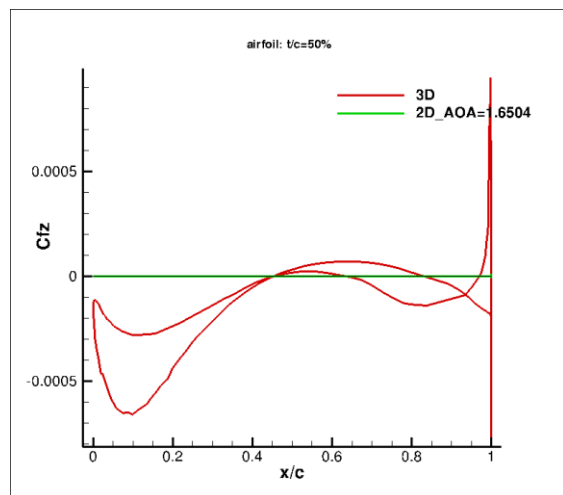


Figure 3.2-69 Friction coefficient “Z” direction. Simulations of the  $t/c=50\%$  airfoil for “case 3”

### 3.2.7 Conclusions

The three-dimensional effects are present all along the blade and for all the studied cases. However, those effects are the more important the closer the section is to the blade root. As a consequence those effects modify more the behaviour of the 50%-thick airfoil than the 30%-thick airfoil with respect to the 2D simulation.

The rotation of the blade seems to delay the separation of the flow, leading to airfoils working with attached flow even when the 2D simulation predicts the stall of the airfoil. Consequently, the airfoils generate more lift and less drag than expected. Obviously, downstream of the separation point the  $C_p$  and  $C_f$  curves of the 2D and the 3D simulations are completely different. However, differences are found also upstream of those positions. To sum up, the separation is delayed when operating in 3D flow conditions. It implies that the flow remains attached for a higher percentage of the chord increasing the lift and

reducing the pressure drag. However, friction increases. Those effects are the more noticeable the closer to the root.

This change in behaviour has to be kept in mind when designing airfoils by means of 2D calculations to take into consideration the real behaviour that they will offer when operating in the blade. These airfoils designed using 2D aerodynamic calculations will experience bigger pressure and lift coefficient during the operation in the blade than the one predicted by the 2D calculations.

### 3.3 State of the art of flat-back and high thickness airfoils

The airfoils that generate the root region of a blade are constrained by strong structural requirements. Those airfoils are usually high-thickness. To start designing thick airfoils a review of some available airfoils will be done. This study will be done through experiments; afterwards, a correction between experiments and computations will be developed.

The experiments of the Delft University ([13] and [14]) have characterized certain thick airfoils used for wind turbines blades roots. Some of those airfoils have been selected to represent the characteristics of this group of high-thickness airfoils.

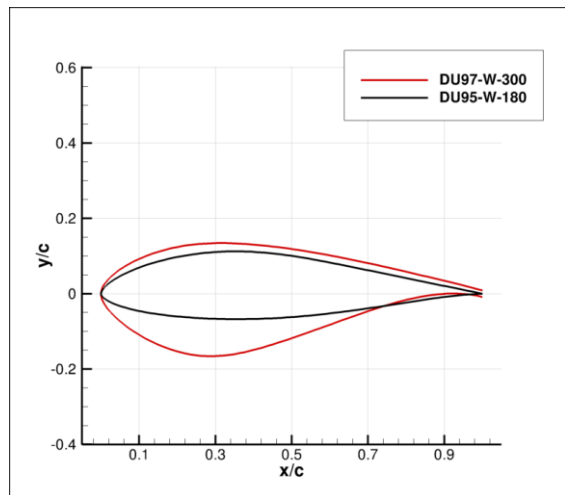


Figure 3.3-1 DU airfoils shape (1)

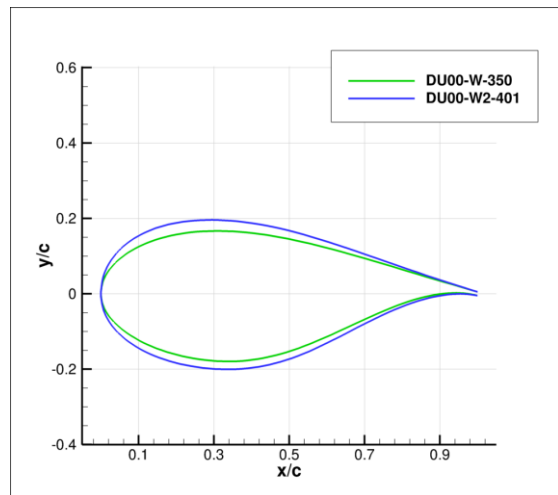


Figure 3.3-2 DU airfoils shape (2)

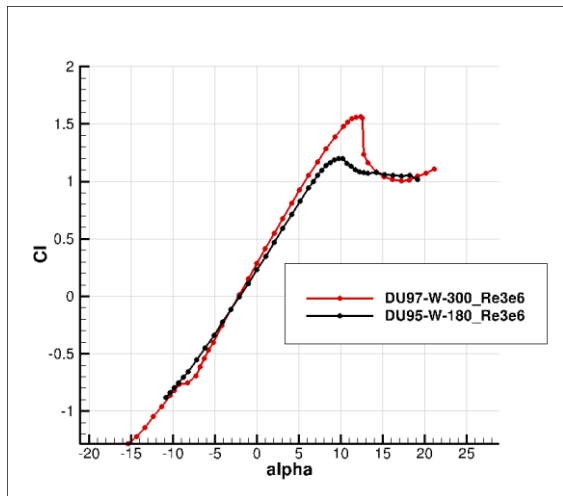


Figure 3.3-3 DU airfoils lift (1). Delft experiments

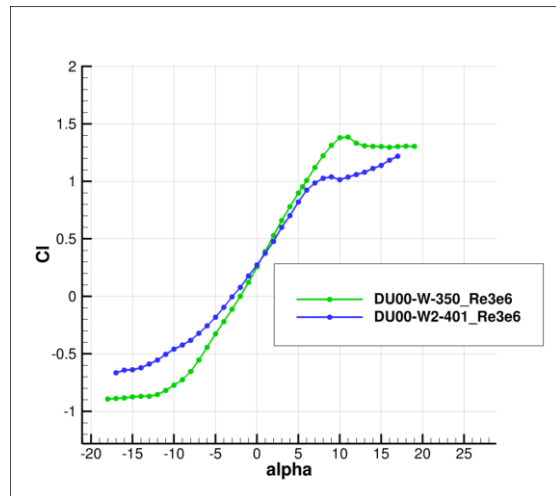


Figure 3.3-4 DU airfoils lift (2). Delft experiments

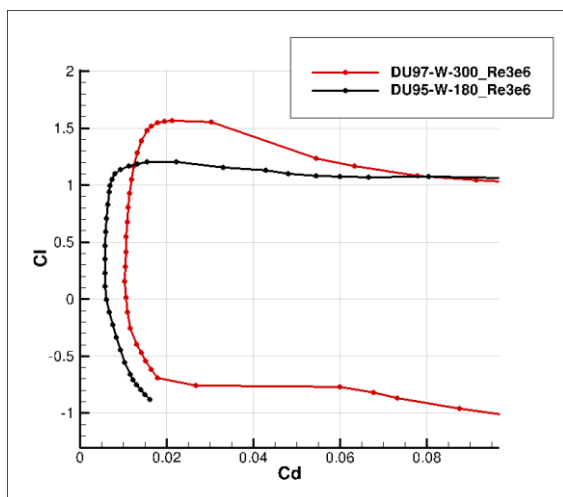


Figure 3.3-5 DU airfoils polar (1). Delft experiments

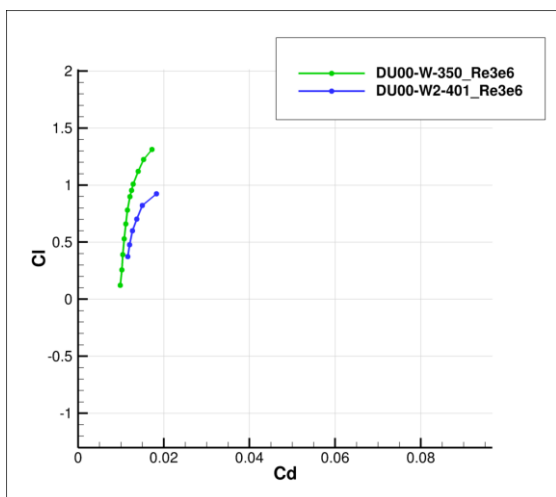


Figure 3.3-6 DU airfoils polar (2). Delft experiments

The study of the DU00-W-350 and the DU00-W2-401 shows that increasing the thickness of an airfoil, the lift curve slope is reduced. Moreover, the drag is increased. These two airfoils have the same trailing edge gap, that is why the tendency with the airfoil thickness can be shown for the studied cases. As Figure 3.3-6 shows, few drag data were found for these airfoils.

However, when the effect of thickness and trailing edge gap is added, the tendency is not as clear as shown in Figure 3.3-3 and Figure 3.3-5. From the literature, an increase of the trailing edge leads to bigger lift coefficient and bigger drag. Moreover, an increase in thickness ends up in lower lift coefficient slope and higher drag. Those effects are overlapped when studying the DU97-W-300 and the DU95-W-180. It is obvious that the 35%-thick airfoil has higher drag (because it has both thicker trailing edge and bigger thickness), but it also has higher lift coefficient slope which points out that the effect of that increase in the trailing edge is more important than the increase in airfoil thickness.

The Delft University has designed thick airfoils adequate for the root region of the blade. However, those airfoils have very thin trailing edge. As Haoran Xu et al. describe in [15], an

increase in the trailing edge gap can lead to higher lift coefficient and stronger airfoils. To cover a wider range of thickness and trailing edge gaps, some airfoils of the Stuttgarter Profilkatalog ([16]) have been analysed.

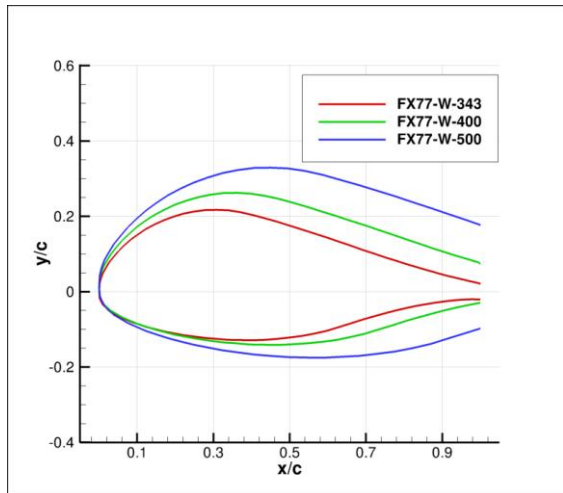


Figure 3.3-7 FX airfoils shape (1)

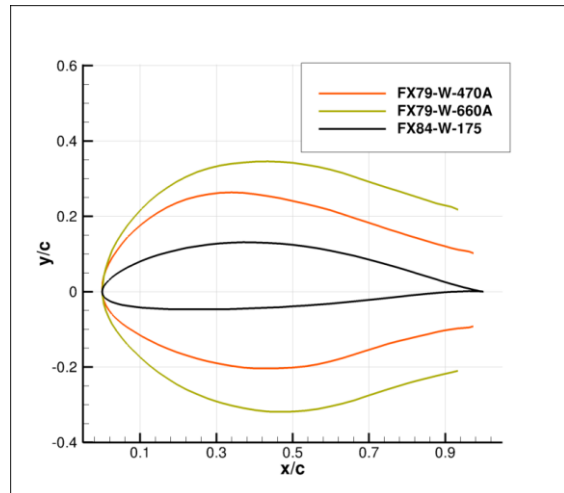


Figure 3.3-8 FX airfoils shape (2)

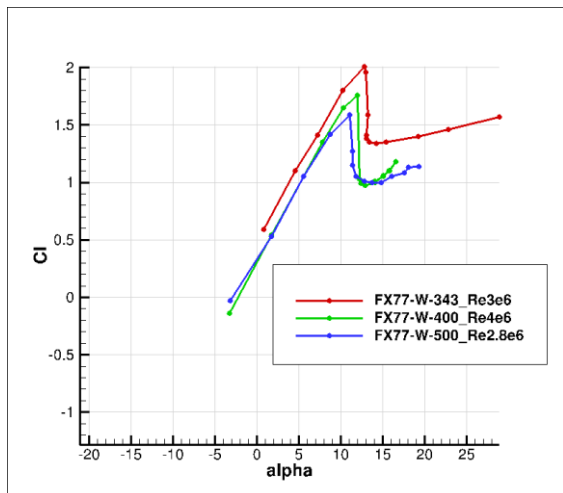


Figure 3.3-9 FX airfoils lift (1). Stuttgart experiments

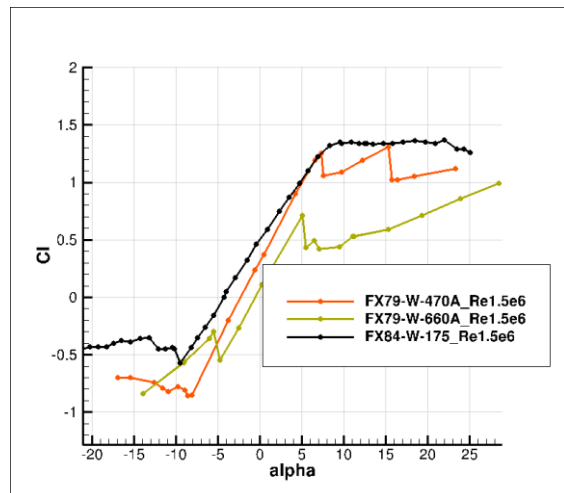


Figure 3.3-10 FX airfoils lift (2). Stuttgart experiments

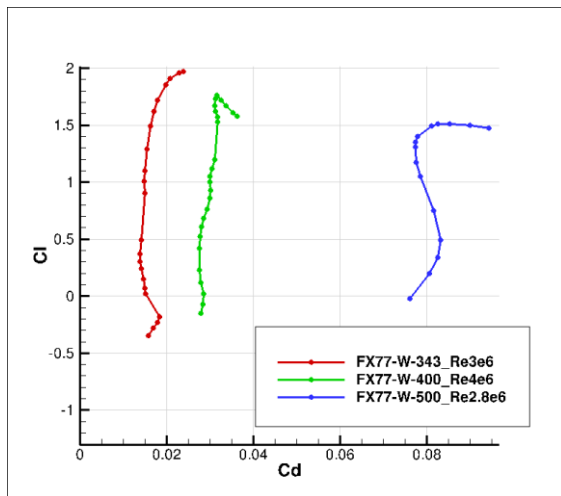


Figure 3.3-11 FX airfoils polar (1). Stuttgart experiments

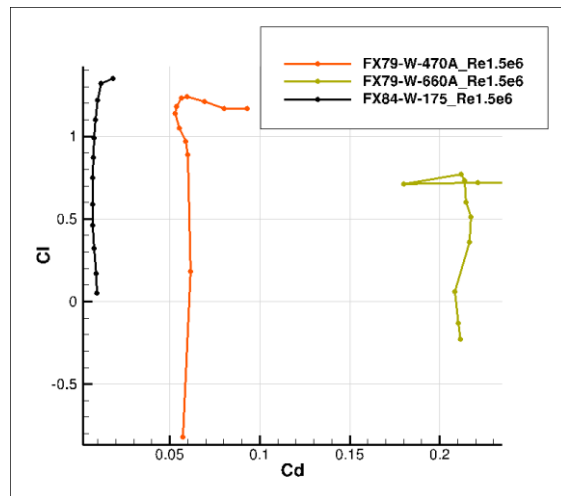


Figure 3.3-12 FX airfoils polar (2). Stuttgart experiments

The FX77 series of airfoils are interesting because each airfoil has been constructed by cutting and scaling the previous profile. It has to be analyzed with care because the Reynolds numbers of the experiments are not the same. In this case the effect of the Reynolds number, the airfoil thickness and the trailing edge gap make it very difficult to obtain a tendency.

For these cases, the drag increases when increasing the thickness and the trailing edge regardless the Reynolds number. The highest lift curve slope is the one of the 40%-thick airfoil and the smallest the one obtained with the 50%-thick airfoil.

Changing from the FX84-W-175 to the FX79-W-470A implies opening the trailing edge and increasing the thickness. Of course the drag is increased, but even with that big increase in thickness, opening of the trailing edge, makes the lift curve slope bigger. However, the stall is more dramatic.

The fact of comparing the FX79-W-470A with the FX79-W-660A shows how this tendency is not always the same. In this case the drag has increased and the slope has decreased because the FX79-W-660A airfoil is too thick and has a too thick trailing edge gap that both the lift and the drag values are worse.

On the one hand, the fact of using non-zero trailing edge gap airfoils will increase the structural properties and will increase the lift (if the trailing edge is not too large). On the other hand it will make the drag bigger. That makes the consideration of blunt trailing edge airfoils interesting for this region of the blade.

Table 3.2-1 shows a sum up of the properties of the studied airfoils to keep in mind as a guideline during the airfoil design.

Airfoil	t/c (%)	TEgap/c (%)	C <sub>L</sub> slope	Max C <sub>L</sub>	AOA Max C <sub>L</sub>	AOA C <sub>L</sub> =0	Min C <sub>D</sub> (DC)	AOA min C <sub>D</sub>
DU95-W-180	18	0	2 π	1.2	10	-2	60	-1
DU97-W-300	30	1.7	2.4 π	1.6	12	-2	100	-5
DU97-W-350	35	1	2.5 π	1.4	11	-2	100	-1
DU00-W2-401	40	1	1.9 π	1.2	17	-3	120	1
FX77-W-343	34	4	2.4 π	2.0	13	0	140	
FX77-W-400	40	11	2.5 π	1.8	12	0	280	1
FX77-W-500	50	27	2.1 π	1.6	11	1	760	0
FX79-W-470A	47	19	2.3 π	1.3	15	-2	530	6
FX-79-W-660A	66	43	2.4 π	1.0	29	-1	1800	5
FX84-W-175	17.5	0	2 π	1.4	22	-4	70	1

Table 3.3-1 – Summary of the state-of-the-art for high-thickness blunt-trailing-edge airfoils characteristics

### 3.4 XFOIL correction for flat-back and high thickness airfoils

The previous section shows how the use of high-thickness and blunt trailing edge airfoils could lead to better airfoils regarding the lift coefficients and the structural properties. XFOIL does not provide good results for this kind of airfoils. It is known to overestimate the lift and underpredict the drag coefficient.

XFOIL has already implemented a correction to account for the trailing edge gap (see [17]). It was developed with airfoil data with trailing edge gap thickness with respect to the chord of 1.7%. As the airfoils studied here are expected to have bigger trailing edge gaps, that formulation is useless. Moreover, as some correction is applied to the results it has been considered that it has no sense to apply a correction like the one proposed by Hoerner in [18] making use of the base drag.

CENER's XFOIL correction is used to improve the optimization by means of correcting the defects of XFOIL in the linear region. For example, if a low drag was desirable, it is compulsory to correct XFOIL drag prediction with the trailing edge value because, other way, the optimizer would not try to reduce the trailing edge thickness.

To modify the lift curve, the slope of the XFOIL output and the experimental curve have been measured in the linear region. Afterwards, all the points of the XFOIL curve have been rotated in such a way that the corrected curve slope and the experimental one are the same. This rotation keeps the AOA constant and modifies the lift coefficient. See Figure 3.4-1. This new lift data is also used in the corrected polar curve.

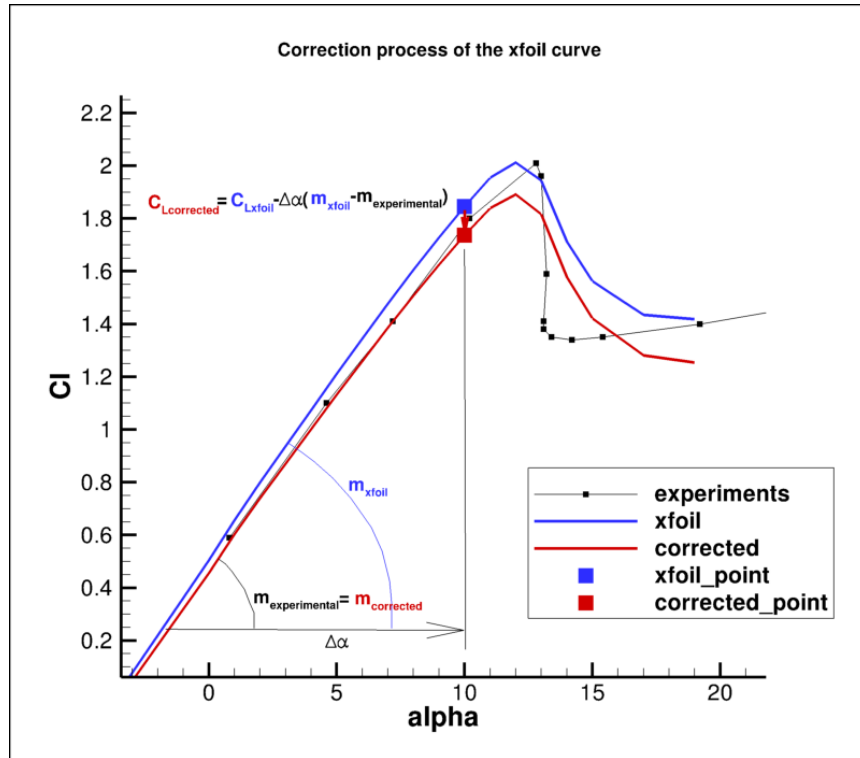


Figure 3.4-1 Explanation of the lift curve modification

To modify the drag coefficient, a representative point of the experimental curve has been chosen. Usually, it has been selected in the linear region taking care of avoiding possible wrong points due to instabilities, etcetera. With this point the relation between the drag predicted with XFOIL and the real one is obtained. Afterwards, all the points are modified with that relation. See Figure 3.4-2.

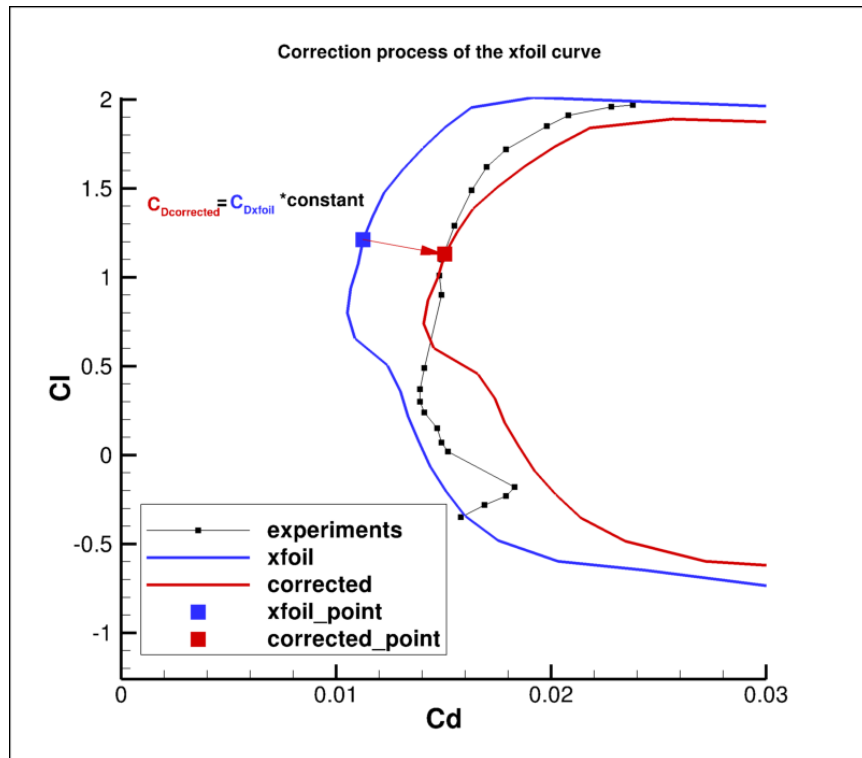


Figure 3.4-2 Explanation of the drag curve modification

The same experiments used previously for the state-of-the-art section has been used to define the correction for the XFOIL data. Only some of the corrections are shown below by means of graphics, but the data available in Table 3.4-1 may be useful. Notice that there is a lack of reliable wind tunnel data for this kind of airfoils, especially for high Reynolds numbers.

The first study groups some DU airfoils.

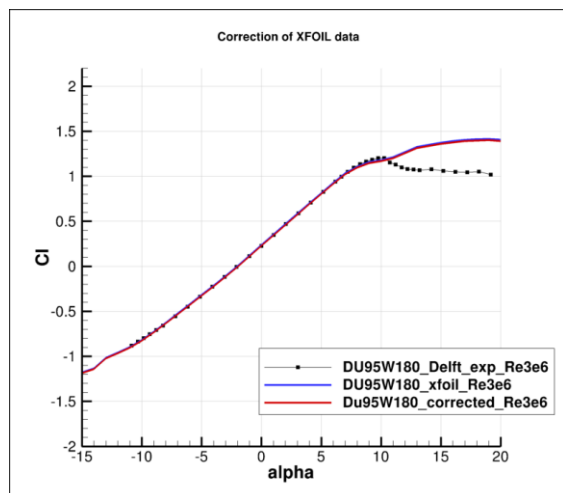


Figure 3.4-3 DU95W180: Delft experiments, XFOIL calculation and modified curve

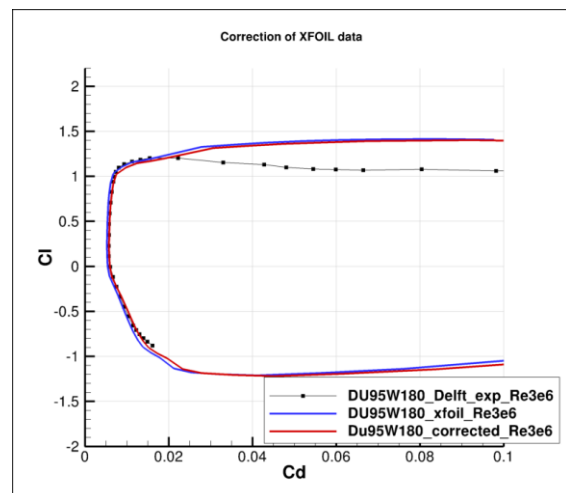


Figure 3.4-4 DU95W180: Delft experiments, XFOIL calculation and modified curve

The DU95W180 is a thin airfoil with zero trailing edge, which makes the XFOIL prediction so close to the experimental data. Good agreement of the drag coefficient shape but slight underprediction of the value.

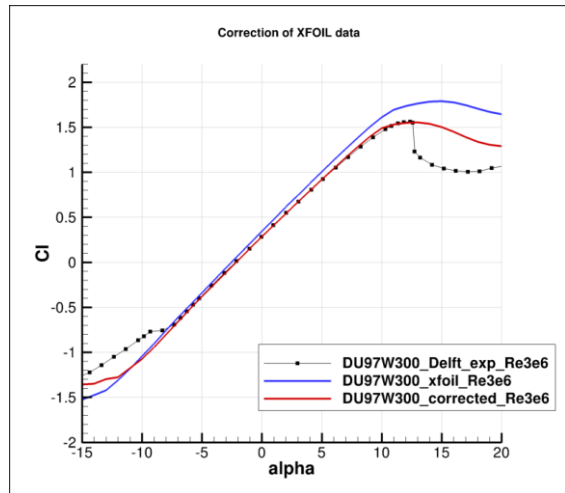


Figure 3.4-5 DU97W300: Delft experiments, XFOIL calculation and modified curve

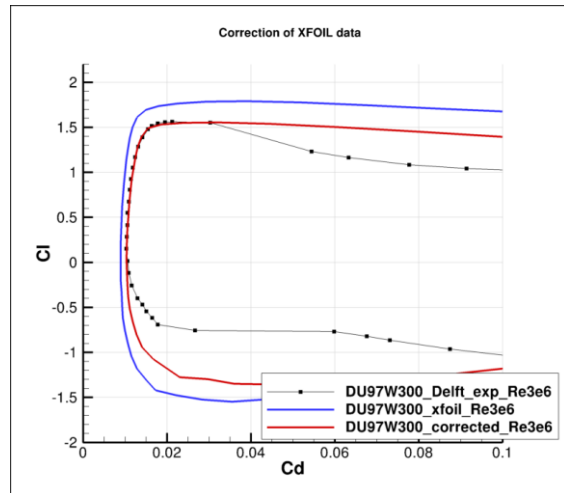


Figure 3.4-6 DU97W300: Delft experiments, XFOIL calculation and modified curve

The DU97W300 is a quite thick airfoil which trailing edge gap is non-zero. All of that make the result begin to separate from experiments. Good agreement of the corrected drag coefficient.

The other group of airfoils includes some of the airfoils designed by Wortmann, which were tested by the Stuttgart University.

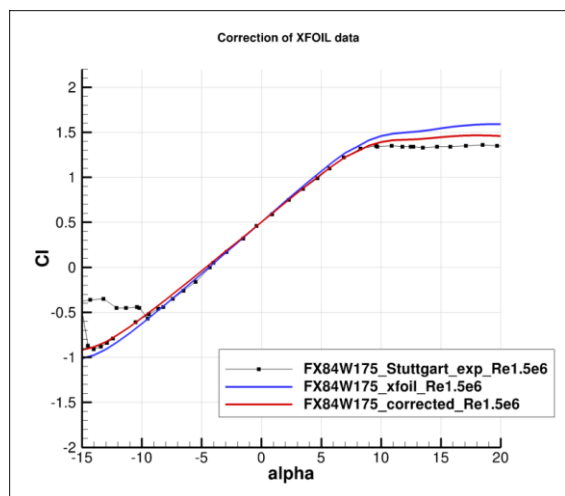


Figure 3.4-7 FX84W175: Stuttgart experiments, XFOIL calculation and modified curve

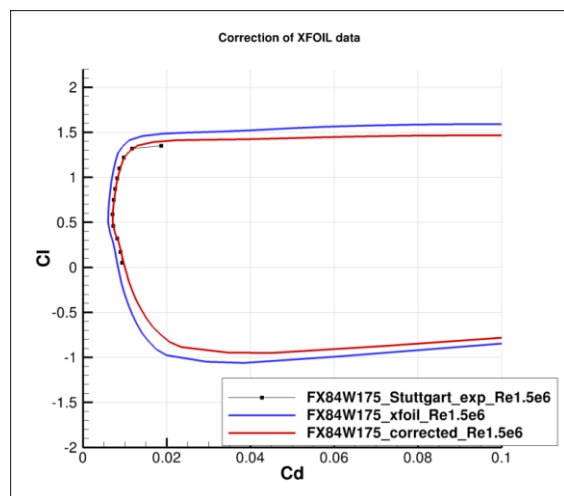


Figure 3.4-8 FX84W175: Stuttgart experiments, XFOIL calculation and modified curve

The FX84W175 is neither a thick nor a blunt trailing edge airfoil, but it has been tested to check that XFOIL also predicts well the Stuttgart experiments if the airfoil is thin and point-ended. As expected the results are in good agreement with experiments

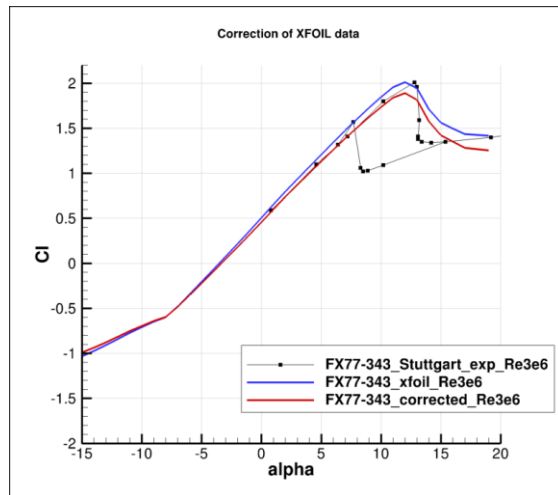


Figure 3.4-9 FX77-343: Stuttgart experiments, XFOIL calculation and modified curve

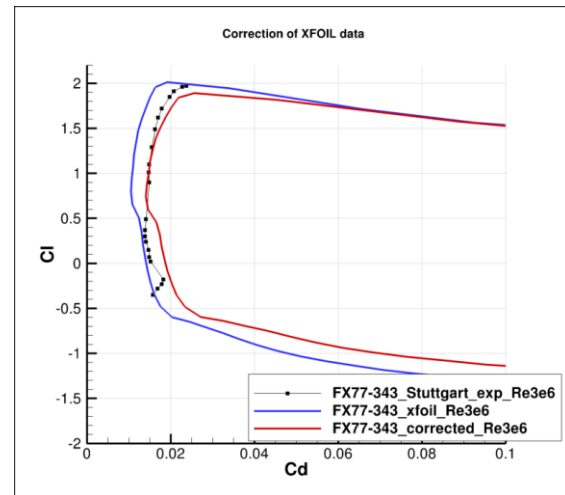


Figure 3.4-10 FX77-343: Stuttgart experiments, XFOIL calculation and modified curve

The agreement reached for the FX77-343 airfoil is good except for the part of the drag curve below  $C_L=0.5$ , which seems to have a very strange behavior.

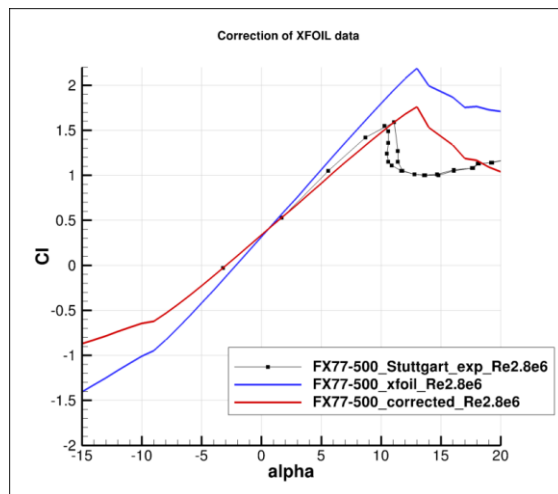


Figure 3.4-11 FX77-500: Stuttgart experiments, XFOIL calculation and modified curve

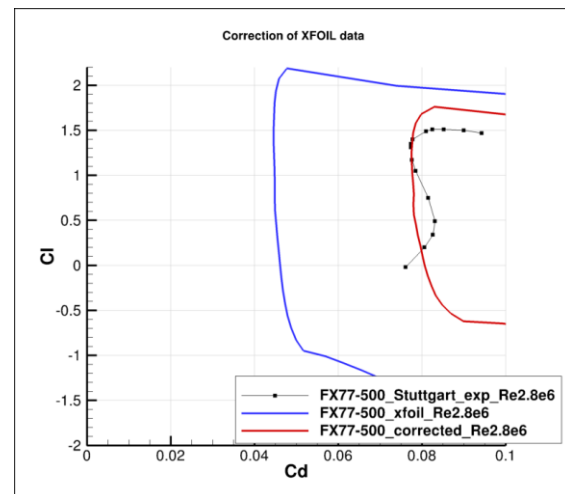


Figure 3.4-12 FX77-500: Stuttgart experiments, XFOIL calculation and modified curve

In the case of the FX77-500 airfoil, the slope was not very clear because the linear region had few points and the slope between them was different from one another. The experimental drag curve seems to be modified by some instability.

Table 3.4-1 shows a sum up of the values used afterwards to develop the correlation.

Airfoil	t/c (%)	TEgap/c (%)	Re	$m_{XFOIL} / m_{experiments}$	$Cd_{experiments} / Cd_{xfoil}$
DU95-W-180	18	0	3e6	1.00	1.10
DU97-W-300	30	1.7	3e6	1.12	1.14
DU97-W-350	35	1	3e6	1.30	1.15
DU00-W2-401	40	1	3e6	1.08	1.13
FX77-W-343	34	4	3e6	1.05	1.34
FX77-W-343	34	4	4e6	1.07	1.21
FX77-W-400	40	11	4e6	1.06	1.98
FX77-W-500	50	27	2.8e6	1.30	1.74
FX79-W-470A	47	19	1.5e6	1.13	1.58
FX-79-W-660A	66	43	1.5e6	1.21	3.45
FX84-W-175	17.5	0	1.5e6	1.06	1.18

Table 3.4-1 – Numerical values used for the correction of XFOIL data

The studied airfoils can be divided into two categories. The first one is composed by the airfoils with low trailing edge gap (smaller than the limit studied by M. Drela in [17]) and the second by the airfoils with high trailing edge thickness. The group with low trailing edge is composed by low to medium-thickness, moreover, the thick-trailing-edge group includes medium to high-thickness airfoils (see Figure 3.4-13). It is a natural division due to the aerodynamic and structural criteria considering that, the properties of airfoils with low thickness and high trailing edge gap and the airfoils' properties with high thickness and zero trailing edge gap are not expected to be very good.

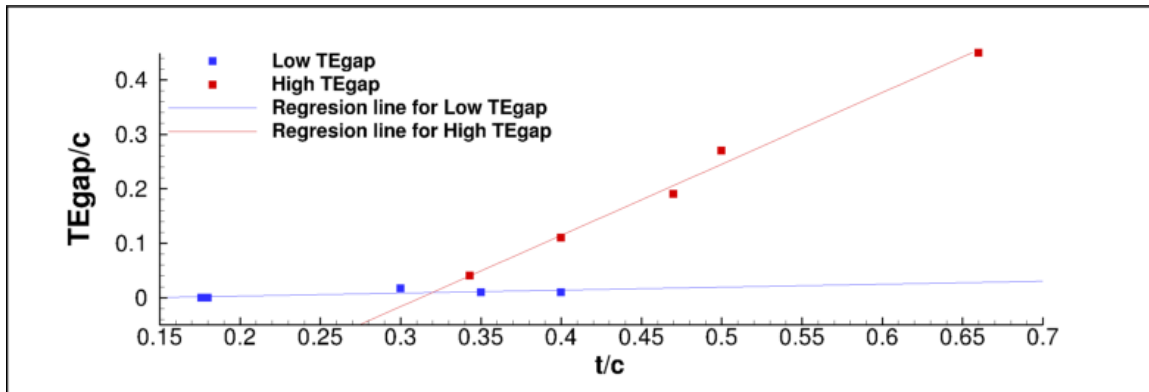


Figure 3.4-13 Relation between the trailing edge gap and the thickness

The first point to be corrected is the slope of the lift curves of the airfoils. It is dependent on both the thickness and the trailing edge gap (see [19]). Moreover, the correlation can be done taking all the data into the account or separating it in the two groups explained above. Among the several options available, the correlation that relates the error in the slope and the trailing edge gap (without any group division) has been chosen (see Figure 3.4-14).

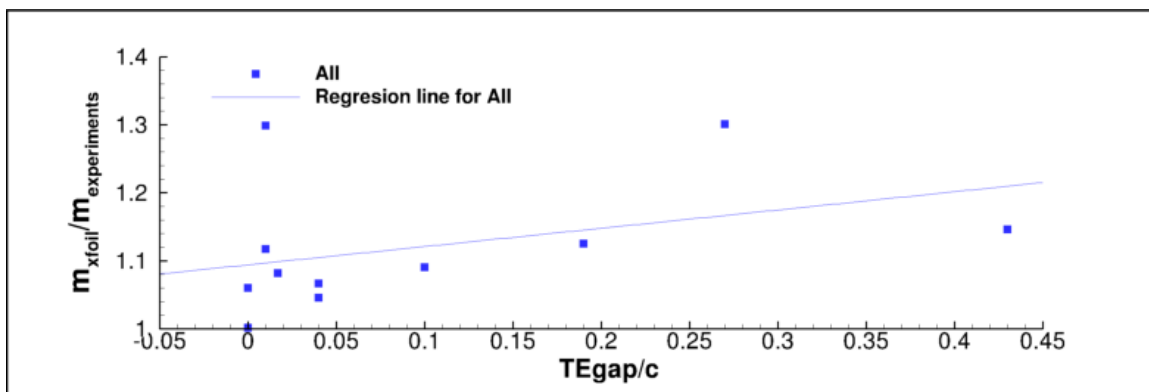


Figure 3.4-14 Relation between the TE gap and the lift slope error for all the airfoils

The other parameter that is known to be wrongly predicted by XFOIL is the drag coefficient. Based on the panel methods' theory, the error in the drag prediction in XFOIL seems to be related to the trailing edge gap, which is not accountable for with that theory. However, XFOIL includes a correction for this value calibrated for airfoils with TEgap/c up to 2%. That is the reason why two correlations have been developed, one for airfoils with TEgap/c bigger than 2% and another one for bigger trailing edges.

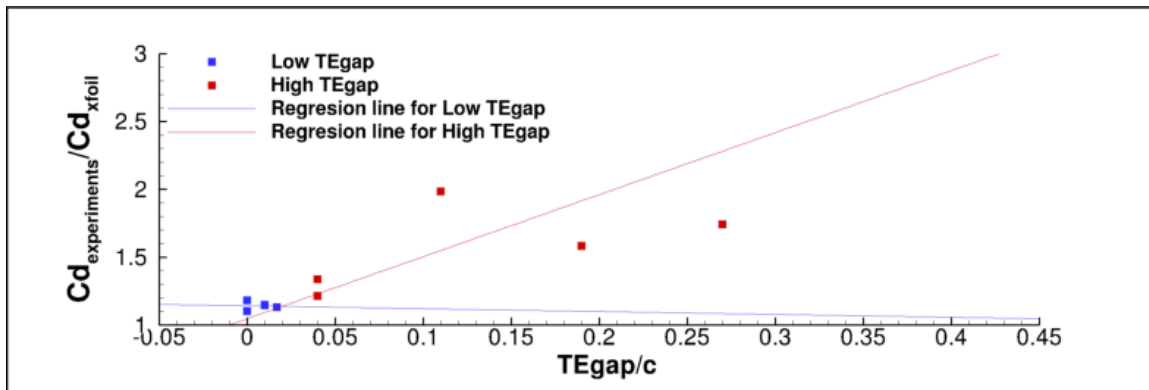


Figure 3.4-15 Relation between the TE gap and the drag coefficient error for airfoils separated in groups

Notice that even for thin airfoils with zero TE gap, the drag is underpredicted by XFOIL around 14%.

### 3.5 Design of root region airfoils

As it was explained previously, there is a need of reducing the cost of energy by means of redesigning the blade root region. As it is a complex region due to the three dimensional flow and the use of non-conventional airfoils heavily constrained by the structural requirements, the previous sections help understanding the flow and the tools capabilities to be applied to the airfoil design.

This section presents the process of airfoil shape optimization by means of genetic algorithms. Later on, a CFD study of the designed airfoils will be accomplished.

After several attempts that tried to maximize the efficiency, or the trust coefficient, etcetera. The following airfoils are designed with the common objective of maximizing the lift, even though, it penalizes the efficiency. Moreover, the importance of the behaviour under contaminated conditions has been considered for the reasons explained afterwards.

Several airfoils have been designed during the optimization work performed under the scope of the INN WIND.EU project. They are classified in different loops and tests. In the following sections four airfoils are presented. Two of them (L12T7 and L12T17) have a thickness to chord ratio of 40% and the other two (L11T6 and L11T17) are 50%-thick airfoils.

Do not forget about the results obtained in Section 3.2. To sum up, airfoils do not behave in the same way when operating in 2D and in 3D situations. The root blade region is characterized by an important amount of radial flow affecting specially the 50%-thick airfoil. For the studied cases, the airfoils show delayed separation when operating under 3D rotatory conditions. That leads to bigger pressure and drag coefficients than predicted by the 2D simulations.

### 3.5.1 Dakota and the Genetic Algorithms

The genetic algorithms are based on Darwin's law of evolution (natural selection) to make any object change as biological evolution will do, towards the optimization of its characteristics. The main idea is that the individuals that are the best adapted to the media are the most prone to reproduce and so, to transmit their “biological parameters” to the following generation. After several generations only the best parameters have survived and so the individual that best fit the environment is obtained.

Translating that to airfoils, it is needed:

- A series of parameters that define the airfoil that will be transferred to the following generation (or not).
- A way of evaluating the performance of the airfoil to assign to each individual a mark in order to decide which one has the best characteristics.
- An algorithm to apply the laws of genetics (mutation, cross-over and selection) to a generation in order to give rise to the following.

The airfoil geometry has been divided in camber plus thickness. Each one of these curves is generated by a Bezier curve. Adding the thickness perpendicularly to the camber, the upper part geometry is obtained; the lower side geometry can be obtained by subtracting the thickness perpendicularly to the camber line. As a Bezier curve is defined by a certain number of parameters, those are the ones that will characterize the airfoil.

Once a generation of airfoils has been created it is needed to evaluate each member's aerodynamic performance. It has been done with XFOIL. After calculating the  $C_l$ ,  $C_d$ , efficiency, etcetera, how good or bad the performance is, has to be automatically determined. That is done by means of an objective function. An objective function is a mathematical function whose inputs are whatever coefficient coming from XFOIL and whose output is a mark (typically between 0 and -10) evaluating the performance of the airfoil. DAKOTA seeks for minimums of the objective function, that is why the lower the mark the better the airfoil. This objective function has to be progressively changed until the adequate one is reached as will be shown afterwards.

The creation of a new generation based on the marks obtained by the previous one by means of the parameters that define each individual has been done with the DAKOTA software (see [20] and [21] for further information). It generates a series of individuals (characterized by their Bezier curve parameters) by means of performing mutation, cross-over and selection on the previous generation individuals conditioned by the mark that the parents have obtained in the objective function.

As an example of how an airfoil evolves through generations some figures are shown. They refer to the optimization case of the 50%-thick airfoil. Figure 3.5-1 shows how the geometry changes. The first generation of airfoils is created assigning randomly the parameters of the Bezier curves. In this case, the objective was to obtain a high lifting airfoil in contaminated conditions ( $n=0.1$  for the eN transition method). Broadly speaking, during the first iterations, the position of the maximum thickness is moved forward (to move the transition point to smaller  $x/c$  positions) and afterwards, the camber of the airfoil grows to increase the lift coefficient. Figure 3.5-2 shows how the value of the objective function of the best airfoil in each generation evolves reaching the convergence.

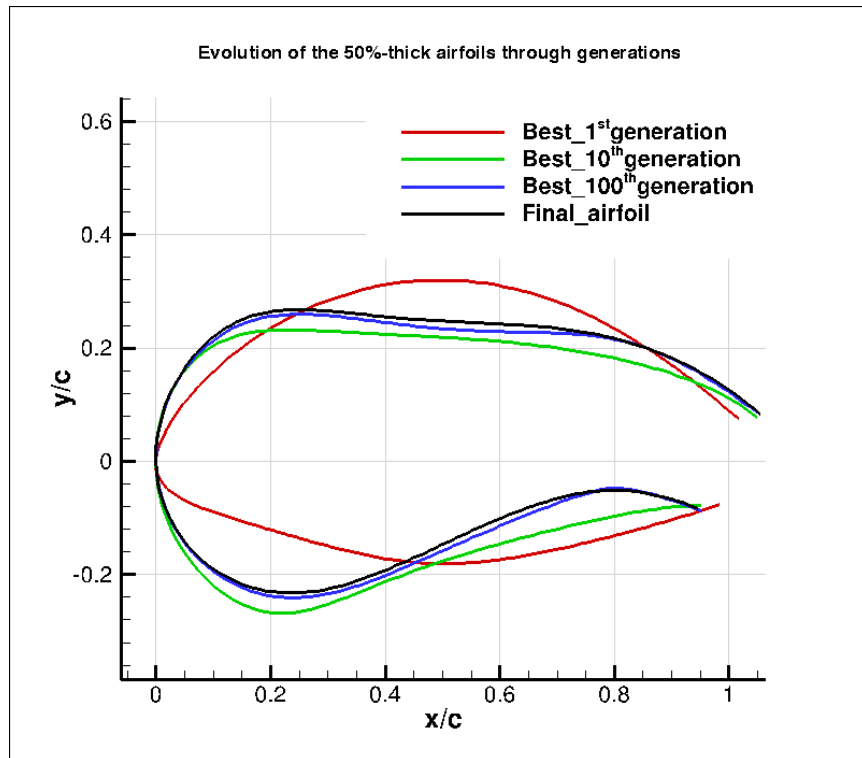


Figure 3.5-1 Evolution of the geometry through generations

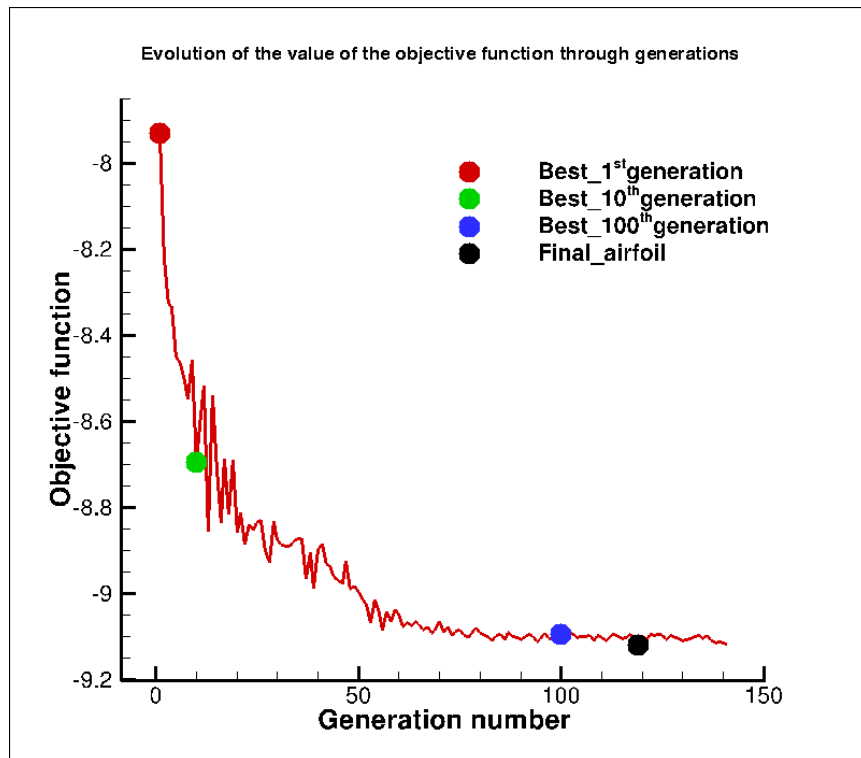


Figure 3.5-2 Evolution of the objective function through generations

### 3.5.2 Setting XFOIL parameters

The airfoils were designed for the rated Reynolds numbers obtained from the reference INN WIND blade. Moreover, the Mach number used was zero because the rated Mach numbers in the root region are very small.

The clean configuration of the blade has been represented by the eN transition method with  $N=9$ , whereas, the contaminated situation has been approximated setting  $N=0.1$ .

According to [14], thick airfoils are especially sensitive to leading edge contamination. That is the reason why that behaviour has to be accounted for even when those airfoils are not the main contributors to AEP.

The working point represented by the case  $N=0.1$  groups more situations apart from the contaminated state. Using  $N=0.1$  implies lowering the threshold in turbulence oscillations that triggers transition. Contamination makes transition happen earlier (among other effects) making the use of this method suitable to represent leading edge contamination. However, there are other causes for transition to happen earlier, for example an unsteady or turbulent inflow. Consequently, the case represented by  $N=0.1$  also represents working conditions that are very likely to take place.

Notice that the XFOIL provided curves are corrected with the previous correlation unless specified.

After the design of the 40%-thick airfoil, two airfoils are presented.

### Design of the L12T7 airfoil

The airfoil called L12T7 was the result of the optimization of the 40%-thick airfoil according to the following objective function and parameters:

<b>Objective function</b>	$F_{obj} = w_1 * C_L(n = 9 ; \alpha = 10^\circ) + w_2(n = 0.1 ; \alpha = 10^\circ)$
<b>Reynolds number</b>	11e6
<b>Mach number</b>	0
<b>Design AOA</b>	10°

Table 3.5-1 – Design parameters for the L12T7

Aerodynamically speaking, the objective function looks for an airfoil with high lift coefficient at 10°. It tries to maximize both the clean and the contaminated configuration but giving more importance to the contaminated one. It was observed that optimizing the airfoils accounting for the contaminated behaviour led to relative good clean behaviour and good roughness sensitivity.

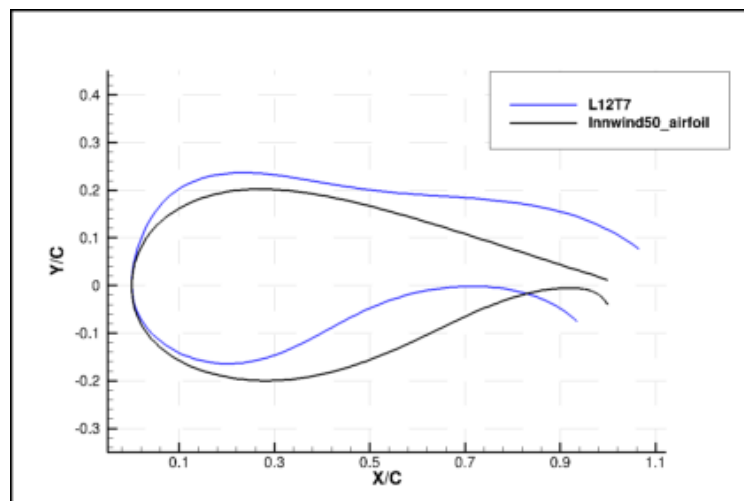


Figure 3.5-3 Reference and new airfoil of the 40% thickness

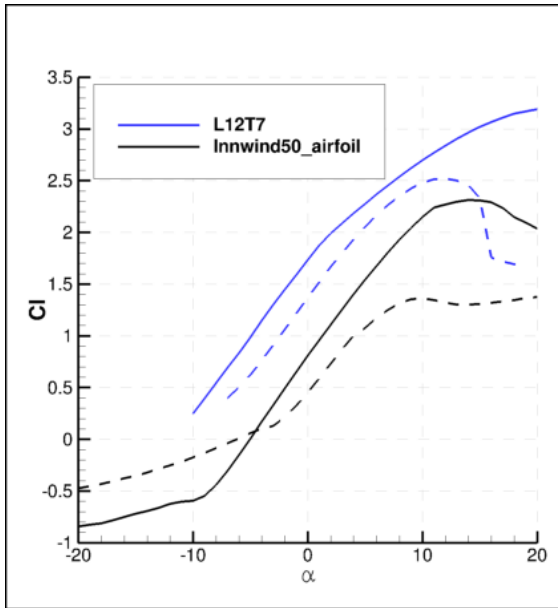


Figure 3.5-4 Lift coefficient calculation with XFOIL for the reference and new airfoil of the 40% thickness. Continuous line  $n=9$ ; dashed line  $n=0.1$ .

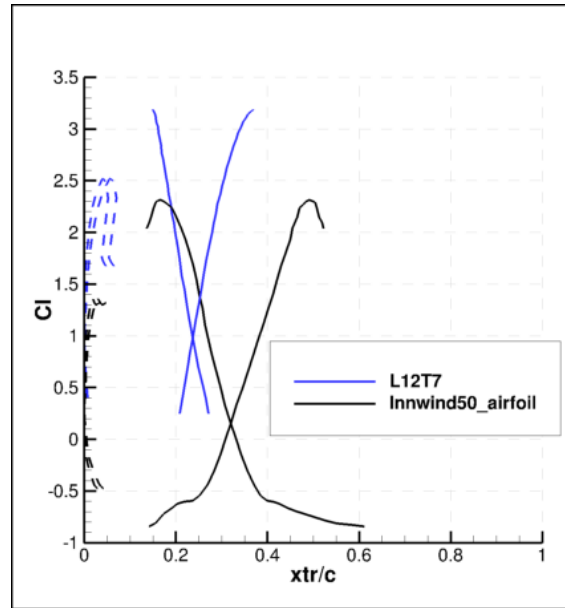


Figure 3.5-5 Transition calculation with XFOIL for the reference and new airfoil of the 40% thickness. Continuous line  $n=9$ ; dashed line  $n=0.1$ .

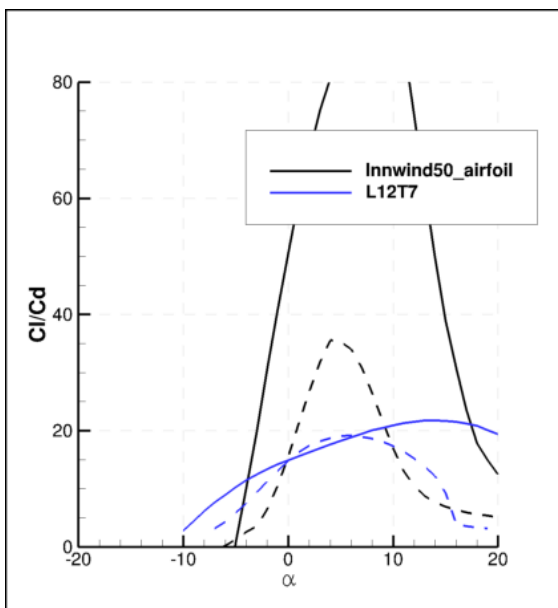


Figure 3.5-6 Efficiency calculation with XFOIL for the reference and new airfoil of the 40% thickness. Continuous line  $n=9$ ; dashed line  $n=0.1$ .

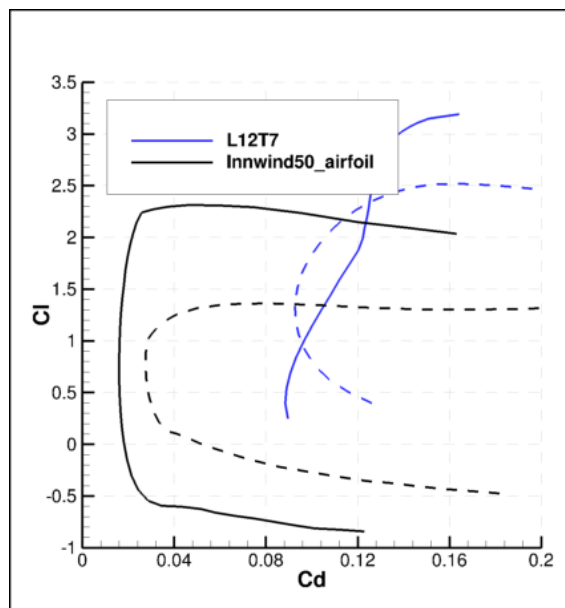


Figure 3.5-7 Polar calculation with XFOIL for the reference and new airfoil of the 40% thickness. Continuous line  $n=9$ ; dashed line  $n=0.1$ .

This airfoil is interesting because it has big lift coefficient in a wide range of angles of attack. Moreover, the deep stall point takes place several degrees after the design point even in contaminated configuration. That means that there is a security margin for gusts, avoiding the airfoil to go into deep stall due to unsteady conditions.

The difference in behaviour between the clean and the contaminated configuration is very small, enhancing the energy production throughout the whole life cycle. That has been achieved placing the transition point very close to the leading edge.

The worst part of the airfoil behaviour is the drag increase mainly related to the increase of the trailing edge thickness and the resulting low efficiency. In addition, the maximum efficiency point is different between the clean and the contaminated configuration. However, the efficiency is more constant with varying AOA than in the original profile, making this characteristic less critical.

### Design of the L12T17 airfoil

Another airfoil (called L12T17) has also been designed with two trailing edge constraints. The trailing edge gap is smaller and vertical in this case. The objective function was also slightly changed as follows:

<b>Objective function</b>
<b>Reynolds number</b>
<b>Mach number</b>
<b>Design AOA</b>
<b>Trailing edge restrictions</b>

$$F_{obj} = w_1 * C_L(n = 9 ; \alpha = 10^\circ) + w_2 * C_L(n = 0.1 ; \alpha = 10^\circ)$$

11e6

0

10°

Vertical trailing edge and  $TE_{gap}/c < 20\%$

Table 3.5-2 – Design parameters for the L12T17

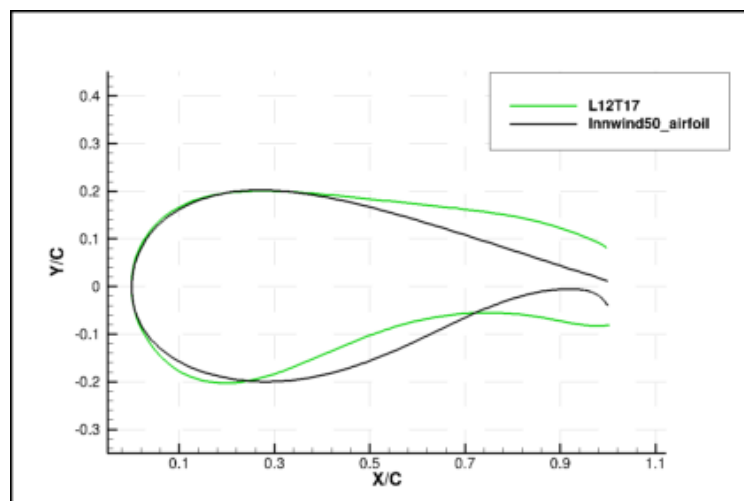


Figure 3.5-8 Reference and new airfoil of the 40% thickness

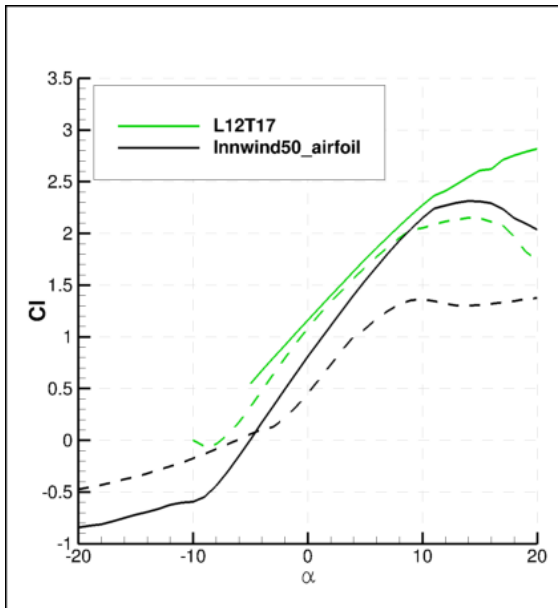


Figure 3.5-9 Lift coefficient calculation with XFOIL for the reference and new airfoil of the 40% thickness. Continuous line  $n=9$ ; dashed line  $n=0.1$ .

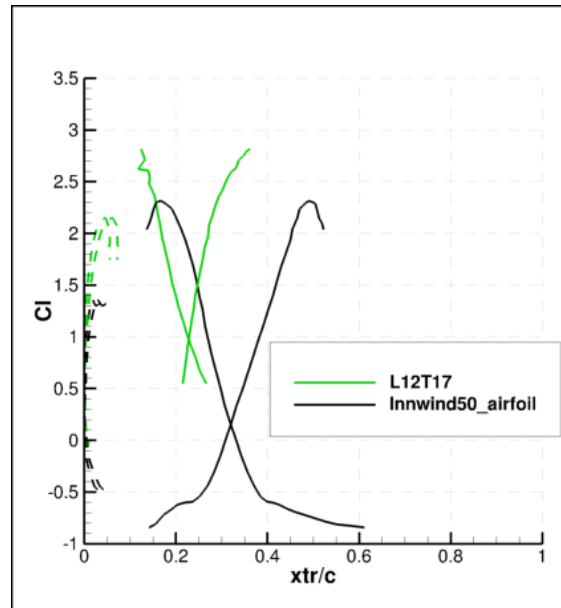


Figure 3.5-10 Transition calculation with XFOIL for the reference and new airfoil of the 40% thickness. Continuous line  $n=9$ ; dashed line  $n=0.1$ .

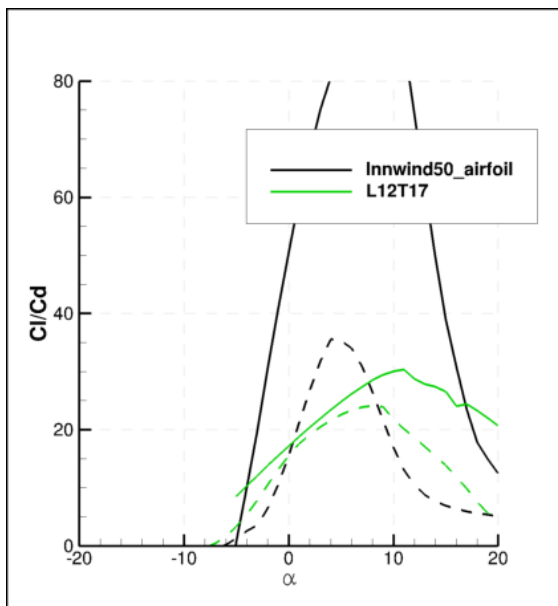


Figure 3.5-11 Efficiency calculation with XFOIL for the reference and new airfoil of the 40% thickness. Continuous line  $n=9$ ; dashed line  $n=0.1$ .

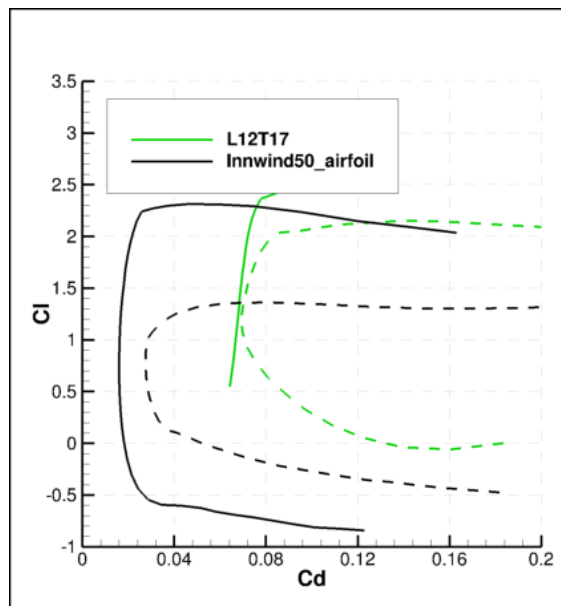


Figure 3.5-12 Polar calculation with XFOIL for the reference and new airfoil of the 40% thickness. Continuous line  $n=9$ ; dashed line  $n=0.1$ .

This airfoil behaviour is very similar to the one shown before. The trailing edge modification directly reduces the lift and the drag coefficient and increases the efficiency.

The airfoil has a big turbulent region which is very interesting and a very similar behaviour in clean and contaminated configurations. The maximum efficiency is now closer between the two states but the efficiency drop with changes in AOA is more pronounced.

### 3.5.3 Design of the 50%-thick airfoil

Two 50%-thick airfoils have also been designed in the following sections.

#### *Design of the L11T6 airfoil*

The following objective function has been used for the design of the L11T6 airfoil:

**Objective function**  
**Reynolds number**  
**Mach number**  
**Design AOA**

$F_{obj} = C_L(n = 0.1 ; \alpha = 10^\circ)$   
 9e6  
 0  
 10°

Table 3.5-3 – Design parameters for the L11T6

The expected output is a 50%-thick airfoil with the maximum value possible of lift coefficient at 10° in contaminated conditions.

Having a big laminar region has two main problems. The first one is the difficulty of maintaining that laminar character in real conditions (due to unsteadiness, turbulence...). And the other one is the sensitivity of the airfoil to the loss of that laminar region. The bigger the laminar region, the bigger the differences behaviour between clean and contaminated condition are.

Both effects are very detrimental to the real airfoil behaviour, pointing the need of having an airfoil with good contaminated behaviour. That is why it was decided to optimize these airfoils in contaminated conditions. Other way, the airfoils generated had a very big laminar region which is expected to be unstable in real conditions (non-uniform inflow ...). For those airfoils, if the laminar region was lost the contaminated performance will be the one applicable, and those airfoils are known to be very sensitive to contamination.

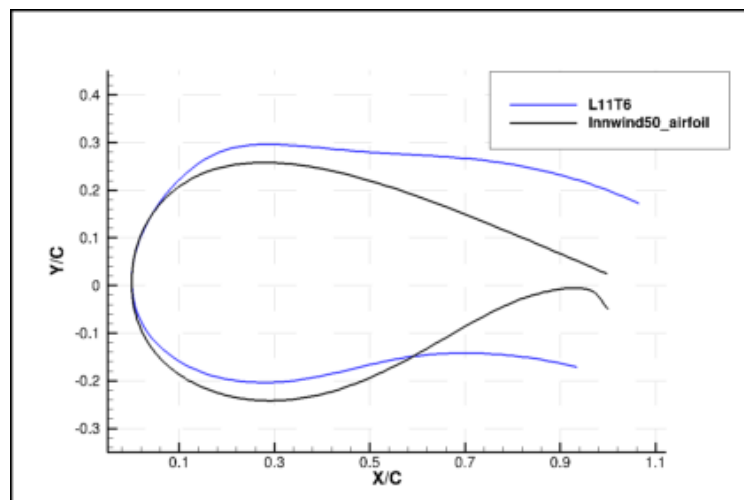


Figure 3.5-13 Reference and new airfoil of the 50% thickness

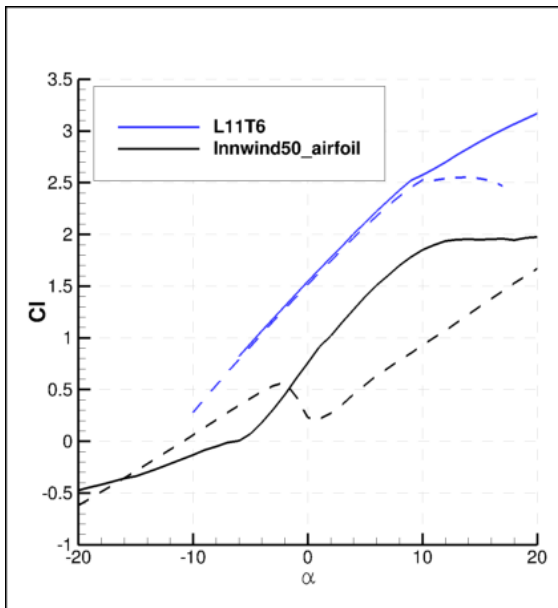


Figure 3.5-14 Lift coefficient calculation with XFOIL for the reference and new airfoil of the 50% thickness. Solid line  $n=9$ ; dashed line  $n=0.1$

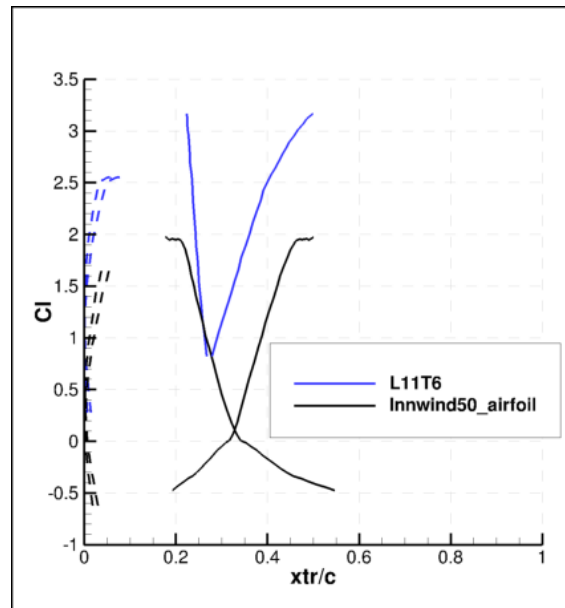


Figure 3.5-15 Transition calculation with XFOIL for the reference and new airfoil of the 50% thickness. Solid line  $n=9$ ; dashed line  $n=0.1$

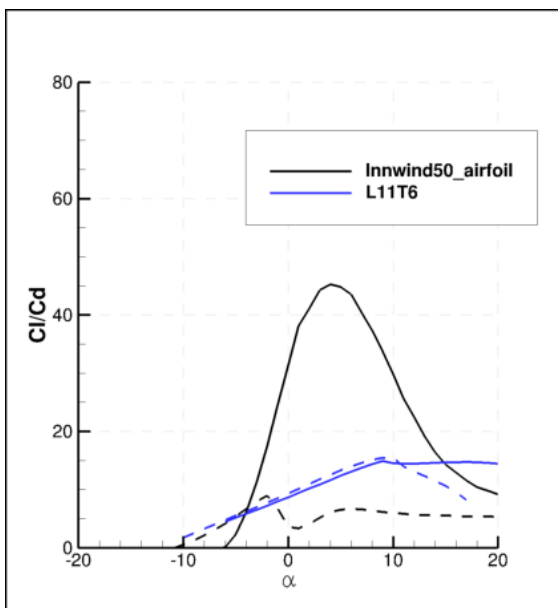


Figure 3.5-16 Efficiency calculation with XFOIL for the reference and new airfoil of the 50% thickness. Continuous line  $n=9$ ; dashed line  $n=0.1$

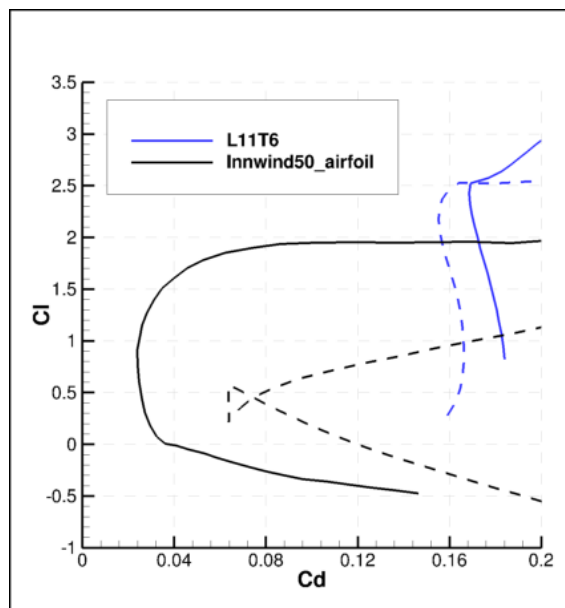


Figure 3.5-17 Polar calculation with XFOIL for the reference and new airfoil of the 50% thickness. Continuous line  $n=9$ ; dashed line  $n=0.1$

This airfoil has very high values of lift coefficient and a big margin between the design point and the deep stall point, even in contaminated configuration. The lift sensitivity to roughness is very small, especially for AOA below the stall point.

That good roughness sensitivity is provided by the closeness of the transition point to the leading edge. The transition happens around the 25% of the chord and it moves very slowly with the angle of attack, which makes the airfoil very robust.

The efficiency in clean configuration is very constant for AOA bigger than the design point. However, the range of maximum efficiency for the contaminated case is very narrow, but it reaches the same values as the clean one.

That strange behaviour (bigger efficiency in contaminated configuration than in the clean one) is related to the smaller drag that the contaminated profile has which is not likely to be maintained neither in the following CFD results nor in the real operation.

### Design of the L11T17 airfoil

The airfoil L11T17 aims to have a smaller trailing edge gap but maintaining the structural and aerodynamic properties. Consequently, a term to maximize the inertia of the airfoil has been included in the objective function:

#### Objective function

$$F_{obj} = w_1 * C_L(n = 0.1 ; \alpha = 10^\circ) + w_2 * INERTIA$$

Reynolds number  
Mach number  
Design AOA  
Trailing edge restrictions

9e6

0

10°

TEgap/c < 20%

Table 3.5-4 – Design parameters for the L11T6

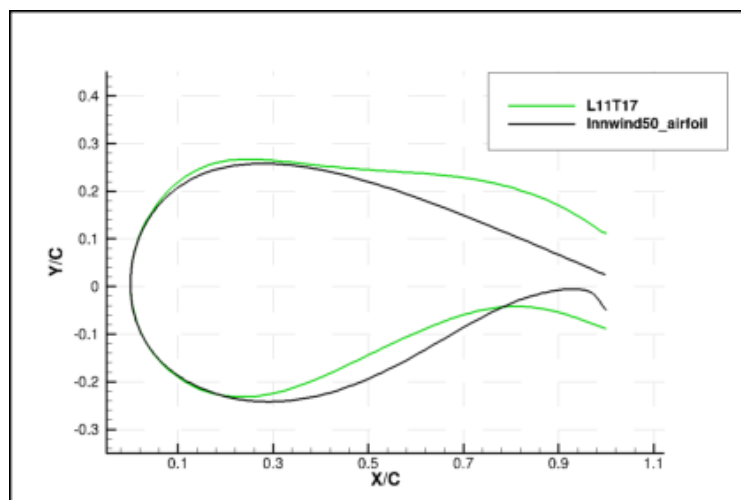


Figure 3.5-18 Reference and new airfoil of the 50% thickness

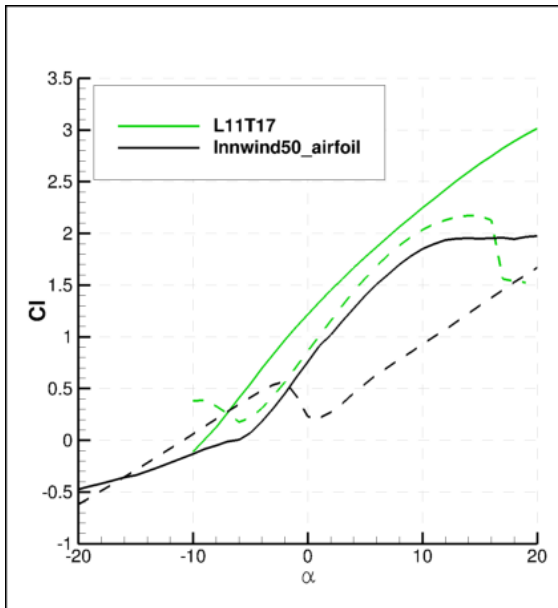


Figure 3.5-19 Lift coefficient calculation with XFOIL for the reference and new airfoil of the 50% thickness. Continuous line  $n=9$ ; dashed line  $n=0.1$

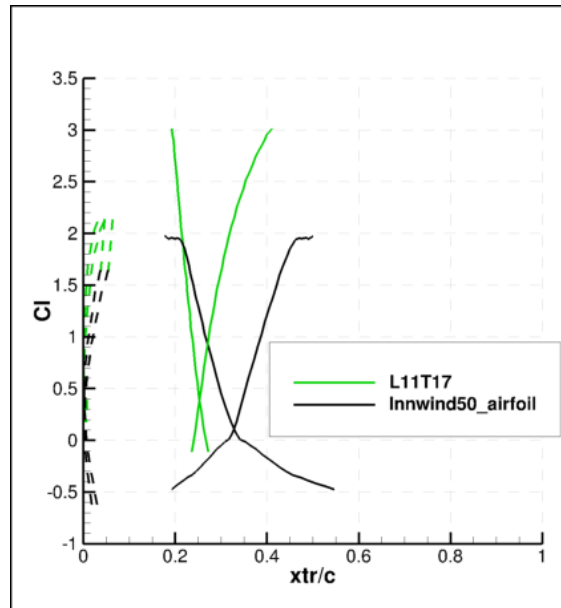


Figure 3.5-20 Transition calculation with XFOIL for the reference and new airfoil of the 50% thickness. Continuous line  $n=9$ ; dashed line  $n=0.1$

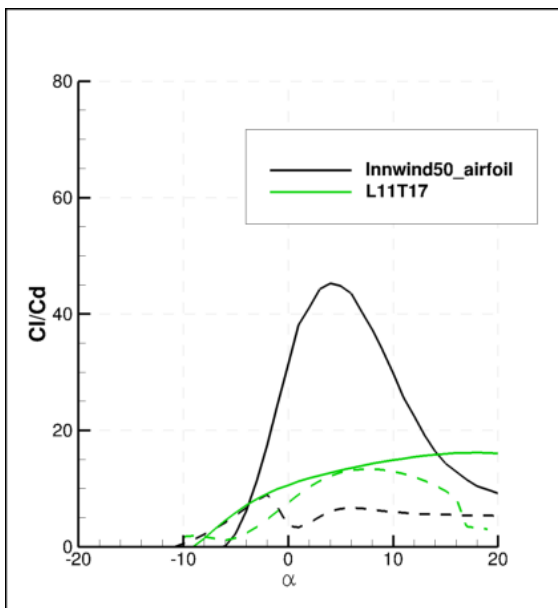


Figure 3.5-21 Efficiency calculation with XFOIL for the reference and new airfoil of the 50% thickness. Continuous line  $n=9$ ; dashed line  $n=0.1$

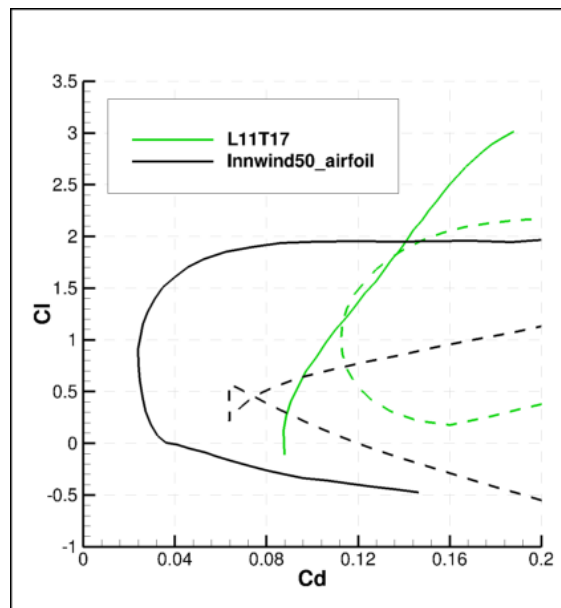


Figure 3.5-22 Polar calculation with XFOIL for the reference and new airfoil of the 50% thickness. Continuous line  $n=9$ ; dashed line  $n=0.1$

As it is expected when a constraint is placed on an optimization algorithm, the airfoil characteristics are slightly worse than those of the L11T6 case. Anyway, it is shown as an example of smaller trailing edge gap airfoil.

This airfoil has worse roughness sensitivity, smaller lift values and bigger drag coefficient. However, the characteristics are better than those of the original airfoil.

The most important characteristics of all the original airfoils and the data coming out from the optimization are shown in Table 3.5-5.

Airfoil	t/c (%)	TEgap/c (%)	C <sub>Lmax</sub> (clean)	C <sub>Dmin</sub> (clean)	C <sub>Lmax</sub> (contam.)	C <sub>Dmin</sub> (contam.)
original Innwind40 airfoil	40	5	2.30	0.02	1.36	0.03
L12T7	40	20	3.20	0.09	2.50	0.09
L12T17	40	16	2.82	0.06	2.15	0.07
original Innwind50 airfoil	50	7	1.95	0.02	1.70	0.06
L11T6	50	37	3.17	0.17	1.50	0.16
L11T17	50	20	3.00	0.09	2.17	0.11

Table 3.5-5 – Corrected XFOIL data for the reference and the design airfoils

### 3.6 CFD study of the designed airfoils

The objective of the optimization was to obtain a big lift coefficient in clean configuration and good roughness sensitivity. XFOIL is the tool used to evaluate the performance of airfoils during the optimization process due to its rapidity, but it is not accurate enough to develop a final analysis of an airfoil, either applying the empirical correction.

To evaluate the behaviour of the airfoils over a more solid base, 2D CFD calculations have been developed with WMB (see description in Section 3.2).

In the cases presented here C type meshes developed with ICEM CFD in its hexa version are used. 500 nodes are distributed along the airfoil profile and the first mesh point is located close enough to the wall to ensure a  $y^+=1$ . In total the 2D meshes use 300.000 points to discretize the domain. The domain boundaries are located 25 chords both upstream and downstream of the airfoil. Fully turbulent calculations are performed using the k- $\omega$  Baseline turbulence method and transitional calculations are performed using the eN transition method. All the calculations presented in this chapter are steady calculations. The aerodynamic coefficients plotted in the following figures are averaged values for 4000 iterations.

#### 3.6.1 40%-thick airfoil

CFD simulations for the 40% airfoil thickness are presented next (L12T7 and L12T17 airfoils). Aerodynamic coefficients and contour plots are included in the following figures.

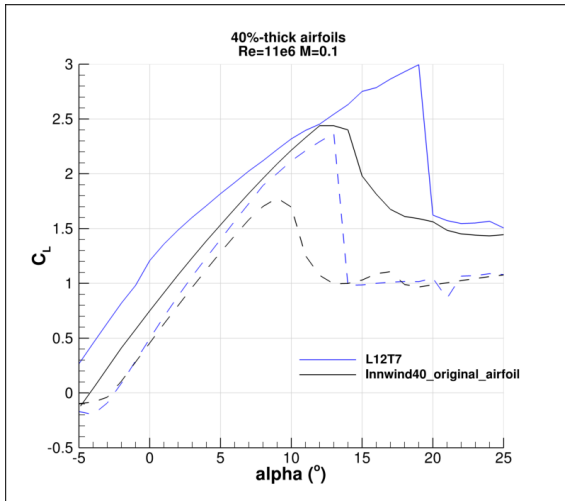


Figure 3.6-1 Lift coefficient calculation with WMB for the reference and new airfoil (L12T7) of the 40% thickness. Solid line, transitional  $n=9$ ; dashed line, fully turbulent

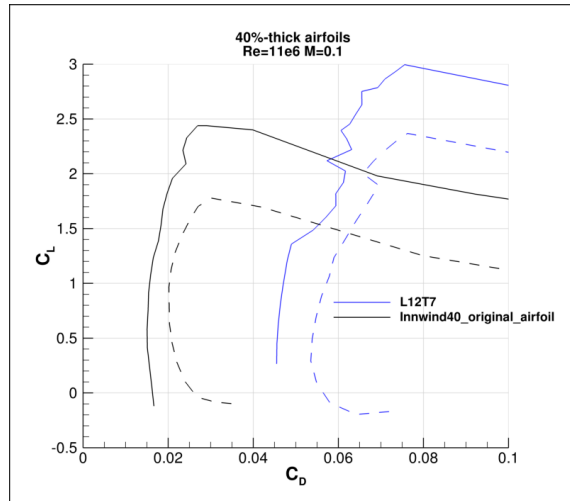


Figure 3.6-2 Polar calculation with WMB for the reference and new airfoil (L12T7) of the 40% thickness. Solid line, transitional  $n=9$ ; dashed line, fully turbulent

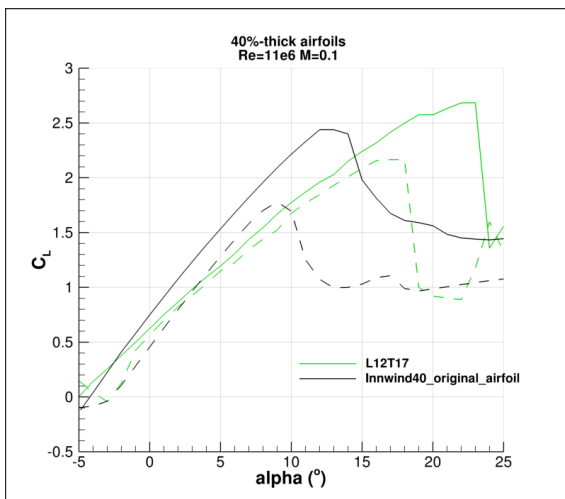


Figure 3.6-3 Lift coefficient calculation with WMB for the reference and new airfoil (L12T17) of the 40% thickness. Solid line, transitional  $n=9$ ; dashed line, fully turbulent

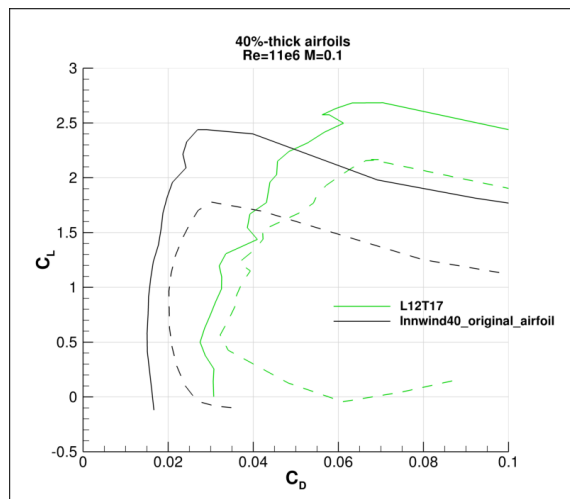
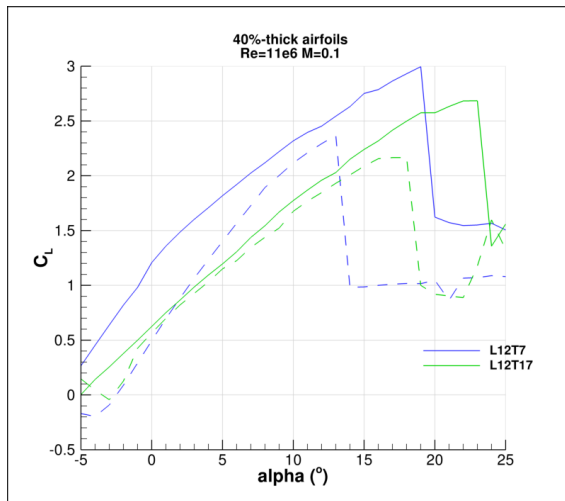
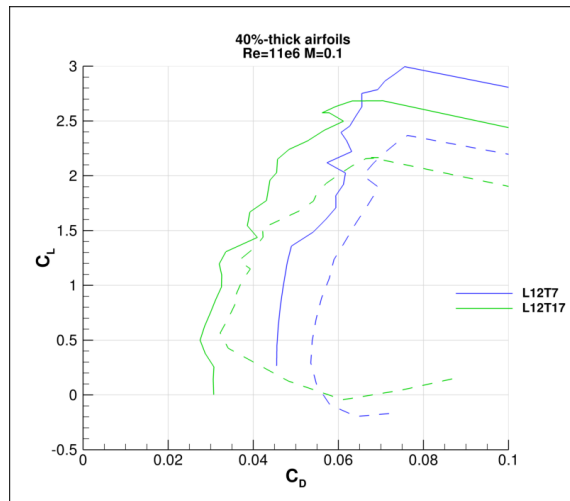


Figure 3.6-4 Polar calculation with WMB for the reference and new airfoil (L12T17) of the 40% thickness. Solid line, transitional  $n=9$ ; dashed line, fully turbulent



**Figure 3.6-5** Lift coefficient calculation with WMB for the two new airfoils of the 40% thickness. Solid line transitional  $n=9$ ; dashed line, fully turbulent



**Figure 3.6-6** Polar calculation with WMB for the two new airfoils of the 40% thickness. Solid line transitional  $n=9$ ; dashed line, fully turbulent

As it can be seen in figures, the tendency of the airfoil characteristics was well predicted by XFOIL. However, the lift curve experience a constant decrease.

The lift characteristics of the L12T7 airfoil are better than those of the original airfoil. It happens for both clean and contaminated cases. The stall point is also delayed. However, the drag coefficient is larger.

The differences between the XFOIL calculation and the CFD one make the L12T17 airfoil characteristics worse than the ones of the original airfoil for the linear region. This airfoil would be useful to be operated at AOA bigger than  $10^\circ$  in contaminated configuration or bigger than  $15^\circ$  for clean configuration. It shows better roughness sensitivity up to bigger angles of attack and goes into the deep stall zone also at higher AOA.

As it can be seen in the previous figures the design philosophy implemented in these airfoils is achieved and observed with the CFD simulations.

The important thing to be pointed is that the flow around these airfoils is expected to be very unsteady. The steady calculations presented here are not able to keep track of an important part of the behaviour of these airfoils. Moreover, even after averaging several cycles of pseudo time steps, the curves show big irregularities due to this unsteadiness. Notice that this point needs further development.

From Figure 3.6-7 to Figure 3.6-12 several contours plots of the different airfoils are shown as a visual representation of the differences in the flow. The new airfoils separate at bigger  $x/c$  positions but they create a bigger recirculation area. This area is bigger in the fully turbulent calculations.

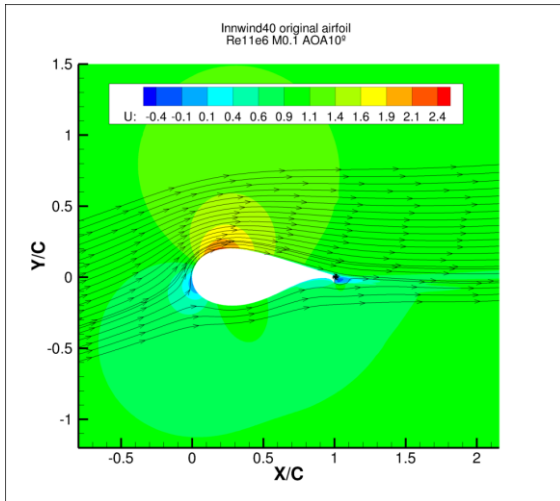


Figure 3.6-7 U velocity contour and streamtraces. 40%-thick reference airfoil. Transitional.

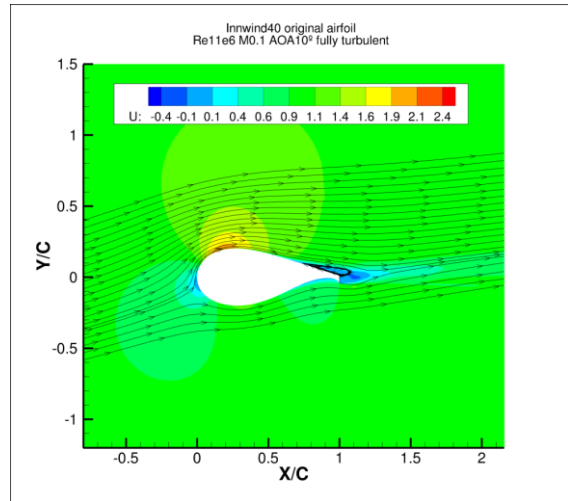


Figure 3.6-8 U velocity contour and streamtraces. 40%-thick reference airfoil. Fully turbulent.

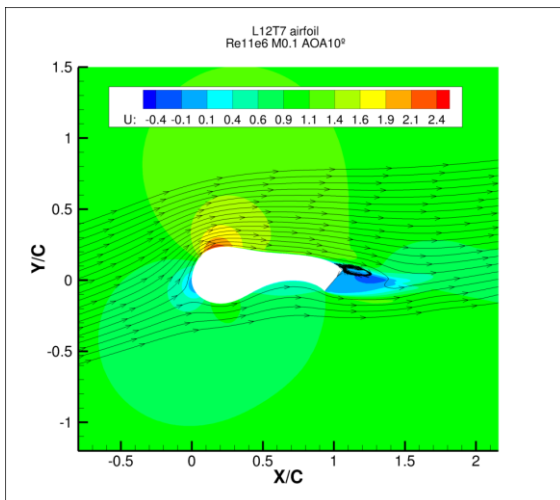


Figure 3.6-9 U velocity contour and streamtraces. L12T7 reference airfoil. Transitional.

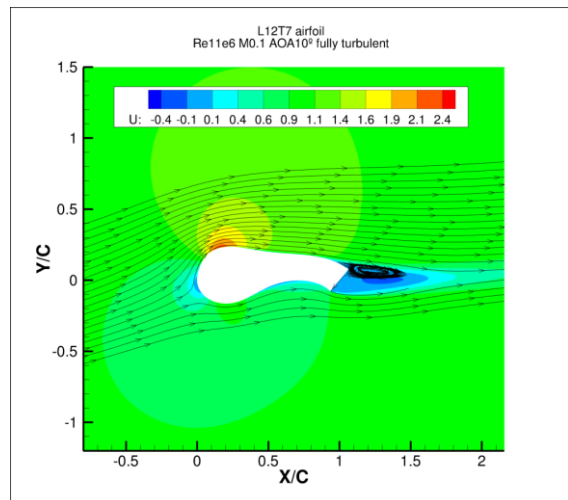


Figure 3.6-10 U velocity contour and streamtraces. L12T7 reference airfoil. Fully turbulent.

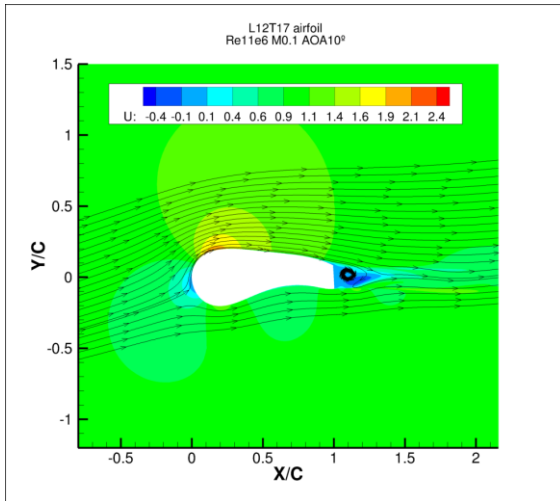


Figure 3.6-11 U velocity contour and streamtraces. L12T17 reference airfoil. Transitional.

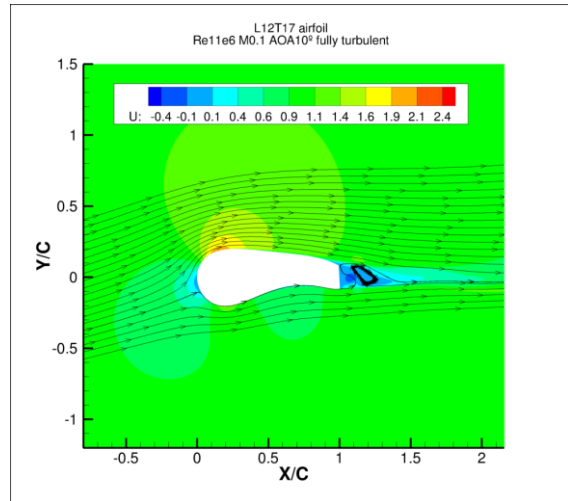


Figure 3.6-12 U velocity contour and streamtraces. L12T17 reference airfoil. Fully turbulent.

### 3.6.2 50%-thick airfoil

The CFD simulations for the 50% airfoils thickness are presented next (L11T6 and L11T17 airfoils). Aerodynamic coefficients and contour plots are included in the following figures.

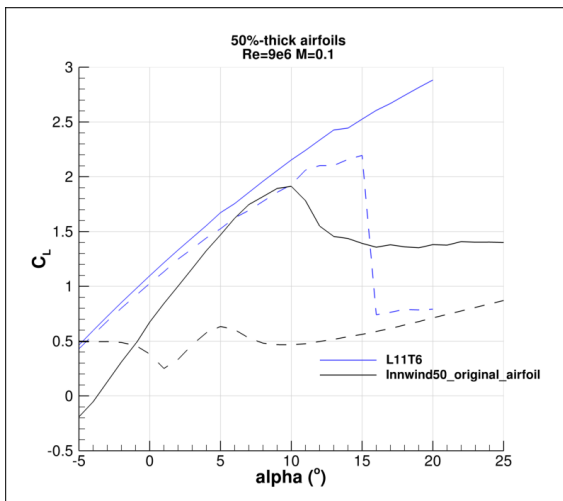


Figure 3.6-13 Lift coefficient calculation with WMB for the reference and new airfoil (L11T6) of the 50% thickness. Solid line transitional n=9; dashed line, fully turbulent

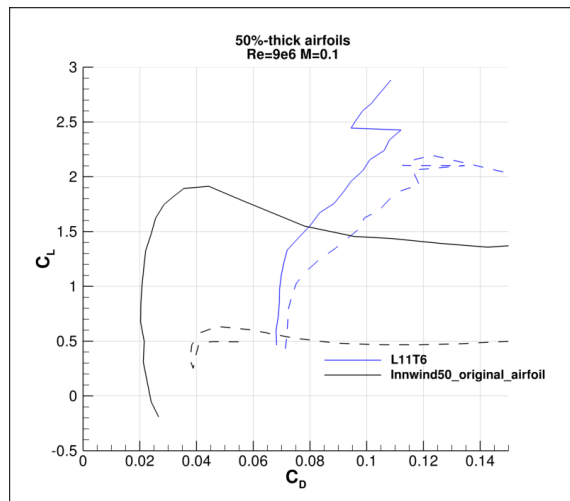


Figure 3.6-14 Polar calculation with WMB for the reference and new airfoil (L11T6) of the 50% thickness. Solid line transitional n=9; dashed line, fully turbulent

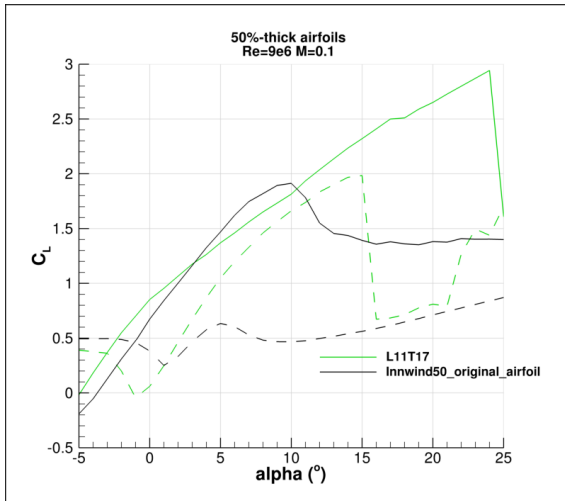


Figure 3.6-15 Lift coefficient calculation with WMB for the reference and new airfoil (L11T17) of the 50% thickness. Solid line transitional  $n=9$ ; dashed line, fully turbulent

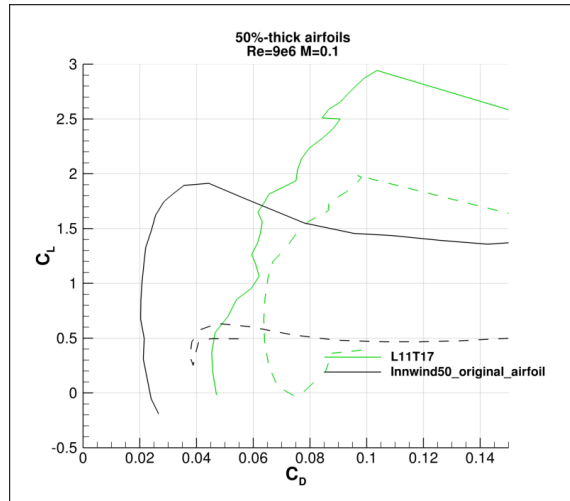


Figure 3.6-16 Polar calculation with WMB for the reference and new airfoil (L11T17) of the 50% thickness. Solid line transitional  $n=9$ ; dashed line, fully turbulent

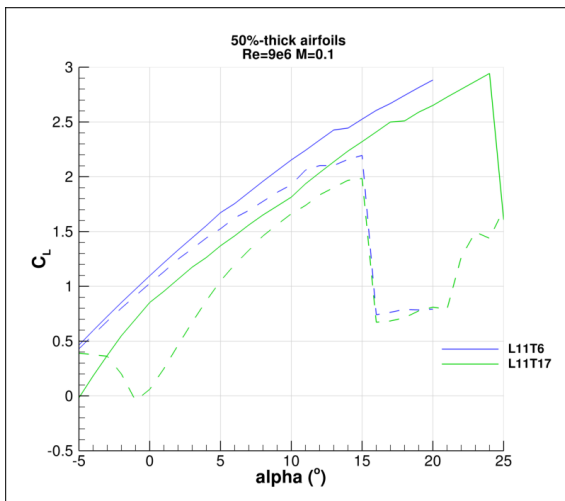


Figure 3.6-17 Lift coefficient calculation with WMB for the two new airfoils of the 50% thickness. Solid line transitional  $n=9$ ; dashed line, fully turbulent

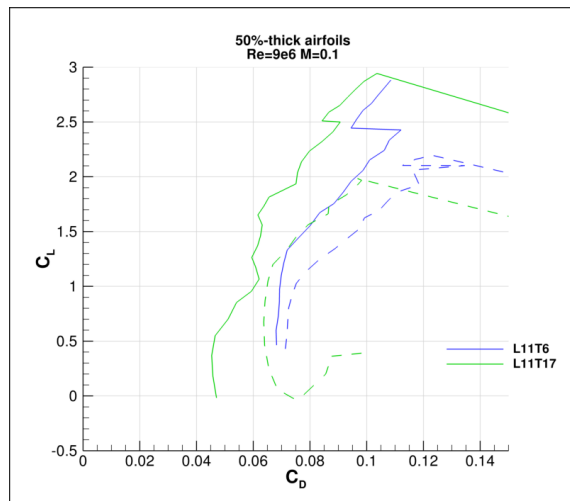


Figure 3.6-18 Polar calculation with WMB for the two new airfoils of the 50% thickness. Solid line transitional  $n=9$ ; dashed line, fully turbulent

Again, a constant lift decrease is appreciated in the curves with respect to XFOIL prediction.

The L11T6 airfoil shows good lift values in the whole range of AOA for clean and contaminated configuration. The stall point takes place several degrees after the design point which is also a desirable characteristic. The drag is bigger than the presented by the original airfoil.

The L11T17 airfoil follows the same tendency as the previous one with some differences to be pointed out. The clean behaviour around the design point is worse than the reference profile and the clean to contaminated differences are bigger than the L11T6 profile. However, this airfoil suffers less drag than the L11T6.

The best characteristics of these airfoils are the good contaminated behaviour and the delayed stall point. However, a drag increase comes across when using these thick-trailing edge airfoils.

In this case, calculations have shown that the flow may be unsteady also.

Figure 3.6-19 to Figure 3.6-24 offer an intuitive representation of the flow.

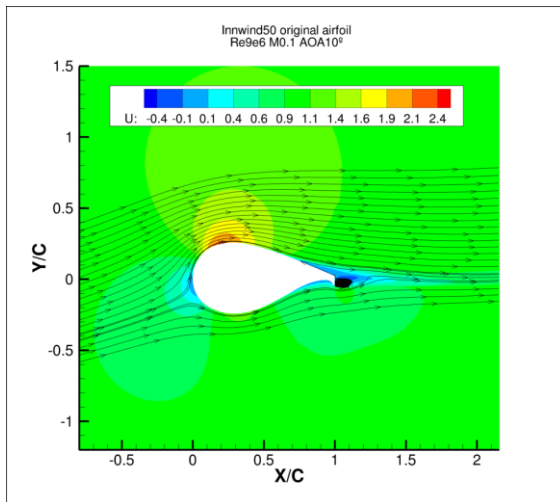


Figure 3.6-19 U velocity contour and streamtraces. 50%-thick reference airfoil. Transitional.

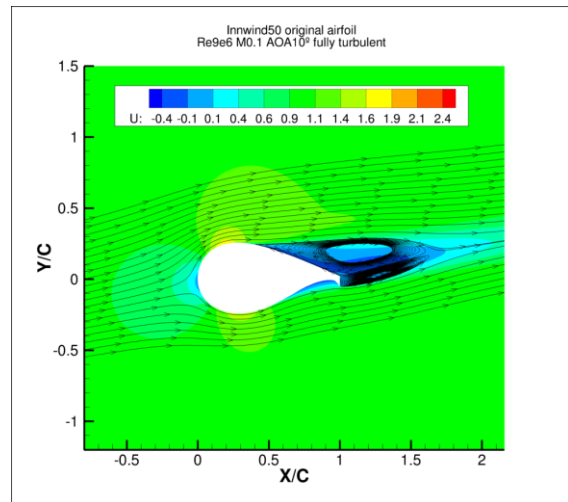


Figure 3.6-20 U velocity contour and streamtraces. 50%-thick reference airfoil. Fully turbulent.

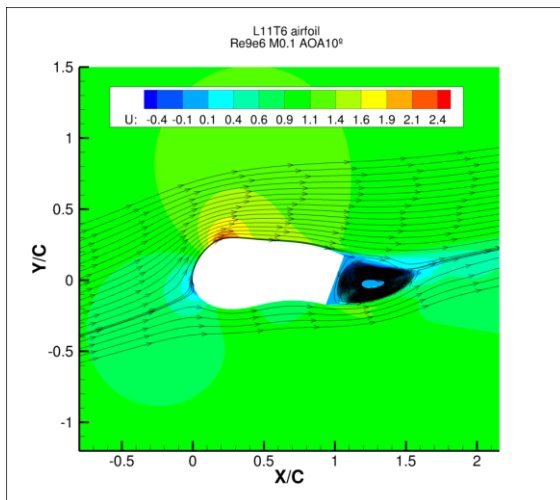


Figure 3.6-21 U velocity contour and streamtraces. L11T6 reference airfoil. Transitional.

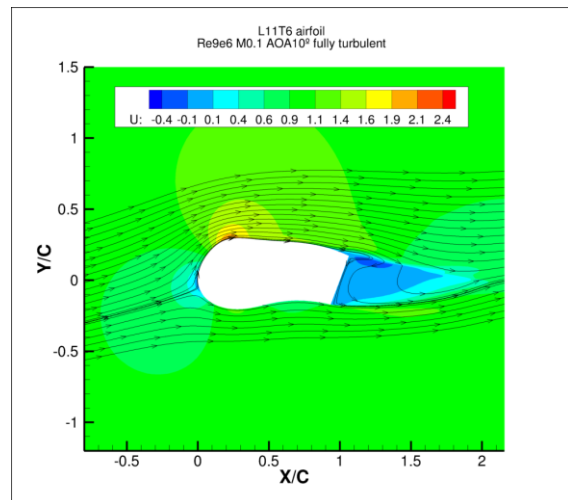


Figure 3.6-22 U velocity contour and streamtraces. L11T6 reference airfoil. Fully turbulent.

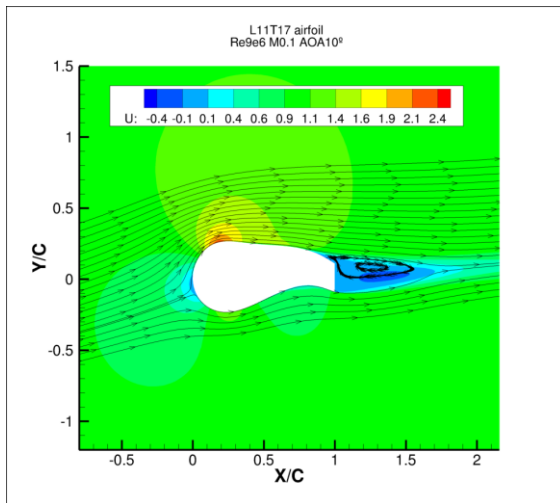


Figure 3.6-23 U velocity contour and streamtraces. L11T17 reference airfoil. Transitional.

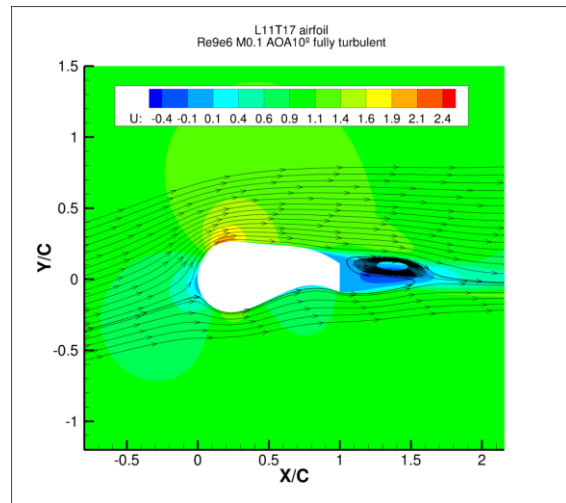


Figure 3.6-24 U velocity contour and streamtraces. L11T17 reference airfoil. Fully turbulent.

Table 3.6-1 is used as a sum up of the CFD analysis of the original and the designed airfoils, including both, the 40%-thick and the 50%-thick airfoils.

Airfoil	t/c (%)	TEgap/c (%)	$C_{Lmax}$ (trans)	$C_{Dmin}$ (trans)	$C_{Lmax}$ (fully)	$C_{Dmin}$ (fully)
original Innwind40 airfoil	40	5	2.44	0.015	1.78	0.021
L12T7	40	20	3.00	0.046	2.37	0.053
L12T17	40	16	2.68	0.026	2.17	0.032
original Innwind50 airfoil	50	7	1.91	0.020	0.84	0.040
L11T6	50	37	2.88	0.068	2.20	0.071
L11T17	50	20	2.94	0.05	1.98	0.07

Table 3.6-1 - WMB data for the reference and the design airfoils

### 3.7 CFD study of special configurations

Apart from the previously presented results including the basic calculations on the designed airfoils, several special configurations have been studied as a guideline for the use of several strategies to enhance some characteristics of the airfoils operating in the blade root region. The following study were only carried on the L11T6 airfoil (50% airfoil thickness), as a representative example of the designed airfoils.

### 3.7.1 Tripping

The tripping of the boundary layer simulates two real life situations. One of them is the voluntary tripping and the other one is the tripping due to roughness deposition.

The first one makes the boundary layer become turbulent with the aim of delaying the separation by means of the energetic mixing provided by the turbulent boundary layer. This is a preliminary study because that effect is usually achieved by vortex generators instead of by simply tripping.

The effect of roughness in the leading edge of the airfoil is usually accounted for by tripping the airfoil. It does not represent the whole effect of roughness but gives an idea of the sensitivity of the airfoil.

The following simulations are performed with the boundary layer tripped at 2% of the airfoil chord in the upper side and 5% of the chord in the lower side in the first case and at the 5% and 10%, respectively, in the second one.

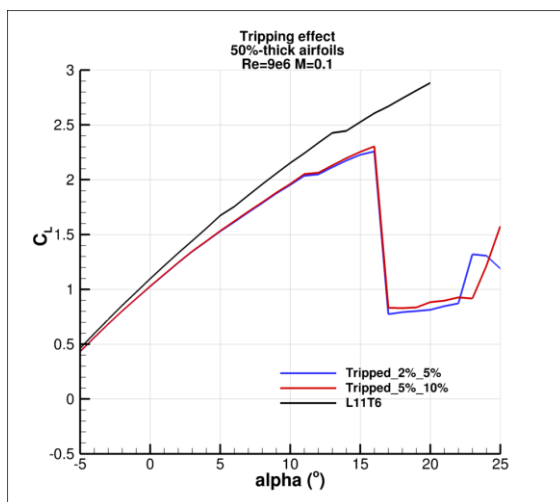


Figure 3.7-1 Lift coefficient for the L11T6 for transitional and tripped calculations.

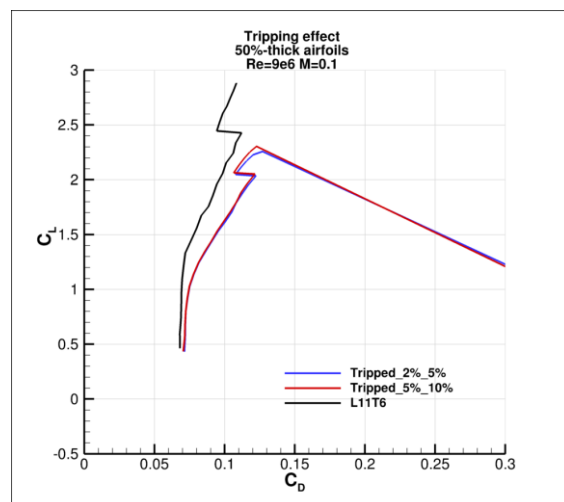


Figure 3.7-2 Polar curve for the L11T6 for transitional and tripped calculations.

When the airfoil is tripped, the slope of the lift curve decreases and the stall point is moved to lower angles of attack. Moreover, the drag coefficient increases. In this case, the behaviour is very similar to the fully turbulent case.

### 3.7.2 Gurney flap

Gurney flaps are passive devices used to enhance lift, consisting on a small plate located at the trailing edge and perpendicular to it. Gurney flaps increase the maximum lift coefficient, decrease the angle of attack of zero lift coefficient while the lift curve slope remains relatively constant, and increase the nose down pitching moment, in the same way as when the camber increases, with very little drag penalty.

The lengths of the flaps used in the study are 2% (called “gurney\_flap\_1”) and 1% (called “Gurney\_flap\_2”).

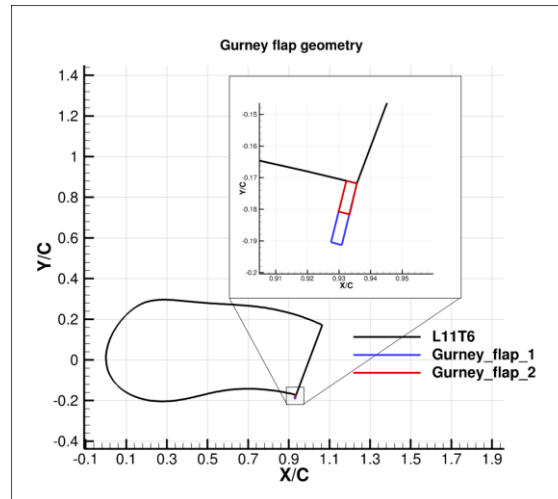


Figure 3.7-3 Gurney flap geometries

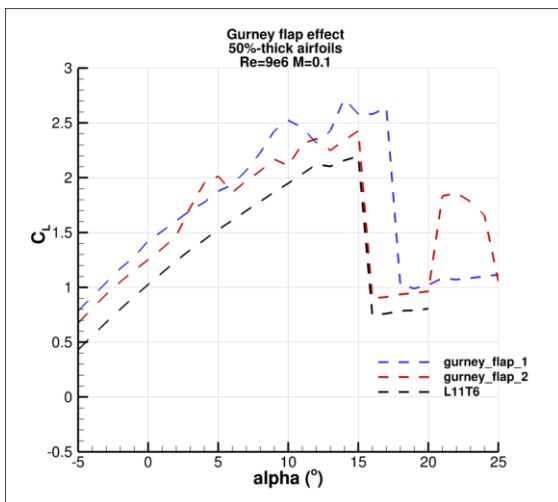


Figure 3.7-4 Lift coefficient for the L11T6 and the gurney flap configurations. Fully turbulent calculations

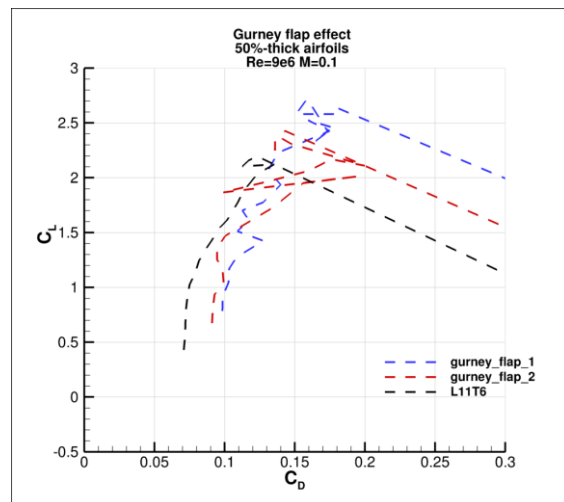


Figure 3.7-5 Polar curve for the L11T6 and the gurney flaps configurations. Fully turbulent calculations

Both geometries imply a lift increase, being that increase the bigger the longer the flap. On the other hand the drag coefficient also increases.

This effect can be interesting to increase the lift coefficient that might be lost if the trailing edge is reduced with the objective of reducing the unsteadiness.

See how the flow is modified in Figure 3.7-6 and Figure 3.7-7.

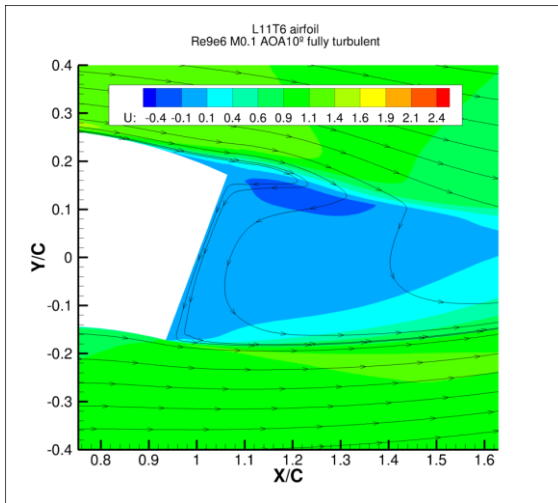


Figure 3.7-6 U velocity contour and streamtraces. L11T6 airfoil. Fully turbulent. TE detail.

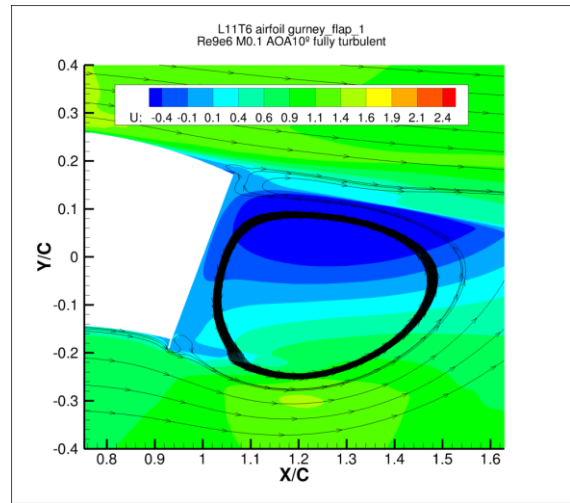


Figure 3.7-7 U velocity contour and streamtraces. L11T6 airfoil with gurney\_flap\_1. Fully turbulent. TE detail.

### 3.7.3 Splitter plate

The splitter plate consists on a flat surface attached to the trailing edge that aims to improve the lift and drag characteristics. There are several geometries but only the simplest one is considered herein. The working principle consist on avoiding (or modifying) the interference between the vortex generated by the upper and the lower side downstream.

In this case the splitter plates are flat plates attached to the trailing edge and perpendicular to it. The one named “Splitter\_plate\_1” has the same length as the trailing edge gap and the “Splitter\_plate\_2” length is equal to one half of the trailing edge gap (see Figure 3.7-8).

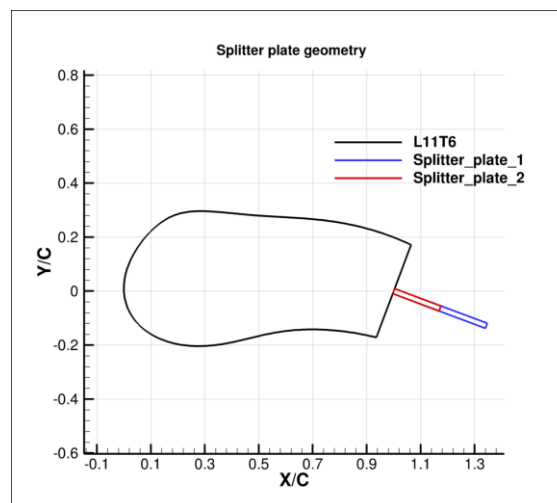


Figure 3.7-8 Splitter plate geometries

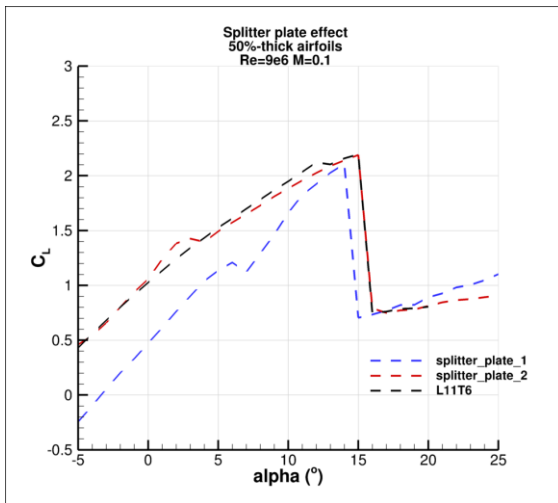


Figure 3.7-9 Lift coefficient for the L11T6 and the splitter plate geometries Fully turbulent calculations

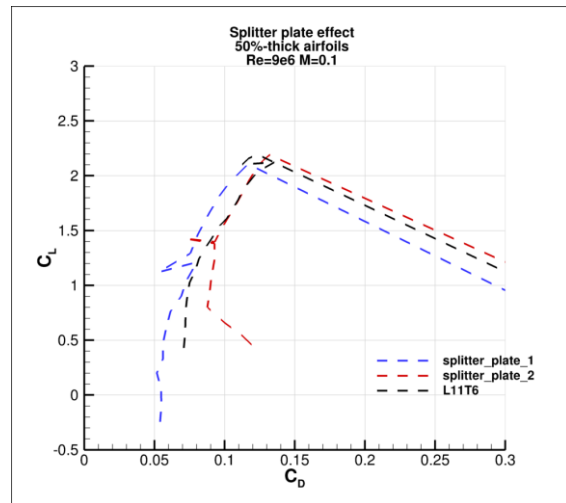


Figure 3.7-10 Polar curve for the L11T6 and the splitter plate geometries. Fully turbulent calculations

The splitter with length equal to the trailing edge gap gives rise to a strong decrease of the lift coefficient (Figure 3.7-9) which is undesirable. On the other hand, it obtains an important drag reduction (Figure 3.7-10); which is the objective of these plates. If the splitter length is chosen equal to one half of the trailing edge thickness, a small lift reduction and drag increase is found.

These plates seems to modify the unsteadiness of the process, but unsteady calculations would be needed to check it.

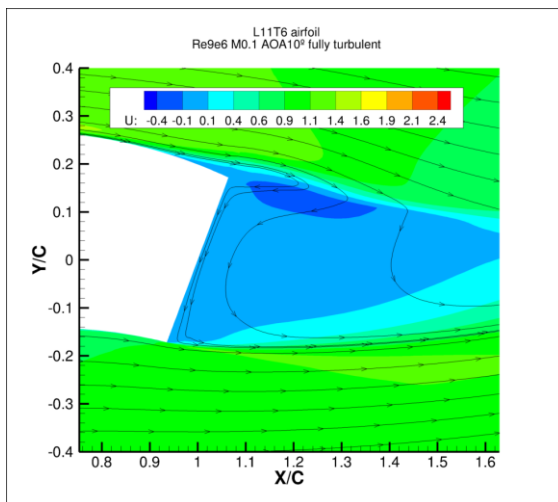


Figure 3.7-11 U velocity contour and streamtraces. L11T6 airfoil. Fully turbulent. TE detail.

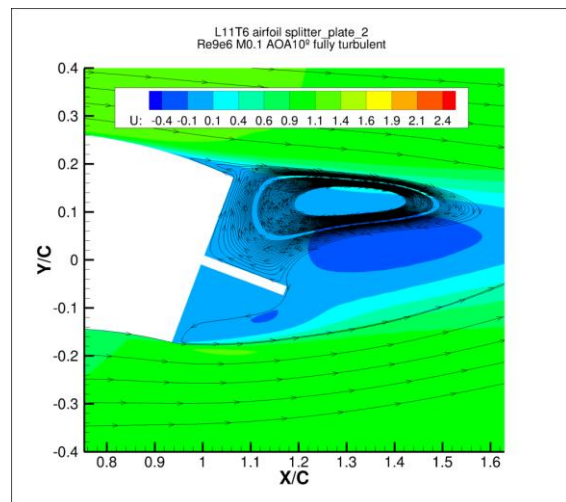


Figure 3.7-12 U velocity contour and streamtraces. L11T6 airfoil with splitter\_plate\_2. Fully turbulent. TE detail.

Table 3.7-1 shows a sum up of the main coefficients of the different configurations studied: tripping, gurney flaps and splitter plates.

Airfoil	$C_{Lmax}$ (trans)	$C_{Dmin}$ (trans)	$C_{Lmax}$ (fully)	$C_{Dmin}$ (fully)
L11T6	2.88	0.068	2.20	0.071
Tripped 2% 5%	2.26	0.071	-	-
Tripped 5% 10%	2.30	0.071	-	-
Gurney flap 1	-	-	2.68	0.100
Gurney flap 2	-	-	2.43	0.089
Splitter plate 1	-	-	2.11	0.055
Splitter plate 2	-	-	2.19	0.089

Table 3.7-1 – WMB data for the L11T6 airfoil and the special configurations

It would be interesting to keep studying different shape and configurations of these devices as they seem to really modify the behaviour of this kind of airfoils, including unsteady calculations.

### 3.8 Synthesis and conclusions

The redesign of the blade root region is one of the options to reduce the cost of energy associated to wind turbines. CENER’s contribution tries to provide some knowledge about the flow in this area and to design new airfoils for this region to enhance the blade performance. The main conclusions are:

- 2D and 3D CFD calculations have been performed in the INN WIND.EU reference blade in order to better understand the flow in the root region. The study of the flow around the blade root shows that this area is characterized by important 3D effects. This region is the most affected by the radial flow. Moreover, the 3D effects are also very important. The airfoils operating in the rotating blade show delayed separation and important differences in pressure and friction coefficients. Another important conclusion obtained is that the airfoils designed with 2D aerodynamic calculations for the root area will experience bigger lift coefficients when working in the blade root area.
- The airfoils designed by CENER under the scope of the INN WIND.EU project have thick trailing edges. These airfoils are well suited for this application because they can improve the aerodynamic characteristics while providing better structural properties which are critical in this region.

CENER’s airfoil design tool has as aerodynamic motor XFOIL which is known not to be adequate to predict the aerodynamic characteristics of high trailing edge thickness airfoils. That is why a study of how XFOIL works for these airfoils has been developed showing that it under predicts the drag coefficient and over predicts the lift slope. From this study some empirical correlations to correct XFOIL

data have been obtained. These empirical correlations need to be completed in the future with experimental data for high Reynolds numbers.

- With CENER airfoil-design tool, four airfoils are provided, two of them with a thickness of the 40% and another two with a thickness to chord ratio of 50%. The new airfoils focus on providing high lift in a wide range of angles of attack, good contaminated performance and smooth stall behaviour. Generally speaking, the airfoils obtained match the design objective of improving high lift coefficient for both clean and rough configurations even though it penalizes the aerodynamic efficiency. For instance, one of the 50% thickness airfoils designed (L11T6) improves the behaviour in contaminated conditions with regard to the airfoil in the INN WIND.EU reference blade.

In addition, all the airfoils designed have been calculated using CFD and the aerodynamic characteristics obtained have mainly the same tendency as the XFOIL calculations. This fact supports the use of XFOIL as aerodynamic tool during the design process.

- The last part of CENER work analyses some trailing edge devices effects on one of the designed airfoils. The tripping of the airfoils show how well the airfoil behaves in contaminated conditions. The gurney flap gets an increase in the lift coefficient but with increasing also the drag coefficient. And finally, the splitter plate seems to be able to reduce the drag coefficient of the airfoils.

There is a need of future work specially to try to reduce the unsteadiness related to the vortex generated at the trailing edge. However, the results show optimistic results because the blade root region can be widely improved by the use of high-trailing-edge airfoils and special trailing edge devices.

## CHAPTER 4 DESIGN OF AIRFOILS FOR LOW INDUCTION ROTORS - CRES

M G Sieros, P Chaviaropoulos

### 4.1 Scope and objectives

The innovative aerodynamic concept that CRES investigates in INNWIND.EU is that of low induction rotors (LIRs). As discussed earlier in [1] and [22], the best way to implement the LIR concept is by using low-lift airfoils, e.g. airfoils having their maximum  $k = C_L/C_D$  at moderate  $C_{LDES}$  (design  $C_L$ ) values. It is not easy, however, to get a high performance, thick enough, airfoil with  $k$  values 100+, which is a normal achievement for the high lift airfoil families. This difficulty is increasing as  $C_{LDES}$  gets smaller. The design of a family of such low lift airfoils aiming to operate in the range of Reynolds and Mach numbers corresponding to a 10MW LIR is the scope of the present work.

### 4.2 Design specifications

Table 4.2-1 shows the operating conditions at different blade sections of a LIR version of the 10MW Reference Wind Turbine of INNWIND.EU. The relative thickness of the airfoils along the original blade span varies from 60% in the near-root section to 21% at the tip. Next to the relative thickness we present the Reynolds and Mach number at rated conditions as well as their minimum value within the turbine operating envelope. Since the same airfoil is used at different spanwise positions there are multiple rows in the table sharing the same thickness. From those we use the highlighted rows to specify our design conditions. To extend the design family including thinner (than 21%) profiles we include two additional entries for tip-profiles with relative thicknesses 18 and 15%.

Section Thickness	Re (rated)	Ma (rated)	Re (Min)	Ma (Min)
60.00%	<b>7.0×10<sup>6</sup></b>	<b>0.05</b>	4.4×10 <sup>6</sup>	0.03
40.10%	<b>11.0×10<sup>6</sup></b>	<b>0.07</b>	7.0×10 <sup>6</sup>	0.05
35.00%	<b>14.0×10<sup>6</sup></b>	<b>0.09</b>	9.0×10 <sup>6</sup>	0.06
30.00%	<b>17.0×10<sup>6</sup></b>	<b>0.12</b>	10.0×10 <sup>6</sup>	0.07
24.00%	<b>20.0×10<sup>6</sup></b>	<b>0.16</b>	12.0×10 <sup>6</sup>	0.10
24.00%	<b>16.0×10<sup>6</sup></b>	<b>0.25</b>	11.0×10 <sup>6</sup>	0.15
24.00%	<b>13.0×10<sup>6</sup></b>	<b>0.30</b>	8.0×10 <sup>6</sup>	0.18
21.00%	<b>20.0×10<sup>6</sup></b>	<b>0.16</b>	12.0×10 <sup>6</sup>	0.10
21.00%	<b>16.0×10<sup>6</sup></b>	<b>0.25</b>	11.0×10 <sup>6</sup>	0.15
21.00%	<b>13.0×10<sup>6</sup></b>	<b>0.30</b>	8.0×10 <sup>6</sup>	0.18
18.00%	<b>16.0×10<sup>6</sup></b>	<b>0.25</b>	11.0×10 <sup>6</sup>	0.15
15.00%	<b>16.0×10<sup>6</sup></b>	<b>0.25</b>	11.0×10 <sup>6</sup>	0.15

Table 4.2-1–Intended thickness and operating conditions

Following our earlier conclusions of [23] the low lift airfoils shall be designed for  $C_{LDES}=0.8$ , instead of  $C_{LDES}=1.2$  to  $1.3$  which is the normal range for high lift profiles. To avoid deep minima (a highly optimized objective function which rapidly deteriorates when the design variables are slightly perturbed) that characterize single point designs, we shall design the airfoils for a maximum mean performance within a range of design lift coefficients  $C_{LDES}=[0.7$  to  $0.9]$  instead of using the single  $C_{LDES}=0.8$  value.

An important issue for the design specifications is the way one handles transition. We are referring to designs at very high Reynolds numbers and, therefore, a back-loaded laminar airfoil may perform significantly better than a front-loaded one which better suits fully turbulent flows. On the other hand it is known that the performance of laminar airfoils may become very poor when the flow is tripped to turbulent. But even if a good part of laminar flow exists over the airfoil it is quite uncertain how the high turbulence content of the atmospheric boundary layer will influence the transition location through the bypass mechanism. To ensure some conservatism in our designs we shall optimize the airfoil shapes for their weighted transitional / fully turbulent performance.

### 4.3 Design methodology

#### 4.3.1 Parameterization

The airfoils are parameterized using Bezier curves with 9-12 control points for representing the complete shape in one piece. The trailing edge thickness is directly set, while the position of maximum thickness and the maximum thickness are controlled through the Bezier parameters. The number of control points was chosen so that the resulting representation could reproduce well-known families (NACA, FFA) with less than 0.5% error.

#### 4.3.2 Objective function

The objective function of the design is the maximization of the airfoil performance (lift over drag) within a desired range of lift coefficients. This can be expressed as

$$\text{Maximize} \left[ \int_{C_{LDES1}}^{C_{LDES2}} \left\{ W_l \left( \frac{C_L}{C_D} \right)_l + W_t \left( \frac{C_L}{C_D} \right)_t \right\} dC_L \right], W_l + W_t = 1$$

Where  $[C_{LDES1}, C_{LDES2}]$  is the range of the design lift coefficient, centred around the actual design point and  $W_l, W_t$  are the laminar / turbulent flow weights. The reason for performing the optimisation for more than a single CL value is to avoid degenerate solutions that display a rapid drop in performance when this value is exceeded.

#### 4.3.3 Constrains

The constraints on the design are imposed through the available range of movement for the control points. The main parameters that are affected are

- Trailing edge thickness (which is fixed at the original value)
- Maximum thickness (specified for each design)
- Maximum thickness location (allowed to shift, but retaining a basic similarity between the airfoil shapes for different thicknesses)

#### 4.3.4 Optimization algorithm

The optimizer used employs a combination of evolutionary and gradient-free methods. The latter are used for the final convergence once the evolutionary method has reached a minimum. The direct solver used for the calculation of the objective function is XFOIL, but the results are checked using more advanced tools, available at NTUA (see Chapter 5 for details), including the compressible CFD code MaPFlow and the strong viscous-inviscid interaction code Foil2w.

#### 4.4 Designed airfoils

Following the design specifications of Table 4.2-1) we produced low-lift profiles with relative thicknesses 15%, 18%, 21%, 24%, 30% and 40%. With the exception of the two ending family members (15% and 40%) where a single low-lift airfoil was designed, we generated for all other thicknesses two low-lift airfoils of different laminar / turbulent flow weighting as well as a high-lift variant for comparison purposes. The laminar / turbulent weighting was set to 30%-70% (denoted as 30-70 from this point on) for one of the low lift airfoils and all high lift airfoils. 10-90 (or 20-80) were the weights for the second low lift airfoils family. The high lift family is designed for  $C_{LDES}=[1.2 \text{ to } 1.4]$ .

##### 4.4.1 18% thick airfoils

Figure 4.4-1 presents the two low lift and one high lift airfoils designed for 18% relative thickness for the Reynolds and Mach number values specified in Table 4.2-1. Clearly, the maximum thickness of the 30-70 profiles (low lift and high lift) is located downstream from the relevant location of the 10-90 profile. The high lift profile is characterized by its increased camber and its reduced thickness in the trailing edge area.

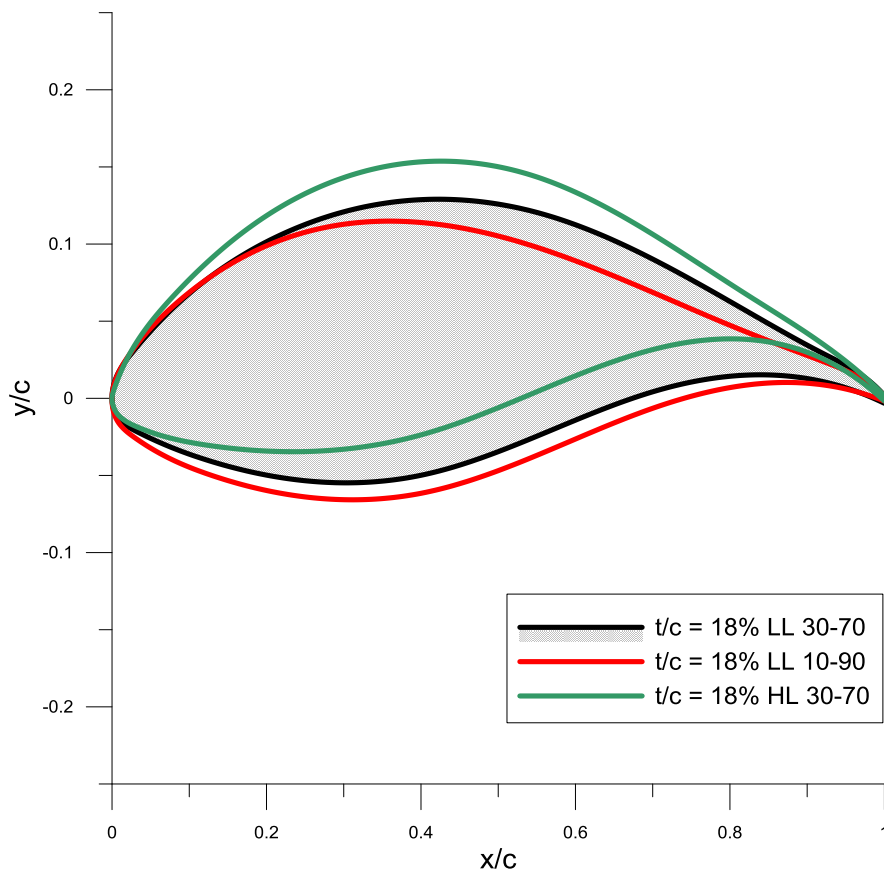


Figure 4.4-1: Three airfoil designs of 18% thickness. LL stands for Low Lift while HL for High Lift. The weighting percentages (laminar – turbulent) are also shown in the legend

Figure 4.4-2 shows at its left the lift and drag versus angle of attack for the 10-90 low lift profile calculated with XFOIL for three different transition settings, fully turbulent, critical amplification or N-factor equal to 4 (addressing high ambient turbulence conditions) and N-factor equal to 9 addressing free-transition. In the right part of the figure we show how the N-factor effects the transition point location along the 18% airfoil suction (top) and pressure side (low). It is seen that the  $C_{LDES}$  corresponds to design a.o.a values of  $[-1,1]$  degrees where the transition point is located at nearly 40% chord at both airfoil suction and pressure sides. This is clearly seen at the laminar pocket of the drag curves too. It is in this laminar pocket where the airfoil efficiency  $L/D$  is expected to get its maximum value.

Airfoil performance curves  $L/D$  versus  $C_L$  for the three profiles are shown in Figure 4.4-3 for the three transition settings considered. Curves in black correspond to performance at fully turbulent flow conditions. It is seen that the three airfoils, although quite different in shape, they have very similar performance up to  $C_L = 1.5$ . This indicates that airfoil performance at fully turbulent conditions is flat and therefore unsuitable to drive alone a well-defined optimization problem.

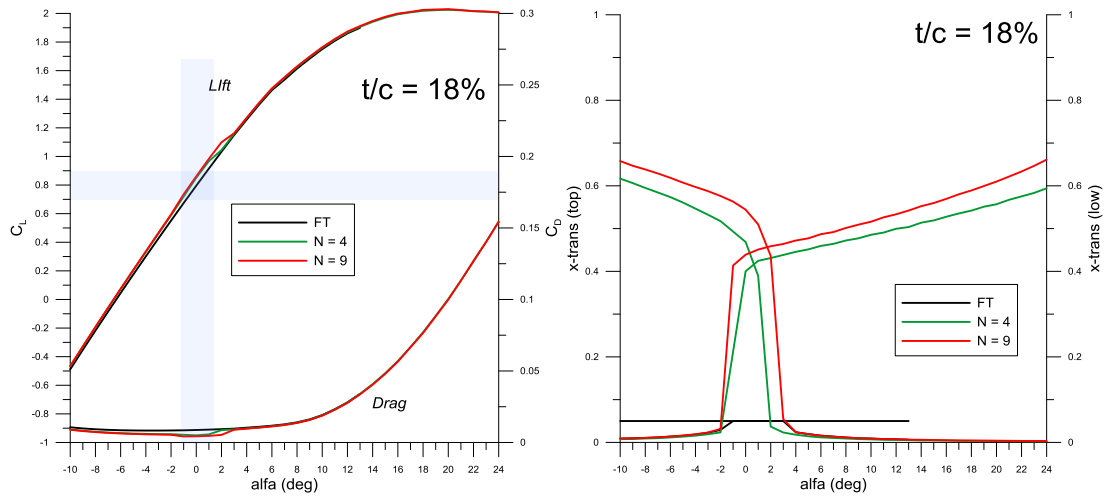


Figure 4.4-2: Lift and drag (left) versus angle of attach 'alfa' for the 18% LL 10-90 airfoil. XFOIL calculations have been performed for three different transition settings, fully turbulent,  $N=4$  and  $N=9$ . The transition location along the airfoil suction and pressure side for different 'alfa' is shown in the right figure

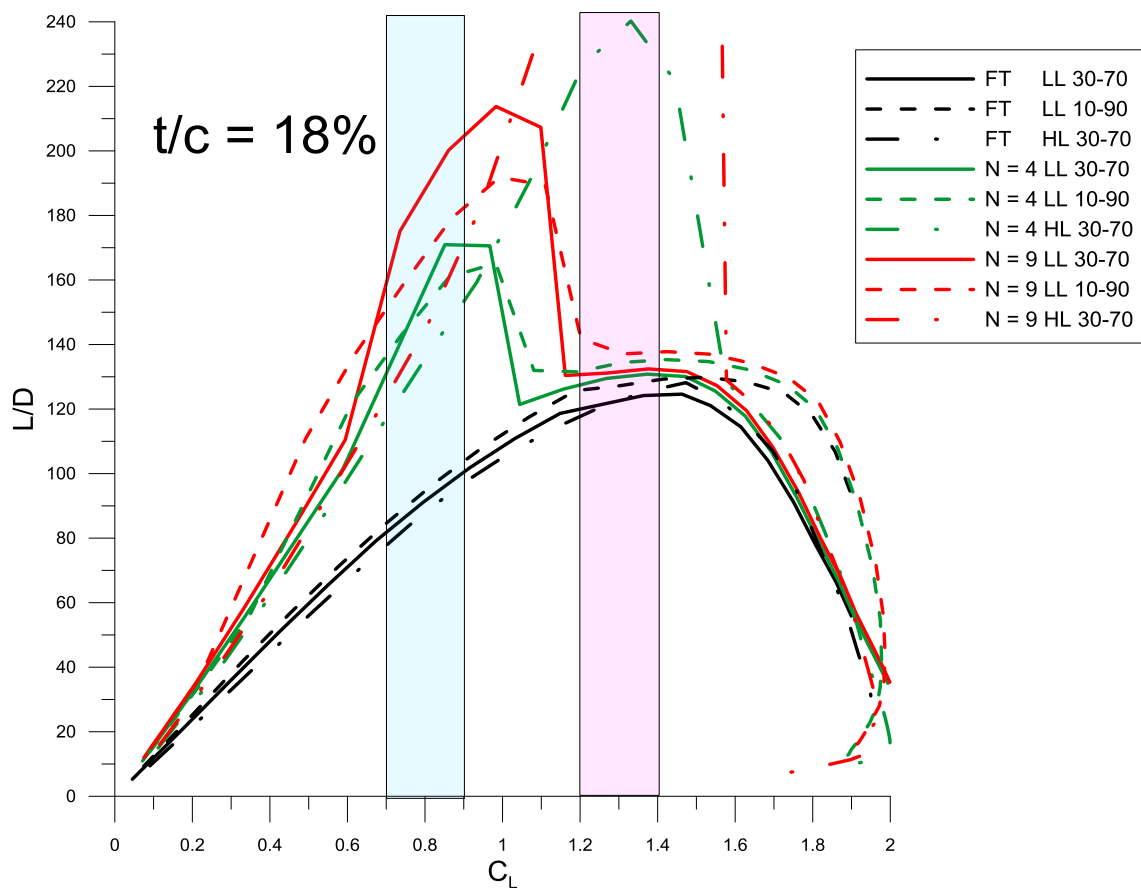


Figure 4.4-3: Performance ( $L/D$ ) of the three 18% airfoils for the three different transition settings considered

The performance of the three 18% airfoils becomes quite distinct when laminar to turbulent transition is taken into account. For both the  $N$ -factors considered it is seen that

the low lift profiles are performing much better than the high lift at their  $C_{LDES}$  range and visa-versa. For the conservative selection of  $N=4$  the low-lift designs are having a performance level that exceeds 160 units (thanks to the very high Reynolds number) while the high-lift airfoil at the same  $C_L$  range is 20 units down. Comparing the two low lift designs it is seen, as expected, that increasing the turbulent weight factor slightly improves the fully turbulent performance compromising, however, the laminar performance (by 10 to 20 performance units when  $N=9$  and much less when  $N=4$ ).

#### 4.4.2 21% thick airfoils

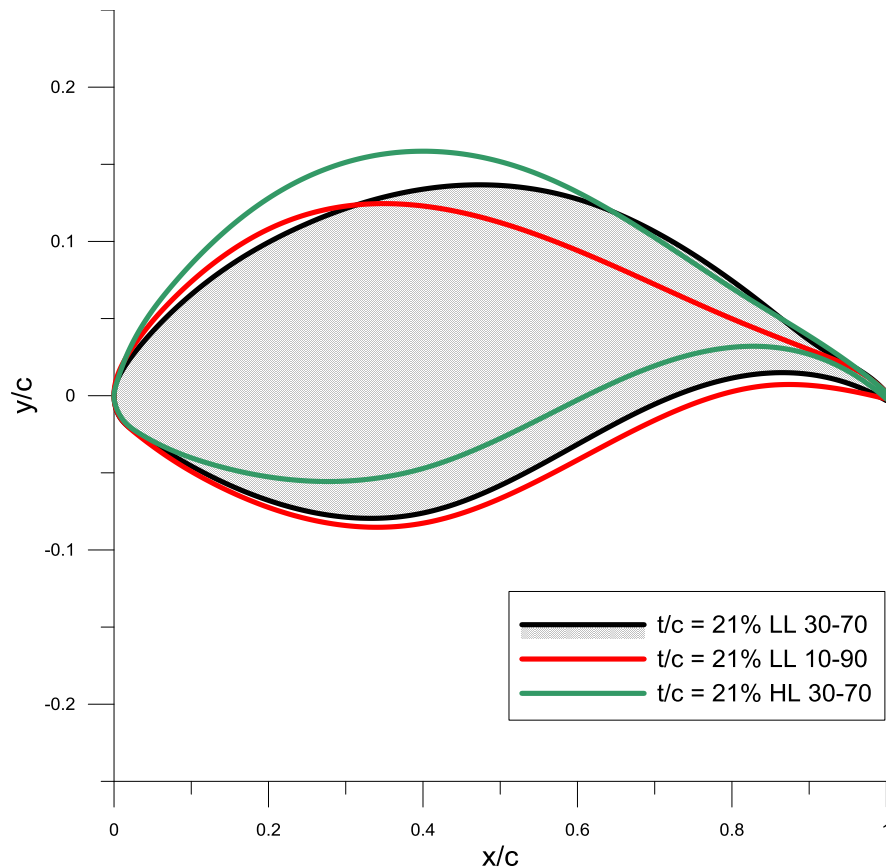


Figure 4.4-4: Three airfoil designs of 21% thickness. LL stands for Low Lift while HL for High Lift. The weighting percentages (laminar – turbulent) are also shown in the legend

Figure 4.4-4 presents the two low lift and one high lift profiles designed for 21% relative thickness for the Reynolds and Mach number values specified in Table 4.2-1.

Figure 4.4-5 presents the lift and drag curves vs. angle of attack and the transition point location along the suction and pressure side of the 21% low lift 10-90 profile.

Figure 4.4-6 presents the performance characteristics of the three 21% profiles. Apart from the drastic loss of performance of the low-lift 30-70 after  $C_L = 1$  at fully turbulent conditions the results are very similar to the ones of the 18% profiles. The performance of the 21% low-lift 30-70 profile is outstanding, approaching even for the  $N=4$  case a value close to 190 units. Even the 10-90 profile slightly exceeds 140 units.

Evidently, these results are subjected to the uncertainty of the XFOIL calculations for thick airfoils at such high Reynolds numbers. These results have to be cross-checked by (at least) additional calculations of the airfoils polar with full CFD.

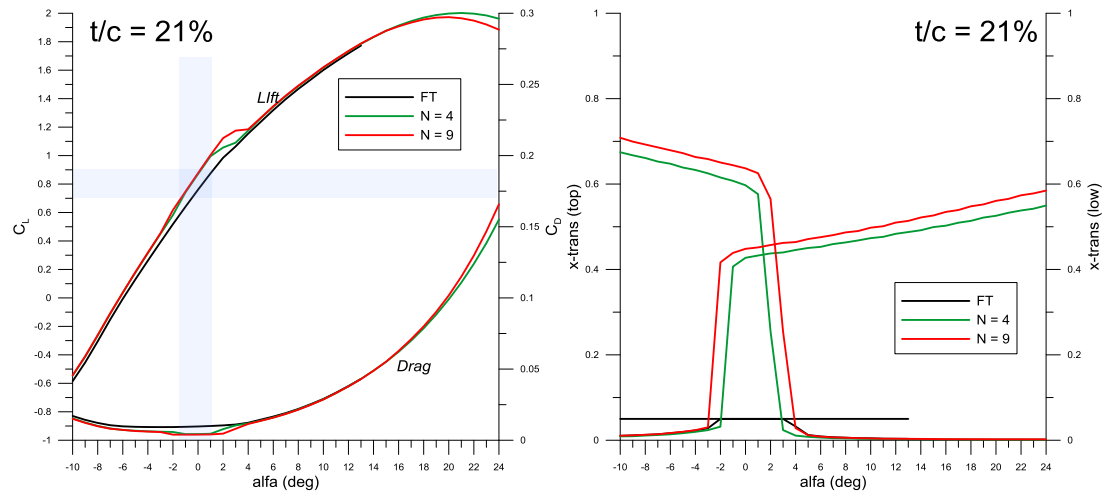


Figure 4.4-5: Lift and drag (left) versus angle of attach 'alfa' for the 21% LL 10-90 airfoil. XFOIL calculations have been performed for three different transition settings, fully turbulent, N=4 and N=9. The transition location along the airfoil suction and pressure side for different 'alfa' is shown in the right figure

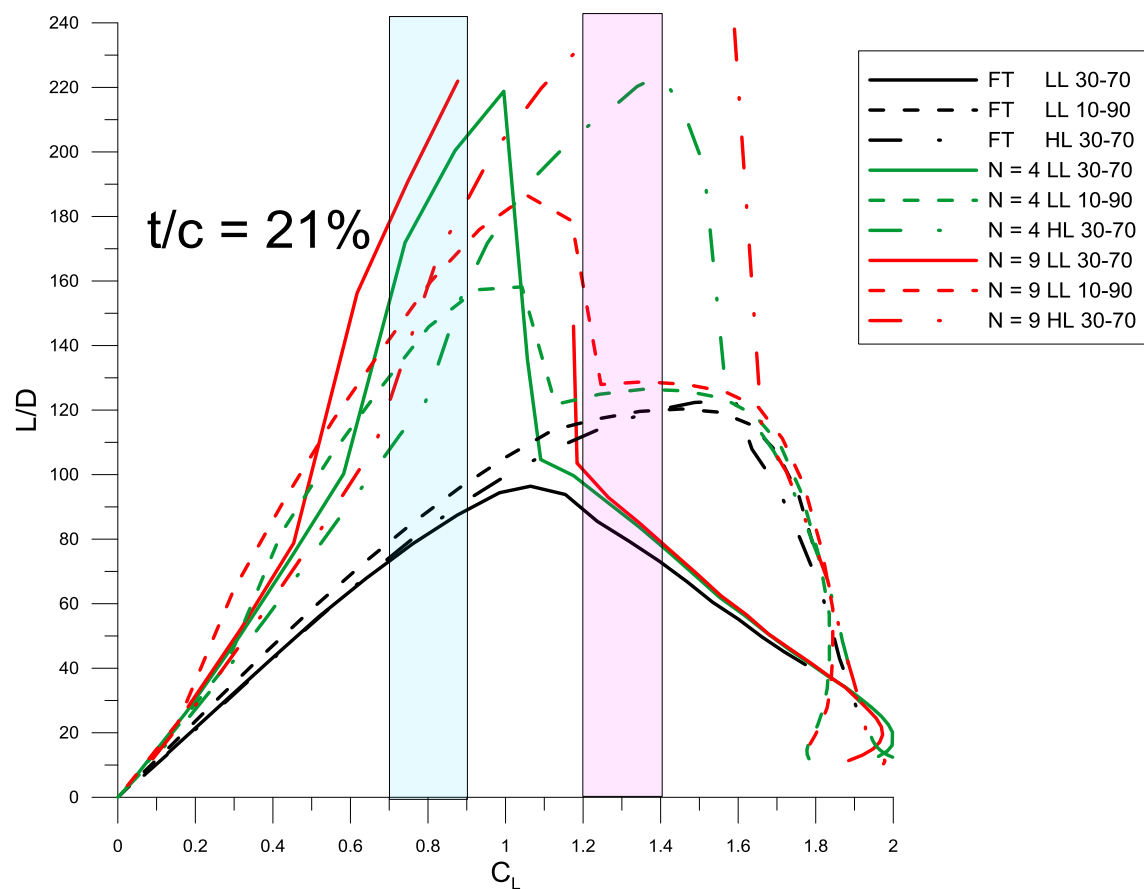


Figure 4.4-6: Performance (L/D) of the three 21% airfoils for the three different transition settings considered

#### 4.4.3 24% thick airfoils

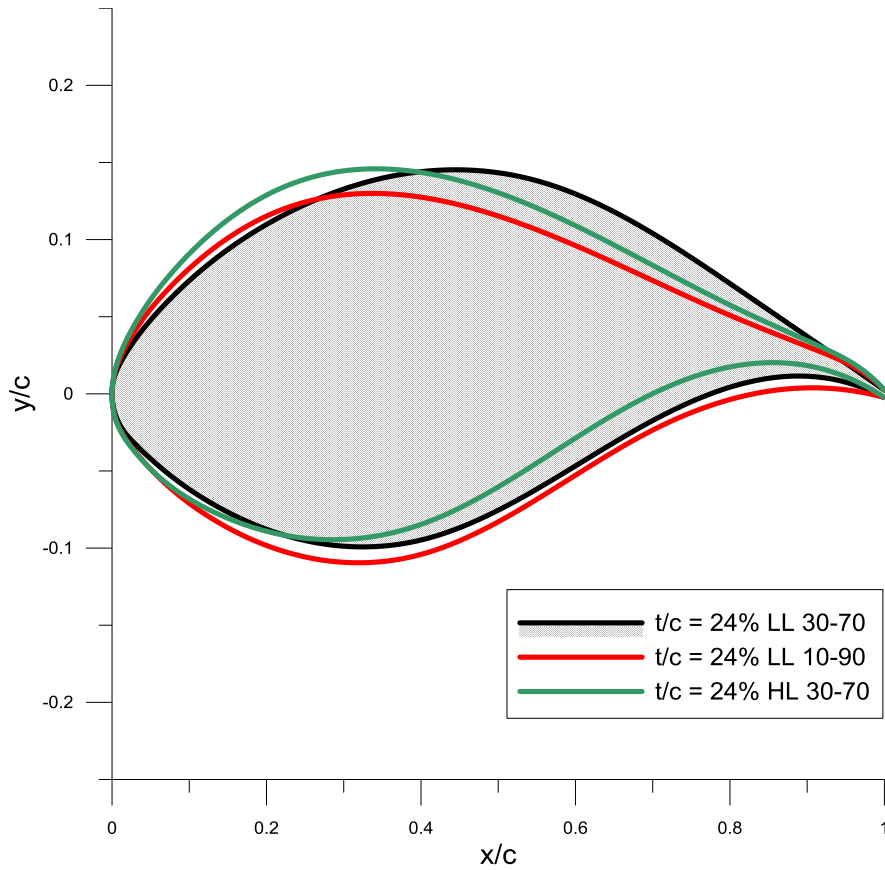


Figure 4.4-7: Three airfoil designs of 24% thickness. LL stands for Low Lift while HL for High Lift. The weighting percentages (laminar – turbulent) are also shown in the legend

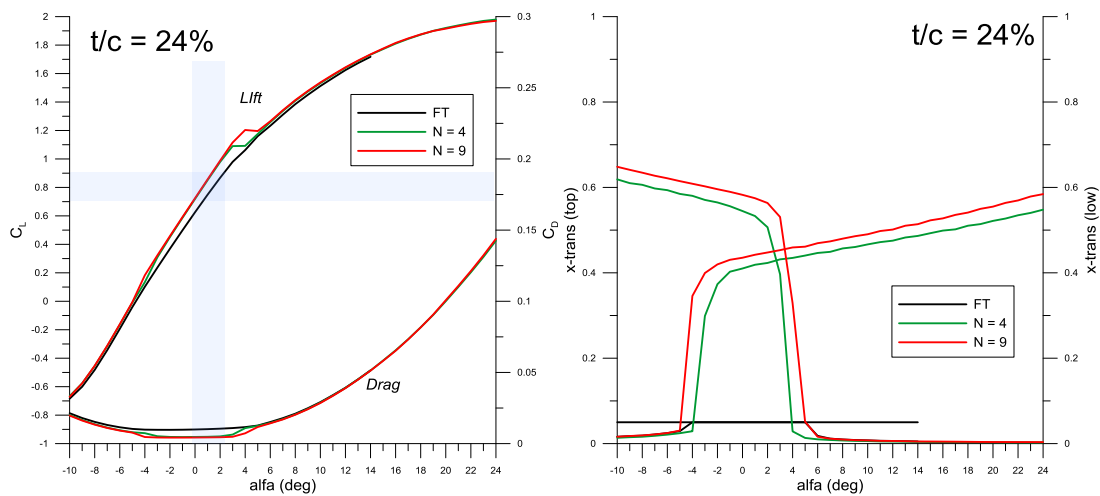


Figure 4.4-8: Lift and drag (left) versus angle of attach 'alfa' for the 24% LL 10-90 airfoil. XFOIL calculations have been performed for three different transition settings, fully turbulent, N=4 and N=9. The transition location along the airfoil suction and pressure side for different 'alfa' is shown in the right figure

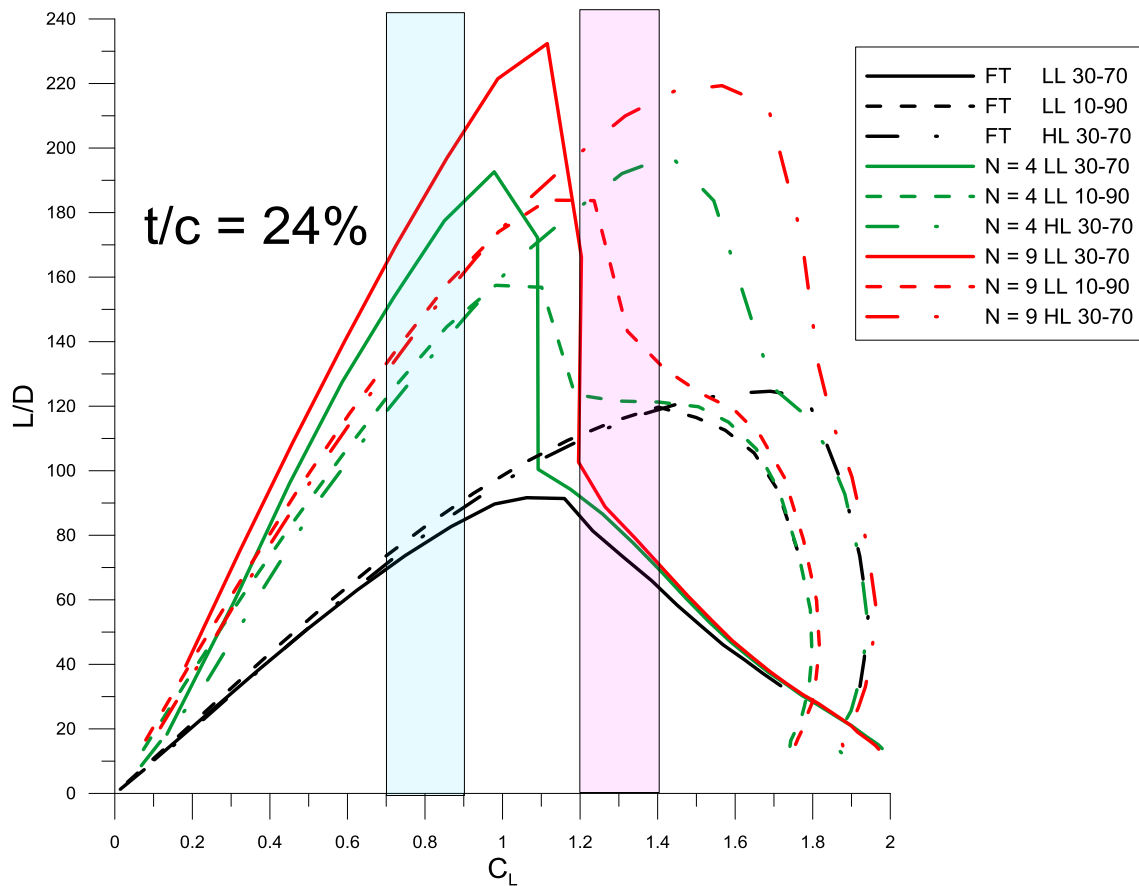


Figure 4.4-9: Performance (L/D) of the three 24% airfoils for the three different transition settings considered

Figure 4.4-7, Figure 4.4-8 and Figure 4.4-9 present shape, polars and performance curves for the 24% profiles. The remarks are quite similar with those made for the earlier members of the three airfoil families.

#### 4.4.4 30% thick airfoils

Similar results are obtained for the 30% thick airfoils and presented in Figure 4.4-10, Figure 4.4-11 and Figure 4.4-12. Note that in the 30% case we preferred to work with 20-80 laminar to turbulent weighting instead of 10-90 since the latter, as the airfoil thickness increases, is moving the maximum thickness location too far upstream. In this case we have included in the figures the polar of the high lift airfoil (for N=4 only) for comparison with the low-lift 20-80. Note also that the laminar pocket of the 30% profiles is wider than that of the thinner designs (actually the width of the laminar pocket is increasing with the airfoil thickness) and that the fully turbulence performance of the 30% airfoils has now dropped to 70 units.

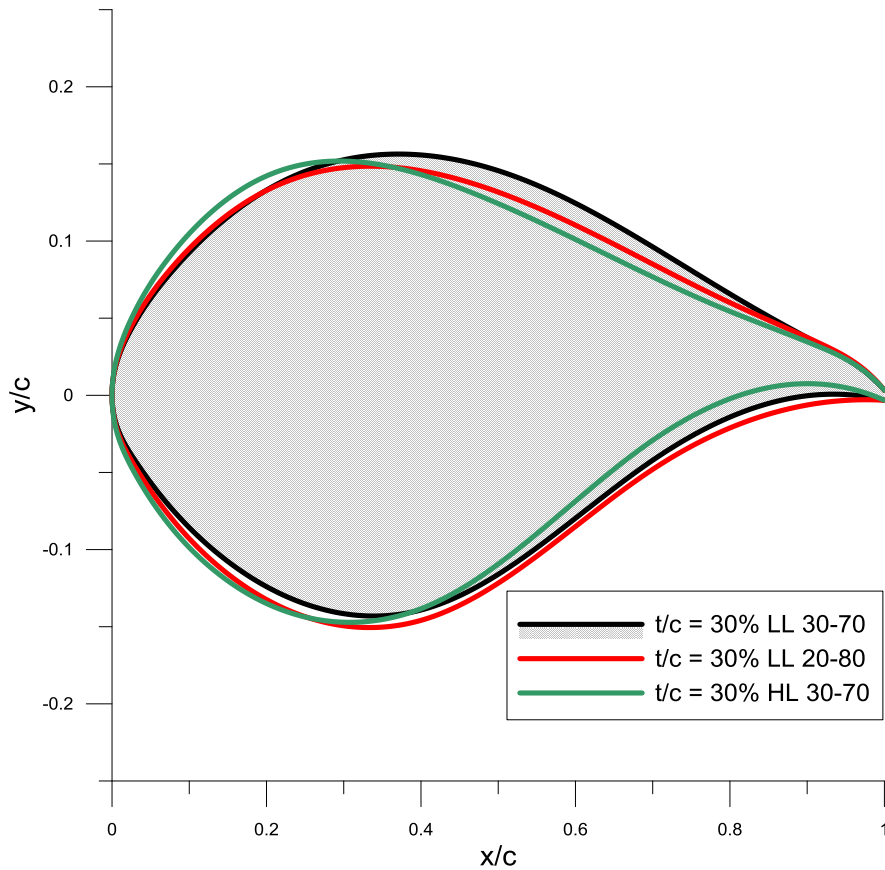


Figure 4.4-10: Three airfoil designs of 30% thickness. LL stands for Low Lift while HL for High Lift. The weighting percentages (laminar – turbulent) are also shown in the legend

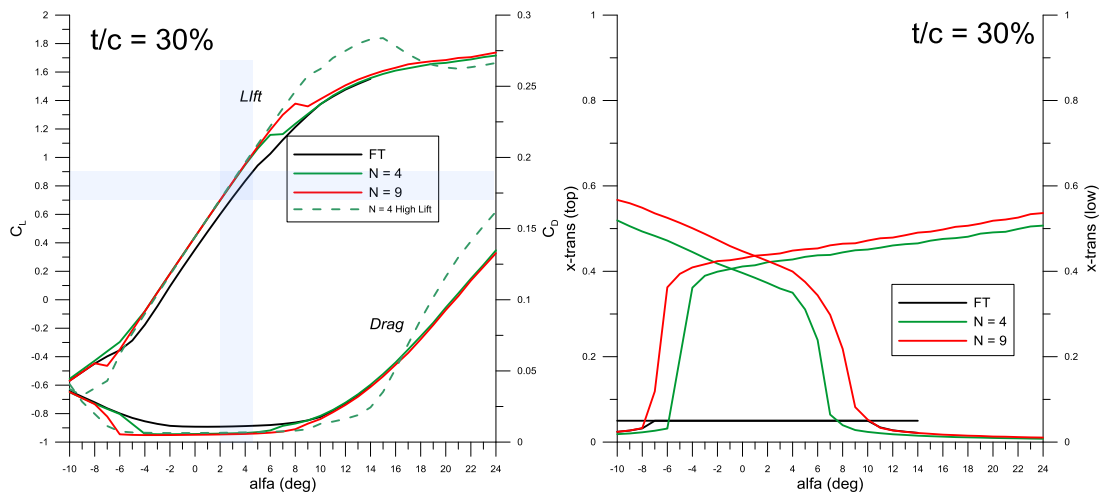


Figure 4.4-11: Lift and drag (left) versus angle of attach 'alfa' for the 30% LL 20-80 airfoil. XFOIL calculations have been performed for three different transition settings, fully turbulent, N=4 and N=9. The transition location along the airfoil suction and pressure side for different 'alfa' is shown in the right figure

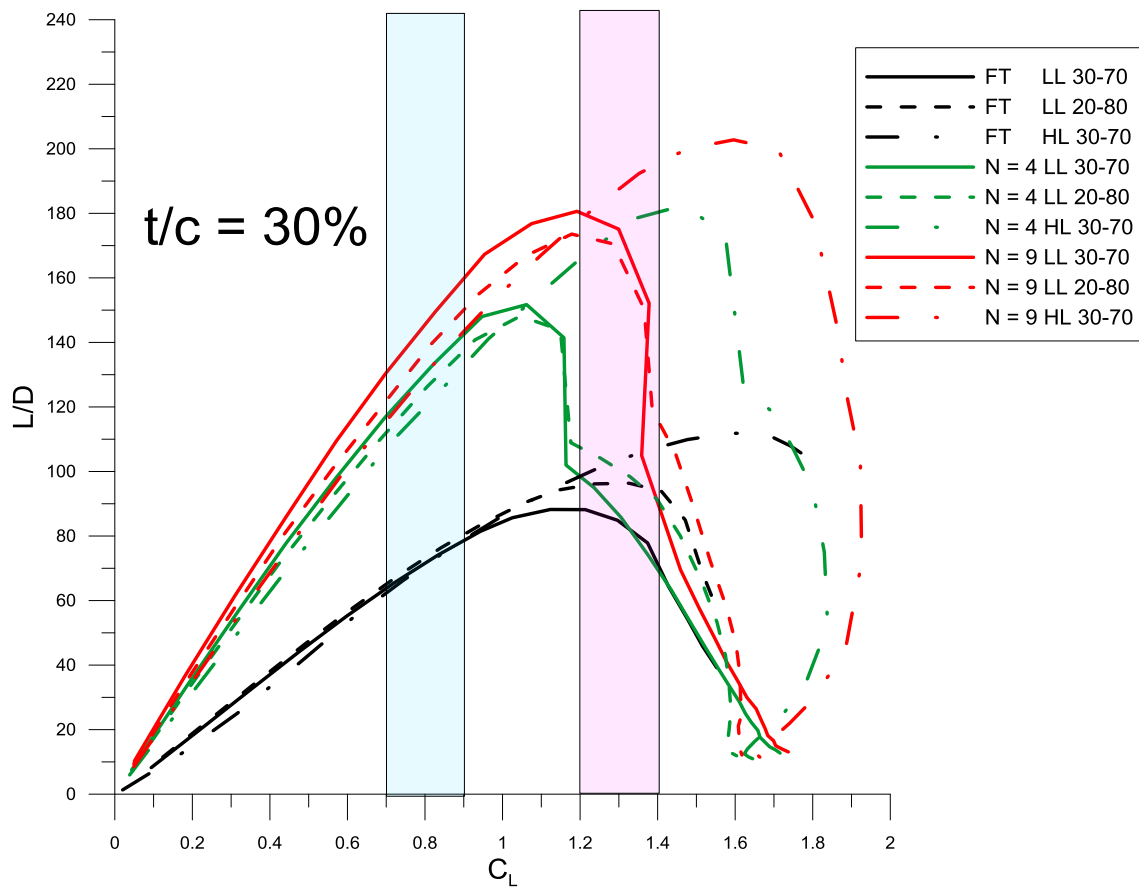


Figure 4.4-12: Performance (L/D) of the three 30% airfoils for the three different transition settings considered

#### 4.4.5 40% thick airfoil

Lastly, we present in Figure 4.4-13, Figure 4.4-14 and Figure 4.4-15 shape, polar and performance results for the single 40% profile designed for low-lift conditions with weights 20-80. As expected the airfoil performance is pretty low now because of the increased thickness. An extra remark is that the transition point location in the design regime is not exceeding any more the 20% chord where the maximum thickness of the profile occurs. In any case, these results are characterized by high uncertainty due to excessive thickness of the airfoil which is beyond the modelling capabilities of XFOIL.

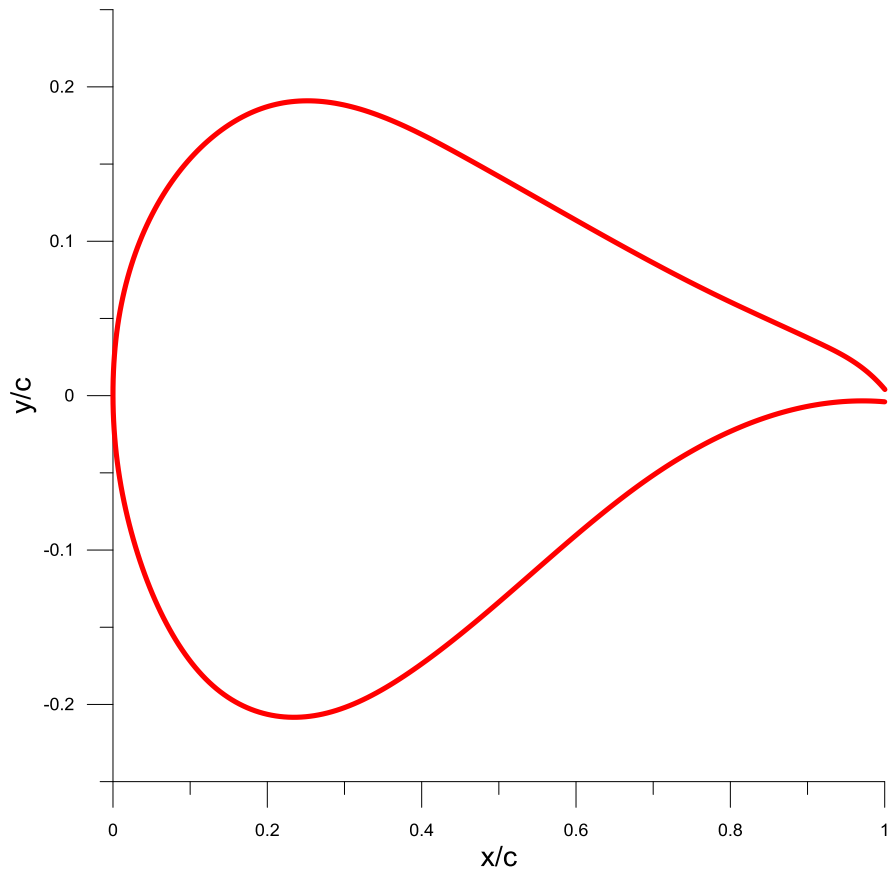


Figure 4.4-13: LL 20-80 airfoil designs of 40% thickness.

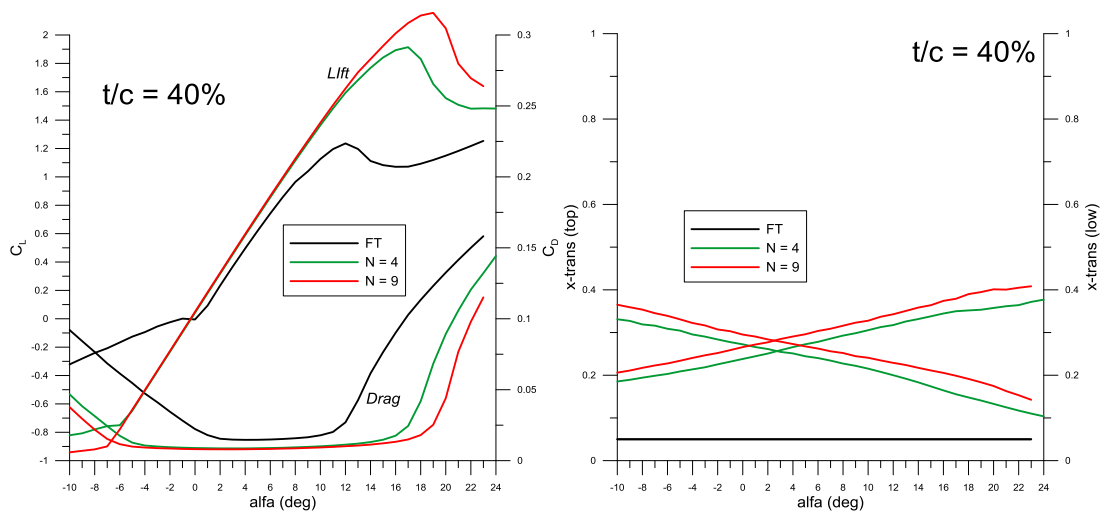


Figure 4.4-14: Lift and drag (left) versus angle of attach 'alfa' for the 40% LL 20-80airfoil. XFOIL calculations have been performed for three different transition settings, fully turbulent, N=4 and N=9. The transition location along the airfoil suction and pressure side for different 'alfa' is shown in the right figure

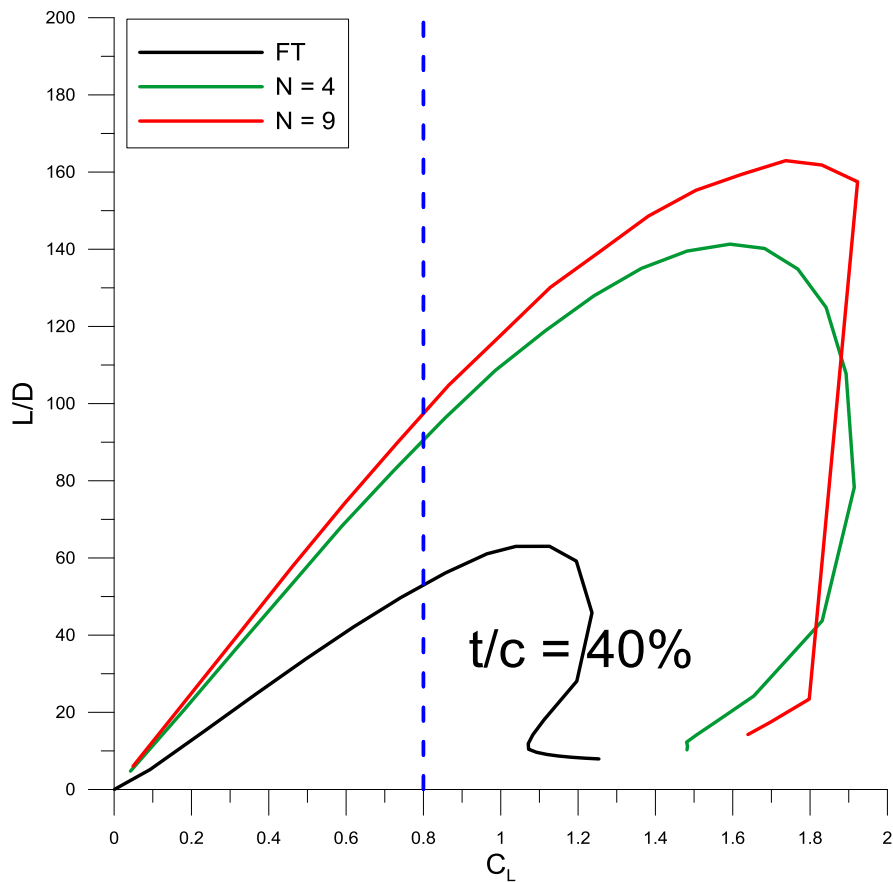


Figure 4.4-15: Performance (L/D) of the three 40% airfoils for the three different transition settings considered

#### 4.4.6 Inter-family comparisons

Figure 4.4-16 presents the two families of low lift profiles designed in this work. At the left we see the 30-70 family comprising airfoils of 18% to 30% thickness and at the right the 10-90/20-80 family which is more complete, having two additional members with 15% and 40% thickness.

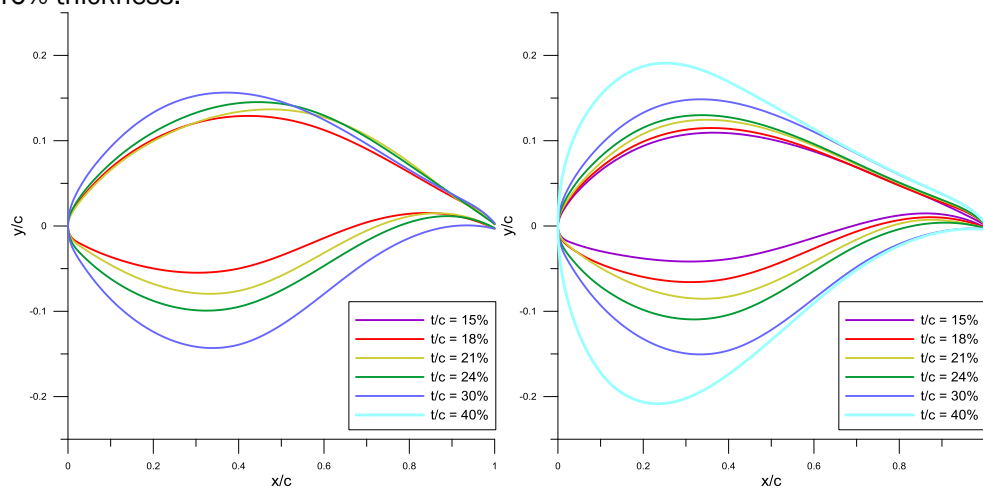


Figure 4.4-16: The family of Low Lift profiles. Left the 30-70 and right the 10-90/20-80 designs

Figure 4.4-17 shows the aerodynamic performance of the two families at fully turbulent flow conditions. Clearly the 30-70 is performing slightly worse than the “more conservative” 10-90/20-80 one. In all cases, with the exception of the 40% airfoil, L/D at the design lift coefficient exceeds 70 units even for the 30% thick profile.

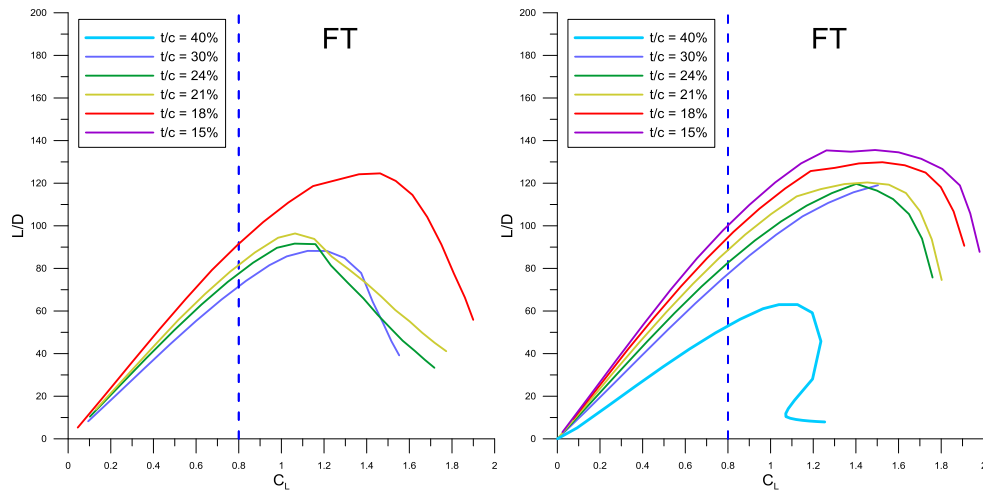


Figure 4.4-17: Performance (L/D) of the Low Lift family profiles at fully turbulent flow conditions. Left the 30-70 and right the 1(2)0-9(8)0 designs

On the contrary, the 30-70 family is performing better (some members like the 21% and 24% much better) than the 10-90 one when the flow is transitional. Figure 4.4-18 demonstrates the statement with calculation done for N-factor equal to 4. It is also seen that in all cases (with the exception of the 40% profile) the performance of the airfoils exceeds 120 units, even at 30% thickness.

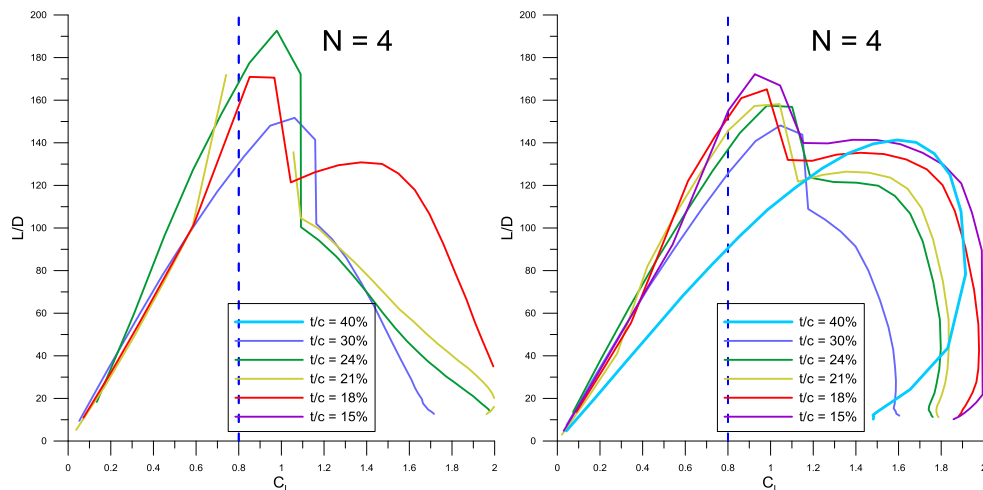


Figure 4.4-18: Performance (L/D) of the Low Lift family profiles for N=4. Left the 30-70 and right the 1(2)0-9(8)0 designs

#### 4.5 Synthesis and conclusions

CRES produced low-lift profiles with relative thicknesses 15%, 18%, 21%, 24%, 30% and 40%. The low lift family is intended for operation on low induction rotors where design lift is moderate.

Two low-lift and one high-lift profile family was designed, the last for comparison purposes. The low-lift families differ in the laminar / turbulent weighting which is driving the design. Using a higher weight for the laminar part the maximum thickness of the profile is moving backwards and its performance around the design point is increasing but at the same time worsens when the profile operates at fully turbulent conditions. In the present case the weighting was set to 30%-70% for one of the low lift and the high lift family. 10-90 (or 20-80) were the weights for the second low lift family.

The 10-90/20-80 family looks more consistent, both geometrically (location of maximum thickness) and performance wise (changing monotonically with the thickness), than the 30-70 one. For these reasons and for introducing some conservatism to the possible energy capture gains of the low induction rotor we suggest using this family for the PI evaluation of the low induction rotors.

## CHAPTER 5 NUMERICAL SIMULATION OF LOW LIFT AND ELLIPTICALLY SHAPED AIRFOILS DESIGNED BY CRES AND WINDTUNNEL MEASUREMENTS ON AIRFOILS WITH DRAG REDUCTION DEVICES - NTUA

*J Prospathopoulos, M Manolesos, S Voutsinas, P Chaviaropoulos*

### 5.1 Scope and objectives

NTUA's contribution consists of investigating the performance of some of the innovative airfoil concepts considered. This investigation includes: the assessment of elliptical shaped airfoils, performance analysis of the low induction airfoils CRES designed using CFD and the conduction of wind tunnel tests for one low induction airfoil both in its sharp TE form and in a flat back version with and without flaps in various configurations.

### 5.2 Computational tools and simulations details

#### 5.2.1 Navier Stokes solver MaPFlow

MaPFlow[24] is a multi-block MPI enabled compressible solver equipped with preconditioning in regions of low Mach flow. The discretization scheme is cell centered and makes use of the Roe approximate Riemann solver for the convective fluxes. In space the scheme is 2<sup>nd</sup> order accurate defined for unstructured grids and applies the Venkatakrishnan's limiter [25]. In time the scheme is also 2<sup>nd</sup> order and implicit introducing dual time stepping for facilitating convergence. The solver is equipped with the Spalart-Allmaras (SA) and the k- $\omega$  SST eddy viscosity turbulence models.

Regarding transition, two models have been implemented, the correlation  $\gamma$ - $Re_{\theta}$  model of Menter [26] and the Granville/Schlichting transition method described in [27]. The first one is a two transport equation model for the intermittency and the momentum thickness Reynolds number. It utilizes local variables easily computed in each cell and does not need boundary layer definition and parameters. The second one is based on boundary layer characteristics expressed in terms of the Polhausen variables. In order to estimate these variables, the velocity on the edge of the boundary layer is computed using the pressure coefficient value on the viscous wall derived by the RANS solver. The instability and transition points are then defined using empirically calibrated diagrams proposed by Granville.

Simulations have shown that the Granville/Schlichting method predicts more accurately the transition locations than the  $\gamma$ - $Re_{\theta}$  model for high Reynolds numbers ( $Re > 10^6$ ), therefore it is adopted for the simulation of the CRES LL airfoils. For the fully turbulent simulations, the k- $\omega$  SST model is used.

The numerical mesh is an O-type grid with 104000 elements, 520 around the airfoil and 200 in the normal to the wall direction, generated using the ICMCFD ANSYS software. The non-dimensional distance of the first node from the wall is less or equal to  $10^{-5}$ , resulting in  $y^+ < 1$ . Steady state simulations are performed for the whole AOA range.

### 5.2.2 Viscous-inviscid interaction solver Foil2w

Foil2W [28] is a viscous-inviscid interaction code developed at NTUA. The potential flow part is simulated by singularity distributions along the airfoil geometry and the wake. The wake is represented by vortex particles which are allowed to freely move with the local flow velocity. The viscous flow solution is obtained by solving the unsteady integral boundary layer equations. The coupling of the two sets of equations is achieved through a transpiration velocity distribution along the airfoil surface that represents the mass flow difference over the boundary layer height between the real viscous flow and the equivalent inviscid flow.

The boundary layer equations are discretized using finite differences and the final set of the non-linear equations are solved simultaneously using the Newton-Raphson algorithm. The boundary layer solution is supplemented by a transition prediction model based on the  $e^N$  spatial amplification theory and by a dissipation closure equation for the maximum shear stress coefficient over the turbulent part.

For the CRES LL simulations, the original blunt airfoil profiles are made sharp using the Xfoil tool and discretized with a number of 140 panels. The exponent of the transition model  $e^N$  is set to  $N=4$  as a more conservative choice in terms of performance.

### 5.3 Performance of elliptically shaped airfoils

This section concerns the assessment of elliptically shaped airfoils. Such forms give the opportunity to apply fast manufacturing and have higher structural properties. At high thicknesses they are suitable for installation in the root region of the blade instead of flat-back airfoils while at larger radial stations they could substitute conventional airfoils by equipping them with extendable flaps or other devices and sets up of the kind presented in 5.5. This explains the reason of here considering medium values of relative thicknesses.

The design of the elliptic versions of an airfoil is based on the following principles:

- Maximum thickness should remain the same as the baseline airfoil
- The elliptic part of the trailing edge should be almost equal to half the maximum thickness of the airfoil.
- Resulting airfoils should have chord length equal to 1 ( $c=1$ ), in order to be directly comparable to their original shape.

An example of such an airfoil that originates from the NTUA-25% airfoil is given in Figure 5.3-1. As with flat-back shapes, the thickness is kept over most of the chord length, which leads to higher lift. However, the efficiency drops because the drag is also increased. One way of retrieving part of the losses is to smoothen the shape at the back.

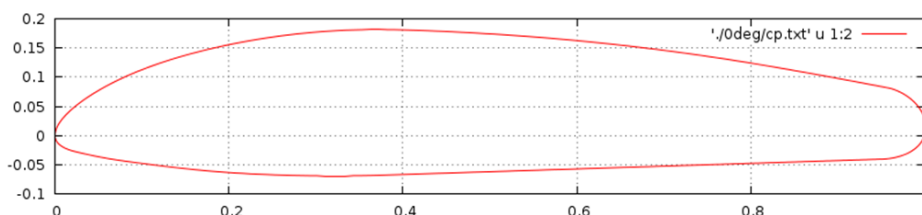


Figure 5.3-1: NTUA-25% elliptic airfoil

### 5.3.1 Results and discussion

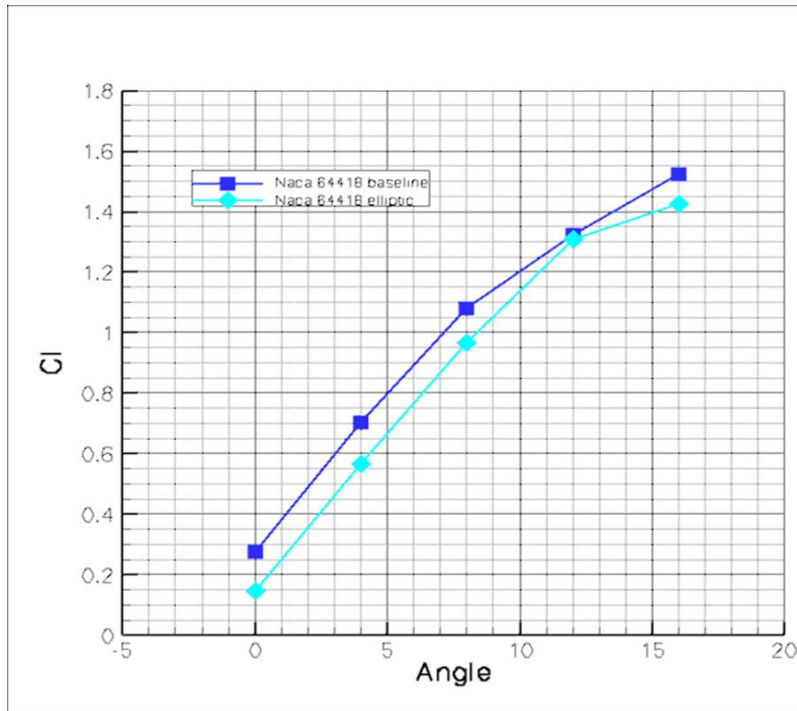
The computations are conducted using the  $k-\omega$ SST turbulence model. All cases have the following characteristics:

- Fully Turbulent airflow
- $Re=10^6$
- $Mach=0.1$

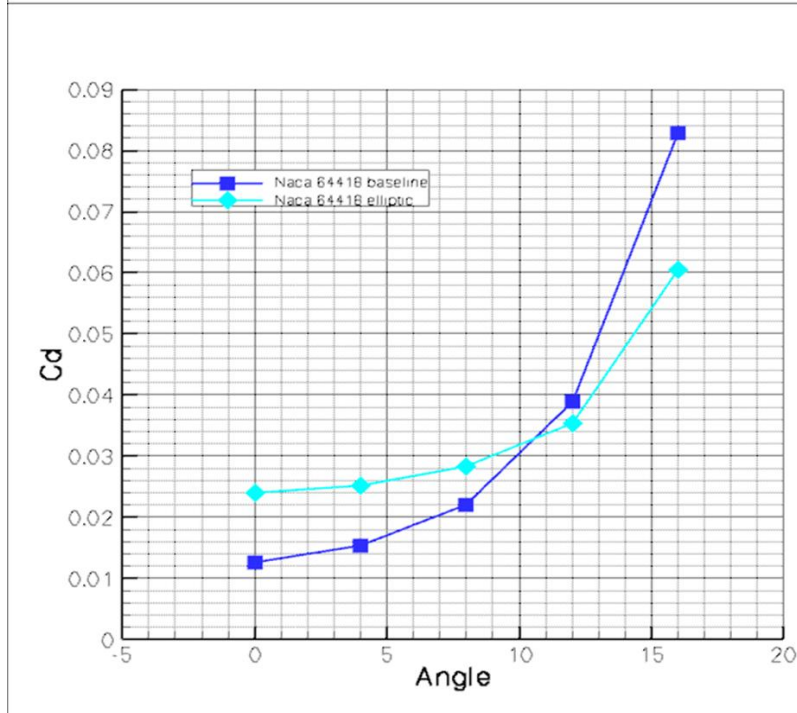
Up to a certain angle of attack steady CFD computations are possible while at higher angles unsteady simulations are performed. Three examples are considered: the NTUA-18% ,25% and the NACA64418.

The comparison of the obtained polars for the NACA64418 is given in Figure 5.3-2. As expected the elliptically shaped airfoil has lower lift and higher drag at low angles of attack so its efficiency drops.

However as depicted in the efficiency plots shown in Figure 5.3-3, as the angle of attack increases, the trend reverses. Also the characteristics of the wake indicate the formation of elongated shear regions that are more quickly diffused (Figure 5.3-4)



Angle	Amplitude
0	0.01473
4	0.01190
8	0.00659
12	0.00093
16	0.04468



Angle	Amplitude
0	0.00162
4	0.00348
8	0.00418
12	0.00133
16	0.01841

Figure 5.3-2 Lift and drag curves for the NACA64418

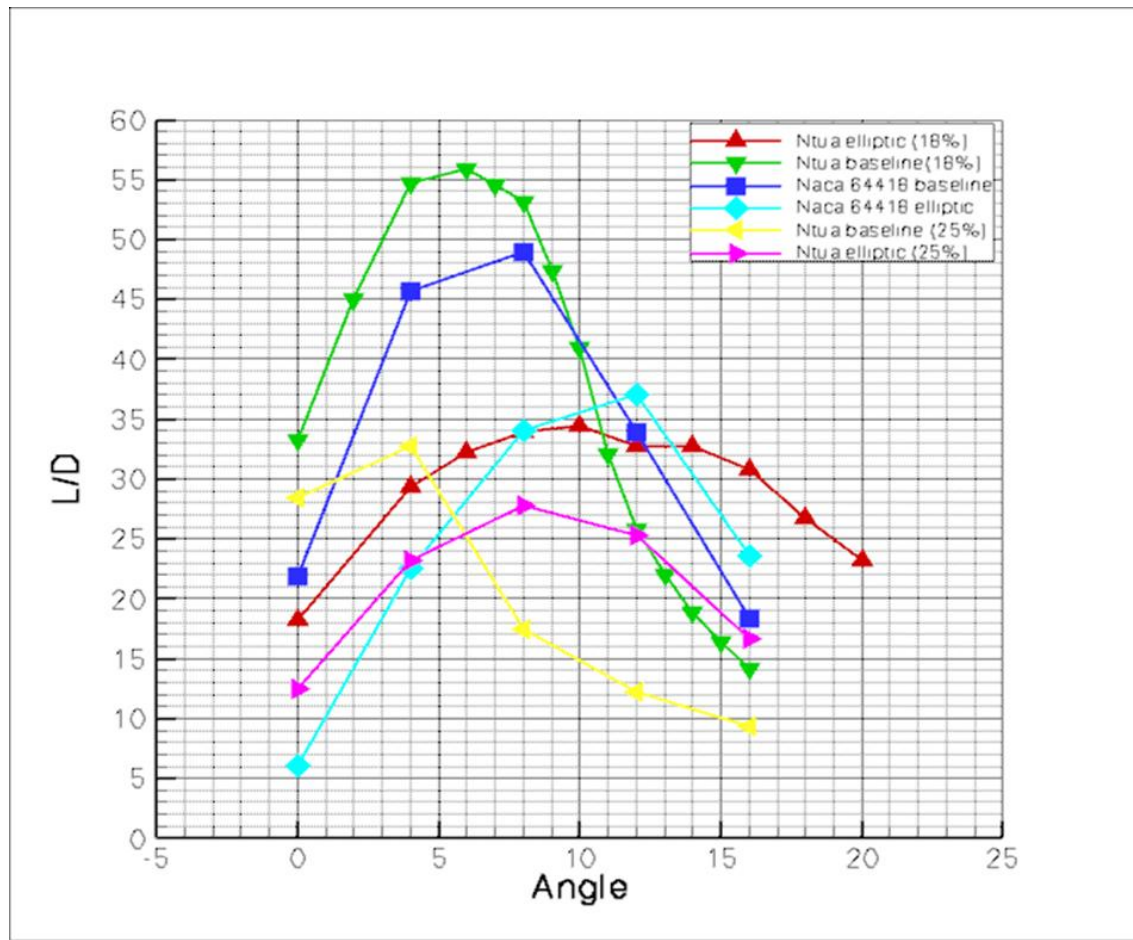
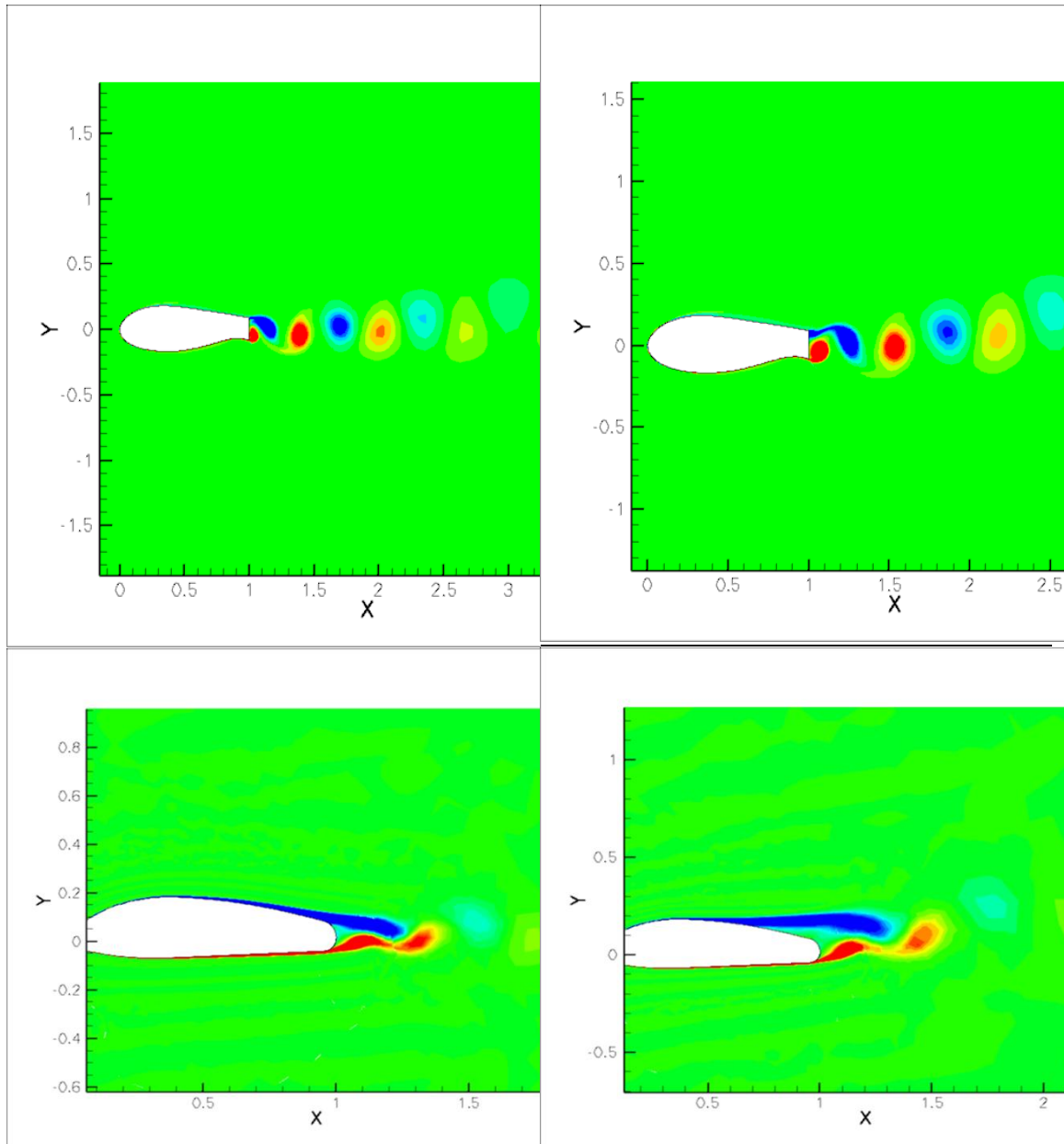


Figure 5.3-3: Comparison of efficiency plots from all the cases considered



8 degrees

16 degrees

Figure 5.3-4: Snapshots indicating the wake development at two angles of attack. Compared to a sharp edged flat back airfoil, instead of well-formed vortex structures, elongated regions of shear are formed that are attenuated quickly.

## 5.4 Performance of CRES' LL 10-90 profiles

The performance of the 10-90/20-80 choice designed by CRES is further evaluated with the MaPFlow compressible Navier-Stokes solver and the Foil2w viscous-inviscid interaction solver. Both MaPFlow and Foil2w simulations are performed at fully turbulent and fixed transition flow conditions using the transition locations predicted by XFOIL. Furthermore, MaPFlow simulations are performed for free transitional flow using the Schlichting-Polhausen transition model.

### 5.4.1 18% thick airfoil

In Figure 5.4-1, the performance (L/D) results for the 18% are presented. At transitional flow conditions, all models predict considerably high values around the design point  $C_{LDES}=0.8$ , ranging between 135 and 150. MaPFlow predictions using the Schlichting-Polhausen transition model seem to be the most conservative ones, predicting the lowest performance. At fully turbulent flow conditions, a lower performance around the design point  $C_{LDES}=0.8$  is expected. Indeed, performance reduces considerably ranging between 85 and 95, but still remains at high levels. It must be noted that there is a significant divergence among the predictions of the different models in the range  $0.8 < C_L < 1.4$  which corresponds to the linear region ( $2^\circ < AOA < 8^\circ$ ). This suggests that a different slope of the  $C_L$ -AOA curve is predicted in that region.

### 5.4.2 21% thick airfoil

As the thickness of the airfoil is increased from 18% to 21%, the XFOIL and the Foil2w codes predict a performance reduction close to 4% at the design point  $C_{LDES}=0.8$ . The MaPFlow CFD code predicts a smaller reduction of almost 2%. This results in smaller differences among the predictions of the models, as shown in Figure 5.4-2.

### 5.4.3 24% thick airfoil

Performance continues to decrease reaching a value between 125 and 135 for transition conditions, whereas, for fully turbulent conditions, the performance reduces to 70-80 (Figure 5.4-3). Similar observations with the 18% and 21% airfoils can be made.

### 5.4.4 30% thick airfoil

Figure 5.4-4 presents the performance predictions for the thickest of the airfoils, the 30% 20-80 airfoil. As thickness increases from 18% to 30%, the total reduction in performance at the design point reaches a percentage between 16% and 21% for transition conditions and a percentage between 23% and 25% for fully turbulent conditions. However, the performance levels remain greater than 100 for transitional conditions, indicating the high efficiency of the LL airfoil family designed by CRES.

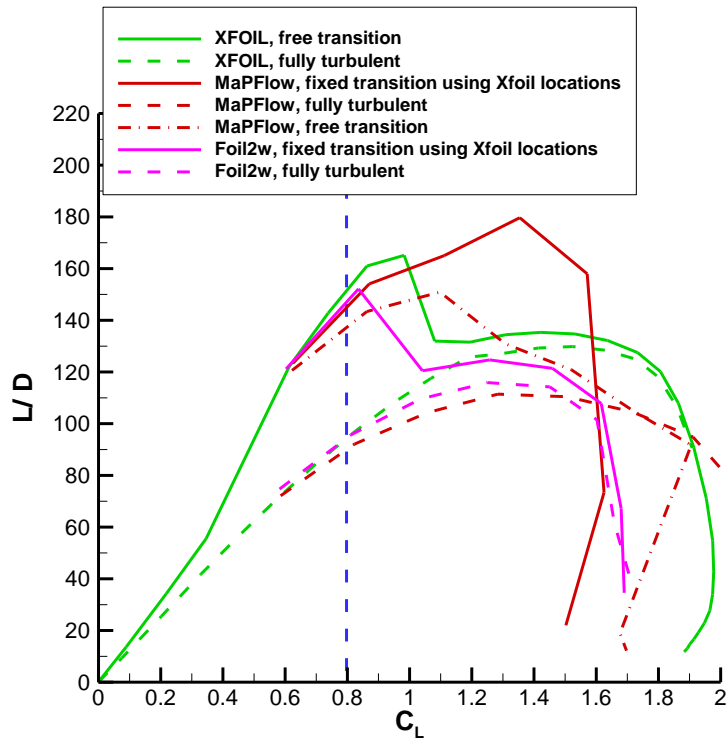


Figure 5.4-1: Performance (L/D) of the 18% LL 10-90 airfoil for transitional and fully turbulent flow conditions. Comparison among MaPFlow (CFD solver), Foil2w (viscous-inviscid interaction solver) and XFOIL calculations. Fixed transition locations were taken from XFOIL using the  $e^N$  model with  $N=4$

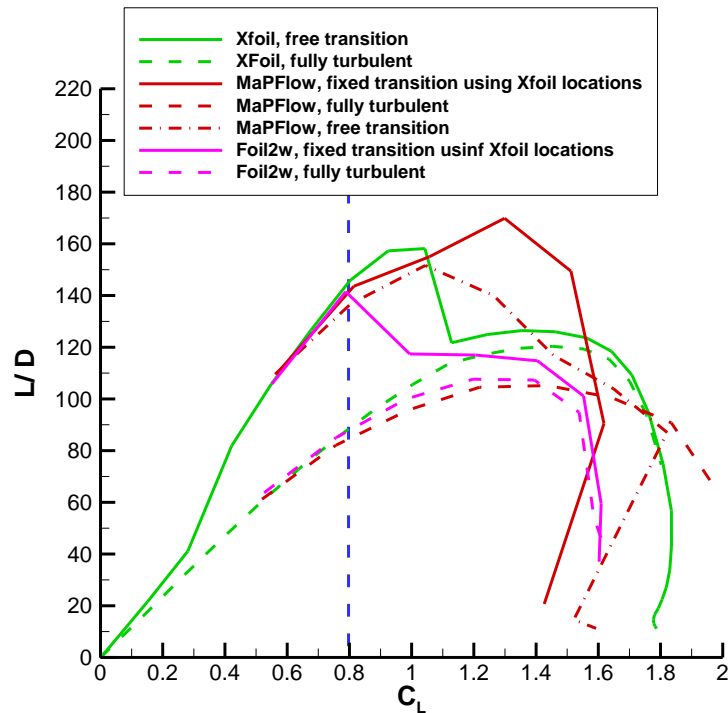


Figure 5.4-2: Performance (L/D) of the 21% LL 10-90 airfoil for transitional and fully turbulent flow conditions. Comparison among MaPFlow (CFD solver), Foil2w (viscous-inviscid interaction solver) and XFOIL calculations. Fixed transition locations were taken from XFOIL using the  $e^N$  model with  $N=4$

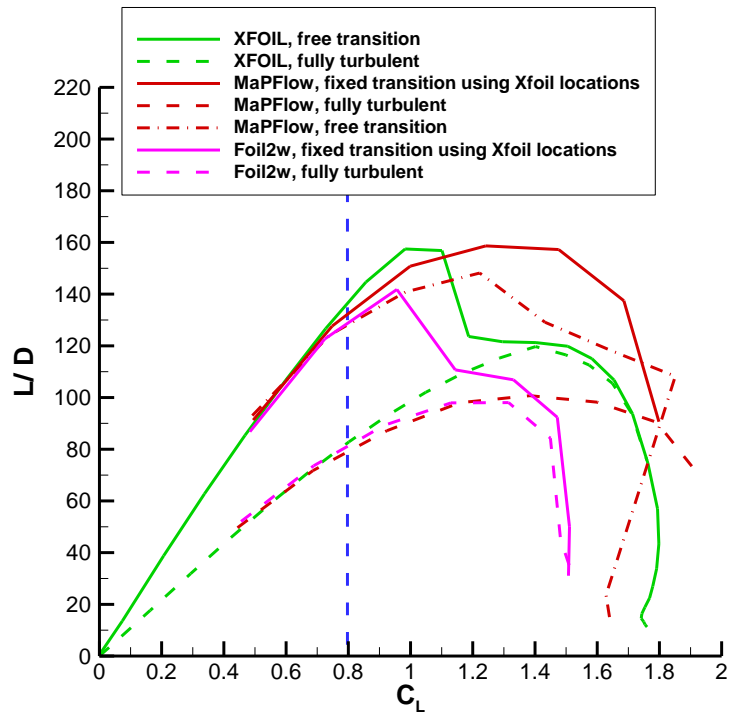


Figure 5.4-3: Performance (L/D) of the 24% LL 10-90 airfoil for transitional and fully turbulent flow conditions. Comparison among MaPFlow (CFD solver), Foil2w (viscous-inviscid interaction solver) and XFOIL calculations. Fixed transition locations were taken from XFOIL using the  $e^N$  model with  $N=4$

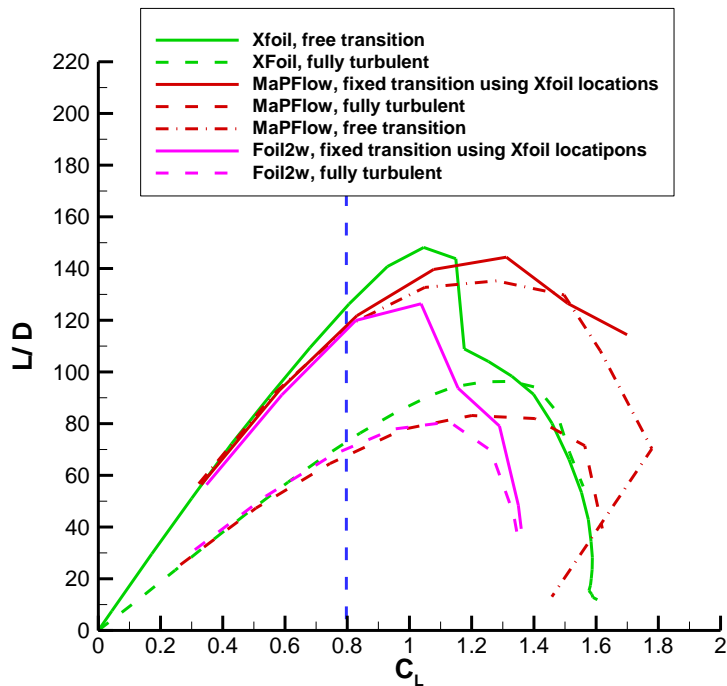


Figure 5.4-4: Performance (L/D) of the 30% LL 20-80 airfoil for transitional and fully turbulent flow conditions. Comparison among MaPFlow (CFD solver), Foil2w (viscous-inviscid interaction solver) and XFOIL calculations. Fixed transition locations were taken from XFOIL using the  $e^N$  model with  $N=4$

## 5.5 Wind tunnel measurements for the 30% profile

### 5.5.1 Description of the experimental set-up

#### *Airfoil models*

The baseline model was an earlier version, referred as LI30, of the 30% thick low induction 30-70 profile designed by CRES. This profile version was used because the experiments had to be scheduled and the models had to be manufactured and instrumented well before the final airfoil designs presented in the earlier sections.

Based on the thin TE profile a profile with the same overall thickness and a ~10% thick TE was designed (LI30-FB10, see Figure 5.5-1). The profile was generated by adding thickness to the thin TE airfoil camber line gradually from  $x/c=0.4$  so that at the TE the added thickness is  $0.1c$ .

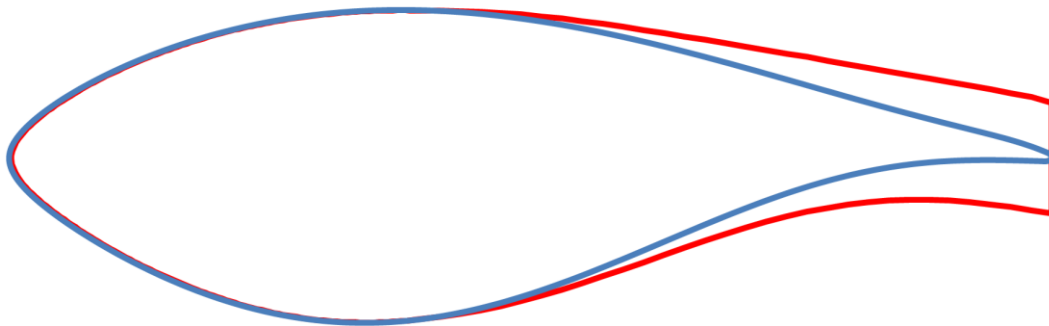


Figure 5.5-1: The LI30 and the LI30-FB10 airfoil profiles

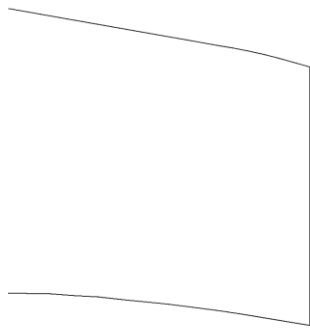
#### *Drag Reduction Devices*

The performance of various drag reduction devices was examined on the LI30-FB10 airfoil. The devices were separated in two groups. The first group consisted of three devices commonly used for such purposes (Splitter plate, Cavity and Offset Cavity), a variation of the Cavity (Extended Cavity) and a new Flap device, all shown in Figure 5.5-2. The Extended Cavity is similar to the Cavity, but the plates are neither parallel to the airfoil chord nor to each other, as they follow the curvature of the airfoil sides at the TE. The second group of devices is shown in Figure 5.5-3 and consisted of combinations of the Flap with the Splitter plate and the lower part of the Cavity, Offset Cavity and Extended Cavity. All results concerning the drag reduction devices concern a clean airfoil, i.e. no tripping was applied.

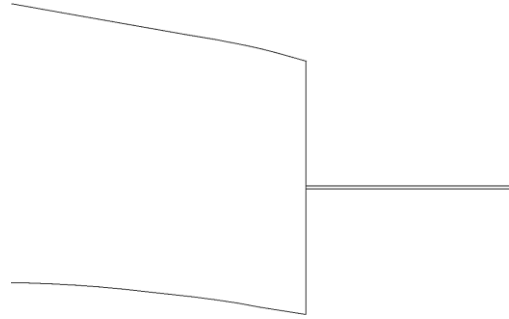
The Flap is a flat plate located at  $20^\circ$  with respect to the airfoil chord. Unlike usual TE airfoil flaps, where the flap top side is fed with high speed flow from the airfoil lower side,

in the present case the lower flap side is fed by the flow from the top airfoil side. To the best of the authors' knowledge such a device has not been previously tested on FB airfoils.

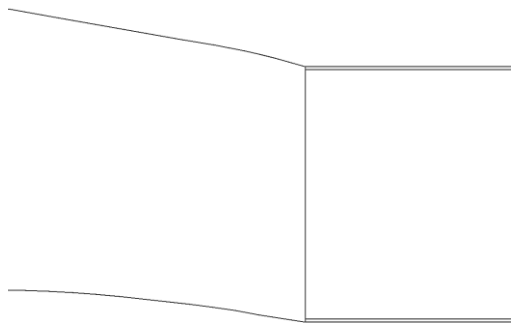
All devices were constructed by 2mm thick aluminum sheet and their span was equal to the wing span. The Splitter, Cavity, Offset Cavity and Extended Cavity were 43mm long (or  $0.81h$ , where  $h = 53\text{mm}$  is the TE height). The Flap was 33mm long or  $0.62h$ , its TE being at 40mm downstream of the airfoil TE. In the wind tunnel model the Flap was based on rods that were bolted on the wing model TE every 20cm. The drag was measured at the centre of the wing span and between two consecutive rods to avoid any interference. A drawing of the wing model with the Flap + Splitter device is given in Figure 5.5-4, where one of the rods can be seen.



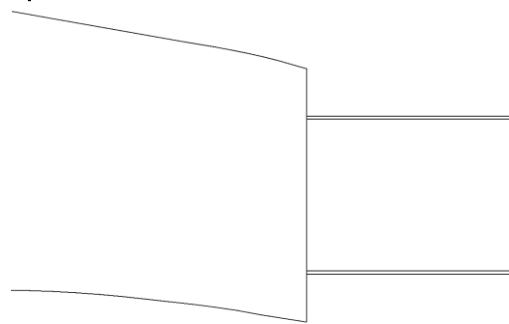
Plane airfoil



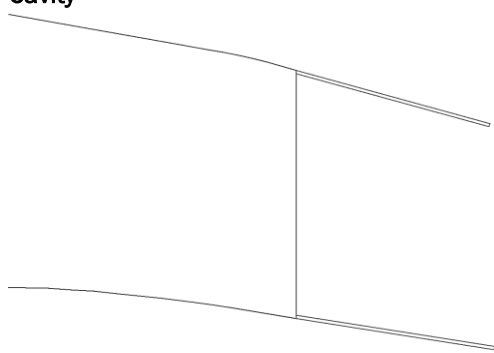
Splitter



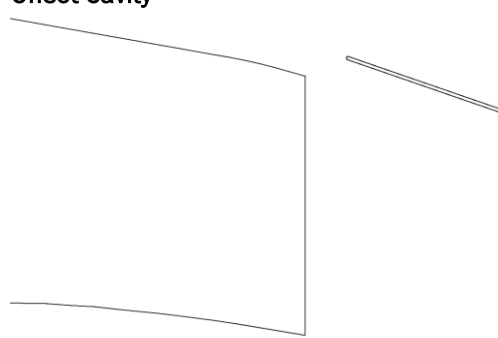
Cavity



Offset Cavity

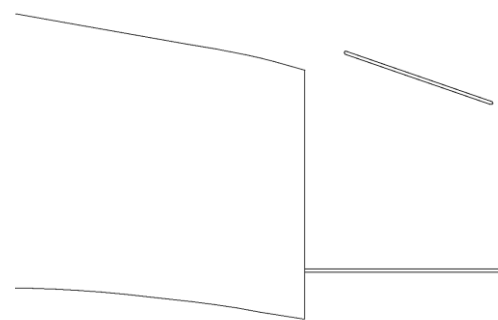
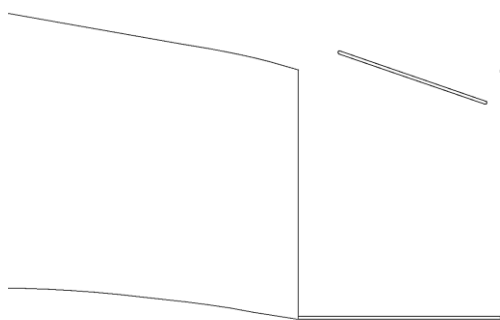


Extended Cavity



Flap

Figure 5.5-2: Detail of the FB airfoil TE. 1<sup>st</sup> group of Drag Reduction Devices



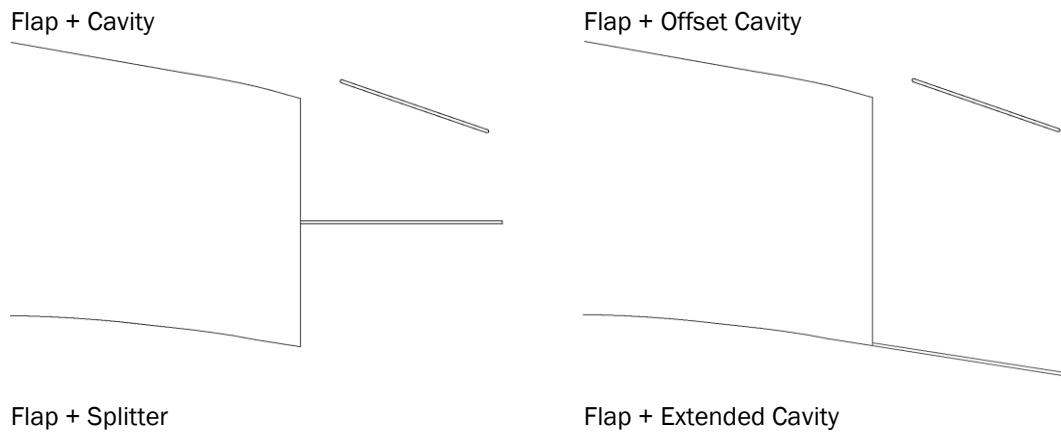


Figure 5.5-3: Detail of the FB airfoil TE. 2<sup>nd</sup> group of Drag Reduction Devices

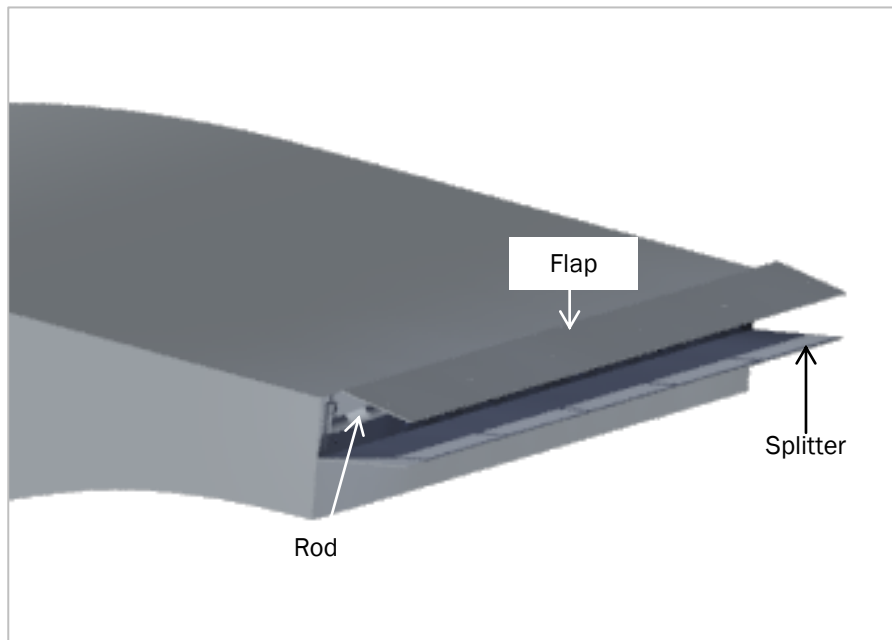


Figure 5.5-4: Drawing of the wing model with Flap + Splitter device

### Wind Tunnel

All experiments were performed at the small test section (1.4m×1.8m, height × width) of the National Technical University of Athens (NTUA) wind tunnel, where the turbulence intensity is  $\leq 0.2\%$ . A schematic view of the test set up is given in Figure. The wing models spanned the test section vertically and fences were used in order to minimize the effect of the wind tunnel wall boundary layer. The models had a chord of  $c = 0.5\text{m}$  and the fences were 1m apart, setting the wing AR to 2.0. All experiments were performed at  $Re = 1.5e6$ .

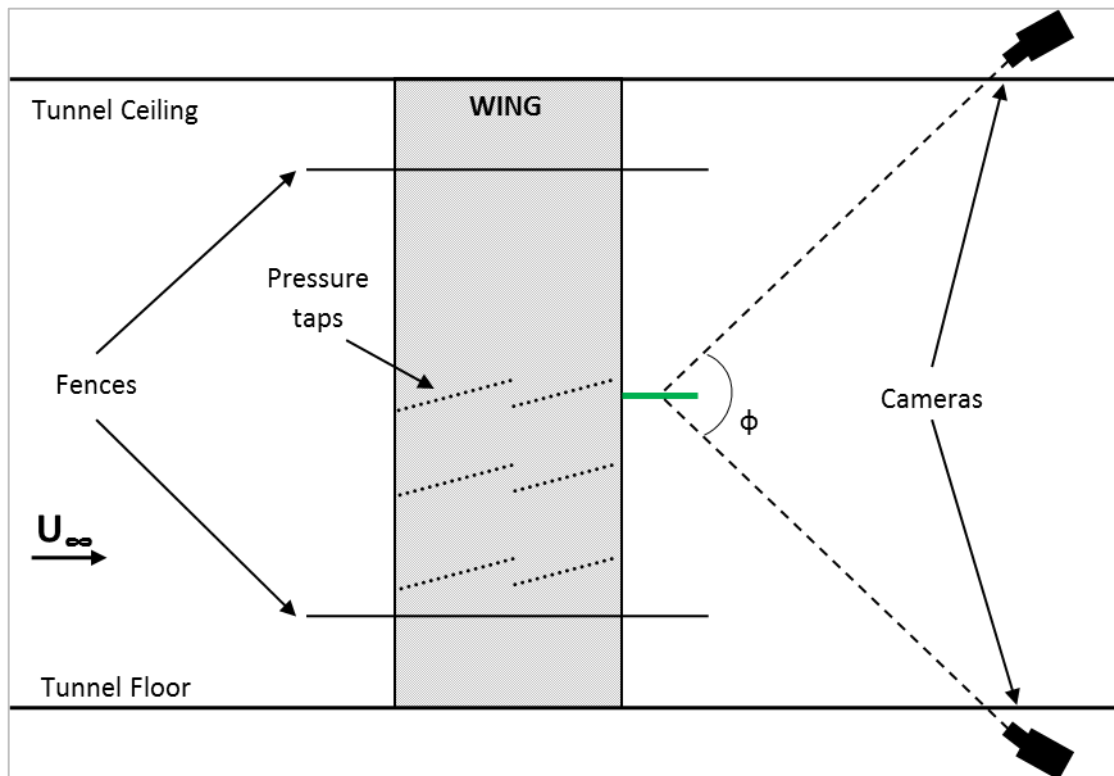


Figure 5.5-5: Schematic planform view of the test setup showing the wing, the fences, the pressure and the Stereo PIV cameras along with the measurement plane and the camera contained angle ( $\phi$ ) is also indicated.

### Pressure Measurements

The wing model was equipped with three chordwise sets of pressure taps, at different spanwise locations. Data reported here concern the measurements from the taps located at the centre of the wing span. In total 62 pressure taps were used, four of which were located at the wing TE. In addition, a wake rake was used to record the pressure. The rake consisted of 55 total pressure tubes and five static pressure tubes. It was positioned 1.8c downstream of the wing TE and could move both in the spanwise direction and in the direction normal to the wing span. Four 32-channel MicroDaq Pressure Scanners (manufactured by Chell Instruments) were used to obtain 30" long measurements at 40Hz and 50Hz.

The lift and pressure drag coefficients were computed from the pressure distribution around the airfoil. The wake rake drag coefficient was computed from the wake pressure distribution according to [29]. The reported drag coefficient value is always the larger of the two. Standard wind tunnel corrections were applied to the measured data, also according to [29].

### Tripping tape

Zigzag (ZZ) tape was used to trip the flow on both sides of the airfoils for the fully tripped cases. For the LI30 airfoil the ZZ tape was 0.1mm high and it was located at 5% chord on both sides of the airfoil. For the LI30-FB10 airfoil the ZZ tape was 0.08mm high and it was located at 3% chord on both sides of the airfoil.

### ***Stereo PIV Measurements***

The flatback airfoil and the four best performing drag reduction configurations were examined using Stereo PIV. All measurements concern a plane normal to the wing axis at the centre of its span, see Figure 5.5-5. The cameras were located above and below the test section, 85cm or 1.7c downstream of the wing TE. All Stereo PIV measurements were taken with the wing at  $\alpha = -0.6^\circ$  and at  $Re = 1.5e6$ . For each case 1000 snapshots were taken and the results presented here are the averaged data.

A 200mJ Nd:YAG PIV laser (Litron Lasers) with dual cavities was used to create a 1.8mm thick light sheet at the measurement plane. The flow was seeded with oil droplets of 1 $\mu$ m mean diameter created by a commercial generator (TSI model 9307). Two 12-bit TSI Powerview Plus™ 4MP Cameras with Sigma 150mm f/2.8 lenses were used to obtain the data. The camera contained angle ( $\phi$  in Figure 5.5-5) was  $\phi \approx 88^\circ$ .

The pulse separation time was set to 8  $\mu$ sec was used as higher values would increase the measurement noise and make peak detection harder. For all planes the number of spurious vectors was always below 5% and spurious vectors were replaced using a 3 $\times$  3 local mean. The particle displacement was in all cases less than 1/4 of the 32  $\times$  32px final interrogation area which was 1.8  $\times$  1.8mm in actual dimensions.

Under optimal conditions the minimum displacement that can be accurately estimated is 0.1px ([30] and [31]). The corresponding minimum resolvable velocity for a pulse separation time of 8  $\mu$ sec was  $U_{res} = 0.7$ m/s or 1.5% of  $U_\infty$ . Any estimated velocity lower than this value is not reliable.

The image processing was done using the Insight 4G (TSI) software. In pre-processing a background reflection image was subtracted from the measurement images to remove unwanted reflections. In processing, the overlap between interrogation areas was set to 50% and a Gaussian peak estimator

In Figure 5.5-6, the measured time averaged stream-wise velocity value for different sample sizes is plotted. The data concern a point right after the plane wing TE, i.e. a point in the most unsteady region of the flow.

A horizontal solid black line is drawn at the velocity value based on the maximum number of snapshots (1000). Above and below this line, two parallel dotted lines are drawn at a distance equal to the minimum resolvable velocity ( $U_{res} = 0.7$ m/s). The 95% confidence interval is given with a blue dashed curved. For 1000 snapshots, the 95% confidence interval is comparable to  $U_{res}$ .

### Sample size effect

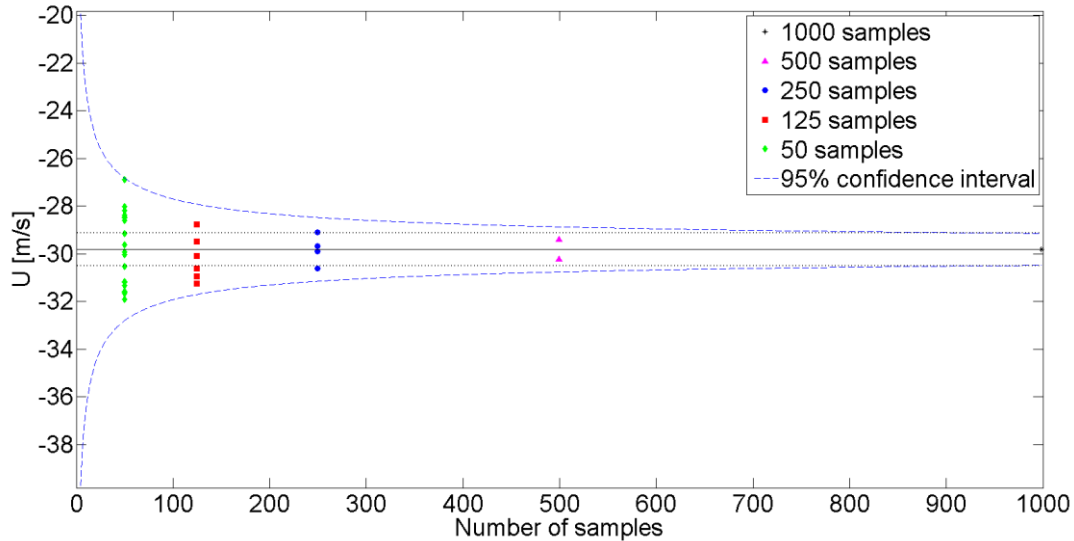


Figure 5.5-6: Sample size effect on the measured streamwise velocity component (U) at a point right after the plane wing TE.

#### Hot wire measurements

Hot wire measurements were performed at the wake of the flatback airfoil with and without TE drag reduction devices. The hot wire was located  $0.57c$  downstream of the wing TE, at the centre of the wing TE with the wing located at  $\alpha = 0^\circ$ , see Figure 5.5-7. The spanwise location of the probe was the same as the Stereo PIV measurement plane, i.e. at the centre of the wing span.

A single wire probe was used to examine the spectral content of the wake. The sampling rate was 4000HZ and the sample time was 8.2 sec.

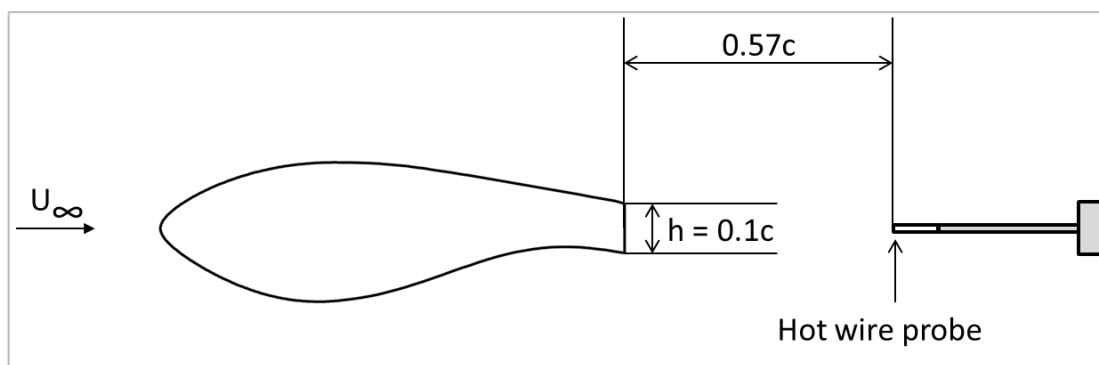


Figure 5.5-7: Hot wire probe location

## 5.5.2 Pressure measurement results

#### LI30 and LI30-FB10 airfoils

The LI30 airfoil was measured at  $Re = 1.5e6$  for a range of angles of attack ( $-3^\circ \leq \alpha \leq 20^\circ$ ) with a clean surface (free transition) and with a ZZ tape on both sides (tripped). Figure

5.5-8, Figure 5.5-9, and Figure 5.5-10 give the force coefficient variations. It appears that at this Re number the specific airfoils is very sensitive to tripping as the efficiency is significantly reduced and the linear part of the  $C_l$  polar is limited between  $3^\circ \leq \alpha \leq 8^\circ$ .

The flatback airfoil (Figure 5.5-11 TO Figure 5.5-13) appears insensitive to early transition. Compared to the thin TE airfoil  $C_{lmax}$  is increased significantly, as is  $C_d$  throughout the polar. As a result the airfoil efficiency is less than the thin TE airfoil.

Separation is 3D for both airfoils and stall cells appear on the airfoils under separated flow conditions.

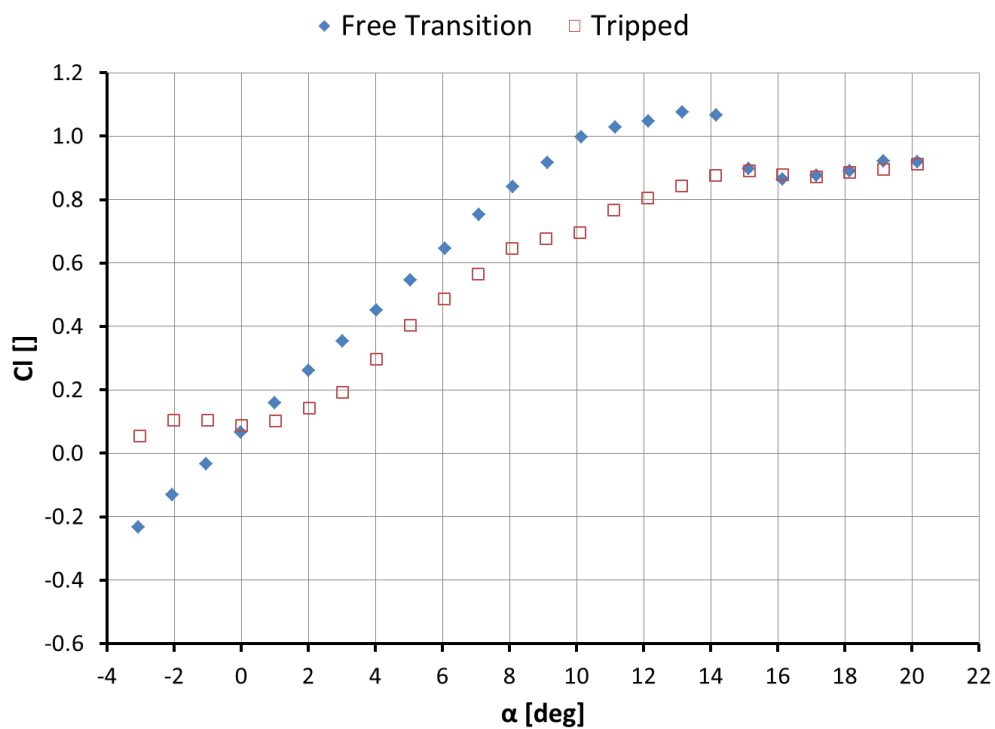


Figure 5.5-8: Lift coefficient variation with angle of attack for the LI30 airfoil under tripped and untripped conditions

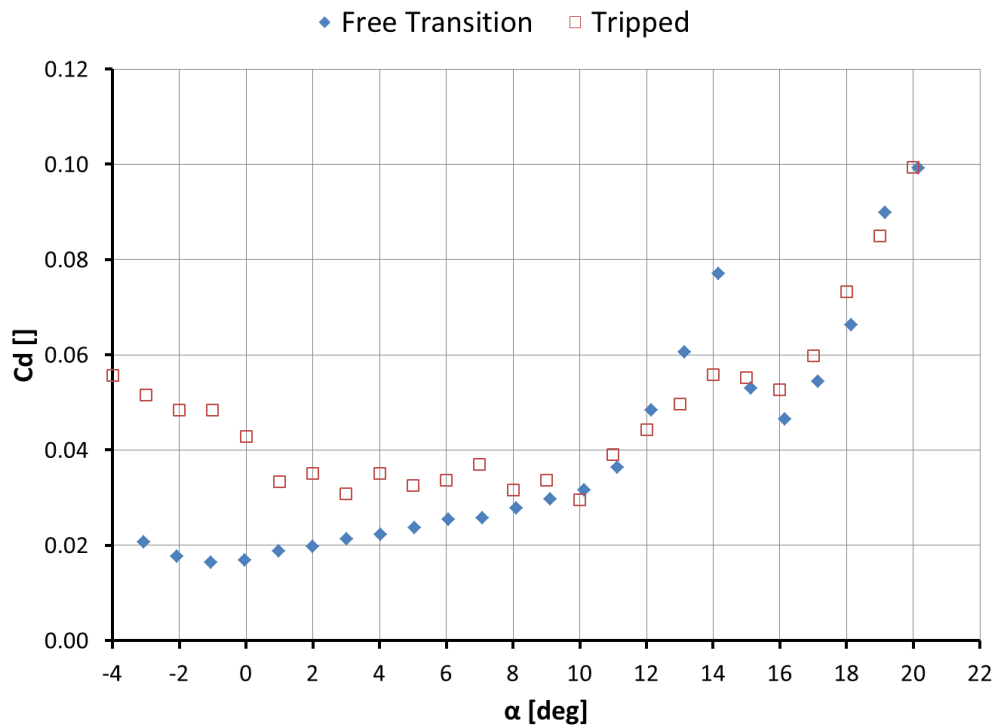


Figure 5.5-9: Drag coefficient variation with angle of attack for the LI30 airfoil under tripped and untripped conditions

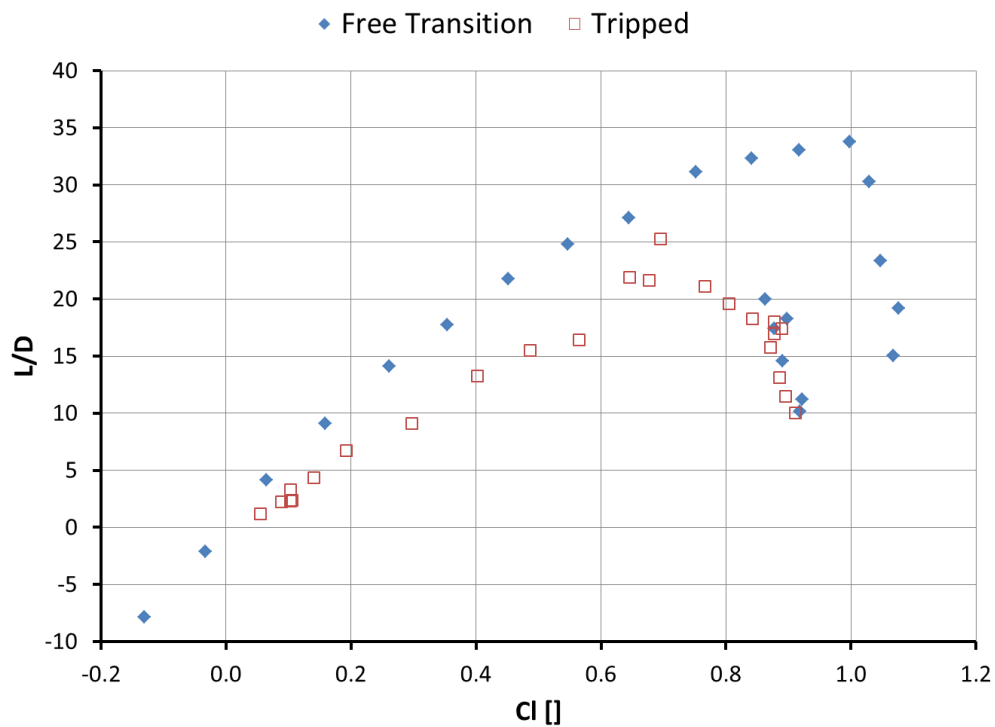


Figure 5.5-10: L/D variation with lift coefficient for the LI30 airfoil under tripped and untripped conditions

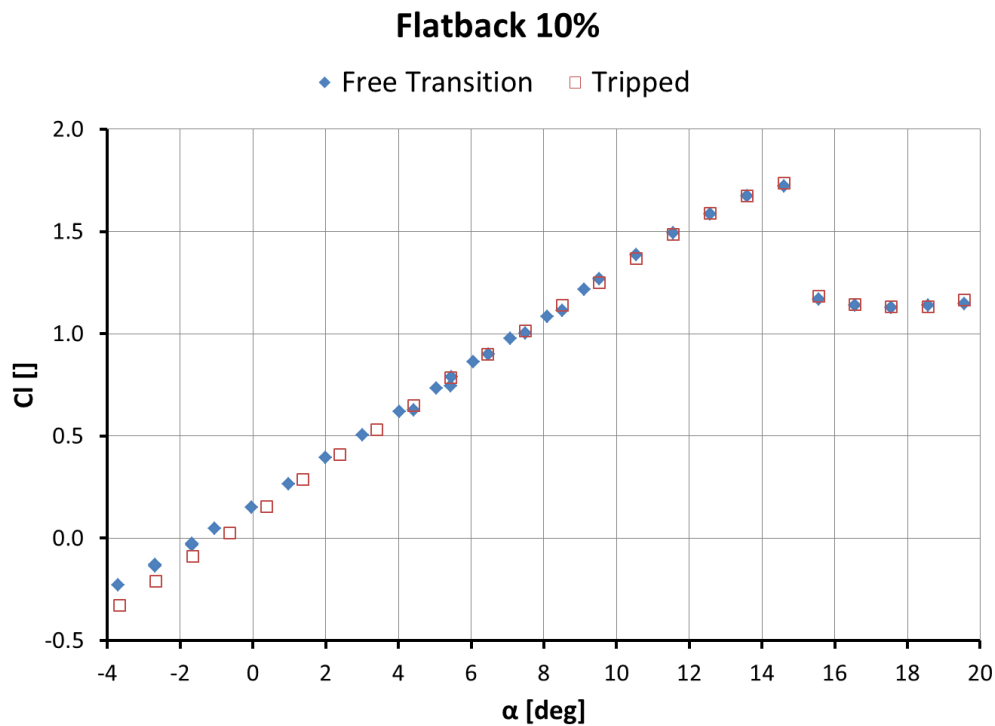


Figure 5.5-11: Lift coefficient variation with angle of attack for the LI30 airfoil under tripped and untripped conditions

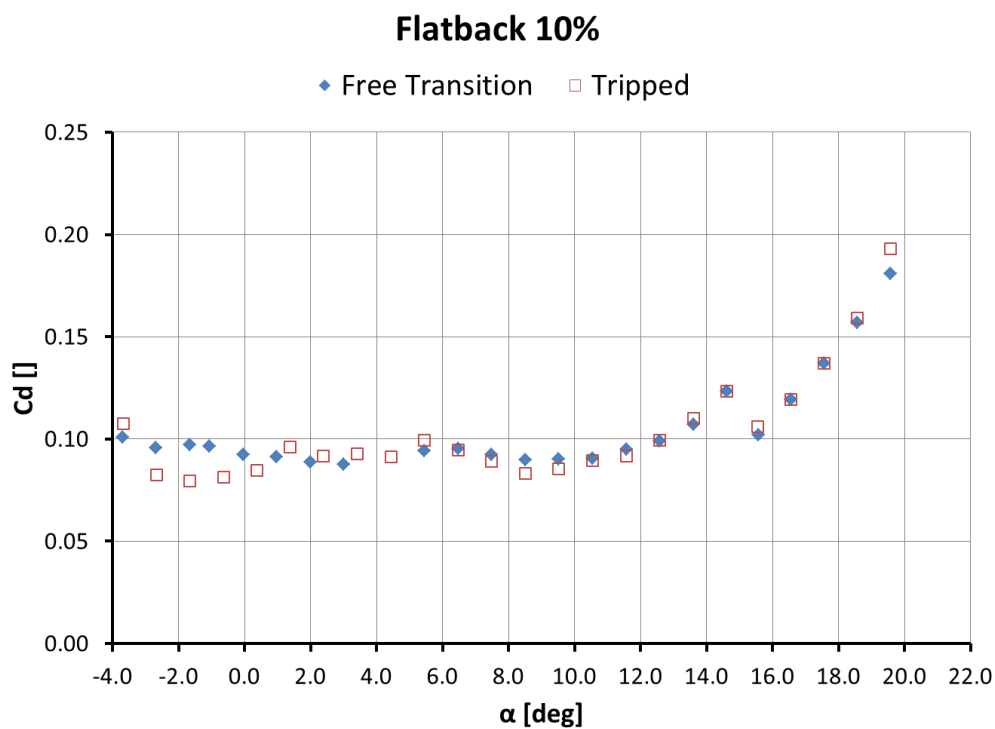


Figure 5.5-12: Drag coefficient variation with angle of attack for the LI30 airfoil under tripped and untripped conditions

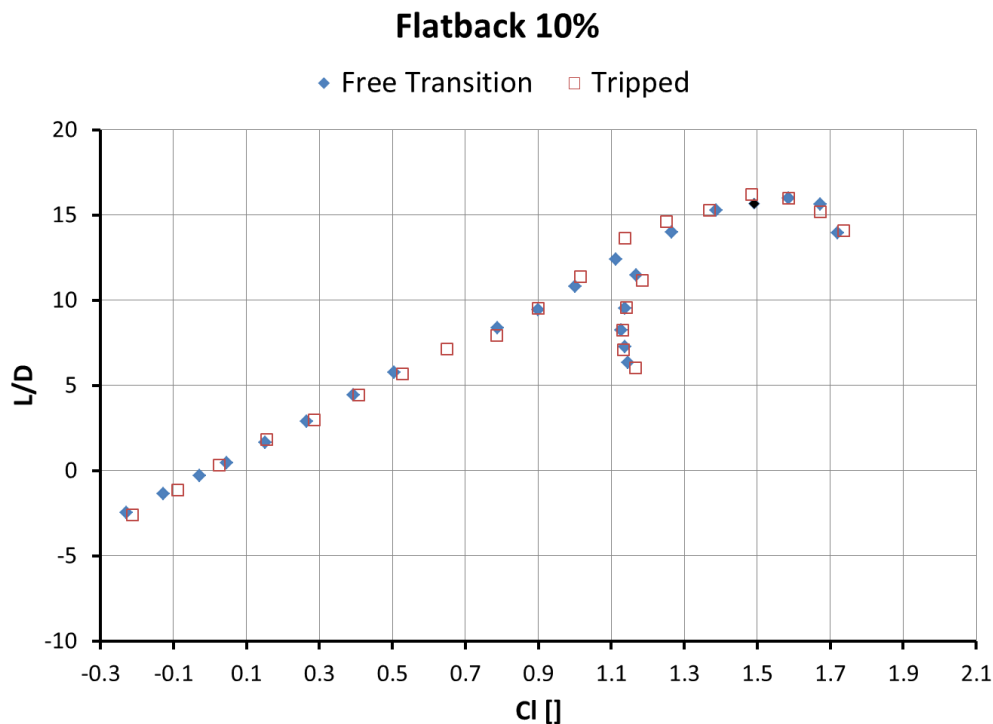


Figure 5.5-13: L/D variation with lift coefficient for the LI30 airfoil under tripped and untripped conditions

### Drag Reduction Devices

#### 1<sup>st</sup> Group of Drag Reduction Devices

The performance of the first set of drag reduction devices (Splitter, Cavity, Extended Cavity, Offset Cavity and Flap) compared to the plane flat back airfoil is given in Figure 5.5-14 ( $C_l$  vs.  $\alpha$ ), Figure 5.5-15 ( $C_d$  vs.  $\alpha$ ), and Figure 5.5-16 ( $L/D$  vs.  $C_l$ ). All devices resulted in lower drag values at angles of attack  $\alpha < 8^\circ$ . The biggest drag reduction was achieved by the Offset Cavity. In terms of lift in the pre-stall region, only the Extended Cavity performed better than the plane airfoil. Stall was delayed by  $2^\circ$  when the Extended Cavity or Cavity was used. The Flap delayed Stall by  $1^\circ$ , whereas the Splitter and the Offset Cavity did not affect  $\alpha_{Clmax}$ .

In terms of  $L/D$ , which is crucial in wind turbine blade design, the Offset Cavity, the Splitter and the Flap outperform the plane airfoil in the region  $0.1 < C_l < 1.4$ . The Cavity and the Extended Cavity perform similar to the plane airfoil up to  $C_l \leq 1.1$  and worse in the region  $1.1 < C_l < 1.5$ .

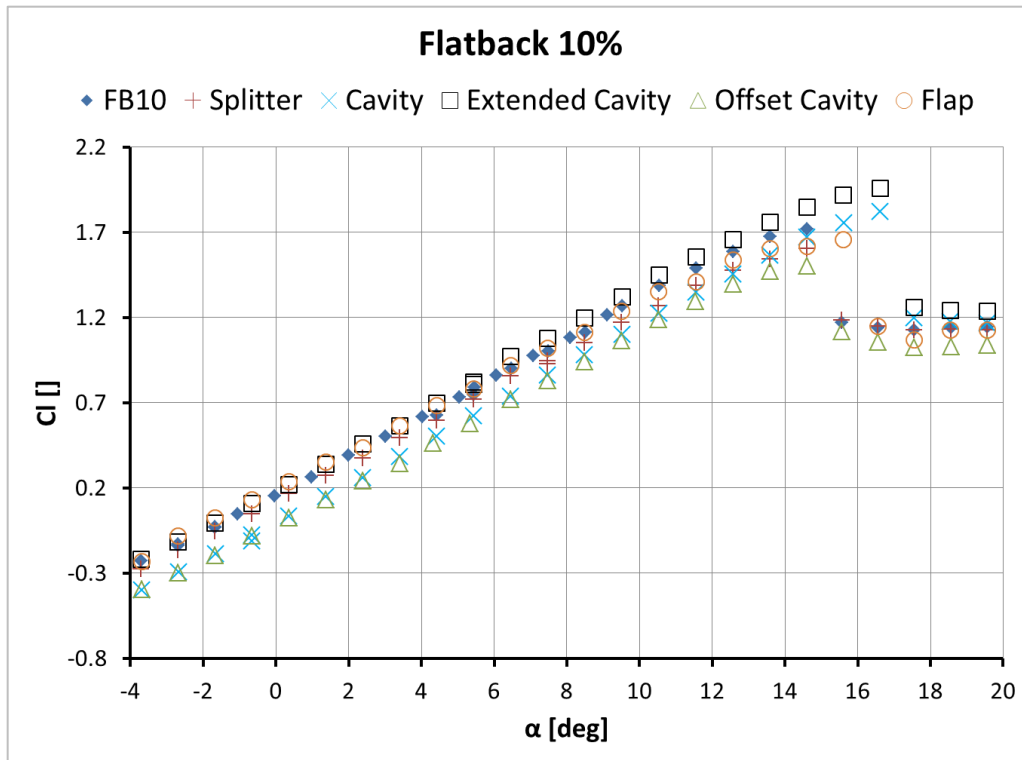


Figure 5.5-14: Lift coefficient variation with angle of attack. Comparison between the plane airfoil and the airfoil with Splitter, Cavity, Extended Cavity, Offset Cavity and Flap

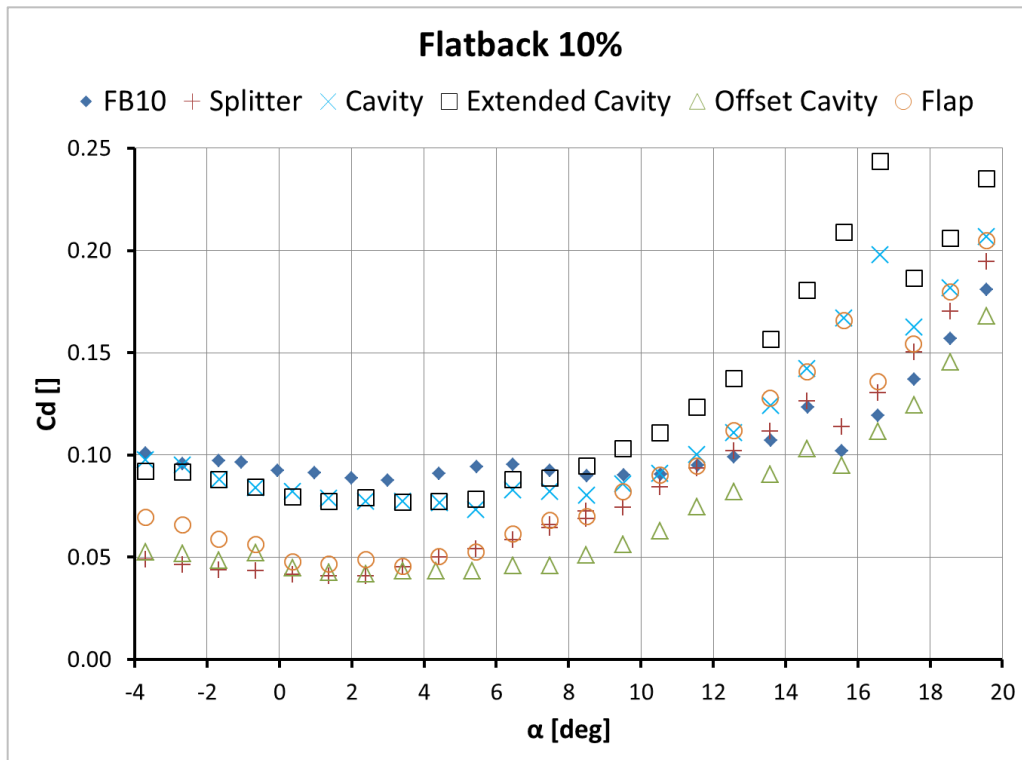


Figure 5.5-15: Drag coefficient variation with angle of attack. Comparison between the plane airfoil and the airfoil with Splitter, Cavity, Extended Cavity, Offset Cavity and Flap

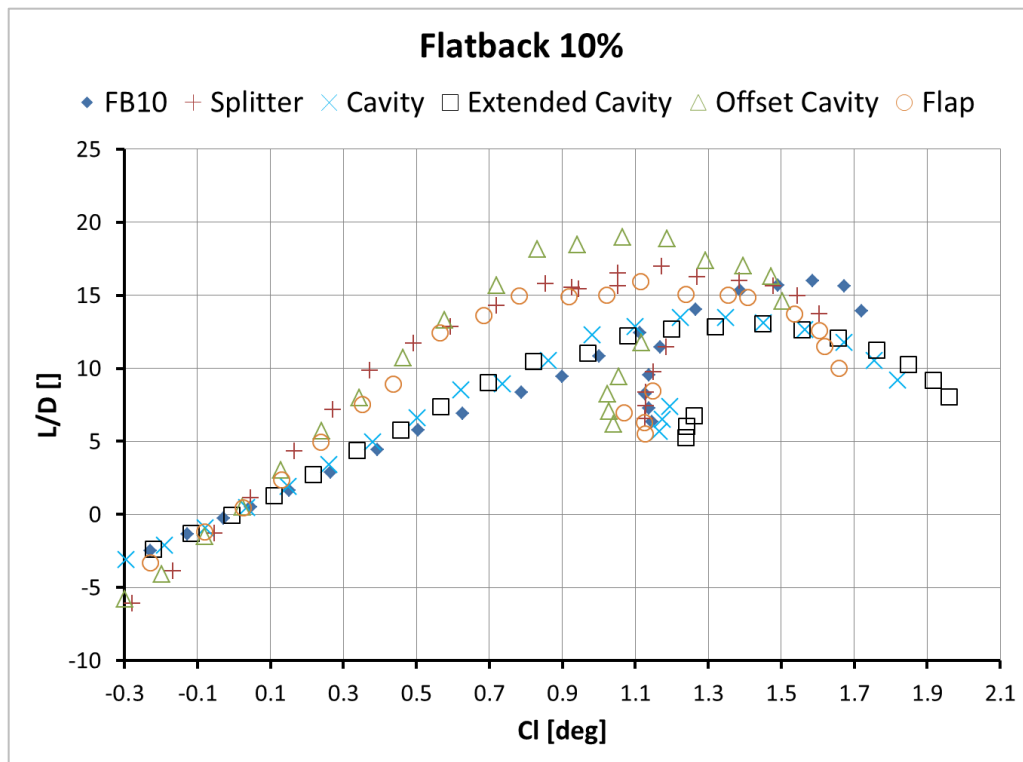


Figure 5.5-16: L/D variation with lift coefficient. Comparison between the plane airfoil and the airfoil with Splitter, Cavity, Extended Cavity, Offset Cavity and Flap

## 2<sup>nd</sup> Group of Drag Reduction Devices

The Flap was tested in combination with the Splitter, Cavity, Extended Cavity and Offset Cavity, as shown in Figure 5.5-3. Preliminary results showed that the Flap + Cavity and the Flap + Extended Cavity do not outperform the simple Flap device. The Flap + Splitter combination provided small benefits, whereas the Flap + Offset Cavity performed better than any of the devices examined in this investigation, especially in the region  $Cl \approx 0.8$ , which is the design value for a low induction rotor. The lift and drag variation with angle of attack for the 2nd Group of drag reduction devices is shown in Figure 5.5-17 and Figure 5.5-18, respectively. Figure 5.5-19 gives the L/D vs. Cl variation.

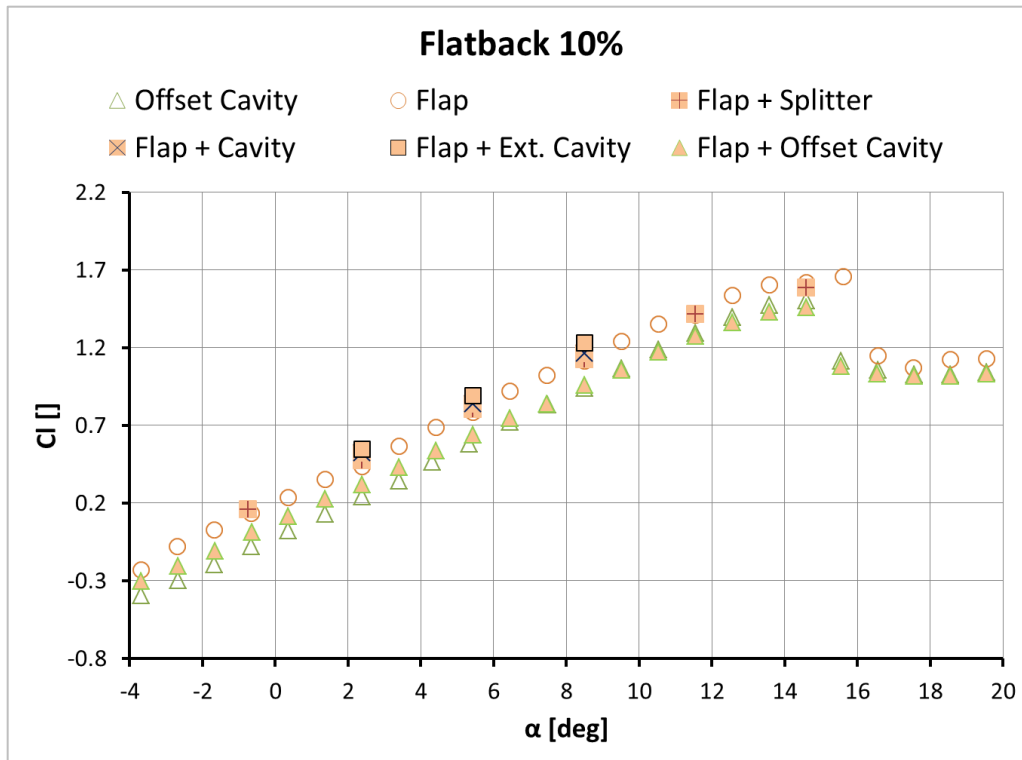


Figure 5.5-17: Lift coefficient variation with angle of attack. Comparison between the airfoil with Offset Cavity, Flap, Flap + Splitter, Flap + Cavity, Flap + Extended Cavity and Flap + Offset Cavity

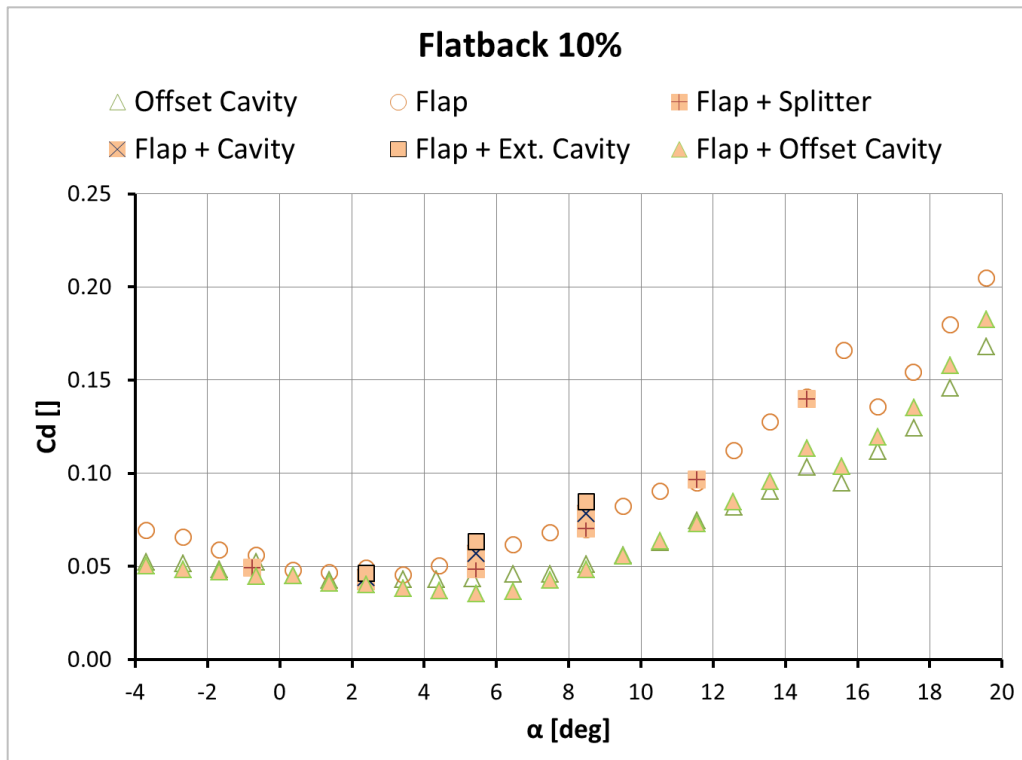


Figure 5.5-18: Drag coefficient variation with angle of attack. Comparison between the airfoil with Offset Cavity, Flap, Flap + Splitter, Flap + Cavity, Flap + Extended Cavity and Flap + Offset Cavity

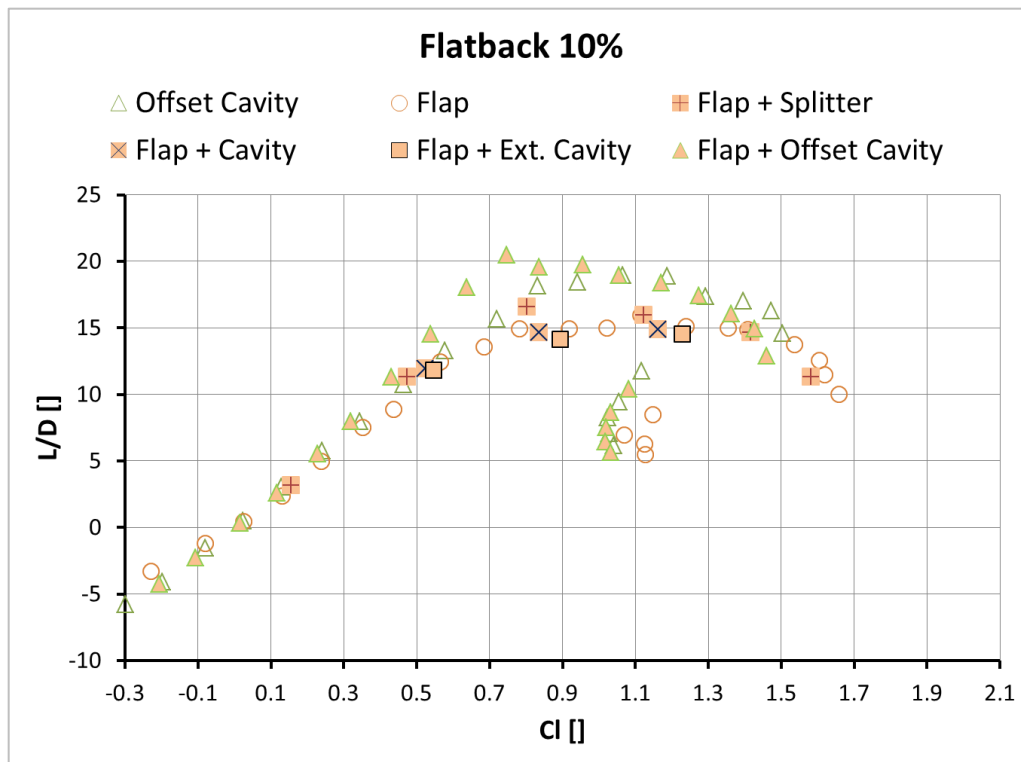


Figure 5.5-19: L/D variation with lift coefficient. Comparison between the airfoil with Offset Cavity, Flap, Flap + Splitter, Flap + Cavity, Flap + Extended Cavity and Flap + Offset Cavity

#### Pressure Distribution around the airfoil

The effect of each of the drag reduction devices on the pressure distribution around the airfoil at  $\alpha = 6.4^\circ$  is shown in Figure 5.5-20 for the Splitter, the Offset Cavity, the Flap and the Flap + Cavity. All devices result in higher base pressure values. The Splitter and the Offset Cavity have a more significant effect on the overall pressure around the airfoil, which explains the lower Cl values for these devices. The Flap raises the base pressure without severely affecting the pressure distribution around the airfoil, regardless if it is used on its own or combined with the Offset Cavity.

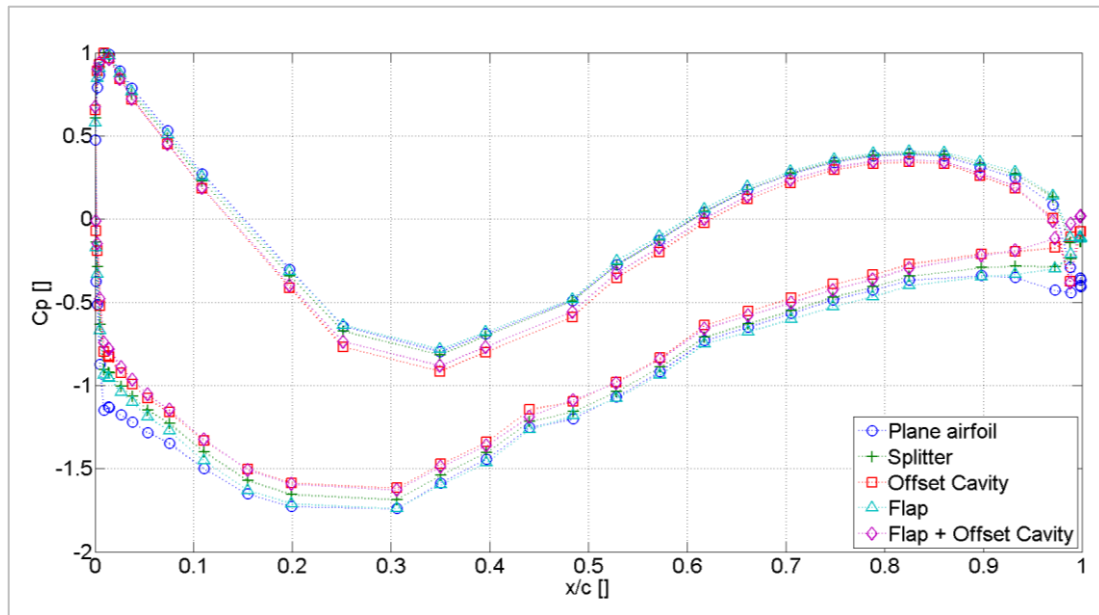


Figure 5.5-20: Pressure coefficient distribution along the wing chord at  $\alpha = 6.4^\circ$  for the plane airfoil and the airfoil with Flap, Offset Cavity and Flap with Offset Cavity

### 5.5.3 Stereo PIV results

The four best performing configurations (Offset Cavity, Splitter, Flap, Flap + Offset Cavity) along with the plane airfoil were examined using Stereo PIV. Results are presented in contour plots in the following manner. The flow is from left to right and the centre of the TE is at  $X/c = 1, Y/c = 0$  and is not shown in the contour plots.

The laser source was located at the side of the airfoil top surface and as a result, the drag reduction devices shadowed part of the measurement plane. The measurement plane for each case is shown in Figure 5.5-21. The shadowed part along with areas affected by reflections has been masked out. All data have been non-dimensionalized with  $U_\infty$  and the wing chord ( $c = 0.5\text{m}$ ).

In Figure 5.5-22 the mean velocity magnitude contours for each case along with time averaged streamlines is shown. The Splitter and Offset Cavity, unlike the Flap, move the centre of the vortices downstream, away from the TE, compared to the main airfoil. Figure 5.5-23 shows the vorticity contours for all cases. The highest vorticity values correspond to regions of high shear and not the vortex centre. For the flap cases two regions of high negative vorticity are observed, one corresponding to the Flap wake and one above the top wake vortex

In Figure 5.5-24, Figure 5.5-25 and Figure 5.5-26 the  $\overline{u'v'}$ ,  $\overline{u'u'}$  and  $\overline{v'v'}$  Re stress contours are presented. The shear Re stress magnitude is an indication of the size and intensity of the shear layers that form downstream of the wing TE. The normal Re stress contours provide information on the intensity of the velocity variation along the vertical and stream-wise direction.

For the plane airfoil case, the two strong shear layers are clearly seen (Figure 5.5-24). The  $\overline{u'u'}$  contours (Figure 5.5-25) reveal two areas of high intensity at the regions where the

free stream is entrained in the wake as the vortices that are shed from the TE are convected downstream. Intense variation of the vertical velocity component is observed in the wake (Figure 5.5-26) due to the meandering movement of the wake. In all cases the higher  $\overline{v'v'}$  values are observed around the saddle point of the mean flow (see Figure 5.5-22) and downstream.

The Re stress structure for the Offset Cavity case is similar to that of the plane airfoil (e.g. compare the Re stress distribution in Figure 5.5-24 and Figure 5.5-26), but the high Re stress region is significantly reduced and moved further away from the wing TE. Normal and shear Re stress values are significantly reduced with the other three devices, most impressively when the Flap + Offset Cavity combination is used. This suggests that a much more stable vortex system is formed compared to all other cases. Preliminary CFD results show that a stable vortex is formed between the Flap and the offset cavity plate.

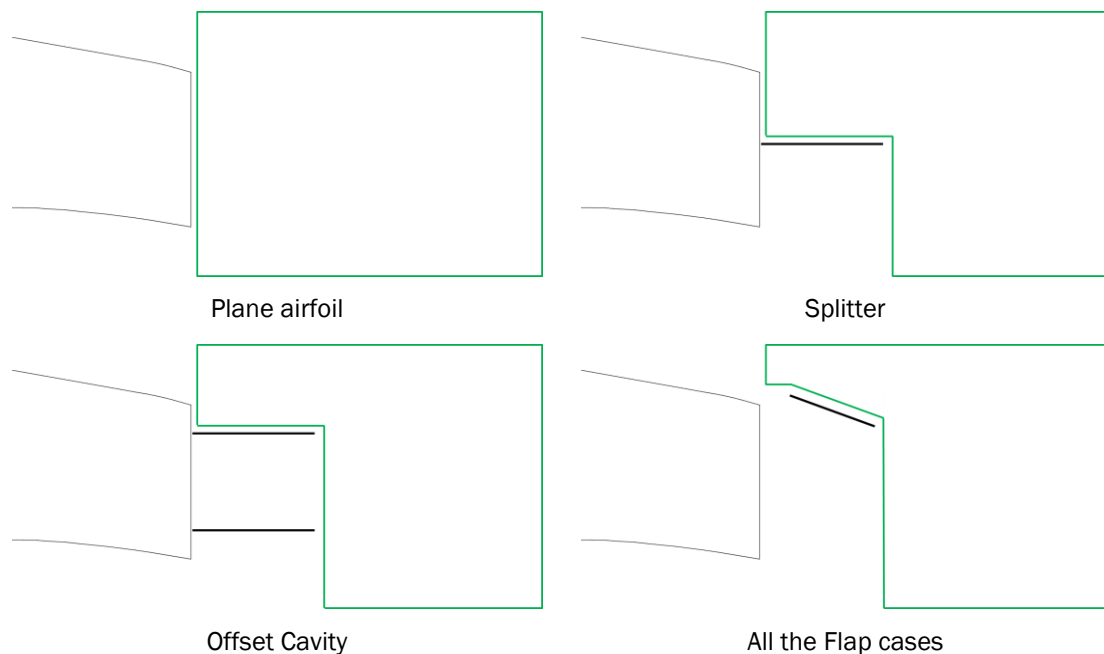


Figure 5.5-21: Stereo PIV measurement window for each case

Plane FB10 Airfoil

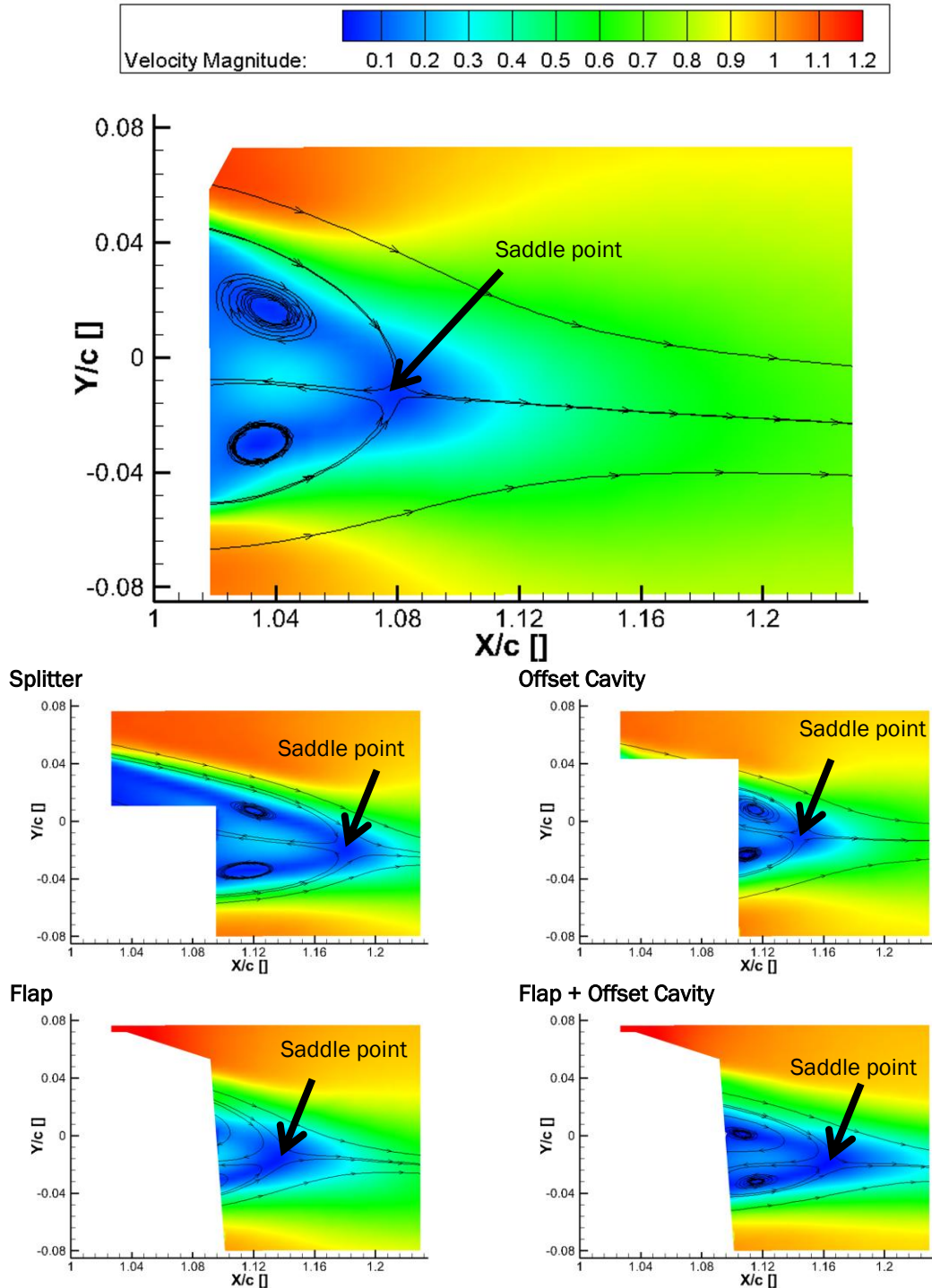


Figure 5.5-22: Mean velocity magnitude contours and streamlines. The location of the saddle point in the wake is also indicated.

Plane FB10 Airfoil

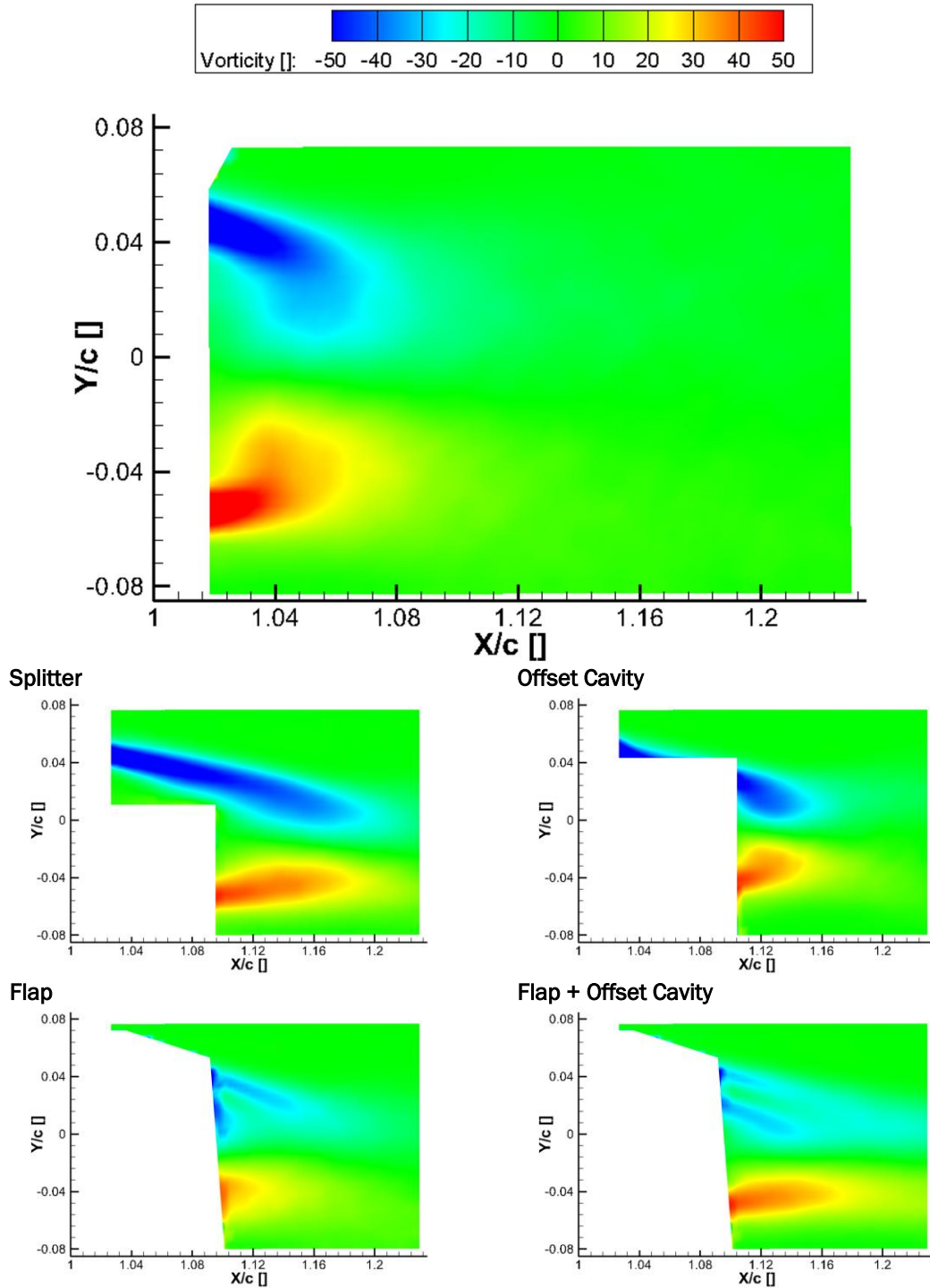


Figure 5.5-23: Spanwise vorticity contours

Plane FB10 Airfoil

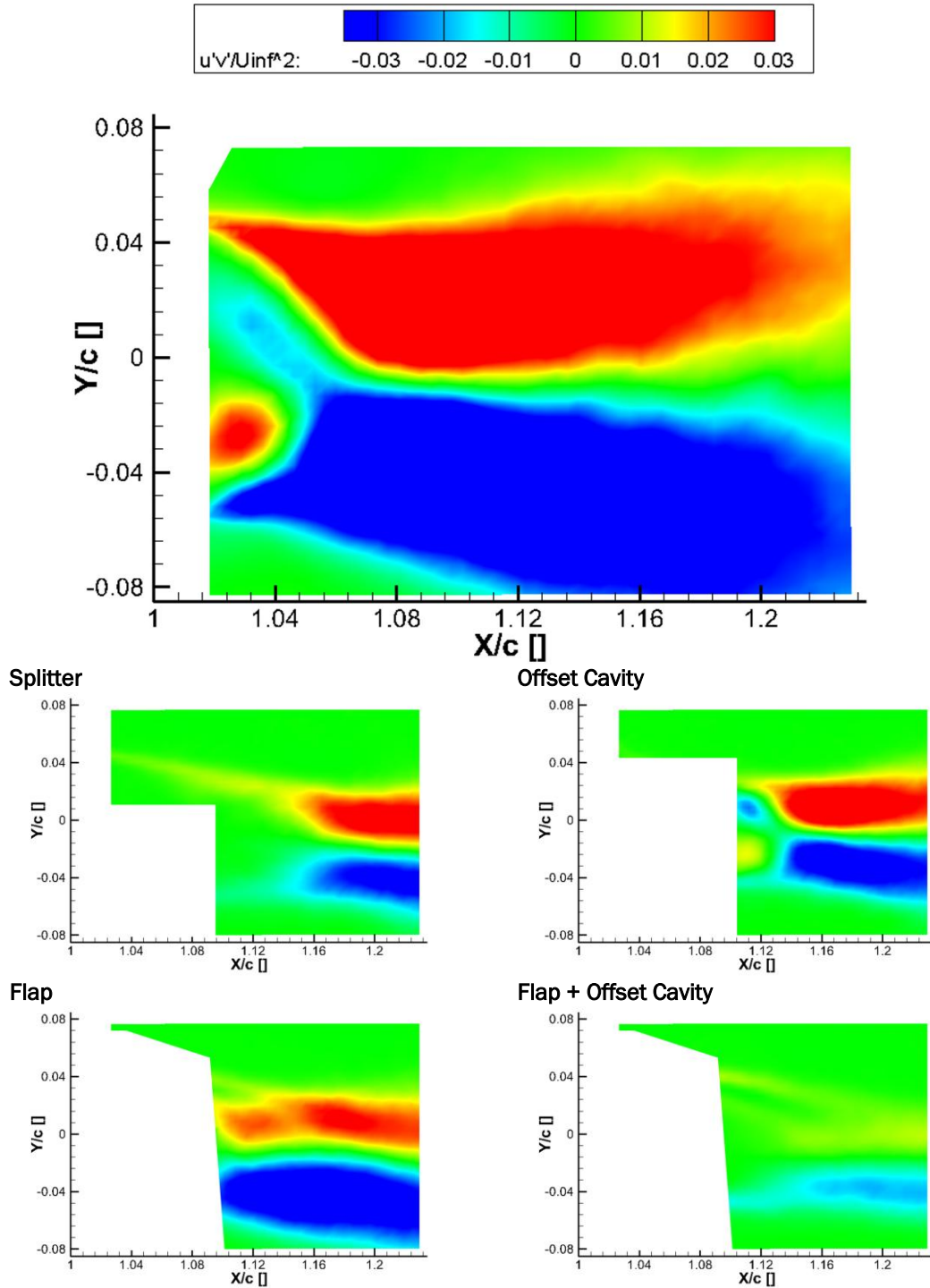
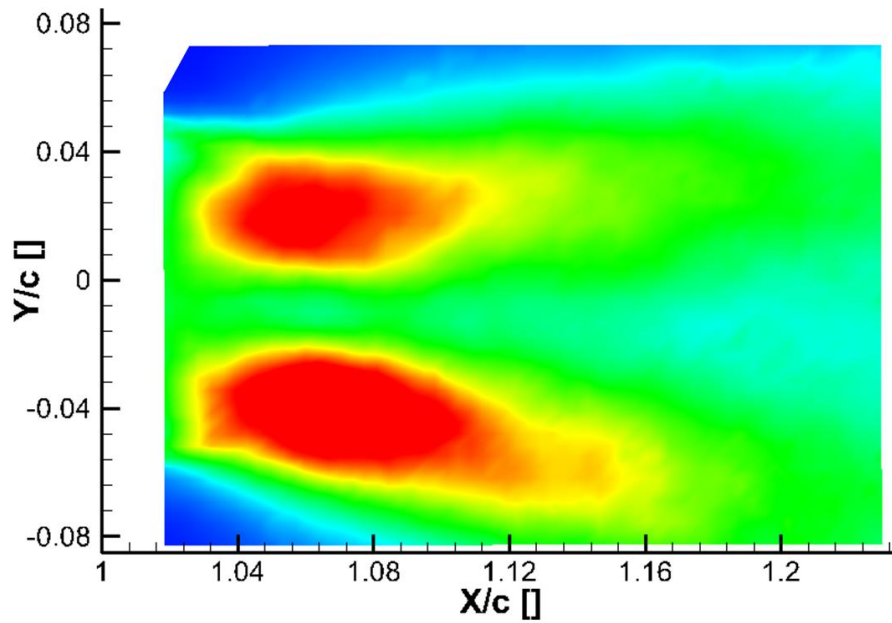
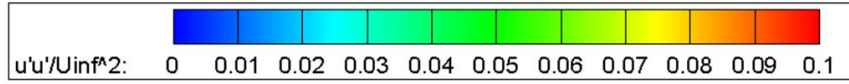
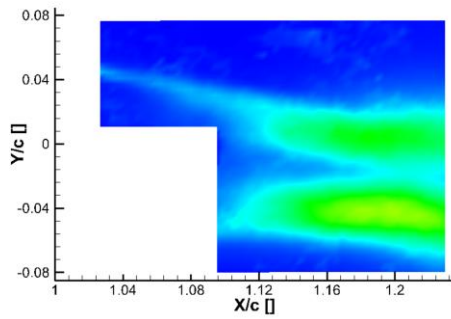


Figure 5.5-24:  $\overline{u'v'}$  shear Reynolds stress contours

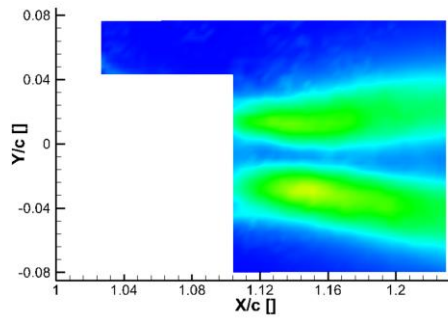
Plane FB10 Airfoil



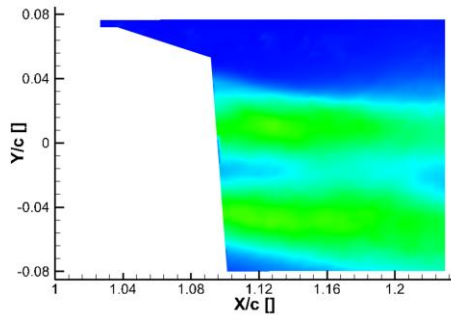
Splitter



Offset Cavity



Flap



Flap + Offset Cavity

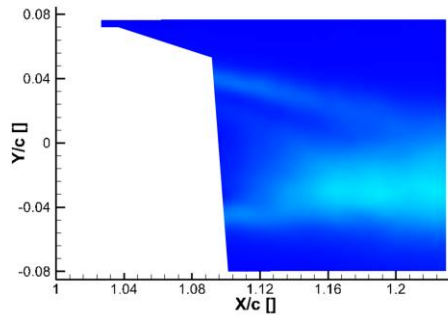


Figure 5.5-25:  $\overline{u'u'}$  normal Reynolds stress contours

Plane FB10 Airfoil

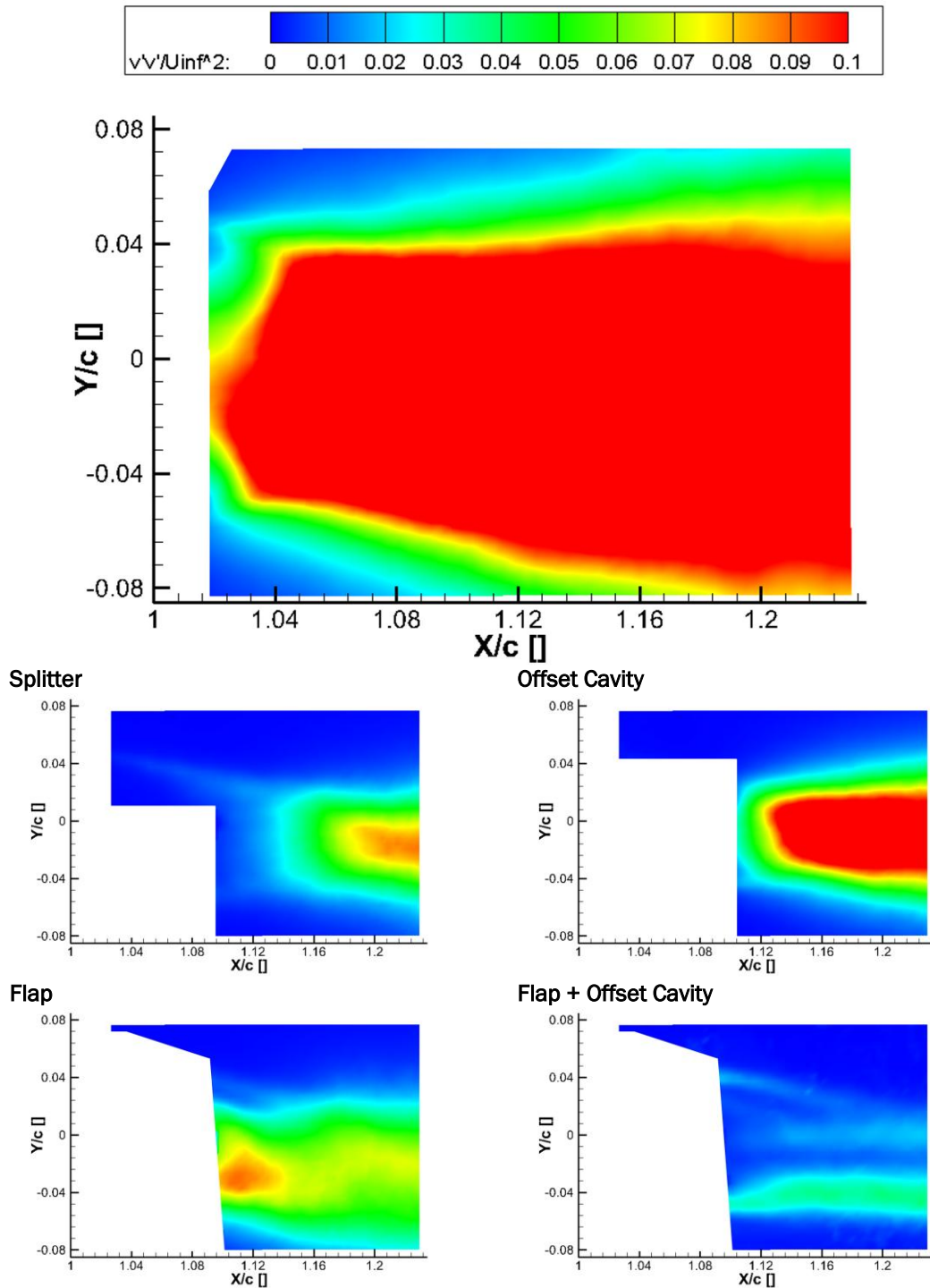


Figure 5.5-26:  $\overline{v'v'}$  normal Reynolds stress contours

### 5.5.4 Hot wire results

For flatback airfoils the Strouhal number is usually defined as

$$St = \frac{fh}{U_\infty} \quad (1)$$

where  $h$  is the TE height.

In the present case, for the TE drag reduction devices, an additional definition is used

$$St^* = \frac{fh^*}{U_\infty} \quad (2)$$

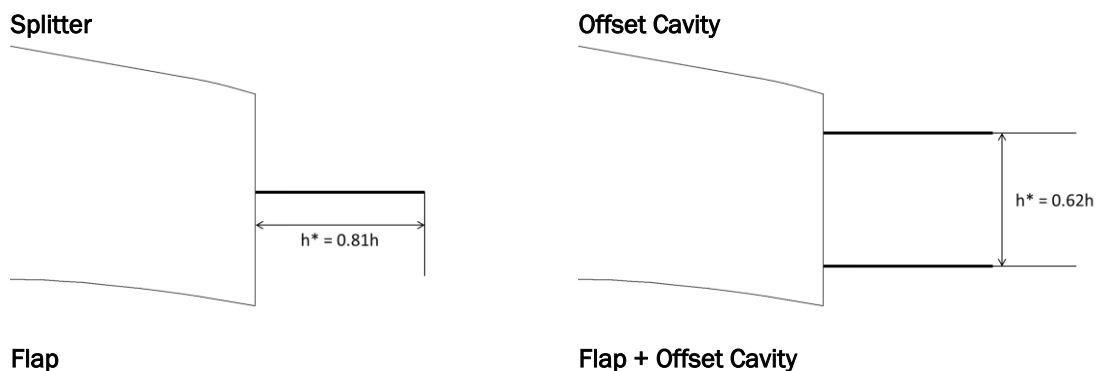
where  $h^*$  is a characteristic height for each device.

The definition of  $h^*$  is somewhat arbitrary for the TE devices. For the Offset Cavity and the Flap + Offset Cavity, it is defined as the vertical distance between the device plates. For the Flap it is defined as the vertical distance between the device plate and the wing TE, while for the Splitter it is defined as the length of the splitter plate, see Figure 5.5-27.

In Figure 5.5-28 both  $St$  and  $St^*$  is plotted for the four drag reduction devices, while only  $St$  is plotted for the plane airfoil. It is observed that  $St = 0.24$  for the plane airfoil, suggesting bluff body vortex shedding, as expected. Compared to the plane airfoil, all devices result in increased  $St$  number and deviations of smaller magnitude (in agreement with PIV findings).

It is remarkable that  $St^*$  remains in the region of bluff body shedding ( $0.20 \leq St^* \leq 0.25$ ). It should be noted, however, that the definition of  $h^*$  is arbitrary, especially for the Splitter, where a distance parallel to the flow is selected (and not normal as usually for bluff bodies). For the Offset Cavity and the Flap, the peak is much sharper, suggesting clearly structured vortices. When the Flap + Offset Cavity device is used, the magnitude peak is almost an order of magnitude smaller than all other devices. Finally in all cases a second peak appears at a value equal to two times the dominant frequency. For the cases without the Flap, a third smaller peak appears at three times the dominant frequency.

As a general conclusion it can be said that the large amplitude slow vortex shedding of the plane airfoil is transformed into lower amplitude faster oscillations when the TE devices are used. The most effective device appears to be the Flap + Offset Cavity combination.



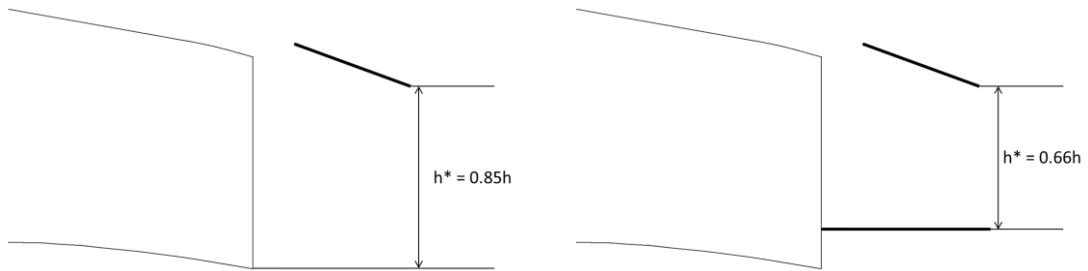
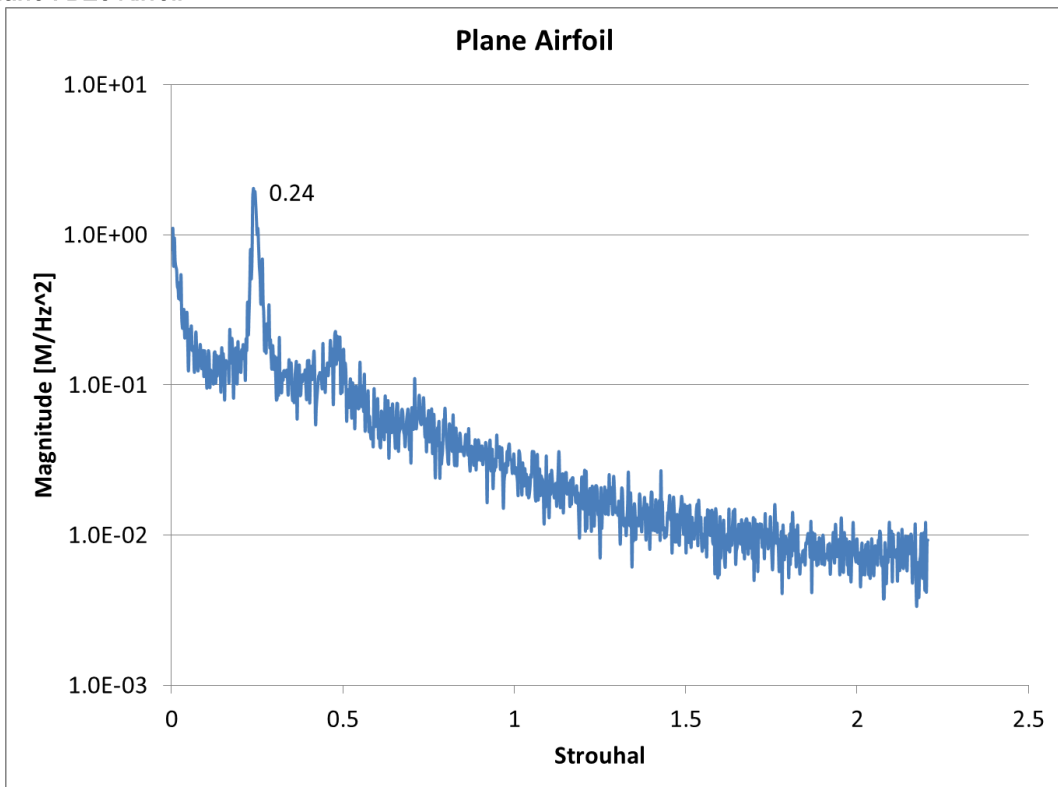
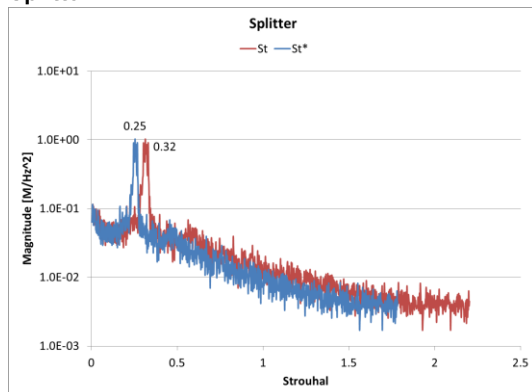


Figure 5.5-27: Definition of  $h^*$  for each TE device

Plane FB10 Airfoil

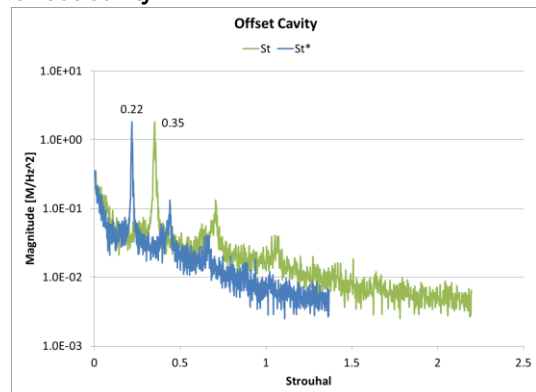


Splitter



Flap

Offset Cavity



Flap + Offset Cavity

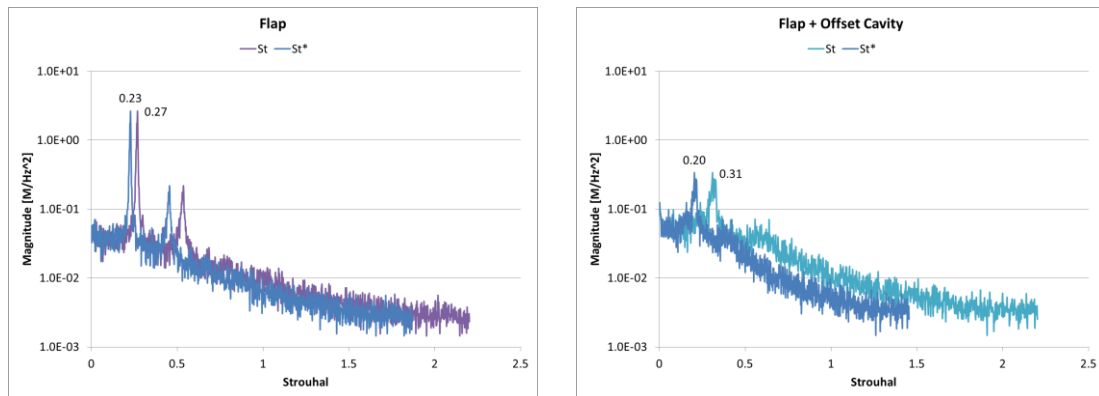


Figure 5.5-28: St and St\* data for the plane airfoil and the four best performing drag reduction devices

### Discussion

The 30% thin TE airfoil (LI30) appears to be very sensitive to flow tripping, a characteristic which is not true for the flatback version of the airfoil (LI30-FB10). The latter airfoil appears insensitive to tripping, but as all flatback airfoils have significantly increased drag.

In total nine trailing edge add-ons were tested on the flatback airfoil, seven of which had the desired effect of improving the L/D. The best results were obtained when one of the new devices (the Flap + Offset Cavity combination) was used. The L/D was increased by 138% (from 8.4 to 20) at the design lift coefficient design region,  $Cl \approx 0.8$ .

Four configurations (Offset Cavity, Splitter, Flap, Flap + Offset Cavity) were examined using Stereo PIV and hot wire measurements. The Re stress contours and the spectral plots suggest that they all reduce the amplitude of the unsteadiness of the wake, while they increase the shedding frequency.

It is worth noting that this was a proof-of-concept investigation for the Flap device. This add-on was not optimized in any way (e.g. Flap angle of attack, chord, profile), which leaves plenty of room for improvement.

Flaps have been shown to provide load reduction on wind turbine blades (e.g. [32]), when placed on thin TE airfoils. The ability of the new Flap device to actively control load on a wing should also be investigated.

## 5.6 Synthesis and conclusions

NTUA's contribution is distinguished in three parts:

- a) assessment of elliptical shaped airfoils
- b) performance analysis of the low induction airfoils designed by CRES
- c) conduction of wind tunnel tests for the 30% thick low induction airfoil designed by CRES, and its flat back version using different trailing edge add-on devices.

The first part analysis showed that the elliptical shape lowers the performance of an airfoil at low angles of attack because of the decreased lift and the increased drag. This trend is reversed as the angle of attack increases. For the 18% thick airfoils, the trend is reversed at about  $11^\circ$  angle of attack, whereas, for the 25% thick airfoil, the trend is reversed at  $6^\circ$  angle of attack. Therefore, the positive effect of the elliptical shape on the airfoil

performance occurs at a wider range of the angle of attack in the case of the thicker airfoil.

The second part analysis showed that the low induction airfoils designed by CRES exhibit a remarkably high performance at the design point  $C_{LDES}=0.8$ , as predicted by different simulation tools. For the 18% airfoil the predicted performance is higher than 135 at transitional flow conditions and higher than 85 at fully turbulent conditions. For the thickest airfoil of 30% the predicted performance decreases but still remains higher than 100 and 60 at transitional flow and fully turbulent conditions, respectively.

The third part experimental analysis showed that the 30% thick low induction airfoil designed by CRES appears to be very sensitive to flow tripping, whereas its flatback version appears insensitive to tripping. Furthermore, the experimental investigation of nine different trailing edge add-ons on the flatback airfoil demonstrated that the best performance improvement at the design point  $C_{LDES}=0.8$  is obtained using the novel device of the “Flap + Offset Cavity combination”. It was also demonstrated that four of the configurations (Offset Cavity, Splitter, Flap, Flap + Offset Cavity) reduce the amplitude of the unsteadiness of the wake, while they increase the shedding non-dimensional frequency.

## CHAPTER 6 DESIGN AND ANALYSIS OF TIP SECTION AIRFOILS TAKING INTO ACCOUNT COMPRESSIBLE EFFECTS

WZ Shen, WJ Zhu, HAa Madsen

### 6.1 Scope and objectives

The innovative airfoil design tool that DTU investigates in INN WIND.EU is the integrated airfoil and rotor design tool [33]. The first part of the task is to check the validity of the design code about compressibility prediction. Both XFOIL [5] and Q<sup>3</sup>UIC [34] codes are validated against the compressible CFD code FLUENT and the wind tunnel measurements performed at LM's wind tunnel in the case of flows past a DTU-LN218 airfoil at  $Re=6 \times 10^6$  and a wind speed of 105 m/s. Design optimization is then performed for a tip section airfoil of a 10 MW two-bladed rotor with a tip speed of 110 m/s. To achieve high power performance at low cost, the airfoil is designed with the objectives of high  $C_p$  and small chord length.

### 6.2 Description of the design method

For designing an airfoil to be used near the blade tip, a novel shape perturbation function method is introduced to optimize the geometry based on existing airfoils and thus simplify the design procedure. The viscos/inviscid interactive code XFOIL is used as the aerodynamic tool for airfoil optimization at a Reynolds number about  $10^7$  and a free-stream Mach number of 0.33 at blade tip.

The integrated design of airfoil family and blade can be started from the BEM analysis of an airfoil section at a given blade station. The core of the analysis is the iterative computation of the power coefficient of a cross-sectional airfoil. Since the power performance is an important measure of a blade, it has often been used as a key reference number during design process. According to the 1D-momentum theory, the solution of the power coefficient is maximized when the axial induction factor is  $a=1/3$ , even though advanced computations show that the maximum power efficiency is obtained at slightly higher axial induction than  $a=1/3$ . With this condition being valid, it can be shown that the power coefficient of an airfoil section can be written as:

$$C_p = [(1 - a)^2 + x(1 + a')^2]xC_t\sigma \quad (6.1)$$

where the solidity is

$$\sigma = 2F\sin^2(\phi)/C_n \quad (6.2)$$

and  $a$  and  $a'$  are the axial and tangential induced velocity interference factors, respectively,  $x$  is the local speed ratio,  $C_t$  and  $C_n$  are the tangential and axial force coefficients, respectively,  $\sigma$  is the rotor solidity,  $\phi$  is the local flow geometry and  $F$  is Prandtl's tip loss function. It is known that Prandtl's tip loss function corrects the assumption of the actuator disk model at tip. Thus for rotors with a finite number of blades the correction has to be implemented to the blade design as well as airfoil design. One of the simplest corrections reads:

$$F = 2 \cos^{-1}(e^{-f})/\pi \quad (6.3)$$

where

$$f = B(R - r)/(2r \sin \phi). \quad (6.4)$$

To compute  $C_t$  and  $C_n$ , the lift and drag coefficients are needed during every iteration of airfoil optimization, such that

$$C_t = c_l(\sin \phi - c_d/c_l \cos \phi) \quad (6.5)$$

$$C_n = c_l(\cos \phi + c_d/c_l \sin \phi) \quad (6.6)$$

The other group of the variables will be iteratively solved due to their dependency. These parameters are the power coefficient  $C_p$ , the local flow angle  $\phi$  and the tangential induction factor  $a'$ . The values of  $C_p$ ,  $\phi$  and  $a'$  are initialized with zero before the first BEM iteration. After several iterations, the highest  $C_p$  for the present flow condition is obtained. The power coefficient and rotor solidity is considered together in the design objective function,

$$Obj = kC_p + (1 - k)\sigma^{-1} \quad (6.7)$$

The  $k$  value is selected such that the power coefficient and the solidity are equally weighted. To obtain a good off-design property, the power coefficient is weighted between clean and rough conditions with angles of attack ranging from  $\alpha=3^\circ$  to  $\alpha=10^\circ$ .

$$C_p = 0.25 \sum_{\alpha=3}^{10} C_p^{clean} + 0.75 \sum_{\alpha=3}^{10} C_p^{rough} \quad (6.8)$$

If the converged solution is found by the optimizer, Eq. (6.8) indicates that the resulted power coefficient is less sensitive to surface roughness and will keep high value over a wide range of AOAs.

### 6.3 Design code validation

In this sub-section, the aerodynamic prediction codes XFOIL and Q3UIC which are used to predict airfoil aerodynamic performance in our design code are validated against wind tunnel measurement and the compressible and incompressible code FLUENT.

To check the prediction capability on compressibility effects, the tunnel tests for the low noise 18% thickness DTU airfoil (DTU-LN218) airfoil performed at the LM wind tunnel are used. In the experiment the highest Reynolds number appearing at an inflow speed of 105 m/s is about  $6 \times 10^6$ . Due to the effect of wall interference and compressibility, the data obtained in wind tunnel flows was corrected into data in free-air with the consideration of compressibility. For the purpose of prediction on the aerodynamic characteristics of wind turbine airfoils, the commercial CFD software FLUENT which solves both the incompressible and compressible Navier-Stokes equations, the viscous-inviscid interaction codes XFOIL and Q3UIC which basically solve the incompressible equations and get compressible effects by correcting the incompressible data into compressible one by using the Karman-Tsien rule. Flows past a clean DTU-LN218 airfoil at Reynolds numbers of 4 and 6 million which correspond to Mach numbers of 0.2 and 0.3 are considered. From Figure 6.1(a), it's found that FLUENT, XFOIL and Q3UIC codes can predict quite well the airfoil characteristics for compressible and incompressible flows. The compressibility effects are small at a Mach number of 0.2, while the effects become more important at a Mach number of 0.3. The compressible lift coefficient in the linear region is about 5% larger than the incompressible one at a Mach number of 0.3. Looking closer at the pressure distribution around the airfoil, the minimum pressure coefficient on the suction side is more negative than the incompressible one, in Figure 6.1(b), which results in the increase of lift.

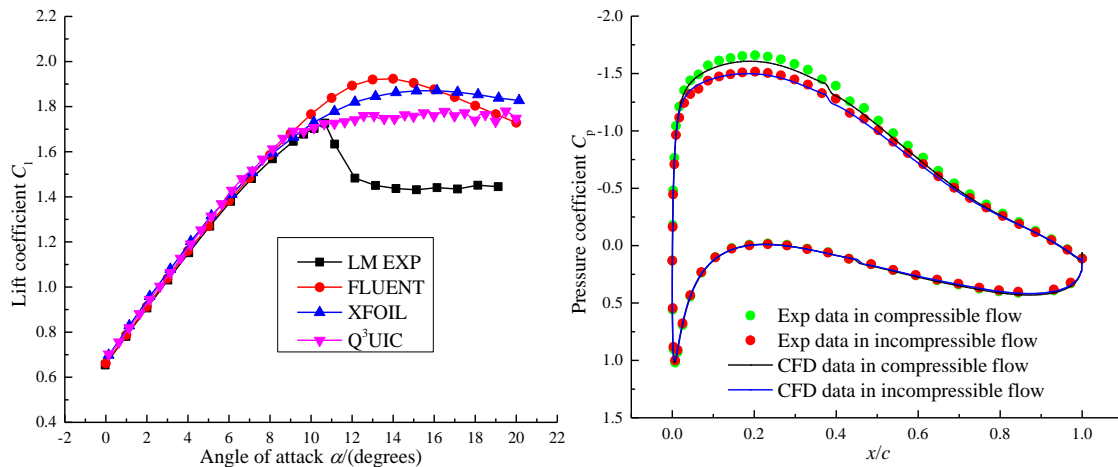


Figure 6.1: (a) Lift coefficients for compressible flows past a clean DTU-LN218 airfoil at a Mach number of 0.3 and a Reynolds number of  $6 \times 10^6$ ; (b) Comparison between the compressible and incompressible surface pressure coefficient at a Mach number of 0.3 and a Reynolds number of  $6 \times 10^6$

## 6.4 Results

Two new airfoils with relative thickness of 18 and 21 are designed. As the designed airfoils are supposed to be used in the tip region of a two-bladed 10 MW rotor, the tip speed and tip-speed-ratio used in the design are 110 m/s and 10, respectively.

The new airfoil with a relative thickness of 18 (DTU-210-18 where 2 means 2 bladed, 10 means 10 MW and 18 is thickness percent) is shown in Figure 6.2. As it was mentioned, the design objective is to achieve a blade with relatively high power coefficient and low solidity. The converged result returns an optimized solidity  $\sigma = 0.00501$ . Therefore the chord length at a given blade section can be calculated as  $c = \sigma \cdot 2\pi r$ . The airfoil is designed at a wide range of angles of attack, and the optimized power coefficient against angle of attack is shown in Figure 6.3. The curves show the results obtained from the clean and rough airfoil. The weighted curve is obtained from Eq. (6.8). First, the power curve is very flat at wide angles of attack; second, the difference between the clean and rough airfoil is very small. These ensure a stable power output under various flow conditions and constant power production during the blade life time. Figures 6.4- 6.6 are the curves of lift, drag and lift to drag ratio. All results illustrate that the present airfoil has low roughness sensitivity. Because the tip speed is assumed at 110m/s, the compressibility effect is also taken into account by using a Mach number of 0.33. With the compressible effect, the XFOIL results show higher lift and drag slopes and earlier stall as shown in Figures 6.7, 6.8.

The same design concept is applied for the airfoil with a relative thickness of 21 (DTU-210-21), see Figure 6.9 for the airfoil profile. Figure 6.10 shows a high power coefficient over wide angles of attack. The optimal solidity is  $\sigma = 0.00525$  for the 21% thick airfoil. Figures 6.11- 6.13 are the curves of lift, drag and lift to drag ratio. The compressibility effects are shown in Figures 6.14, 6.15. The same tendency is observed about the Mach number effect as well as the roughness sensitivity.

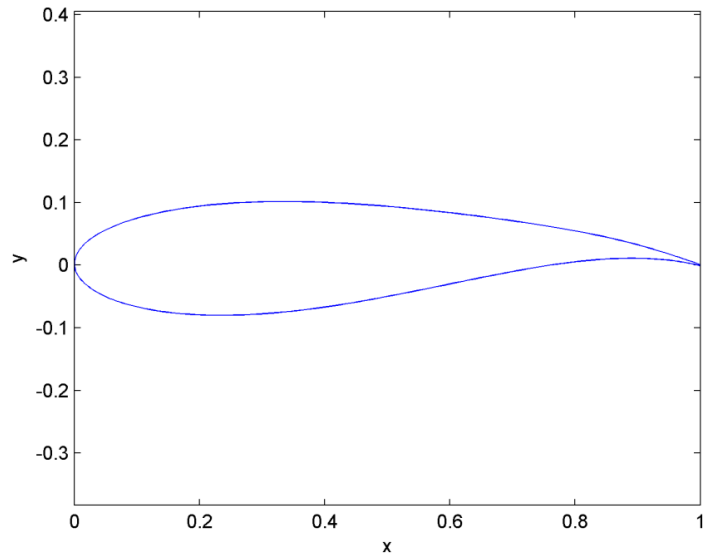


Figure 6.2: DTU-210-18 airfoil

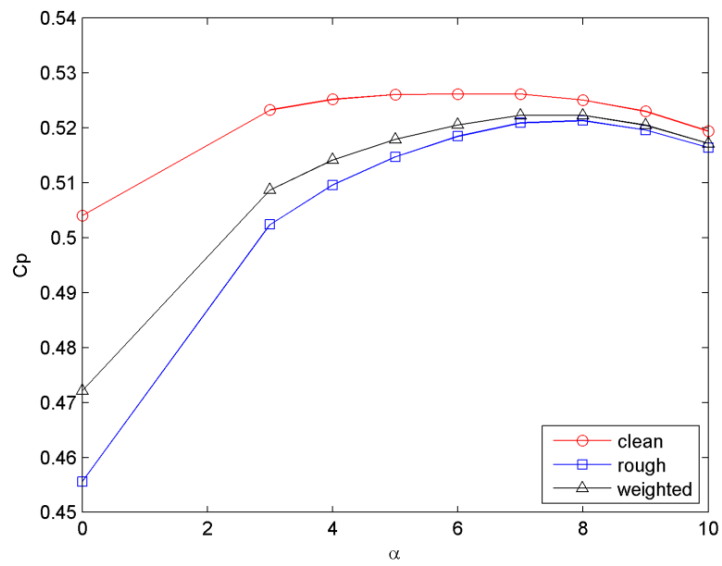


Figure 6.3: Maximum power coefficient of a DTU-210-18 airfoil at TSR=10

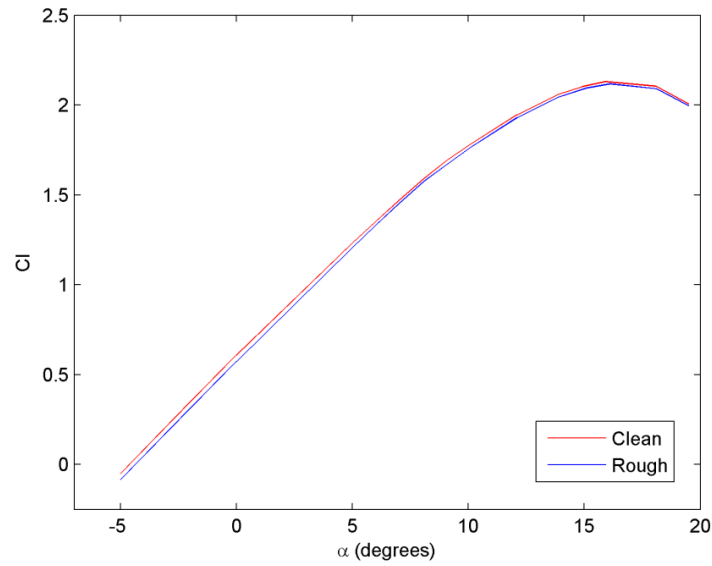


Figure 6.4: Lift curve for the clean and rough DTU-210-18 airfoil at  $Re=10^7$

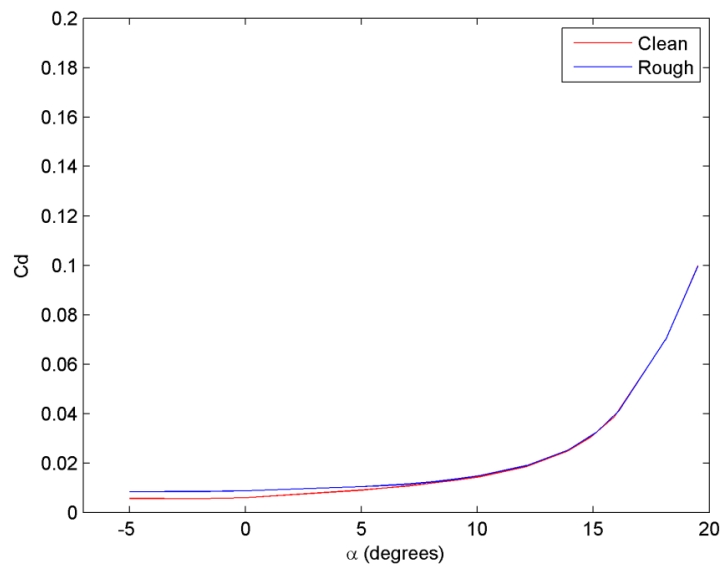


Figure 6.5: Drag curve for the clean and rough DTU-210-18 airfoil at  $Re=10^7$

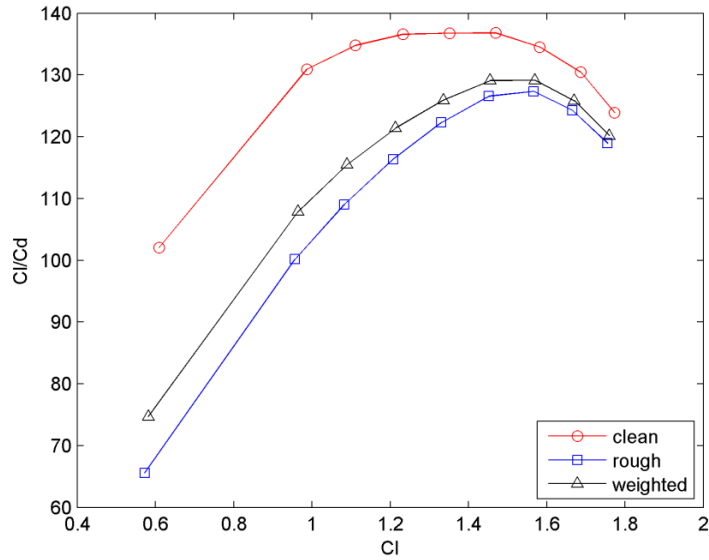


Figure 6.6: Lift to drag ratio of a DTU-210-18 airfoil at  $Re=10^7$

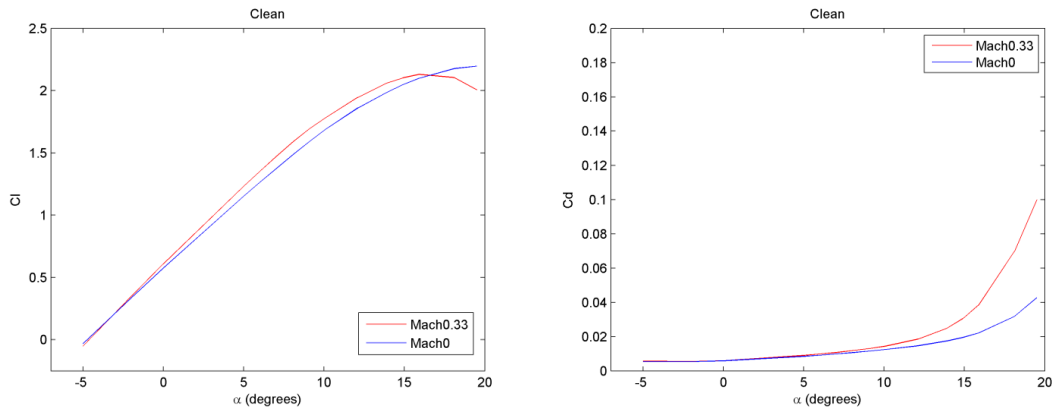


Figure 6.7: Comparisons of the performance of a clean DTU-210-18 airfoil with/without Mach number effect

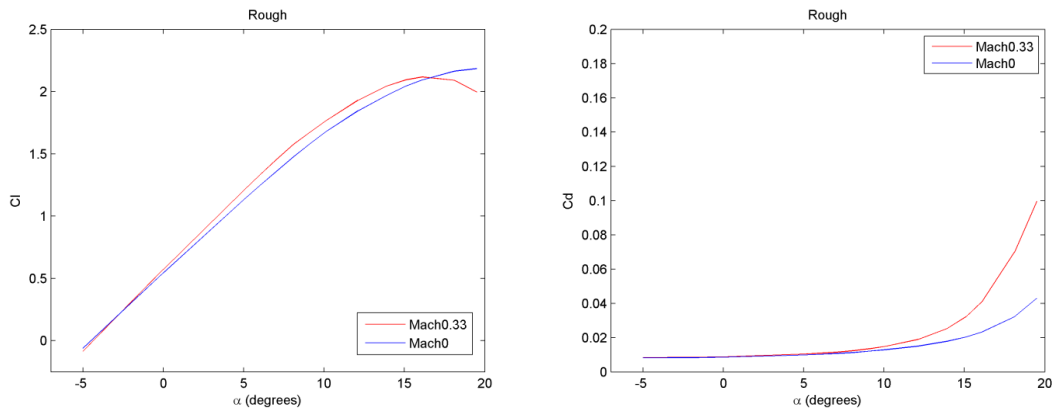


Figure 6.8: Comparisons of the performance of a rough DTU-210-18 airfoil with/without Mach number effect

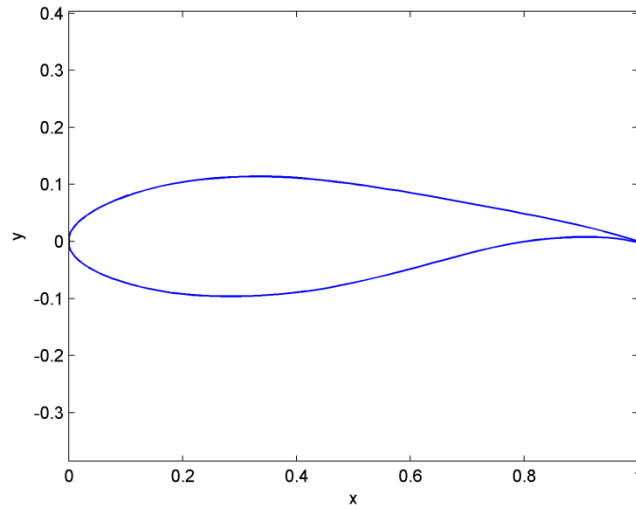


Figure 6.9: DTU-210-21 airfoil

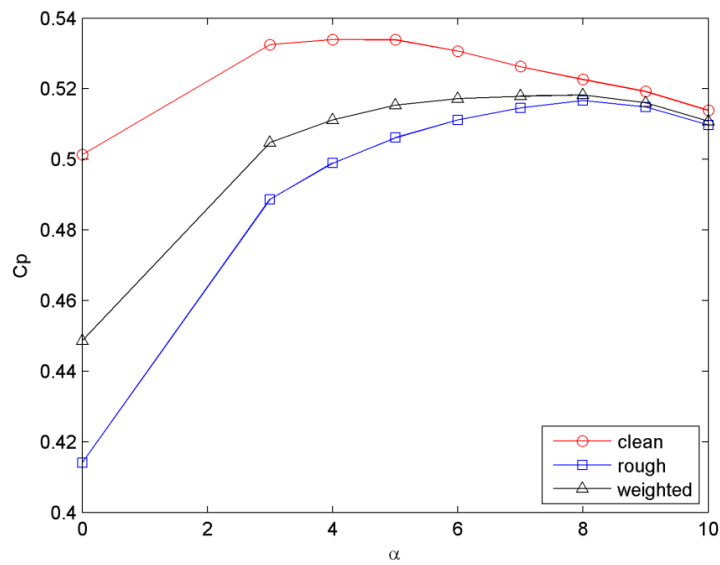


Figure 6.10: Maximum power coefficient of a DTU-210-21 airfoil at TSR=10

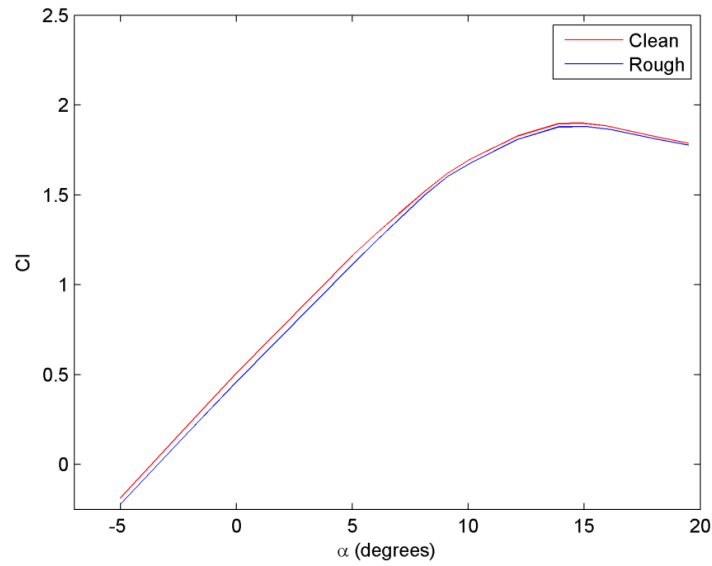


Figure 6.11: Lift curve for the clean and rough DTU-210-21 airfoil at  $Re=10^7$

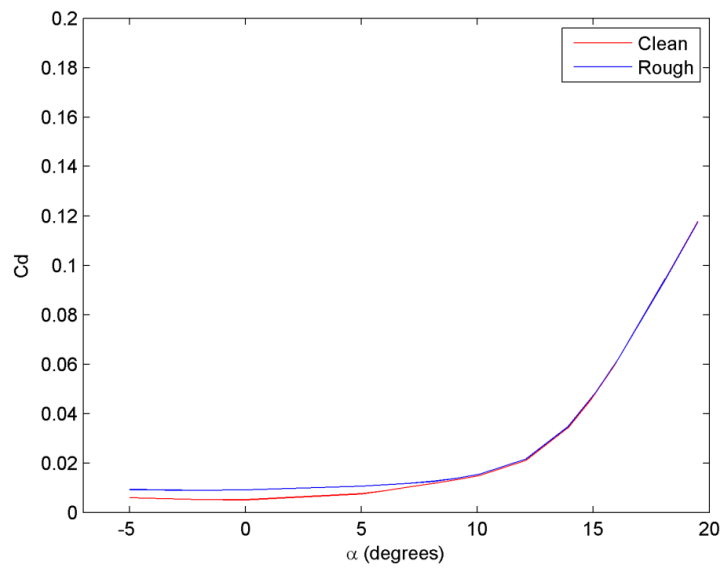


Figure 6.12: Lift curve for the clean and rough DTU-210-21 airfoil at  $Re=10^7$

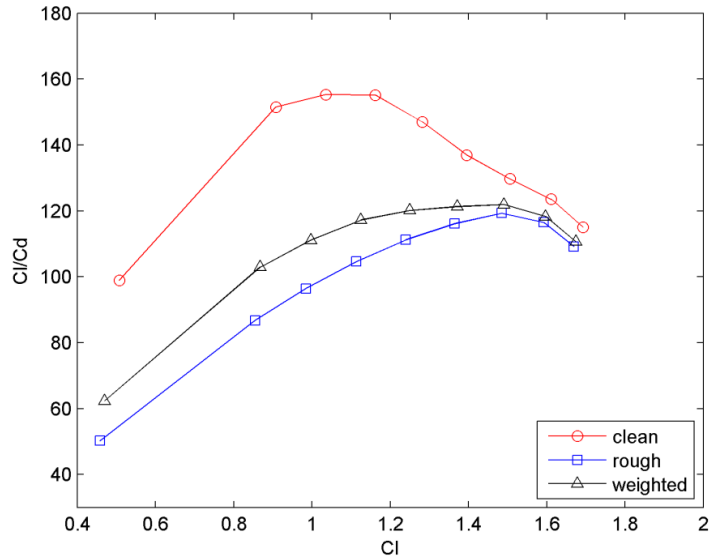


Figure 6.13: Lift to drag ratio of a DTU-210-21 airfoil at  $Re=10^7$

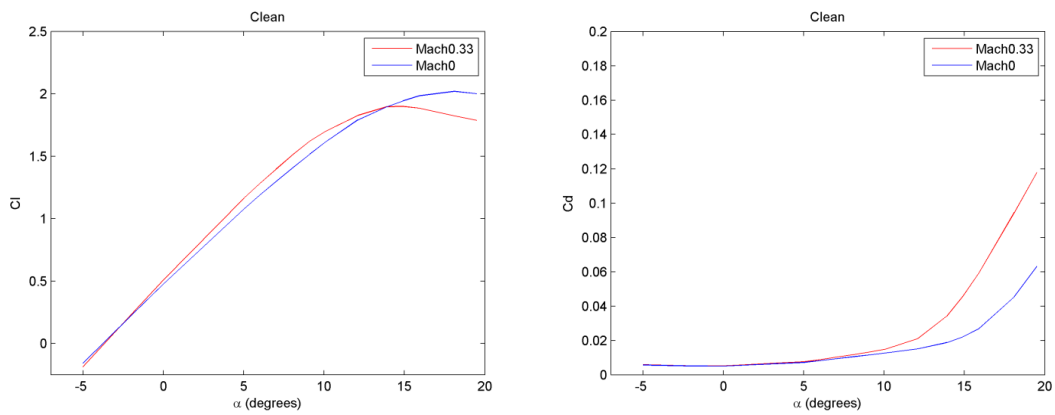


Figure 6.14: Comparisons of the performance of a clean DTU-210-21 airfoil with/without Mach number effect

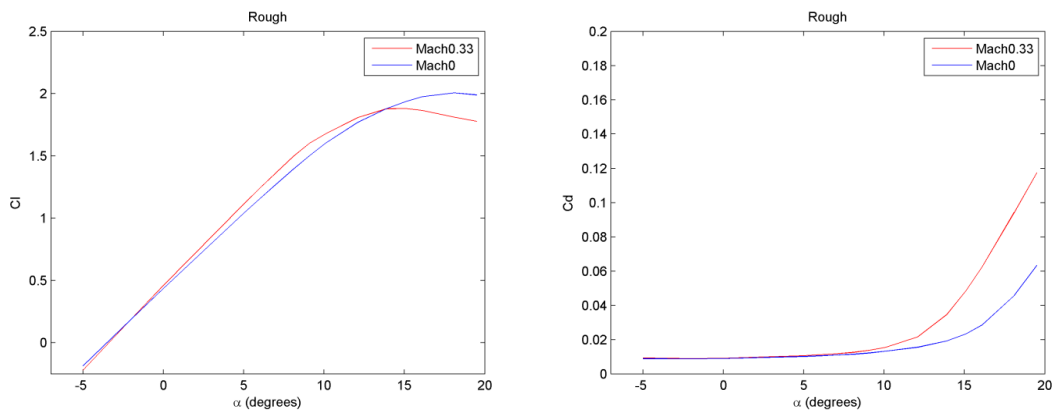


Figure 6.15: Comparisons of the performance of a rough DTU-210-21 airfoil with/without Mach number effect

## CHAPTER 7 SUMMARY AND CONCLUSIONS

### 7.1 Detailed conclusions and assessment

In Chapter 2 new airfoils to large offshore rotors were studied. A complete new airfoil family with three airfoils of 24%, 30% and 36% thickness was designed for replacement of the FFA airfoils on the original reference rotor design. The performance in terms of maximum lift over drag ratio was greatly improved, but the sudden onset of stall and performance decrease in rough conditions is not as desired.

Secondly in Chapter 2 the application of thick airfoils towards the outboard sections was studied using both the current as well as the newly developed airfoils. Hereto 4 blade planform redesigns were performed incorporating two different 30% thick airfoils instead of the 24% thick profile as used for the reference case. A concept with reduced chord length as well as increased absolute thickness was considered. Both quasi steady performance as well as dynamic load case performance in partial load was assessed in terms of power and loads. It becomes apparent that the trends in power performance between the concepts significantly differ between the quasi steady and dynamic simulations. The cause lies in the different performance in off-design conditions. As such it is recommended to use a 'weighted' average over a specified angle of attack range as a criterion for airfoil performance optimization instead of maximum lift over drag ratio together with a stall margin.

Based on the current design investigations, the overall performance of the thick airfoil concepts is judged to be promising. The power performance penalty is limited to non-existent, while the fatigue loads or blade mass show a promising decrease depending on the implementation of the thick airfoils.

Using 2D and 3D CFD calculations CENER have in Chapter 3 investigated the basic aerodynamics in the root region of the INN WIND.EU reference blade. The study of the flow around the blade root shows that this area is characterized by important 3D effects. This region is the most affected by the radial flow. Moreover, the 3D effects are also very important. The airfoils operating on the rotating blade show delayed separation and important differences in pressure and friction coefficients. Another important conclusion obtained is that the airfoils designed with 2D aerodynamic calculations for the root area will experiment bigger lift coefficients when working in the blade root area.

CENER designed four new airfoils for the blade root region, two of them with a thickness of 40% and another two with a thickness to chord ratio of 50%. The new airfoils focus on providing high lift in a wide range of angles of attack, good contaminated performance and smooth stall behaviour. Generally speaking, the airfoils obtained match the design objective of improving high lift coefficient for both clean and rough configurations even though it penalizes the aerodynamic efficiency. For instance, one of the 50% thickness airfoils designed (L11T6) improves the behaviour in contaminated conditions with regard to the airfoil in the INN WIND.EU reference blade.

The last part of CENER work analyses some trailing edge devices effects on one of the designed airfoils. The tripping of the airfoils show how well the airfoil behaves in contaminated conditions. The gurney flap gets an increase in the lift coefficient but with increasing also the drag coefficient. And finally, the splitter plate seems to be able to reduce the drag coefficient of the airfoils.

Airfoil designs for the LIR rotor design were presented by CRES in Chapter 4. The design produced whole families of low-lift profiles with relative thicknesses 15%, 18%, 21%, 24%, 30% and 40%.

Two low-lift and one high-lift airfoil family was designed, the last for comparison purposes. The low-lift families differ in the laminar / turbulent weighting which is driving the design. Using a higher weight for the laminar part the maximum thickness of the profile is moving backwards and its performance around the design point is increasing but at the same time worsens when the profile operates at fully turbulent conditions. In the present case the weighting was set to 30%-70% for one of the low lift and the high lift family. 10-90 (or 20-80) were the weights for the second low lift family. The 10-90/20-80 family looks more consistent, both geometrically (location of maximum thickness) and performance wise (changing monotonically with the thickness), than the 30-70 one. For these reasons and for introducing some conservatism to the possible energy capture gains of the low induction rotor it was suggested to use this family for the PI evaluation of the low induction rotors.

Airfoils from the 10-90/20-80 family were further analysed by CFD at NTUA and the results were presented in Chapter 5. The analysis showed that the low induction airfoils designed by CRES exhibit a remarkably high performance at the design point  $CL_{DES}=0.8$ , as predicted by different simulation tools. For the 18% airfoil the predicted performance is higher than 135 at transitional flow conditions and higher than 85 at fully turbulent conditions. For the thickest airfoil of 30% the predicted performance decreases but still remains higher than 100 and 60 at transitional flow and fully turbulent conditions respectively.

NTUA investigated also in wind tunnel tests various drag reduction devices on a 30% airfoil. The devices were built up of 2mm thick aluminium plates with a width slightly lower than the blunt trailing edge. The plate was added either as a single element on the mid part of the TE forming a Splitter plate or by two plates extending the suction and pressure side, respectively, forming a Cavity. The measurements showed that the devices reduce the drag below stall and reduce the flow unsteadiness. It seems thus promising to use such devices on the inboard airfoils with a blunt trailing edge.

Finally, NTUA analysed by CFD an interesting airfoil with an elliptic cross section. Such forms give the opportunity to apply fast manufacturing and have higher structural properties. At high thicknesses they are suitable for installation in the root region of the blade instead of flat-back airfoils while at larger radial stations they could substitute conventional airfoils by equipping them with extendable flaps or other devices and sets up of the kind presented. Comparing the simulated polars for the NACA64418 it is found as expected that the elliptically shaped airfoil has lower lift and higher drag at low angles of attack so its efficiency drops. However, as the angle of attack increases, the trend reverses. Also the characteristics of the wake indicate the formation of elongated shear regions that are more quickly diffused.

The airfoil design taking into account compressible effects was investigated by DTU and presented in Chapter 6. First the compressible effects on the polars were assessed and it was found that the compressible lift coefficient in the linear region is about 5% larger than the incompressible one at a Mach number of 0.3. Looking closer at the pressure

distribution around the airfoil, the minimum pressure coefficient on the suction side is lower than the incompressible one, which results in the increase of lift.

Next an 18% airfoil was designed for the tip part of the two-blade version of the reference rotor [1] for a tip speed of 110m/s and a tip speed ratio of 10. The optimization target was maximizing the power coefficient and minimizing the rotor solidity with an equal weight on the two parameters. Very good insensitiveness to roughness was observed for the new airfoil which resulted in a power coefficient of about 0.52 for the two bladed rotor which is quite high.

## 7.2 Final comments to airfoil design

It seems that the airfoil design process in almost all cases is influenced by the uncertainty about what turbulence levels the airfoils should be designed at. If a low turbulence level is assumed some high performance airfoils can be designed. However, it is also found that if the actual turbulence level combined e.g. with roughness from bugs is higher than assumed in the design process then the airfoil can have a substantial lower performance compared with a more conservative designed airfoil. More specific information on the operational conditions as concerns influence of the atmospheric turbulence conditions on transition is highly needed.

Almost all airfoil designs are now carried out using numerical optimization procedures. The challenging part is to formulate the optimal constraints and to formulate precisely the optimization target. For the latter it is a challenge for example how to weight structural characteristics against margins to stall and against lift to drag ratio.

## REFERENCES

- [1] “New aerodynamics rotor concepts specifically for very large offshore wind turbines, Edited by H.A. Madsen, L. Bergami and F. Rasmussen. INN WIND.EU D2.11 Deliverable, Sept 2013.”.
- [2] K. Schittkowski, “NLPQLP: A new Fortran implementation of a sequential quadratic programming algorithm - user’s guide, version 1.6,” Department of Mathematics, University of Bayreuth, 2001.
- [3] F. Grasso, “Multi-Objective Numerical Optimization Applied to Aircraft Design,” Università di Napoli Federico II, Naples, Italy, 2008.
- [4] R. v. Rooij, “Modification of the boundary layer calculation in RFOIL for improved airfoil stall prediction,” TU-Delft, 1996.
- [5] M. Drela, “XFOIL: An Analysis and Design System for Low Reynolds Number Airfoils, Conference on Low Reynolds Number Airfoil Aerodynamics,” University of Notre Dame, 1989.
- [6] G. Ramanujam, “Improving Aerodynamic Prediction Methods for Wind Turbine Airfoils,” MSc Thesis, University of Twente, 2015.
- [7] C. Lindenburg, “PHATAS Release ‘APR-2005n’ USERS’s MANUAL. Program for Horizontal Axis wind Turbine Analysis and Simulation,” in *ECN-I-05-005 (revision 8)*, 2011.
- [8] C. Lindenburg, J.G. Schepers, “PHATAS-IV aeroelastic modelling, release “DEC-1999” and “NOV-2000”,” in *ECN-CX-00-027*, 2000.
- [9] H. A. Madsen, F. Bertagnolio, A. Fischer and C. Bak, “Correlation of amplitude modulation to inflow characteristics,” in *Internoise 2014*, Melbourne, 2014.
- [10] E.T.G. Bot, O. Ceyhan, “Blade Optimization Tool User Manual,” in *ECN-E-09-092*.
- [11] “FAST description by Janson Jankman (NREL),” [Online]. Available: <https://nwtc.nrel.gov/FAST>. [Accessed 26 08 2015].
- [12] An evaluation of several methods of determining the local angle of attack on wind turbine blades, S Guntur, N N Sorensen, DTU.
- [13] “Timmer and Van Rooij (Delft University Wind Energy Research Institute), Summary of the Delst university wind turbine dedicated airfoils”.
- [14] “Van Rooij and Timmer, Delft University Wind Energy Research Institute, Roughness sensitivity considerations for thick rotor blade airfoils”.
- [15] “Haoran Xu et al., Aerodynamic analysis of trailing edge enlarged wind turbine airfoils”.
- [16] “D Althaus and F X WortmannStuttgarter Profilkatalog, Universität Stuttgart. Institut für Aerodynamik und Gasdynamik.”.
- [17] “M Drela, Integral boundary layer formulation for blunt trailing edge airfoils”.
- [18] “F Hoerner, Fluid-Dynamic drag”.
- [19] “Hoerner and Borst, Fluid-dynamic lift”.
- [20] “DAKOTA, a multilevel parallel object-oriented framework for design optimization, parameter estimation, uncertainty quantification, and sensitivity analysis: Version 4.0 reference manual. M. S. Eldred et al.”.
- [21] “DAKOTA, A multilevel parallel object-oriented framework for design optimization, parameter estimation, uncertainty quantification, and sensitivity analysis: Version 4.0 User’s Manual. M. S. Eldred”.
- [22] “P.K. Chaviaropoulos and G. Sieros, “Design of Low Induction Rotors for use in large offshore wind farms”, Proc. Scientific Track, EWEA 2014, Barcelona”.
- [23] *New aerodynamics rotor concepts specifically for very large offshore wind turbines, Edited by H.A. Madsen, L. Bergami and F. Rasmussen. INN WIND.EU D2.11 Deliverable, Sept 2013.*
- [24] *Papadakis G. and Voutsinas S.G. 2014 In view of accelerating cfd simulations through*

- coupling with vortex particle approximations in: The Science of Making Torque from Wind Journal of Physics: Conference Series, IOP Publishing Copenhagen pp. 012126.*
- [25] Venkatakrishnan V. 1993 'On the accuracy of limiters and convergence to steady state solutions,' AIAA Paper 93-0880.
- [26] Robin B. Langtry, Florian R. Menter : "Correlation-Based Transition Modeling for Unstructured Parallelized Computational Fluid Dynamics Codes", AIAA Journal, Vol. 47, No. 12, December 2009..
- [27] H. Schlichting : "Boundary Layer Theory", McGraw-Hill, 1968.
- [28] Riziotis V.A. and Voutsinas S.G. 2008 Dynamic stall modelling on airfoils based on strong viscous–inviscid interaction coupling International Journal for Numerical Methods in Fluids 56 2 185-208.
- [29] Barlow, J. B., W. H. Rae, et al. (1999). Low-speed wind tunnel testing. New York, John Wiley & Sons..
- [30] Westerweel, J. (2000). "Theoretical analysis of the measurement precision in particle image velocimetry." *Experiments in Fluids*29(1): S003-S012..
- [31] Foucaut, J. M., B. Miliat, et al. (2004). Characterization of different PIV algorithms using the EUROPIV synthetic image generator and real images from a turbulent boundary layer. *Particle Image Velocimetry: Recent Improvements, Springer: 163-185..*
- [32] Castaignet, D., T. Barlas, et al. (2014). "Full-scale test of trailing edge flaps on a Vestas V27 wind turbine: active load reduction and system identification." *Wind Energy*17(4): 549-564..
- [33] Z. WJ, W. Shen and J. Sørensen, " , Shen WZ, Sørensen JN, "Integrated airfoil and blade design method for large wind turbines," *Renewable Energy*, vol. 70, pp. 172-183, 2014.
- [34] N. Garcia, J. Sørensen and W. Shen, "Garcia NR, Sørensen JN, Shen WZ, "A strong viscous-inviscid interaction model for rotating airfoils," *Wind Energy*, vol. 17, pp. 1957-1982, 2014.

